Unsteady Aerodynamic and Aeroelastic Analysis of Flapping Flight

Pradeep Gopalakrishnan

Dissertation submitted to the faculty of the Virginia Polytechnic Institute and State University in partial fulfillment of the requirements for the degree of

Doctor of Philosophy
In
Mechanical Engineering

Dr. Danesh K. Tafti, Chair
Dr. Kenneth S. Ball
Dr. Mark Paul
Dr. Adrian Sandu
Dr. Robert W. Walters

December 8, 2008
Blacksburg VA

Keywords: Micro air vehicles, Flapping flight aerodynamics, Hovering flight, Forward flight, Flexible flapping wing, Boundary fitted moving grid, Large Eddy Simulation, Aeroelastic analysis

Unsteady Aerodynamic and Aeroelastic Analysis of Flapping Flight

Pradeep Gopalakrishnan

Abstract

The unsteady aerodynamic and aeroelastic analysis of flapping flight under various kinematics and flow parameters is presented in this dissertation. The main motivation for this study arises from the challenges facing the development of micro air vehicles. Micro air vehicles by requirement are compact with dimensions less than 15-20 cm and flight speeds of around 10-15 m/s. These vehicles operate in low Reynolds number range of 10,000 to 100,000. At these low Reynolds numbers, the aerodynamic efficiency of conventional fixed airfoils significantly deteriorates. On the other hand, flapping flight employed by birds and insects whose flight regime coincides with that of micro air vehicles offers a viable alternate solution.

For the analysis of flapping flight, a boundary fitted moving grid algorithm is implemented in a flow solver, *GenIDLEST*. The dynamic movement of the grid is achieved using a combination of spring analogy and trans-finite interpolation on displacements. The additional conservation equation of space required for moving grid is satisfied. The solver is validated with well known flow problems such as forced oscillation of a cylinder, a heaving airfoil, a moving indentation channel, and a hovering fruitfly.

The performance of flapping flight is analyzed using Large Eddy Simulation (LES) for a wide range of Reynolds numbers and under various kinematic parameters. A spiral Leading Edge Vortex (LEV) forms during the downstroke due to the high angle of attack, which results in high force production. A strong spanwise flow of the order of the flapping velocity is observed along the core of the LEV. In addition, the formation of a negative spanwise flow is observed due to the tip vortex, which slows down the removal of vorticity from the LEV. This leads to the instability of the LEV at around mid-downstroke. Analysis with different rotation kinematics shows that a continuous rotation results in better propulsive efficiency as it generates thrust during the entire flapping cycle. Analysis with different angles of attack shows that a moderate angle of attack which results in complete shedding of the LEV offers high propulsive efficiency. The analysis of flapping flight at Reynolds numbers ranging from 100 to 100,000 shows that higher lift and thrust values are obtained for $Re \geq 100$. The critical reasons are that at higher Reynolds numbers, the LEV is closer to the surface and as it sheds and convects it covers most of the upper surface. However, the Reynolds number has no or little effect on the lift and thrust as identical values are obtained for Re=10,000 and 100,000. The analysis with different tip shapes shows that tip shapes do not have a significant effect on the performance. Introduction of stroke deviation to kinematics leads to drop in average lift as wing interacts with the LEV shed during the downstroke.

A linear elastic membrane model with applied aerodynamic load is developed for aeroelastic analysis. Analysis with different wing stiffnesses shows that the membrane wing outperforms the rigid wing in terms of lift, thrust and propulsive efficiency. The main reason for the increase in force production is attributed to the gliding of the LEV along the camber, which results in a high pressure difference across the surface. In addition, a high stiffness along the spanwise direction and low stiffness along the chordwise direction results in a uniform camber and high lift and thrust production.

To my family

Acknowledgement

Working on my PhD dissertation was a rewarding experience. I would like to thank my mentors, friends and family for their support and making this experience more enjoyable. I would like to thank first and foremost my advisor, Dr. Danesh Tafti. He consistently motivated me towards success and provided support when needed. He was always there for us in the lab and I am grateful for his guidance in making this dissertation a success.

I would like to thank my committee members Dr. Kenneth Ball, Dr. Mark Paul, Dr. Adrian Sandu, and Dr. Robert Walters for providing constructive feedback. I would also like to thank Dr. Mayuresh Patil for his help in developing the membrane model for the wing.

I would like to thank all my lab mates: Aroon, Ali, Mohammad, Sai, Naresh, Jose, Kohei, Sunil, Amit, John and Nagi, for making the lab a fun place for research. I greatly enjoyed all the wonderful discussions in the lab which covered almost every aspect in the world.

I specially thank all my Blacksburg friends: Ajit, Anu, Avyu, Arun, Rajesh, Parthi, Siva and Vidya. They made my stay at Blacksburg enjoyable with many pleasant memories, which I will cherish forever. I greatly enjoyed their company and I am thankful for their friendship.

Finally I would like to thank my family: my mom, dad and sister. Even though they are 8000 miles away from Blacksburg they offered me unconditional love and the best support one can ever wish for.

Table of Contents

List of Figures

Chapter 1

Chapter 2

Chapter 3

Chapter 4

Chapter 5

Appendix

List of Tables

Chapter 1: Introduction

Micro Air Vehicles (MAVs) by virtue of their small size and maneuverability can provide an indispensable vehicle for advance surveillance and reconnaissance missions. MAVs by requirement are compact with dimensions less than 15-20 cm and flight speeds of around 10-15 m/s with gross takeoff weights of 200g or less and which operate in the low Reynolds number (10,000-100,000) regime. At these low Reynolds numbers, the aerodynamic efficiency (lift to drag ratio) of conventional fixed airfoils rapidly deteriorates at Re<100,000 as shown in Fig.1.1 from McMasters and Henderson[1].The chief reason for the deterioration in the performance is that at low Reynolds numbers, the boundary layer remains laminar downstream of the location of minimum pressure on the airfoil making it very susceptible to flow separation as the angle of attack increases resulting in an early onset of stall (Carmichael[2]). In addition, because of the low aspect ratio wings used in MAVs, the tip vortex covers a major part of the wing and the aerodynamic performance is affected greatly by the shedding of the tip vortices (Pelletier et al.[3]).

Small birds and insects whose flight regime coincides with that of MAVs use flapping wings to provide both lift and thrust to overcome the deteriorating performance of fixed wings. They do this by taking advantage of unsteady flow mechanisms using wing kinematics evolved over millions of years. The kinematics of wing motion is often a complex combination of translation and rotation in the stroke plane with significant morphological changes for optimal flow control. Hence understanding the unsteady aerodynamics of flapping wings is critical to the design of efficient MAVs. Whereas it may not be possible to mimic the exact nature of bird and insect flight in its full natural complexity, understanding the major unsteady flow mechanisms employed for efficient flight and translating those to simple kinematics is required.

A number of unsteady aerodynamic mechanisms such as *clap and fling*[4], *delayed stall*[5,6], *wake capturing*[7], and, *rotational circulation*[7] have been proposed to explain the generation of lift in birds and insects. The clap and fling mechanism was proposed by Weis and Fogh[4] based on the flight of small wasps. This mechanism is

used by small insects whose flight regime ranges from Reynolds number of 10-100. The main disadvantage of clap and fling mechanism is the mechanical damage caused to the wings. This and the fact that the mechanism loses its lift producing effectiveness at higher Reynolds number (Re>200) [8-10], clap and fling is only limited to very small insects and is not used by larger insects and birds.

In case of large insects and birds, the wing stroke typically consists of four kinematic portions: two translational phases (upstroke and downstroke) with high angles of attack, and two rotational phases (pronation and supination), where the wing rapidly rotates and reverses its direction. During the downstroke, air swirls around the leading edge and forms a Leading Edge Vortex (LEV). This LEV increases the bound vortex circulation and hence the lift (Fig.1.2). In a fixed airfoil, the formation of the LEV leads to dynamic stall within 3-4 chord lengths of travel. However in insects, the LEV is stable for the entire downstroke and during this period, the insect covers a distance of more than 8 chord lengths. The stability of the LEV which leads to *delayed stall* is responsible for the high lift production.

While delayed stall explains the lift generated during the translational kinematics, *rotational circulation* and *wake capture* mechanisms are proposed for the high lift produced during the rotational period. However, the validity of these models is unclear and some studies[11,12] have provided alternate reasoning for enhanced force production during the rotational period. The relative contribution of these mechanisms varies according to the kinematics of wing motion and flight conditions. However, since wing translation usually comprises a major part of the kinematics, the LEV dynamics is the most influential factor affecting overall lift and thrust generated by a flapping wing.

For successful development of the MAV, it is necessary to develop a reliable and efficient tool for analyzing the complex nature of flapping flight under various conditions. Earlier attempts were made to develop analytical models derived from aerodynamic theories to explain the generation of lift and thrust produced by flapping flight. Conventional steady state aerodynamic theories do not account for flow separation near the leading edge and the unsteady vortex shedding, which are critical ingredients of

flapping flight. Hence, many studies built quasi-steady, and unsteady models [13-20] by including unsteady effects into existing aerodynamic theories. However, the applicability of these models to a wide range of parameters remains questionable. Experimental studies[7,21-25] have focused on hovering flight to identify critical flow structures involved in the flapping flight. These studies either involved flow visualization of actual insect flight or the use of mechanical models. They provided insight into the unsteady mechanisms, in particular the delayed stall mechanism, and the structure of the LEV. Critical draw backs of experimental investigations are difficulties in changing the kinematics, in simulating all possible flight conditions, and in measuring lift and thrust. Recently CFD studies mostly focusing on hovering flight [10,26-28] have been carried out. These studies employ different moving grid techniques such as rigid rotation, overset grid method and boundary fitted finite volume method based on Arbitrary Legrangian-Eulerian (ALE) method to simulate flapping flight. The main advantages of the CFD studies are that they provide high fidelity solutions and can be readily applied to different kinematics and different flight conditions.

Despite a large number of studies available related to flapping flight, there are a number of shortcomings in the following areas.

- There are no studies available for flapping flight at Reynolds number in the range of 10,000 to 100,000, which is more relevant to MAVs.
- Insects employ different kinematics at different flight conditions to achieve the required thrust[22]. However, most of the previous studies have concentrated only on hovering flight, which require no thrust.
- Analysis of *flexible* flapping wing involves complex non-linear interactions of aeroelastic and aerodynamic effects. In order to reduce the complexity of the problem, previous studies have used 2D analysis and/or simplified the motion into pitching and plunging airfoil[29-31] and/or simplified the aerodynamic analysis using potential flow solutions[32] and/or made the assumption of low Reynolds numbers.

- Most of the previous computational studies have used either overset grid methods or immersed boundary methods. These methods are accurate at low Reynolds number unsteady flows (large scale laminar unsteady structures, thick boundary layers, etc.), but progressively deteriorate in accuracy at higher Reynolds numbers which are more relevant to MAVs – the immersed boundary method diffuses out near wall shear layers, whereas volume interpolation errors between grids in an overset method has an adverse effect on resolved grid turbulence
- For an accurate analysis of flapping flight at high Reynolds number it is necessary to resolve complex three-dimensional turbulent flow. Most of the previous studies employed either URANS[31] or more recently DES modeling[30] for this purpose. These methods are not particularly accurate in predicting transitioning shear layers[33] which play an important role in the breakdown of LEV and tip vortex. Hence, LES capability is needed, which does an excellent job in capturing shear layer transition.

The thesis focuses on developing a high fidelity CFD solver for complex boundary movement and application to unsteady aerodynamics and aeroelastic analysis of forward flapping flight. The dissertation presents the work in four standalone chapters. In the second chapter, the development of the boundary fitted moving grid solver in a structured-multiblock framework is presented. The solver is capable of resolving the complex boundary movement and it offers high accuracy even at high Reynolds numbers as the boundary is fully resolved. In addition, the solver has a wide range of turbulence modeling capability ranging from Unsteady Reynolds Averaged Navier-Stokes equation (URANS) to Large Eddy Simulation (LES). The solver is validated with classical flow problems such as forced oscillation of a cylinder, a heaving airfoil, and a moving indentation channel (Appendix). Further, its capability in simulating complex boundary movement is illustrated with a two-dimensional analysis of dragonfly flight (Appendix), and with an analysis of hovering fruitfly. The third chapter details the first study made in analyzing the effect of kinematic parameters on the performance of a forward flapping flight at Re=10,000 using LES. The timing and duration of rotation kinematics and the

angle of attack are varied and their effects on the aerodynamics performance are studied based on the resulting flow structures and the lift and thrust variation. The fourth chapter presents the simulations carried out at Reynolds numbers ranging from 100 to 100,000 and their effect on the aerodynamic performance. In addition, analysis is carried out with different wing tip shapes and with stroke deviation introduced into the kinematics. Their effects on the stability of the LEV and on force production are analyzed. In the fifth chapter, the development of a linear elastic membrane model (Appendix) used for the aeroelastic analysis and its coupling with the flow solver are detailed. The aeroelastic analysis is carried out with different pre-stress conditions and the effect of wing deformation on the flow structure and force production is investigated.

1.1 Figures

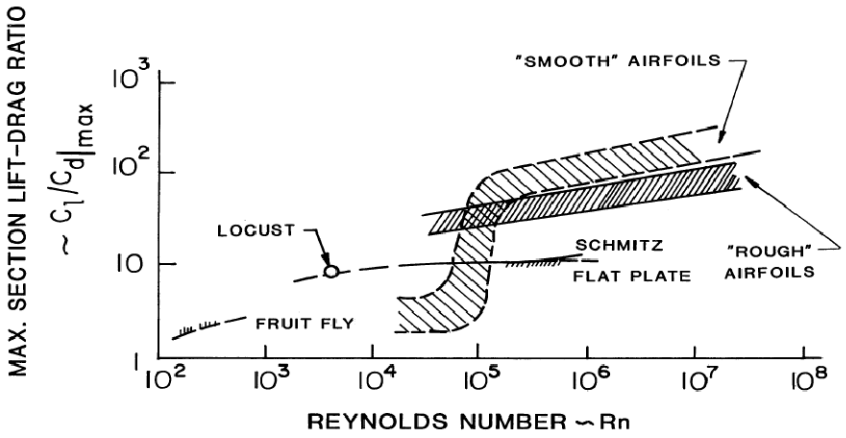

From Mcmasters, J. H. and Henderson, M. L., Tec. Soaring, 1980[1]

Fig.1.1 Variation of aerodynamic efficiency with Reynolds number. The aerodynamic efficiency of the smooth airfoils drops rapidly when Reynolds number is less than 100,000

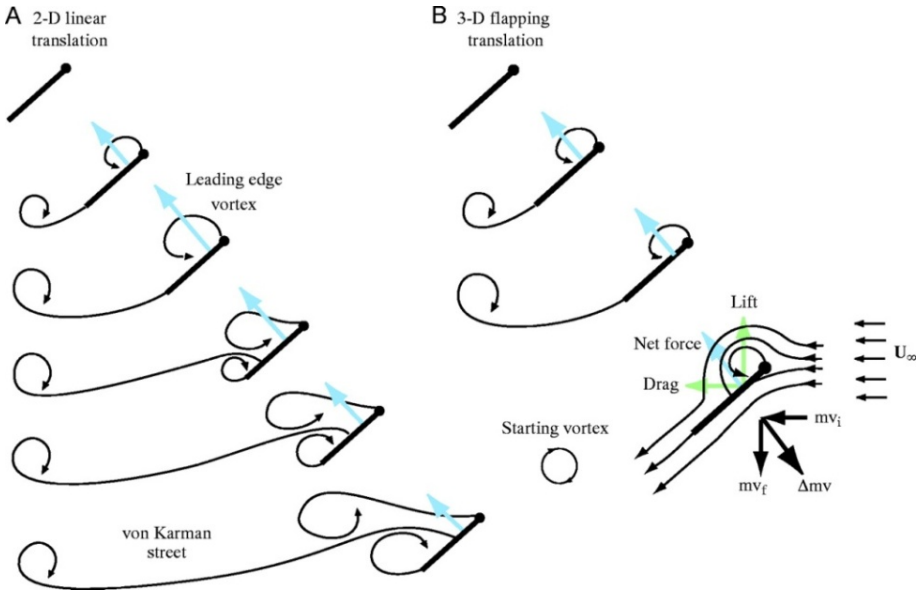

From Sane, Journal of Experimental Biology, 2003[34]

Fig.1.2 2-D linear translation compared to 3-D Flapping translation A) 2-D translation forms leading and trailing vortex at the start. During translation, the trailing vortex sheds leading to the growth of LEV followed by its shedding. B) In case of 3D flapping, at the start of translation, leading and trailing edge vortices form similar to 2-D. After the trailing vortex sheds, the LEV does not grow and reaches a constant size.

1.2 References

[1] Mcmasters, J. H. and Henderson, M. L. Low Speed Single Element Airfoil Synthesis. Tec. Soaring 1980;2:1-21.

[2] Carmichael, B. H., "Low Reynolds Number Airfoil Survey," NASA Contractor Report (Nov 1981).

[3] Pelletier, A. and Mueller, T. J. Low Reynolds Number Aerodynamics of Low-Aspect-Ratio, Thin/Flat/Cambered-Plate Wings. Journal of Aircraft Oct 2005;37:825-832.

[4] Weis-Fogh, T. Quick Estimate of Flight Fitness in Hovering Animals, Including Novel Mechanisms for Lift Production. The Journal of Experimental Biology 1973;59:169-230.

[5] Dickinson, M. H. and Götz, K. G. Unsteady Aerodynamic Performance of Model Wings at Low Reynolds Numbers. The Journal of Experimental Biology 1993;174:45-64.

[6] Ellington, C. P., Berg, C. V. D., Willmott, A. P., and Thomas, A. L. R. Leading-Edge Vortices in Insect Flight. Nature 1996;384:626-630.

[7] Dickinson, M. H., Lehmann, F.-O., and Sane, S. P. Wing Rotation and the Aerodynamic Basis of Insect Flight. Science 1999;284:1954-1960.

[8] Lehmann, F.-O., Sane, S. P., and Dickinson, M. The Aerodynamic Effects of Wing–Wing Interaction in Flapping Insect Wings. The Journal of Experimental Biology 2005;208:3075-3092.

[9] Miller, L. A. and Peskin, C. S. A Computational Fluid Dynamics of 'Clap and Fling' in the Smallest Insects. The Journal of Experimental Biology 2005;208:195-212.

[10] Sun, M. and Yu, X. Aerodynamic Force Generation in Hovering Flight in a Tiny Insect. AIAA Journal July 2006;44:1532-1540.

[11] Walker, J. A. Rotational Lift: Something Different or More of the Same? The Journal of Experimental Biology 2002;205:3783-3792.

[12] Sun, M. and Tang, J. Unsteady Aerodynamic Force Generation by a Model Fruit Fly Wing in Flapping Motion. The Journal of Experimental Biology 2002;205:55-70.

[13] Osborne, M. Aerodynamics of Flapping Flight with Application to Insects. The Journal of Experimental Biology 1951;28:221-245.

[14] Zbikowski, R. On Aerodynamic Modeling of an Insect-Like Flapping Wing in Hover for Micro Air Vehicles. Phil. Trans. R. Soc. Lond. A Jan 2002;360:273-190.

[15] Ansari, S. A., Zbikowski, R., and Knowles, K. Aerodynamic Modelling of Insect-Like Flapping Flight for Micro Air Vehicles. Progress in Aerospace Sciences 2006;42:129-172.

[16] Ellington, C. The Aerodynamics of Hovering Insect Flight I. The Quasi-Steady Analysis. Philosophical Transactions of the Royal Society of London 1984;305:1-15.

[17] Ellington, C. The Aerodynamics of Hovering Insect Flight IV. Aerodynamic Mechanisms. Philosophical Transactions of the Royal Society of London 1984;305:79-113.

[18] Ellington, C. The Aerodynamics of Hovering Insect Flight VI. Lift and Power Requirements. The Journal of Experimental Biology 1984;305:145-181.

[19] Walker, J. and Westneat, M. Mechanical Performance of Aquatic Rowing and Flying. Proc. R. Soc. London Ser B 2000;267:1875-1881.

[20] Sane, S. P. and Dickinson, M. H. The Aerodynamic Effects of Wing Rotation and a Revised Quasi-Steady Model of Flapping Flight. The Journal of Experimental Biology 2002;205:1087-1096.

[21] Ellington, C. P. The Novel Aerodynamics of Insect Flight: Applications to Micro-Air Vehicles. The Journal of Experimental Biology 1999;202:3439–3448.

[22] Thomas, A. L. R., Taylor, G. K., Srygley, R. B., Nudds, R. L., and Bomphrey, R. J. Dragonfly Flight: Free-Flight and Tethered Flow Visualizations Reveal a Diverse Array of Unsteady Lift-Generating Mechanisms, Controlled Primarily Via Angle of Attack. The Journal of Experimental Biology 2004;207:4299-4323.

[23] Sane, S. P. and Dickinson, M. H. The Control of Flight Force by a Flapping Wing: Lift and Drag Production. The Journal of Experimental Biology 2001;204:2607-2626.

[24] Dickinson, M. H. The Effects of Wing Rotation on Unsteady Aerodynamic Performance at Low Reynolds Numbers. The Journal of Experimental Biology 1994;192:179-206.

[25] Tarascio, M. J., Ramasamy, M., Chopra, I., and Leishman, J. G. Flow Visualization of Micro Air Vehicle Scaled Insect-Based Flapping Wings. Journal of Aircraft Apr 2005;42:385-390.

[26] Liu, H., Ellington, C. P., Kawachi, K., Berg, C. V. D., and Willmott1, A. P. A Computational Fluid Dynamic Study of Hawkmoth Hovering. The Journal of Experimental Biology 1998;201:461–477.

[27] Wang, J. K. and Sun, M. A Computational Study of the Aerodynamics and Forewing–Hindwing Interaction of a Model Dragonfly in Forward Flight. The Journal of Experimental Biology 2005;208:3785-3804.

[28] Ramamurti, R. and Sandberg, W. A Three-Dimensional Computational Study of the Aerodynamic Mechanisms of Insect Flight. The Journal of Experimental Biology May 2002;205:1507-1518.

[29] Tang, J., Viieru, D., and Shyy, W. Effects of Reynolds Number and Flapping Kinematics on Hovering Aerodynamics. 45th AIAA Aerospace Sciences Meeting and Exhibit, Reno, Nevada Jan 2007;

[30] Lian, Y., Ol, M. V., and Shyy, W. Comparative Study of Pitch-Plunge Airfoil Aerodynamics at Transitional Reynolds Number. 46th AIAA Aerospace Sciences Meeting and Exhibit, Reno, Nevada Jan 2008;

[31] Unger, R., Haupt, M. C., Horst, P., and Windte, J. Structural Design and Aeroelastic Analysis of an Oscillating Airfoil for Flapping Wing Propulsion. 46th AIAA Aerospace Sciences Meeting and Exhibit, Reno, Nevada January 2008;

[32] Gogulapati, A., Friedmann, P. P., and Shyy, W. Nonlinear Aeroelastic Effects in Flapping Wing Micro Air Vehicles. 49th AIAA/ASME/ASCE/AHS/ASC Structures, Structural Dynamics, and Materials, Schaumburg, IL April 2008;

[33] Viswanathan, A. K. and Tafti, D. K. Detached Eddy Simulation of Turbulent Flow and Heat Transfer in a Two-Pass Internal Cooling Duct. Int. J. Heat and Fluid Flow 2006;27:1-20.

[34] Sane, S. P. The Aerodynamics of Insect Flight. Journal of Experimental Biology 2003;206:4191-4208.

Chapter 2: A Parallel Boundary Fitted Dynamic Mesh Solver for Applications to Flapping Flight[‡]

Abstract

A parallel numerical solution procedure for unsteady incompressible flow is developed for simulating the dynamics of flapping flight. A collocated finite volume multiblock approach in a general curvilinear coordinate is used with Cartesian velocities and pressure as dependent variables. The Navier-Stokes equations are solved using a fractional-step algorithm. The dynamic grid algorithm is implemented by satisfying the space conservation law by computing the grid velocities in terms of the volume swept by the faces. The dynamic movement of grid in a multiblock approach is achieved by using a combination of spring analogy and Trans-Finite interpolation. The spring analogy is used to compute the displacement of block corners, after which Trans-Finite interpolation is applied independently on each computational block. The performance of the code is validated in forced transverse oscillations of a cylinder in cross flow, a heaving airfoil, and hovering of a fruitfly. Finally, the unsteady aerodynamics of flapping flight at Re=10,000 relevant to the development of micro air vehicles is analyzed for forward flight. The results show the capability of the solver in predicting unsteady aerodynamics characterized by complex boundary movements.

Nomenclature

$\vec{a}^{i}$ = Contravariant basis vectors

a = Amplitude of oscillation

A = a/D, Non-dimensional amplitude of cylinder

C = Airfoil chord length

C_L = Coefficient of lift

C_T = Coefficient of thrust

D = Diameter of the cylinder

[‡] This chapter is submitted to Computers and Fluids on Jan 2008, and is currently under review.

E = Energy transfer from fluid to cylinder

f = Frequency of flapping

f_0 = fD/U_∞. Non-dimensional frequency of cylinder

$F_{x/y}$ = Force acting on the wing; suffix x, y- direction

g^{ij} = Contravariant metric tensor

$\sqrt{g}$ = Jacobian of the transformation

$\sqrt{g}U^j$ = Contravariant flux vector

$\sqrt{g}U^j_g$ = Contravariant flux due to grid movement

J = Advance ratio; U_∞/U_f; Ratio of the flight velocity to the flapping velocity

k = $2\pi fc/U_\infty$, Non-dimensional frequency of airfoil

h = a/c, Non-dimensional frequency of airfoil

kh = Plunge velocity

p = Pressure

$P_{x/\zeta}$ = Power required; suffix x- flapping and ζ - rotation

R = Semi-wingspan; distance from flapping axis to wing tip

Re = Reynolds number

Re_t = Inverse of the turbulent viscosity

u_i = Cartesian velocity vector

u_i^g = Cartesian Grid velocity vector

U_∞ = Free stream velocity; Forward flight velocity

U_f = Flapping velocity; $2\Phi fR$

$\vec{x}$ = Physical space coordinate

$\vec{\xi}$ = Computational space coordinate

$\alpha_{u/d/eff}$ = Angle of attack; suffix u-upstroke, d-downstroke, and eff-effective

β = Stroke plane angle

η_{prop} = Propulsive efficiency

ϕ = Flapping amplitude

Φ = Total flapping amplitude (max to min)

ν = Kinematic viscosity

ρ = Torsional angle

τ = Shear stress on the surface of the wing

ω_ζ = vorticity; suffix – ζ component

Ω_ζ = Angular velocity of the wing; suffix – ζ component

2.1 Introduction

Micro Air Vehicles (MAVs) by requirement are compact with dimensions less than 15-20 cm and flight speeds of around 10-15 m/s with gross takeoff weights of 200g or less and which operate in the low Reynolds number (10,000-100,000) regime. At these low Reynolds numbers, the aerodynamic efficiency (lift to drag ratio) of conventional fixed airfoils significantly deteriorates due to laminar flow separation, magnified effect of tip vortices, and inability to maintain steady flight in wind gusts. On the other hand, birds and insects employ flapping flight with considerable changes in wing orientation and angle of attack to generate thrust and lift for all flight conditions. Hence, understanding unsteady aerodynamics involved in flapping flight is critical for the development of light weight MAVs. The simulation of flapping flight poses a number of challenges. Chief among them is the ability to resolve the complex wing kinematics, which requires the resolution of the flow field near moving boundaries. One such method is the use of body-fitted dynamic grids.

Dynamic moving meshes have a wide range of practical applications in calculating free surface flows, fluid-structure interaction, and two phase flows, rotor-stator interaction, and flow in mixing vessels, among others. For these problems, a conventional Eulerian approach is not sufficient to represent the moving boundaries, whereas a purely Lagrangian approach will result in excessive mesh deformation. Hirt et al.[1] first presented the Arbitrary Lagrangian Eulerian (ALE) method for solving flow on a time-dependent grid, in which the solution is obtained in two phases. In the first phase, the solution is advanced by a Lagrangian step, followed by a rezoning phase which is solved using an Eulerian approach. The critical step in the ALE method is the rezoning phase,

where the grid movement can be chosen based on the flow field or boundary movement. Many previous studies employed ALE with slight modifications in the implementation to solve flow problems on moving grids such as fluid-structure interaction[2] and free surface flows[3-6].

Thomas et al.[7] solved hypersonic flow around blunted cones on moving grids by combining the Lagrangian and Eulerian phase of ALE into a single step. In this method, the Navier-Stokes are solved in a moving coordinate system, in which the effects of mass and momentum flux due to grid movement are included into the governing equations. In addition to the mass and momentum equations, an additional equation arises due to the deformation of the control volumes, which is termed as a Geometric Conservation Law (GCL) by Thomas et al.[7] and as Space Conservation Law (SCL) by Demirdzic[8,9]. The SCL condition relates the change in volume of a cell to the grid velocity. Many previous studies[7-9] showed that the failure to satisfy the SCL condition leads to artificial mass sources or sinks in the flow domain. The SCL condition was satisfied in Thomas et al.[7] by introducing a time dependent transformation of physical space into a curvilinear coordinate system, $\xi(t)$ and by computing the grid velocity based on $d\xi / dt$. In the study by Demirdzic[8], the SCL condition was satisfied for a two dimensional Cartesian grid by computing the grid velocity based on the known grid position. Demirdzic[8] also showed that the error involved in their method increased with time step. The method was later improved by Demirdzic[9], where the grid velocity was computed from the volume swept by the faces.

In moving boundary flow problems, the accuracy and stability of the solution is strongly dependent on the quality of the grid generated (rezoning) before each time step. The grid generation can be done in multiple ways[10] such as using elliptic grid generation methods[4,11-13], spring analogy methods[14], and algebraic grid generation methods[15-19]. Johnson et al.[11] solved the equation of linear elasticity, which is a Poisson equation for grid velocity, to generate the mesh based on the motion of fluid boundaries or interfaces. Ushijima et al.[4] used elliptic grid generation to generate a boundary conforming grid at every time step. These methods based on elliptic equations

can be applied to complex movements without a large deterioration of mesh quality. However, solving a Poisson equation at each time step is computationally expensive. In the spring analogy[14], each edge of a cell is assumed to be a spring with stiffness inversely proportional to its length. The displacement of the node is then computed by solving a large system of equations based on static equilibrium, which is also computationally intensive. In unsteady flow problems, the grid has to be updated at each time step, which necessitates the use of a rezoning method having a low computational cost. Trans-Finite Interpolation (TFI) based on the displacement of block corners was employed to study the flow over pitching airfoils by Dubuc et al.[15] and Li et al.[19]. In addition to the TFI on corner displacements, the block corner displacement was computed based on spring analogy by Sadeghi et al.[18] and Tsai et al.[16]. These methods based on algebraic grid generation offer a good grid quality at a low computational cost. In the present study, TFI coupled with the spring analogy[16] is used for rezoning.

Previous studies have used different numerical methods and algorithms to solve for flow in moving coordinate systems depending on the application. Thomas et al.[7] used an implicit Beam and Warming method to solve the compressible flow equations on a moving structured grid. In the study by Demirdzic et al.[9], a SIMPLE like method was employed to solve incompressible flow in a moving indentation channel. Pan et al.[20] used Bell's Godunov-projection method to solve the flow inside a deforming tube. In this study, the Navier-Stokes equations are solved by a projection method[21] in a generalized coordinate system.

The objective of this paper is to develop a moving grid capability in a generalized coordinate Navier-Stokes solver[22] for direct and Large-Eddy Simulations (LES) of turbulence for application to flow problems with complex boundary movements. The paper describes in detail the conservative equations, the implementation of the SCL condition, and the method used for rezoning in a structured grid-unstructured block topology. The algorithm is then validated in forced vibrations of a cylinder in cross-flow, a plunging airfoil, and the hovering flight of a fruitfly. Finally, forward flapping flight at

Re=10000 is analyzed to identify the critical flow structures involved and their effect on force production.

2.2 Methodology

2.2.1 Governing Equations

The governing equations for unsteady incompressible viscous flow in a moving grid coordinate system consist of space, mass, and momentum conservation laws. The equations are mapped from physical $(\vec{x})$ to logical/computational space $(\vec{\xi})$ by a boundary conforming transformation $\vec{x} = \vec{x}(\vec{\xi})$, where $\vec{x} = (x, y, z)$ and $\vec{\xi} = (\xi, \eta, \zeta)$. The equations are non-dimensionalized by a suitable length (L^*) and velocity scale (U^*) and written in conservative nondimensional form as:

Space:

$$\frac{\partial}{\partial t}\left(\sqrt{g}\right) - \frac{\partial}{\partial \xi_j}\left(\sqrt{g} U^j_g\right) = 0 \tag{2.1}$$

Mass:

$$\frac{\partial}{\partial \xi_j}\left(\sqrt{g} U^j\right) = 0 \tag{2.2}$$

Momentum

$$\frac{\partial}{\partial t}\left(\sqrt{g} u_i\right) + \frac{\partial}{\partial \xi_j}\left(\left[\sqrt{g} U^j - \sqrt{g} U^j_g\right] u_i\right)$$

$$= -\frac{\partial}{\partial \xi_j}\left(\sqrt{g}\,(\vec{a}^{\,j})_i\, p\right) + \frac{\partial}{\partial \xi_j}\left(\left(\frac{1}{\mathrm{Re}} + \frac{1}{\mathrm{Re}_t}\right)\sqrt{g}\, g^{jk}\, \frac{\partial u_i}{\partial \xi_k}\right) \tag{2.3}$$

where $\vec{a}^{\,i}$ are the contravariant basis vectors, $\sqrt{g}$ is the Jacobian of the transformation, g^{ij} is the contravariant metric tensor, $\sqrt{g} U^j = \sqrt{g}\left(\vec{a}^{\,j}\right)_k u_k$ is the contravariant flux

vector, $\sqrt{g}U_g^j = \sqrt{g}\left(\vec{a}^j\right)_k u_k^g$ is the contravariant flux vector due to grid velocity u^g, u_i is the Cartesian velocity vector, and p is the pressure. In the above formulation, the grid velocity u^g is not used explicitly. Instead, the grid contravariant flux vector is employed which is directly computed based on the SCL. The non-dimensional time used is t^*U^*/L^* and the Reynolds number is given by U^*L^*/ν. Re_t is the inverse of the subgrid eddy-viscosity which is modeled as

$$\frac{1}{\mathrm{Re}_t} = C_s{}^2(\sqrt{g})^{2/3}\left|\overline{S}\right| \tag{2.4}$$

where $\left|\overline{S}\right|$ is the magnitude of the strain rate tensor given by $\left|\overline{S}\right| = \sqrt{2\overline{S_{ik}}\,\overline{S_{ik}}}$ and the Smagorinsky constant $C_s{}^2$ is obtained via the dynamic subgrid stress model (Germano et al.[23]). To this end, a second test filter, denoted by $\hat{G}$, is applied to the filtered governing equations with the characteristic length scale of $\hat{G}$ being larger than that of the grid filter, $\overline{G}$. The test filtered quantity is obtained from the grid filtered quantity by a second-order trapezoidal filter which is given by $\hat{\phi} = \frac{1}{4}(\overline{\phi}_{i-1} + 2\overline{\phi}_i + \overline{\phi}_{i+1})$ in one dimension. The resolved turbulent stresses, representing the energy scales between the test and grid filters, $L_{ij} = \widehat{\overline{u_i}\overline{u_j}} - \hat{\overline{u}}_i\hat{\overline{u}}_j$, are then related to the subtest, $T_{ij} = \widehat{\overline{u_i}\overline{u_j}} - \hat{\overline{u}}_i\hat{\overline{u}}_j$, and subgrid-scales stresses $\tau_{ij} = \overline{u_iu_j} - \overline{u}_i\overline{u}_j$ though the identity, $L_{ij}^a = T_{ij}^a - \hat{\tau}_{ij}^a$ The anisotropic subgrid and subtest-scale stresses are then formulated in terms of the Smagorinsky eddy viscosity model as:

$$\widehat{\tau_{ij}^a} = -2C_s^2(\sqrt{g})^{\frac{2}{3}}\widehat{\left|\overline{S}\right|\overline{S_{ij}}} \tag{2.5}$$

$$T_{ij}^a = -2C_s^2\alpha(\sqrt{g})^{\frac{2}{3}}\left|\hat{\overline{S}}\right|\widehat{\overline{S_{ij}}} \tag{2.6}$$

Using the identity

$$\widehat{L_{ij}^a} = \widehat{L_{ij}} - \frac{1}{3}\delta_{ij}L_{kk} - 2C_s^2\left(\sqrt{g}\right)^{\frac{2}{3}}\left[\alpha\left|\hat{\overline{S}}\right|\widehat{\overline{S_{ij}}} - \widehat{\left|\overline{S}\right|\overline{S_{ij}}}\right] = -2C_s^2\left(\sqrt{g}\right)^{\frac{2}{3}}M_{ij} \tag{2.7}$$

Here α is the square of the ratio of the characteristic length scale associated with the test filter to that of grid filter and is taken to be $\left[\hat{\overline{\Delta}}_i / \overline{\Delta}_i = \sqrt{6}\right]$ for a representative one-dimensional test filtering operation. Using a least-squares minimization procedure of Lilly, a final expression for C_s^2 is obtained as:

$$C_s^2 = -\frac{1}{2}\frac{1}{(\sqrt{g})^{2/3}}\frac{L_{ij}^a \bullet M_{ij}}{M_{ij} \bullet M_{ij}} \tag{2.8}$$

The value of C_s^2 is constrained to be positive by setting it to zero when $C_s^2 < 0$.

2.2.2 Parallel Algorithm

The current study employs a multiblock framework which facilitates parallelization. The computational domain is divided into overlapping blocks, which are then distributed to multiple processors, the maximum number of which are limited by the total number of blocks. Each block has a separate data structure and the Message Passing Interface (MPI) is used for data transfer across processors. Further, within each block, virtual cache blocks are used while solving linear systems. A detailed description of the software architecture can be found in Tafti[22].

2.2.3 Solution Algorithm

The algorithm decouples the grid movement from the application of fluid conservation laws. The steps involved in the calculation of unsteady flow in the dynamic grid system can be summarized as follows

1) The initial grid is read and the values of dependent variables are initialized.

2) The nodes on moving boundaries are displaced based on a prescribed or induced motion and velocity boundary conditions are computed based on the displacement.

3) The boundary movement is then transmitted to the interior of the domain in the rezoning phase. The transmittal of the boundary motion to the volume grid motion is done in a hierarchy of steps.

   a. First the corner displacements of each computational block are computed using the spring analogy.
   b. Second, the corner displacement of each block is transmitted to the nodal distribution in block edges, block faces, and block volumes, respectively, by using a modified TFI procedure. This step completes the rezoning phase.

   It is noted that rezoning is only implemented when the mesh deforms. If instead the boundary movement is uniformly transmitted into the domain as in a certain class of problems, the rezoning step is not necessary.

4) New grid metrics and the contravariant flux due to grid movement are computed by satisfying the SCL condition (Eq. 2.1).

5) The mass and momentum equations given by Eqs. (2.2-2.3) are advanced in time using a fractional-step algorithm to complete the time step.

At the next time advancement, steps 2 to 5 are repeated.

2.2.4 Rezoning Phase

The rezoning is done at the start of the time step to adjust the grid based on boundary movement. The location of the moving boundary at a new time is evaluated based on the prescribed or induced motion. The velocity of the moving boundary is then computed as $\vec{u}_b = d\vec{x}/dt$ and applied as a boundary condition. The rezoning is carried out in two steps. In the first step the movement of each block corner is computed by using a spring analogy similar to that of Tsai[16]. In the parallel architecture (Fig.2.1a), since blocks are located on different processors, the evaluation of block corner displacements is carried out on a master processor. For the case shown in Fig.2.1a, the displacement of the internal corner is evaluated based on the movement of the external corners, which are

located either on a moving or a fixed boundary. Then the displacement of block corners is broadcast to all processors. In the second step the modified TFI[15,16,18] based on corner displacements is carried out for each block. The main advantage of the modified TFI is that it can be carried out in parallel. By using the same interpolation technique across processors, same grid distribution is obtained at block interfaces residing on different processors, hence eliminating any extra communication between processors. Further, since the TFI is applied only on displacement. i.e. the displaced grid is obtained by adding interpolated displacements to the old grid locations, the quality of the initial grid is maintained for simple boundary movements. The steps involved in rezoning for a two dimensional geometry is shown in Fig.2.1(b-d).

2.2.5 Spring Analogy

In the spring analogy, each edge of a block is considered as a spring having a stiffness inversely proportional to its length, and is given by

$$k = \frac{1}{\left[dx^2 + dy^2 + dz^2\right]^{p/2}} \tag{2.9}$$

where the power p is used to control the stiffness of each edge, and a value of unity is used in this study. A longer edge will have a low value of the spring constant and will undergo a larger deformation. The shearing motion (skewness) of the blocks is controlled by adding two diagonal springs for each face and four cross-diagonal springs for each block. Hence in two-dimensions, each interior spring node (corner) in the network is connected to 8 nodes, which nominally increases to 24 in three-dimensions. After defining the spring network, the displacement of internal block corners is computed by solving an equation for static equilibrium with the displacement of external corners specified as boundary conditions. The equation is solved using a predictor-corrector iterative process. In the predictor step the displacement is advanced based on previous values and in the corrector step new values are computed based on static equilibrium.

Predictor Step:

$$\delta x_i^* = 2\delta x_i^m - \delta x_i^{m-1} \tag{2.10}$$

Corrector Step:

$$\delta x_i^{m+1} = \frac{\sum_{j,j\neq i} k_{ij}\delta x_j^*}{\sum_{j,j\neq i} k_{ij}} \tag{2.11}$$

where k_{ij} is the spring stiffness from corner points *i* to *j* and δx_i^m is the displacement of the corner point *i* at the m^{th} iteration.

2.2.6 Trans-Finite Interpolation (TFI)

After finding the displacement of block corners, one, two and three dimensional TFI is carried out to transmit the corner deformation into the volume grid. One dimensional TFI is first applied to each edge, for example for a ξ direction edge (low west edge) it is given by

$$\Delta\vec{x}_{i,1,1} = (1-\alpha_{i,1,1})\Delta\vec{x}_{1,1,1} + \alpha_{i,1,1}\Delta\vec{x}_{i\,\max,1,1} \tag{2.12}$$

where α is control function along ξ direction and is computed as

$$\alpha_{i,1,1} = s_{i,1,1} / s_{i\,\max,1,1} \tag{2.12a}$$

where $s_{i,1,1}$ is the arc length, which is computed as

$$s_{i,j,k} = s_{i-1,j,k} + \sqrt{(x_{i,j,k} - x_{i-1,j,k})^2 + (y_{i,j,k} - y_{i-1,j,k})^2 + (z_{i,j,k} - z_{i-1,j,k})^2} \tag{2.12b}$$

Followed by the edge interpolation, two and three dimensional TFIs are employed to obtain interpolated values for surface and volumes, respectively. The three dimensional TFI is given by a Boolean sum of interpolations along ξ, η, and ζ directions

$$\Delta\vec{x}_{i,j,k} = U + V + W - UV - VW - UW + UVW \tag{2.13}$$

where univariate interpolants are given by

$$U = (1-\alpha_{i,j,k})\,\Delta\vec{x}_{1,j,k} + \alpha_{i,j,k}\;\Delta\vec{x}_{i\max,j,k}$$

$$V = (1-\beta_{i,j,k})\,\Delta\vec{x}_{i,1,k} + \beta_{i,j,k}\;\Delta\vec{x}_{i,j\max,k} \tag{2.13a}$$

$$W = (1-\gamma_{i,j,k})\,\Delta\vec{x}_{i,j,1} + \gamma_{i,j,k}\;\Delta\vec{x}_{i,j,k\max}$$

and the tensor products are given by

$$\begin{aligned} UV = {} & (1-\alpha_{i,j,k})\,(1-\beta_{i,j,k})\Delta\vec{x}_{1,1,k} + (\alpha_{i,j,k})\,(1-\beta_{i,j,k})\Delta\vec{x}_{i\max,1,k} \\ & + (1-\alpha_{i,j,k})\,\beta_{i,j,k}\Delta\vec{x}_{1,j\max,k} + \alpha_{i,j,k}\;\beta_{i,j,k}\Delta\vec{x}_{i\max,j\max,k} \end{aligned} \tag{2.13b}$$

$$\begin{aligned} VW = {} & (1-\beta_{i,j,k})\,(1-\gamma_{i,j,k})\Delta\vec{x}_{i,1,1} + (\beta_{i,j,k})\,(1-\gamma_{i,j,k})\Delta\vec{x}_{i,j\max,k} \\ & + (1-\beta_{i,j,k})\,\gamma_{i,j,k}\Delta\vec{x}_{1,j,k\max} + \beta_{i,j,k}\;\gamma_{i,j,k}\Delta\vec{x}_{i,j\max,k\max} \end{aligned}$$

$$\begin{aligned} UW = {} & (1-\alpha_{i,j,k})\,(1-\gamma_{i,j,k})\Delta\vec{x}_{1,j,1} + (\alpha_{i,j,k})\,(1-\gamma_{i,j,k})\Delta\vec{x}_{i\max,j,1} \\ & + (1-\alpha_{i,j,k})\,\gamma_{i,j,k}\Delta\vec{x}_{1,j,k\max} + \alpha_{i,j,k}\;\gamma_{i,j,k}\Delta\vec{x}_{i\max,j,k\max} \end{aligned}$$

$$\begin{aligned} UVW = {} & (1-\alpha_{i,j,k})\,(1-\beta_{i,j,k})(1-\gamma_{i,j,k})\Delta\vec{x}_{1,1,1} + \alpha_{i,j,k}\;(1-\beta_{i,j,k})(1-\gamma_{i,j,k})\Delta\vec{x}_{i\max,1,1} \\ & + (1-\alpha_{i,j,k})\,\beta_{i,j,k}(1-\gamma_{i,j,k})\Delta\vec{x}_{1,j\max,1} + (1-\alpha_{i,j,k})\,(1-\beta_{i,j,k})\gamma_{i,j,k}\Delta\vec{x}_{1,1,k\max} \\ & + \alpha_{i,j,k}\beta_{i,j,k}(1-\gamma_{i,j,k})\Delta\vec{x}_{i\max,j\max,1} + \alpha_{i,j,k}(1-\beta_{i,j,k})\gamma_{i,j,k}\Delta\vec{x}_{i\max,1,k\max} \\ & + (1-\alpha_{i,j,k})\beta_{i,j,k}\gamma_{i,j,k}\Delta\vec{x}_{1,j\max,k\max} + \alpha_{i,j,k}\beta_{i,j,k}\gamma_{i,j,k}\Delta\vec{x}_{i\max,j\max,k\max} \end{aligned}$$

2.2.7 Space Conservation Law

After the rezoning phase, new grid metrics are computed. The grid contravariant flux due to grid movement $\sqrt{g}U_g^j$ is evaluated using the SCL condition. The satisfaction of SCL condition is explained by using a simple two dimensional control area as shown in Fig.2.2. The dotted and solid lines represent the cell faces at time level n and n+1, respectively. The shaded area in Fig.2.2 represents the area swept by the east face. The contravariant flux at time n+1/2 for the east face is computed as:

$$\sqrt{g}U_g^p = \frac{\delta V^p}{dt} \tag{2.14}$$

where p = e, w, n, or s, and δV^p is the area swept by the face p.

The swept area used in Eq. (2.14) is calculated using triangulation[20,24]. The area swept by the east face is computed by adding the area of the triangles (Fig.2.2) "00-10-11" and "00-11-01" as follows,

$$\delta V^{e} = \frac{1}{2}\left(\vec{X}_{00-10} \times \vec{X}_{00-11}\right) + \frac{1}{2}\left(\vec{X}_{00-11} \times \vec{X}_{00-01}\right) \tag{2.15}$$

The vectors used in Eq. (2.15) are computed based on new and old coordinate values and their direction is from old to new. Further, the order of vectors used in the cross product is selected properly as given by Eq. (2.15) to have a proper sign for the change in volume. For the case shown in Fig.2.2, the volumes swept by the east and north face, (δv^e, δv^n), are positive, while the volumes swept by the west and south face, (δv^w, δv^s), are negative. By combining Eq. (2.1) and Eq. (2.14), it can be shown that the contravariant flux computed as above, satisfies the SCL condition

$$\frac{\sqrt{g}^{\,n+1} - \sqrt{g}^{\,n}}{dt} = \frac{\partial}{\partial \xi_j}\left(\sqrt{g} U^j_g\right)^{n+1/2} = \frac{\delta V^e - \delta V^w + \delta V^n - \delta V^s}{dt} \tag{2.16}$$

In three-dimensions, the satisfaction of SCL is an extension to the method described above, where the volume swept by the faces is used to find the contravariant fluxes. Now the 3D volume is computed by dividing the cell into 24 tetrahedrons by connecting the cell center point to the vertices and to the centers of cell faces. After simplification the volumes are computed[20] as:

$$V = \frac{1}{3} \sum_{n=i,\,j,\,k} \frac{1}{2}\left(\vec{S}_{n+1} + \vec{S}_n\right) \bullet \left(\vec{X}_{n+1} - \vec{X}_n\right) \tag{2.17}$$

where $\vec{S}_{n+1}$ is the normal area vector of the face n+1, computed using Eq.15 and $\left(\vec{X}_{n+1} - \vec{X}_n\right)$ is the vector connecting the center of opposite cell faces.

2.2.8 Numerical Algorithm

After evaluating the new grid metrics and the grid contravariant fluxes, the integration of the Navier-Stokes equations is carried out. The governing equations (2.2-2.3) are discretized with a conservative finite-volume formulation on a non-staggered grid topology. The Cartesian velocities and pressure are calculated and stored at the cell center, whereas contravariant fluxes are stored and calculated at the cell faces. The temporal advancement is performed in two steps, a predictor step, which calculates an intermediate velocity field, and a corrector step, which calculates the updated velocity at the new time step by satisfying discrete continuity. In the predictor step the contribution of pressure gradient to momentum balance is completely neglected[22].

2.2.8.1 Predictor Step

$$\frac{\sqrt{g}^{n+1}\tilde{u}_i - \sqrt{g}^{n} u_i^n}{\Delta t} = D_i - C_i \tag{2.18}$$

where D_i is the diffusion term and C_i is convection due to flow and grid movement. In this study, convection and diffusion terms are treated implicitly by a Crank-Nicolson scheme.

Convection Terms

$$C_i = \frac{\partial}{\partial \xi_j}\left(\sqrt{g}U^j u_i\right)^{n+1/2} - \frac{\partial}{\partial \xi_j}\left(\sqrt{g}U_g^j u_i\right)^{n+1/2} \tag{2.19}$$

The values of grid contravarient fluxes, available at time level n+1/2 from SCL condition are used in the momentum equation.

$$C_i = \frac{1}{2}\left[\frac{\partial}{\partial \xi_j}\left(\sqrt{g}U^j u_i\right)^n + \frac{\partial}{\partial \xi_j}\left(\sqrt{g}U^{j\,n+1}\tilde{u}_i\right)\right.$$

$$\left. - \frac{\partial}{\partial \xi_j}\left(\sqrt{g}U_g^{j\,n+1/2} u_i^n\right) - \frac{\partial}{\partial \xi_j}\left(\sqrt{g}U_g^{j\,n+1/2}\tilde{u}_i\right)\right] \tag{2.19a}$$

The contravarient fluxes at time level n+1 is linearized using a two-step (n and n-1 time level) second order extrapolation as:

$$\sqrt{g}U^{j\,n+1} = 2\sqrt{g}U^{j\,n} - \sqrt{g}U^{j\,n-1} \tag{2.19b}$$

Diffusion Terms

$$D_i = \frac{1}{2}\left[\frac{\partial}{\partial\xi_j}\left(\left(\frac{1}{\mathrm{Re}}+\frac{1}{\mathrm{Re}_t}\right)\sqrt{g}\,g^{jk}\,\frac{\partial u_i^n}{\partial\xi_k}\right)+\frac{\partial}{\partial\xi_j}\left(\left(\frac{1}{\mathrm{Re}}+\frac{1}{\mathrm{Re}_t}\right)\sqrt{g}\,g^{jk}\,\frac{\partial\tilde{u}_i}{\partial\xi_k}\right)\right] \tag{2.20}$$

2.2.8.2 Corrector Step

In this step, the continuity equation is used to derive the pressure equation, which is solved to obtain the pressure field at time level *(n+1).* The procedure used in formulating the pressure equation is represented as follows:

First the intermediate cell face contravariant fluxes are constructed as follows

$$\sqrt{g}\tilde{U}^{j} = \sqrt{g}\left(\vec{a}^{\,j}\right)_i\tilde{u}_i \tag{2.21}$$

Then, the correction form of the cell centered Cartesian velocities and cell face contravariant fluxes are written as:

$$u_i^{n+1} = \tilde{u}_i - \Delta t(\vec{a}^{\,j})_i\,\frac{\partial p^{n+1}}{\partial\xi_j} \tag{2.22}$$

$$\sqrt{g}\,(U^i)^{n+1} = \sqrt{g}\tilde{U}^i - \Delta t\sqrt{g}\,g^{ik}\,\frac{\partial p^{n+1}}{\partial\xi_k} \tag{2.23}$$

Finally, Eq. (2.23), in conjunction with Eq. (2.2), is used to derive the pressure equation, which takes the form:

$$\frac{\partial}{\partial\xi_j}\left(\sqrt{g}\,g^{jk}\,\frac{\partial p^{n+1}}{\partial\xi_k}\right) = \frac{1}{\Delta t}\frac{\partial\sqrt{g}\tilde{U}^j}{\partial\xi_j} \tag{2.24}$$

By using the contravariant fluxes at the cell faces in constructing the pressure equation, the method emulates a staggered grid arrangement. The pressure field at level *n+1* is then used to correct the nodal Cartesian velocities and the cell face contravariant fluxes using Eq. (2.22) and Eq. (2.23), respectively.

2.3 Results

In order to validate the algorithm and the capability of the solver, three fluid problems are simulated, namely forced oscillation of a cylinder in cross flow, a heaving airfoil, and hovering flight of a fruitfly. The lift and thrust variation in all cases are compared with previous experimental and numerical studies. In case of an oscillating cylinder, two amplitudes in different energy transfer regimes are studied and the lift variation is compared with a previous spectral element analysis. In case of the plunging airfoil, the wake structures and thrust produced are compared with experimental data and inviscid theory. The hovering fruitfly is analyzed using a 60 block grid, which exemplifies the effectiveness of the present algorithm in solving complex boundary movement. The thrust and lift values obtained are validated with previous experiments. Finally, the unsteady aerodynamics of flapping flight of a rectangular wing with aspect ratio of 4 is analyzed at Re =10,000 for forward flight using LES.

2.3.1 Flow over an Oscillating Cylinder

The results of vortex structure and energy transfer during forced oscillation[25,26] could be used to understand vortex induced vibration (VIV) of bluff bodies. In particular, by analyzing forced oscillations it is possible to evaluate the flow regimes where VIV can occur. The average energy transfer in forced oscillation can be negative or positive depending on the amplitude and the frequency of oscillation. For a cylinder oscillating near the natural shedding frequency of a stationary cylinder, the vortex shedding changes to match the oscillation frequency. The range of frequencies where this resonance occurs is termed as lock-in or entrainment regime[27,28]. In a previous study by Stewart[26], the effect of the amplitude of forced oscillations in the lock-in regime on vortex shedding was evaluated at *Re*=200 with two-dimensional computations. Since the lock-in regime extends the onset of wake turbulence from *Re*=150 to approximately *Re*=310, two-

dimensional studies provide accurate results for *Re*=200. In the lock-in regime, if the amplitude of oscillation is increased, the energy transfer from fluid to cylinder changes from positive to negative accompanied by a 180^o phase shift in the vortex shedding frequency. The VIV requires a positive energy transfer from fluid to cylinder to overcome structural damping. Hence the amplitude at which energy transfer changes from positive to negative signifies an upper limit for the amplitude, which can be sustained by VIV.

In the present study, a sinusoidal oscillation is applied to the cylinder,

$$y(t) = A\cos(2\pi f_0 t) \tag{2.25}$$

where f_o is the non-dimensional frequency of forced oscillation fD/U_∞, and A is non-dimensional amplitude of oscillation (a/D) . Similar flow parameters as Stewart[26], *Re=200* and an oscillating frequency, f_0 of 0.2 are chosen. The simulation is carried out for two amplitudes A=0.199, and 0.696. The non-dimensional energy transfer from the fluid to cylinder is given by

$$E = \frac{1}{D}\int_0^T \dot{y} C_L \, dt \tag{2.26}$$

where C_L is the coefficient of lift, $\dot{y}$ is the velocity of the oscillating cylinder and T is non-dimensional time for one period of oscillation. Fig.2.3 shows the extent of the computational domain used in this study. A total of nine computational blocks are used. The domain extends 40*D* downstream of the cylinder, and 15*D* upstream and to the side boundaries. A uniform velocity is specified at the inlet, while an inviscid convective outflow boundary condition is specified at the outlet. A time-dependent velocity boundary condition, which is based on a known displacement, is specified on the surface of the cylinder. The computation is carried out in parallel and the rezoning based on the movement of the cylinder is successfully applied for the multiblock approach.

Figure 2.4 shows the wake structure for both amplitudes with solid and dashed lines representing positive and negative vortices, respectively. At low amplitude, the wake

structure is similar to the Karman vortex shedding mode, in which two single vortices (*2S*) are shed for every cycle. At high amplitude, a pair of positive vortices and a single negative vortex (*P+S*) is generated in each cycle. The variation of lift profiles matches well with the previous study by Stewart[26] as shown in Fig.2.5. For *A*=0.199, the phase shift between the displacement and the lift is 270^o while it is only 90^o for *A*=0.699. The variation of instantaneous energy transfer shows that the energy transfer in case of low amplitude is always positive, while it oscillates between a high negative and low positive energy transfer for A=0.696. The net energy transfer for *A*=0.199 is positive and it is negative for *A*=0.696.

2.3.2 Heaving Airfoil

Flow around oscillating airfoils has been investigated by many researchers to analyze wing flutter, aero-acoustic noise generation, and propulsion mechanism of birds, fish and insects. When the airfoil undergoes plunging it generates thrust at high plunge velocities. This effect is known as Knoller-Betz effect and has been verified by many experimental and numerical studies[29-31]. An analytical expression for aerodynamic forces acting on an oscillating airfoil-aileron was provided by Theodorsen[32] using linearized potential flow theory. Garrick[33] extended the study of Theodorsen and computed the thrust and propulsive efficiency of an oscillating airfoil in terms of Bessel functions and they are given by

$$y(t) = h\cos(kt)$$

$$C_{Tmean} = \pi(kh)^2(F^2 + G^2) \tag{2.27}$$

$$C_{Lpeak} = \pi/2\,(kh)\,(F^2 + G^2 + kG/2 + k^2/16)^{1/2}$$

$$\eta_{prop} = (F^2 + G^2)/G$$

where h is the non-dimensional amplitude *a/c*, c is the chord length, k is the non-dimensional frequency $2\pi fc/U_\infty$, f is the dimensional frequency, U_∞ is the free stream velocity, *F(k/2)* and *G(k/2)* are the real and imaginary components of the Theodorsen[32] function.

Lai et al.[29] conducted an experimental investigation of plunging airfoils at different frequencies *k* and at low amplitudes *h*. They observed three types of wake vortex structures at different values of plunge velocity *kh*. At low values of *kh*, the wake resembles a normal Karman wake which is indicative of drag. At $kh \approx 0.2$, a neutral wake was observed which contains two same sign vortices shed during one half cycle. At high values of *kh*, the wake contains downstream inclined reverse Karman vortex streets, which generates thrust. Tuncer et al.[30] and later Young et al.[31] conducted numerical investigations in the same range of parameters. The computed wake structure showed good agreement with the experiments.

Simulations of plunging NACA 0012 airfoil at $Re=2x10^4$ and at frequency k =7.86 is carried out for various amplitudes, using an 18 block computational domain with 121 thousand computational cells. The grid consists of 120 grid points along each surface of the airfoil and 168 points normal to the airfoil. At $Re=2x10^4$ the flow is assumed to be laminar and there are 35 grid points inside the boundary layer at the trailing edge. A grid refinement study was carried out at *kh*=0.6 and a change in mean coefficient of thrust of less than 0.2% was obtained for a 50% increase in the total number of cells (150x210 grid). This established that the grid distribution of 120x168 was sufficient and the thrust and lift coefficient obtained were grid independent.

The results are validated with the experiments[29], in which they used dye visualization techniques to classify the different types of wake vortex patterns. Fig.2.6 shows the wake structure and vorticity contours at a low plunge velocity *kh*=0.1. The vortex wake shown by particle traces (Fig.2.6b) compares well with the experimental[29] flow visualization (Fig.2.6c). Vorticity contours (Fig.2.6a) show that the wake vortex structure is similar to a normal Karman street with a clockwise vortex on top and a counter clockwise vortex at the bottom, which result in a momentum deficit in the wake thus producing drag. At this low plunge velocity, two same sign vortices are shed during one half cycle.

On increasing the amplitude, the experimental results at *h*=0.025 show a neutral wake with two mushroom shaped vortices facing upwards and downwards resulting in zero

drag (Fig.2.7d). The present simulation is carried out for three values of amplitude (0.02, 0.025, 0.03) close to the neutral wake and these results are shown in Fig.2.7. The wake vortex structure at h=0.02 (Fig.2.7a) matches well with the experimental results at h=0.025. A similar deviation was observed in the numerical study of Young et al.[31]. For amplitudes h=0.02, and 0.025 two same sign vortices are generated, but for h=0.025, the vortex pair combines in the wake (Fig.2.7b). For h=0.03, lock-in occurs and the wake consists of downstream tilted mushroom vortices. In this range of plunge amplitude kh 0.16 to 0.24, the value of mean drag changes from negative to positive.

For plunging velocities kh>0.4, the wake now contains strongly downstream inclined mushroom vortices (Fig.2.8) with positive and negative vortices located above and below the center line, which is the reverse of the Karman vortex street. These vortices entrain surrounding fluid and result in a jet like flow and thus produces a momentum surfeit.

For further validation, analysis of heaving airfoil is carried out by varying the reduced frequency at constant amplitude h=0.25 similar to the experiment of Heathcote et al.[35]. The comparison of mean thrust with Garrick and previous experimental and numerical studies are shown in Fig.2.9. The values show excellent comparison with the experiments. Further, the trend in thrust variation matches well with Garrick. Since the inviscid solution of Garrick does not account for viscous drag and the separation at the trailing edge, it predicts high values of thrust [34]. The present study also predicts higher thrust values closer to Garrick than the numerical study of Tuncer et al.[30].

Variation of maximum lift and propulsive efficiency are shown in Fig.2.10. The propulsive efficiency based on Garrick's theory depends only on reduced frequency and it approaches a constant value of 0.5 as the frequency increases. In the present study the efficiency is computed as

$$\eta_{prop} = \frac{\int_o^\tau C_T U \, dt}{\int_o^\tau C_L \dot{y} \, dt} \tag{2.28}$$

where τ is the cycle time . The present study predicts higher values of peak lift than that of Garrick solution due to the presence of leading edge separation. The predicted viscous propulsive efficiency is much lower than the theory and matches well with the experimental results[35]. The efficiency reaches a maximum value of 0.28 for a plunging velocity of 0.4 and drops for high values of *kh*.

Table.2.1 Kinematic parameters and non-dimensional numbers for flapping flight

Parameters	***Description***
Stroke Plane	The plane defined by three points: wing base (B), and the wingtip at maximum (T_T) and minimum angular position (T_B). During hovering, the stroke plane will be near horizontal and during forward flight, it will be vertical.
Stroke plane angle, β	Angle between the stroke plane and the horizontal plane. It ranges from 0^o for hovering to 90^o for forward flight
Angle of attack, α	Angle between the wing direction (from trailing edge to leading edge) and the direction of motion.
Torsional angle, ρ	Angle between the wing direction and the direction perpendicular to stroke plane.
Flapping amplitude, ϕ	Angle between rotation axis of the wing and the plane perpendicular to the stroke plane.
Deviation angle, γ	The angle between the rotation axis of the wing and the stroke plane.
Reynolds number, $\frac{U_f C}{\nu}$	Defined based on mid-span chord length, C and flapping velocity, $U_f = 2\Phi Rf$ where Φ - total flapping amplitude (max to min) R - semi wing-span (length wing) f - frequency of flapping
Advance ratio, $J = \frac{U_\infty}{U_f}$	Ratio of the flight velocity to the flapping velocity

2.3.3 Hovering flight of fruitfly

Flapping flight of insects has received much attention from researchers due to their ability to generate thrust and lift at low Reynolds number, where conventional airfoils have a low lift to drag ratio due to flow separation. The kinematics involved in normal flapping flight is divided into two translation motions corresponding to up and down strokes and two rotational motions (pronation and supination) corresponding to

stroke reversals. Pronation is done before the downstroke and supination is done before the upstroke. Fig.2.11 shows the critical kinematic parameters of flapping flight with their definitions given in Table 2.1.

The hovering flight of a fruitfly [36] is studied to validate the current solver. The planform of the robofly wing (Fig.2.12) obtained from Sane and Dickinson[36] is used to develop the grid. The coordinate (x,y,z) is used for the fixed frame, where the y-z plane represents the stroke plane (Fig.2.11). The coordinates (ξ,η,ζ) are used for the moving frame fixed with the wing, where ξ is along the chordwise direction, η is perpendicular to the wing, and ζ is along the spanwise direction (Fig.2.12a). The computational domain is made of 60 blocks with about 3 million cells. The domain boundaries are placed at 10 times the chord length from the edges of the wing on all sides except the symmetry surface, which is located at 0.6 times the chord length from the wing base (Fig.2.12a). The symmetric boundary condition is applied along the axis of flapping, while a zero velocity boundary condition is applied at all other faces.

The simulation is carried out for four flapping cycles using 60 processors on System-X at Virginia Tech. A triangular wave form for flapping angle and a square wave form for rotation angle (Fig.2.13), similar to that of the experiment[36] are employed. The normalized value of $t^*=t/t_{cycle}$ from 0 to 0.5 represents the downstroke whereas 0.5 to 1.0 represents the upstroke. The midstroke angle of attack is 50^o for both strokes and the rotation is carried out symmetrically with a total duration t^* of 0.16. The stroke plane angle is $\beta=0^o$and the total flapping amplitude is $\Phi=60^o$. A fluid viscosity of 120 cSt and density 880 kg/m^3 and frequency of flapping 168 mHz along with the actual lengths of robofly wing (25cm) are used to compute the Reynolds number for the current simulation[36]. The Reynolds number based on the characteristic length L=10cm (maximum chord length) and tip velocity is 73.

The quality of the deformed grid is checked at different times of the flapping cycle to ensure the effectiveness of TFI and the spring analogy. Three different views of the deformed grid during the start of the downstroke, which is at a maximum stroke angle, is

shown in Fig.2.12b-d. The quality of the initial grid is maintained throughout the calculation, which resolves the flow field near the tip and leading and trailing edges.

The time variation of lift and thrust forces are evaluated during fourth flapping cycle and compared with experimental results (Fig.2.14). Since the stroke plane is horizontal ($\beta = 0^o$), the lift force is given by $-F_x$ and the thrust force by $-F_y$. The lift force compares reasonably well, in particular good agreement is observed during the upstroke, while the values differ during the downstroke. Since the kinematics is symmetrical and the freestream velocity is zero, the values of lift should be identical for the upstroke and downstroke. However, the experimental results show a deviation of around 50% between upstroke and downstroke, most likely due to uncertainties in force measurements and slight differences in the kinematics. The comparison of thrust force shows reasonable agreement in the trend but the values differ in magnitude. Similar quantitative deviations have been reported by previous numerical studies[37-39].

The pressure contours and streamlines in a chordwise plane at $\xi=2$ at different times are shown in Fig.2.15. Since the downstroke and upstroke are symmetrical, only the results during the downstroke are used to analyze the flow structure. During the start of the downstroke, a high pressure region forms at the bottom surface of the wing due to the sudden deceleration of the wing at the end of the upstroke, which when combined with the rotation results in the formation of a Leading Edge Vortex (LEV) and a peak in lift and thrust at time $t^*=0.05$. The LEV grows and reaches a maximum size at time $t^* \sim 0.4$ to 0.45, and sheds during rotation which reduces the lift and thrust production. At time t^* of 0.5 (not shown) the pressure contours are similar to that of $t^*=0$ with positive pressure now on the top surface of the wing.

2.3.4 Forward Flight at Reynolds number of 10,000

Flapping flight generates both thrust and lift efficiently at low Reynolds numbers, which makes it attractive for MAVs. Employing flapping flight reduces the requirement of a separate propulsive system making it attractive for light MAVs. In the current study, flapping flight at Re = 10,000 and at advance ratio, J of 0.5 is studied to evaluate the

unsteady aerodynamics involved and its effect on the force production. A rectangular wing with an aspect ratio of 4 as shown in Fig.2.16a is used for the analysis. A total of 60 blocks with about 8 million cells is used for the simulation. The downstream boundary is placed at 15 chord lengths from the trailing edge while other boundaries are located at a distance of 10 chord lengths. Constant free-stream velocity boundary conditions are applied at all inlet faces and an outflow condition is specified at the downstream face. A symmetry condition is applied at the base of the wing.

A sinusoidal flapping and symmetric rotation with duration t* of 0.1 is employed. Angle of attacks of 70^o and 45^o are used for the downstroke and upstroke, respectively. A lower value of angle of attack during the upstroke is used to reduce the down force. The stroke plane angle is kept at $\beta=90^o$ (vertical direction) and the total flapping amplitude is 60^o. In forward flight, both flapping velocity and freestream velocity determine the effective angle of attack of the flow as shown in Fig.2.16b. In addition, the effective angle of attack varies along the span of the wing with a maximum value at the tip. For the advance ratio of 0.5 and α_d of 70, the α_{eff} varies from -30^o to 33^o from base to tip. During the upstroke the value of α_{eff} varies from 45^o to -18^o.

The results obtained during the fourth flapping cycle are used for the analysis. Instantaneous variation of lift and thrust coefficients (normalized based on flapping velocity and planform area) is shown in Fig.2.17. During the first half of the downstroke, the lift increases due to the formation of the LEV and reaches a maximum value of 2.5 at time 0.2. This value is around three times higher than the maximum coefficient of lift, 0.75, of a 2D thin plate under steady state condition. The thrust production is positive during most part of the downstroke except during the rotation at the end of the stroke. The contribution from the pressure force is dominant and the torsional angle determines the ratio of thrust to lift force produced by the LEV. During the upstroke, a low pressure region forms on the bottom surface leading to a negative lift force, but the magnitude is less than that during the downstroke due to a lower angle of attack. The thrust production is positive during a large part of the upstroke with two peaks obtained at t* =0.75 and at t*=0.95. The average coefficient of lift and thrust are 0.59 and 0.33. For a typical semi-

wingspan *R*=7.5cm, the lift produced can support 394 grams and the thrust force generated is 1.08 N.

The isosurface of vorticity at different times are shown in Fig.2.18. The vorticity isosurface at t*=0.2 show a spiral LEV (negative vorticity) with maximum strength near the tip. The LEV does not extend up to the base as the effective angle of attack near the base is negative. The pressure and ω_ζ contours at time t* =0.25 along the chordwise plane at ζ=3, Fig.2.19, show a detached low pressure region on the top surface of the wing. At this time the LEV separates near the tip and the low pressure region is replaced by the entrainment of fluid from the freestream. Figure 2.20a shows the particle traces obtained by releasing particles along the leading edge at t*=0.25. The particle traces show a spiral LEV which is still attached near the base and lifted from the wing near the tip. The spanwise velocity contours at t*=0.25 along the center of the LEV shown in Fig.2.20b indicate the presence of a strong spanwise velocity of the order of the flapping velocity from the base to the tip. Similar results were obtained by the flow visualization studies conducted by Ellington[40] using a large mechanical model of a hawkmoth, *flapper* at (Re~4000). They showed a spiral LEV with a spanwise velocity comparable to the flapping velocity during the downstroke and also suggested that the spanwise flow removed the vorticity from the LEV and stabilized it. However, the present results show that the spanwise flow does not stabilize the LEV. The critical reason is the presence of strong negative spanwise flow near the tip shown by the curved arrow in Fig.2.20b, which prevents the removal of vorticity from the LEV. Hence the vorticity starts building up near the tip both due to the high angle of attack and the convection of vorticity from the base. This increase in vorticity leads to instability in the LEV and subsequent separation from the wing. At time t*=0.3, the LEV near the tip separates completely from the wing (Fig.2.18) and the lift coefficient is low. The rotation starts at the end of the downstroke at around t*=0.45, which increases the angle of attack near the base from negative to positive. This results in the formation of a small vortex near the base, shown by the isosurface of vorticity at t*=0.5 (Fig.2.18) and the lift coefficient reaches a second peak.

The behavior of flow during the upstroke is very much similar to the downstroke. During the upstroke the angle of attack is low and hence there is no clear formation of the LEV and the vorticity contours (Fig.2.18) show a small vortex near the tip at time t*=0.7 which corresponds to maximum negative lift production during the upstroke. The vorticity and pressure contours at t*=0.75, Fig.2.19, shows the vorticity and low pressure region on the bottom surface. Since the torsional angle is negative, this low pressure region results in thrust throughout the upstroke. The vortex becomes unstable at around t* of 0.8 (Fig.2.18) and a drop in negative lift occurs. During the rotation as the angle of attack near the base becomes negative, the negative vorticity covers most of the wing (Fig2.18 t* =1.0), which results in a second peak in negative lift and thrust.

The power required for flapping (P_x) and rotation (P_ζ) (Fig.2.21) are computed based on the torque generated by the fluid forces and angular velocity of the wing:

$$\begin{aligned} \mathrm{T} &= \int r \times (p + \tau)\ ds; \\ P &= T.\Omega \end{aligned} \tag{2.29}$$

where r is the radius from the axis, p is the pressure, τ is the shear stress and Ω is the angular velocity of the wing. The power required for acceleration of the wing is neglected as the typical weights of flapping wings are small. The power requirement (normalized based on fluid density, tip velocity and chord length, $\rho u_t^3 C^2$) follows a similar trend as that of lift and thrust. A peak in power requirement for flapping of around 5 occurs at t*=0.2 during the downstroke, which corresponds to the formation of the LEV. The power required during the upstroke is much lower than that during the downstroke due to lower force production. The power requirement for rotation reaches a maximum value of 2 during the middle of rotation. The average power required for flapping and rotation are 1.37 and 0.23 respectively, and the propulsive efficiency (Eq. 2.30) is 19.59%. The present simulation shows that flapping flight is capable of supporting the weight of MAVs and produces a propulsive thrust force.

$$\eta_{prop} = \frac{\mathrm{F_T U_\infty}}{\mathrm{P}} \tag{2.30}$$

2.3.5 Summary and Conclusion

A moving grid algorithm with a rezoning capability is presented in a multiblock, multiprocessor environment within the framework of a fractional-step method. The rezoning of the grid was carried out using a combined spring analogy and TFI, which provides a framework for parallelization in the multiblock approach. The space conservation law required for a dynamic grid system is satisfied by evaluating the grid contravariant fluxes. The method is validated for three flow problems. The forced vibration of a cylinder is analyzed using a nine block computational domain for two amplitudes. At low amplitude, the positive energy transfer from fluid to cylinder is obtained with normal Karman wake vortices. The negative energy transfer accompanied with a change in wake vortex structure to P+S (a pair of positive and a single negative vortex) modes is obtained at high amplitude. The variation of lift and wake structure are in good agreement with previous computational studies. In the heaving airfoil, three different types of vortex wakes; drag producing wake, neutral wake, and a thrust wake are observed at different plunge velocities. The reverse Karman vortex sheet is observed at high plunging velocities, which entrain surrounding fluid and produces a momentum surfeit. The variation of mean thrust, peak lift and efficiency with amplitude compared well with previous studies. The hovering flight of a fruitfly is analyzed using a 60 block grid. The rezoning employed maintains the initial grid quality throughout the flapping cycle and the calculated lift and thrust characteristics compare well with previous experiments. Finally, flapping flight at Re=10,000 relevant to the development of MAVs is analyzed using LES. For the kinematics used, a spiral LEV forms during the downstroke which results in peak lift and thrust. The LEV gets unstable during the middle of the downstroke despite the presence of a strong spanwise flow. The lift force obtained supports 394 grams and thrust force of 1.08 N is generated with a propulsive efficiency of 19.59%.

Acknowledgements

The calculations were performed on Virginia Tech's Terascale computing facility, System-X. The support is gratefully acknowledged.

2.4 Figures

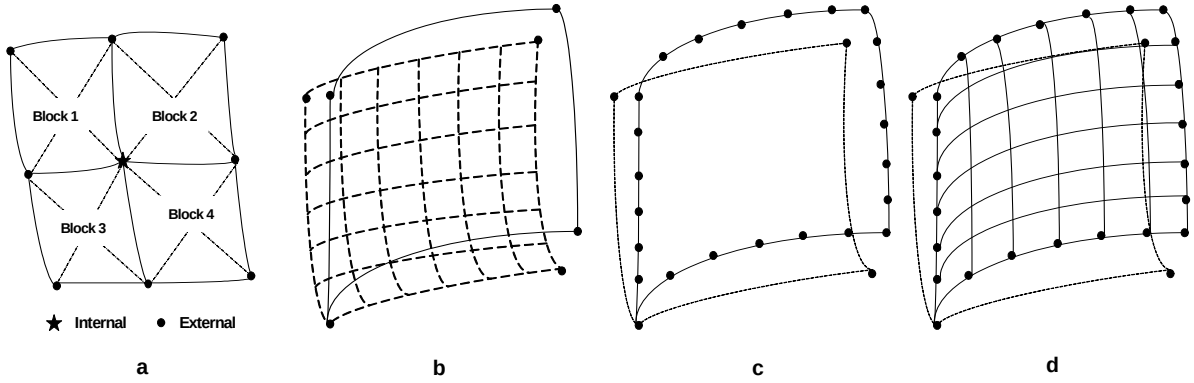

Fig.2.1 a) Displacement of internal node is computed by the master processor which is then broadcasted to each processor. The dotted line shows the additional diagonal springs. b) Initial grid of block 1 shown in dotted lines with the new corner nodes from master processor. c) TFI used to redistribute nodes along edges d) TFI used to redistribute nodes in face

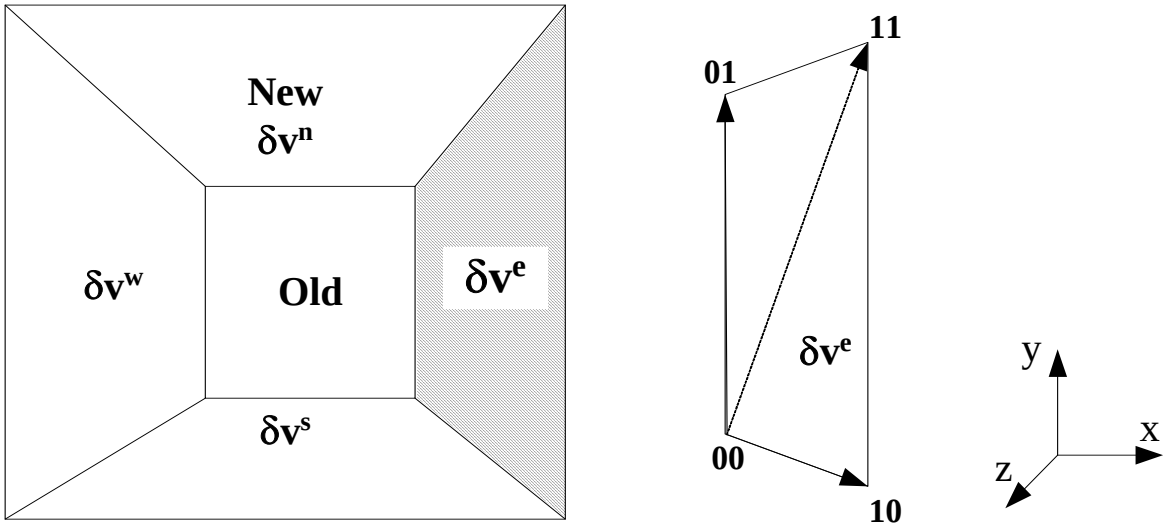

Fig.2.2 Deformation of two dimensional control volume (shaded area represents area swept by east face)

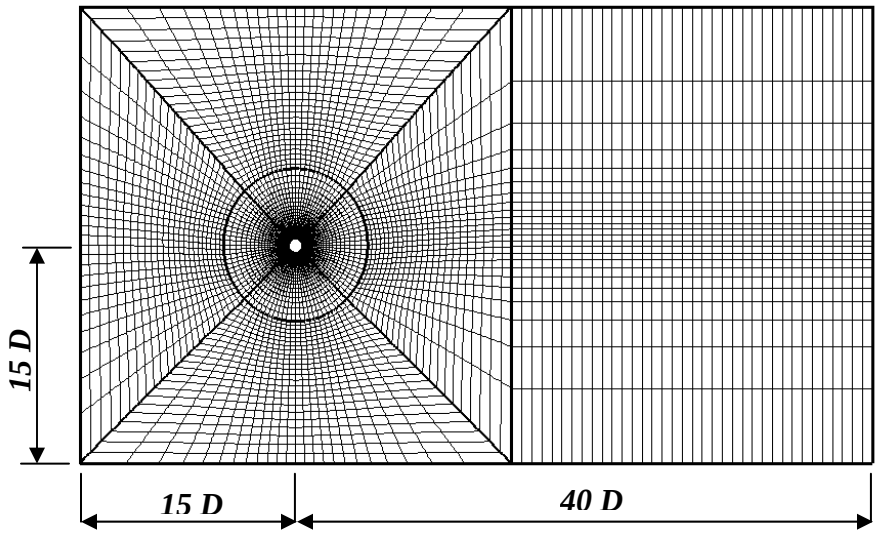

Fig.2.3 Computational domain for flow over oscillating cylinder (Every other 5th grid line is shown)

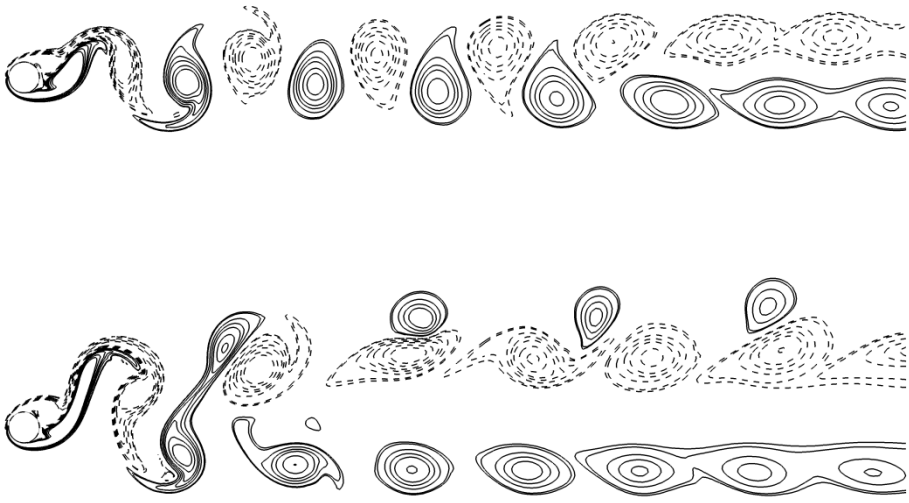

Fig.2.4 Wake structure showing (2S) Karman vortex shedding mode for low amplitude A=0.199 (top) and P+S shedding mode for A=0.696 (bottom)

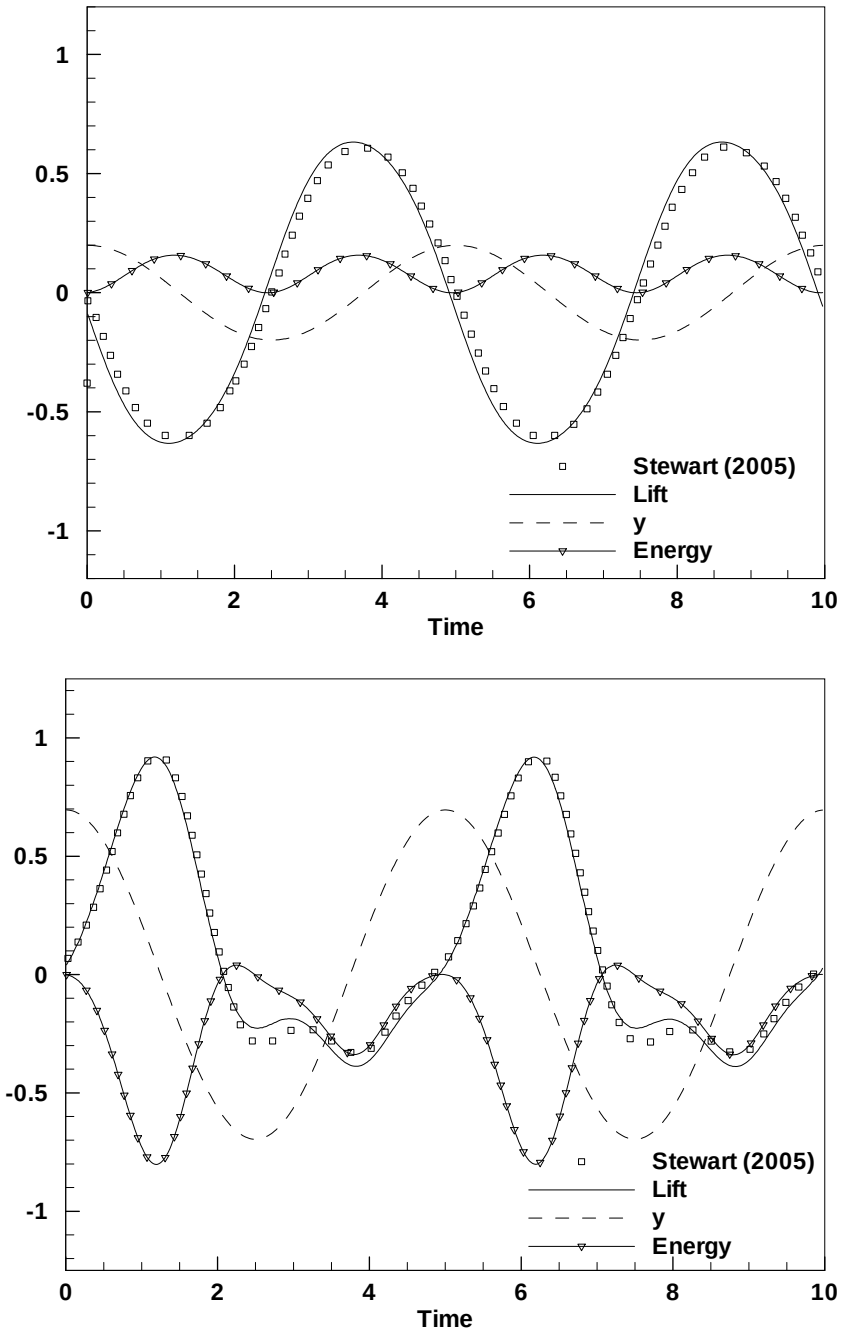

Fig.2.5 Comparison of lift frequency with previous study by Stewart et al. for A=0.199 and A=0.696. The instantaneous Energy transfer is also depicted in the graph.

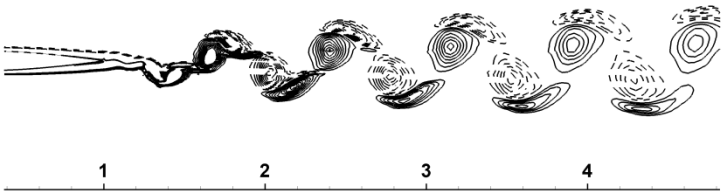

(a)

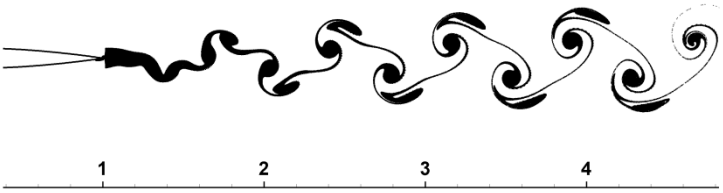

(b)

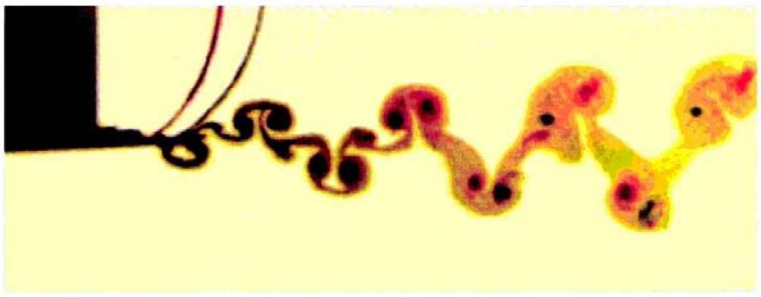

(c)

From Lai, J. C. S. and Platzer, M. F, AIAA Journal, 1999[29]

Fig.2.6 Wake comparison at k=7.86 and h=0.0125. a) vorticity contour with negative contours (clockwise) shown as dotted lines and positive contours (counter clockwise) as solid lines, b) Particle trace and c) Experimental dye visualization

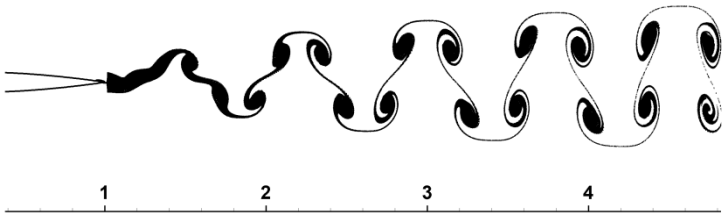

(a)

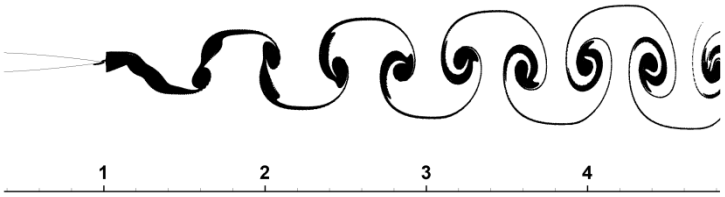

(b)

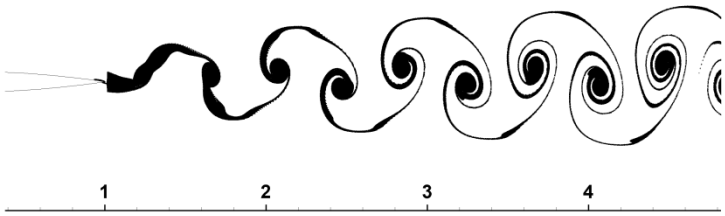

(c)

(d)

From Lai, J. C. S. and Platzer, M. F, AIAA Journal, 1999[29]

Fig.2.7 Wake comparison at k=7.86 and a) *h* = 0.02 b) *h* = 0.025 c) *h* = 0.03 d) experimental dye visualization for h = 0.02

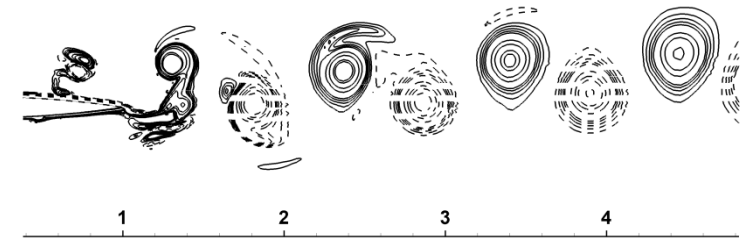

(a)

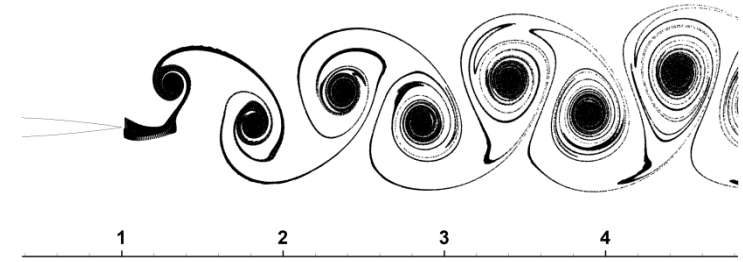

(b)

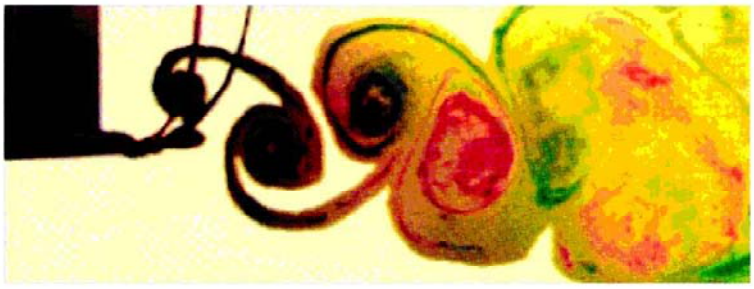

(c)

From Lai, J. C. S. and Platzer, M. F, AIAA Journal, 1999[29]

Fig.2.8 Wake comparison at k=7.86 and h=0.1. a) vorticity contour with negative contours (clockwise) shown in dotted lines and positive contours (counter clockwise) in solid lines, b) Particle trace and c) experimental dye visualization

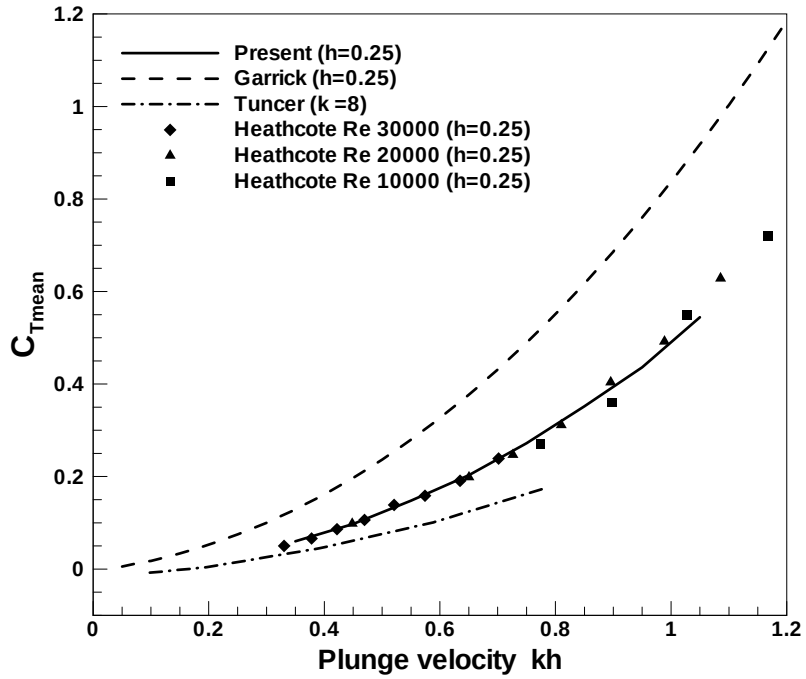

Fig.2.9 Comparison of mean thrust for different plunge velocities

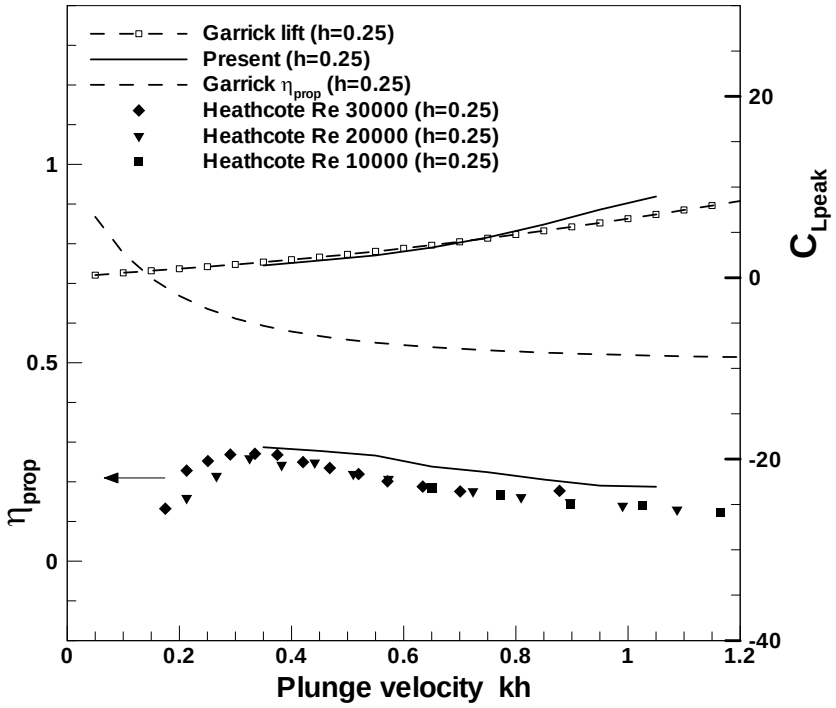

Fig.2.10 Variation of maximum lift coefficient and propulsive efficiency for different values of plunge velocity

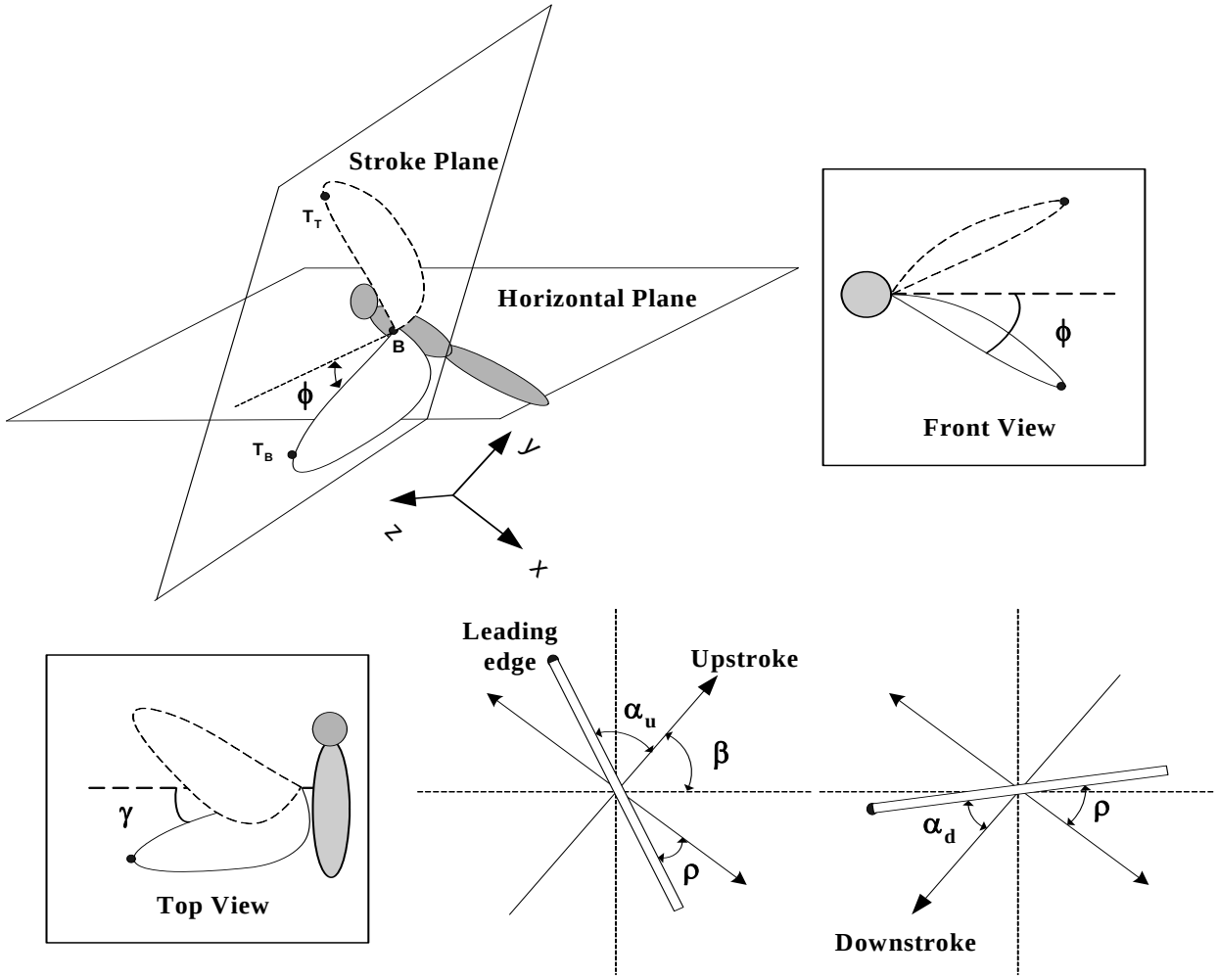

Fig.2.11 Kinematic parameters

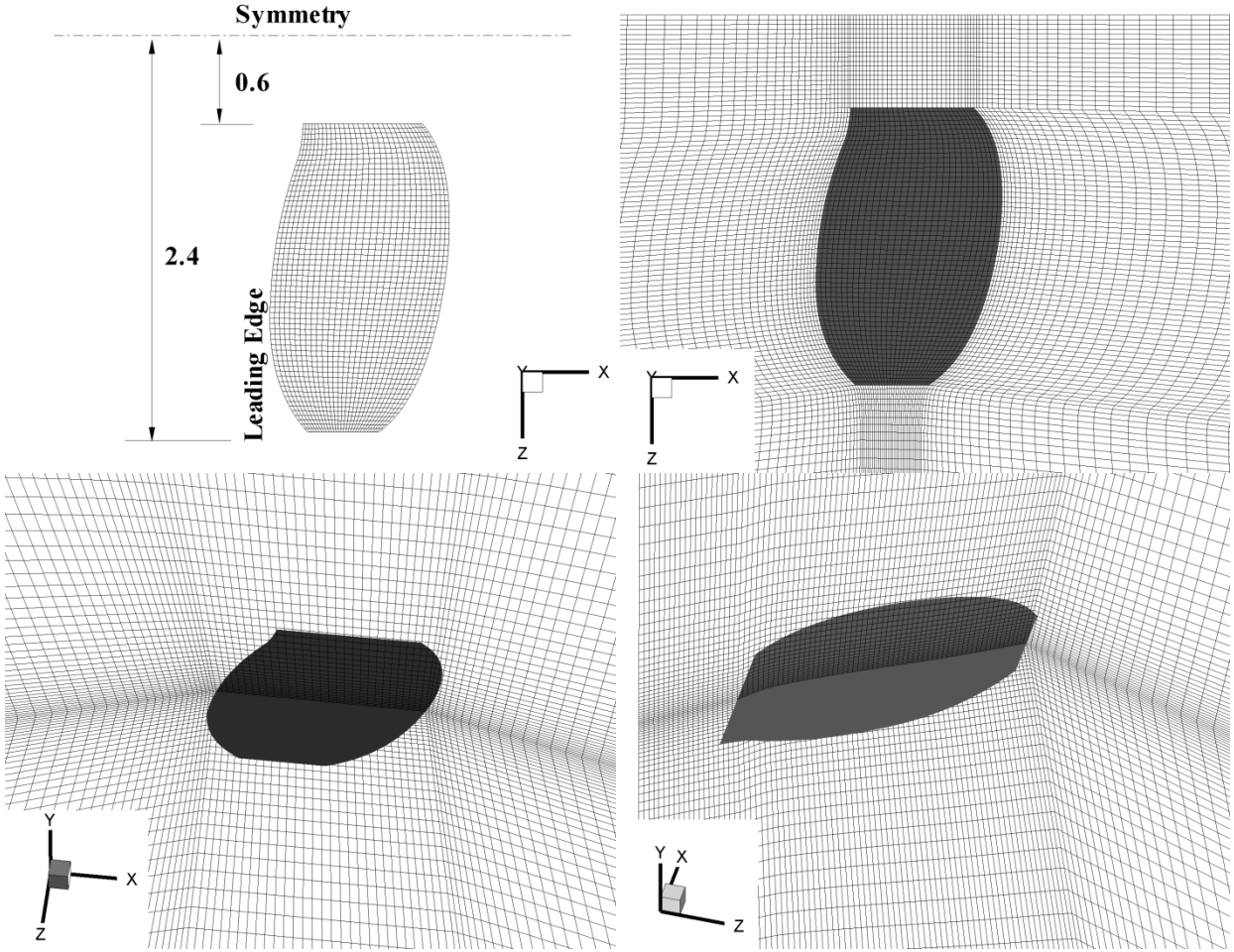

Fig.2.12 a) Planform of the wing used in the study. Deformed grid at maximum stroke angle along the b) planform c) chordwise direction d) spanwise direction

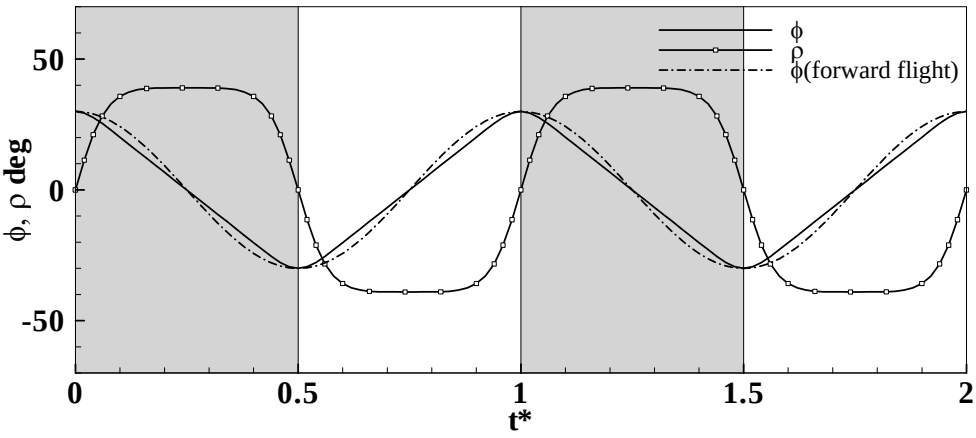

Fig.2.13 Variation of flapping angle and torsional angle (shaded region represents downstroke).

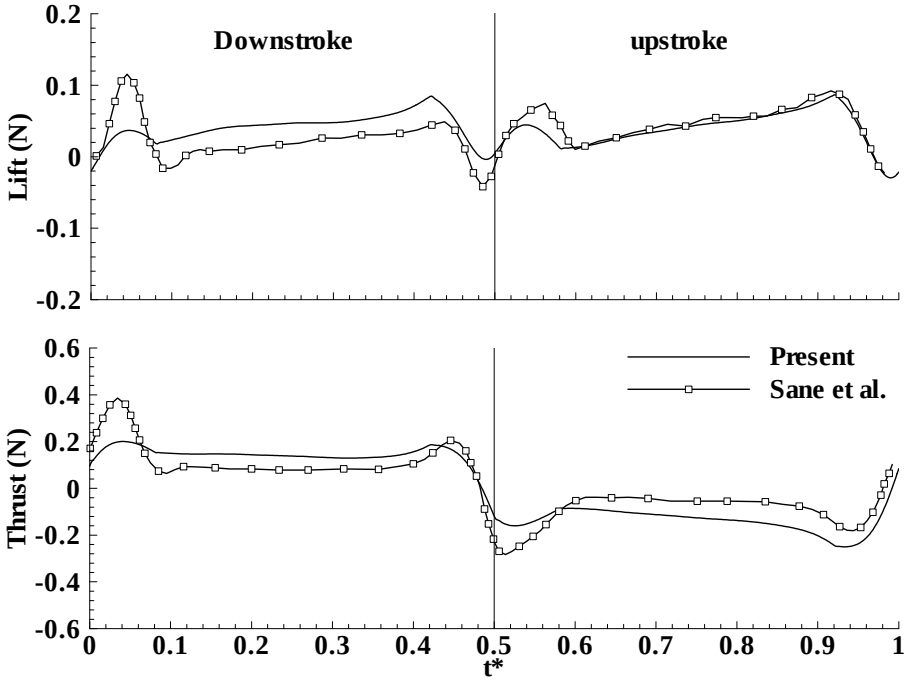

Fig.2.14 Variation of lift and thrust forces for hovering fruitfly

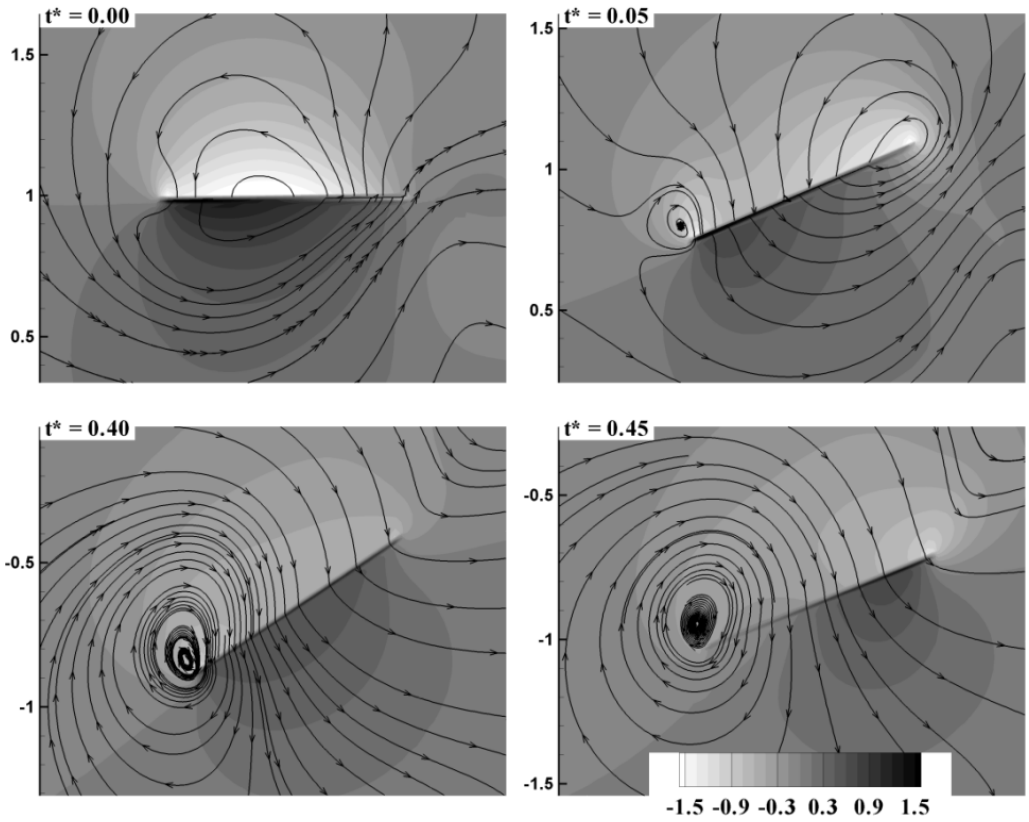

Fig.2.15 Pressure contours and streamlines along chordwise plane at ζ=2.

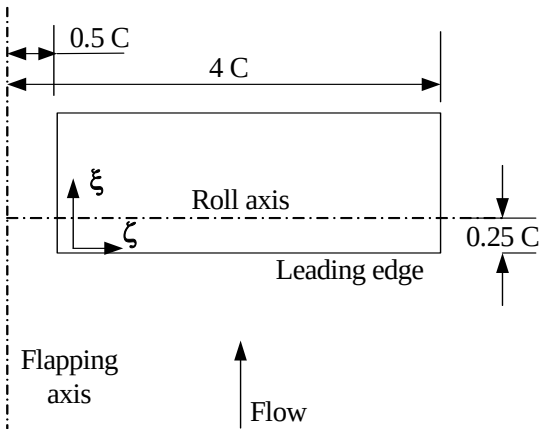

(a)

During Downstroke

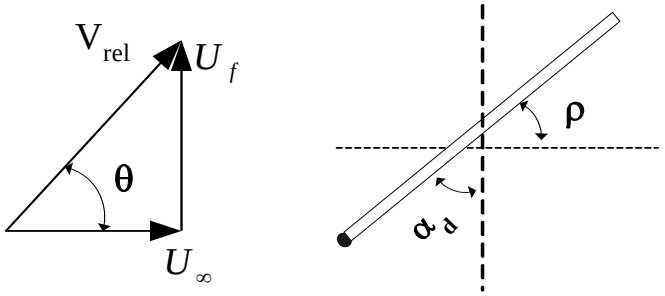

$\theta = \tan^{-1}[U_f / U_\infty]$ $\quad \alpha_{eff} = \theta - \rho$

$= \tan^{-1}[1/J]$ $\quad = \theta + \alpha_d - 90^o$ **(b)**

Fig.2.16 (a) Rectangular wing configuration (b) Effective angle of attack

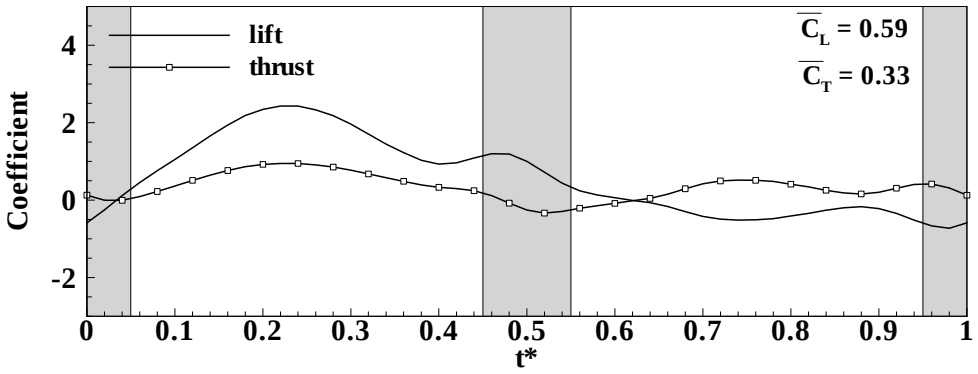

Fig.2.17 Variation of lift and thrust coefficients (shaded region represents rotation)

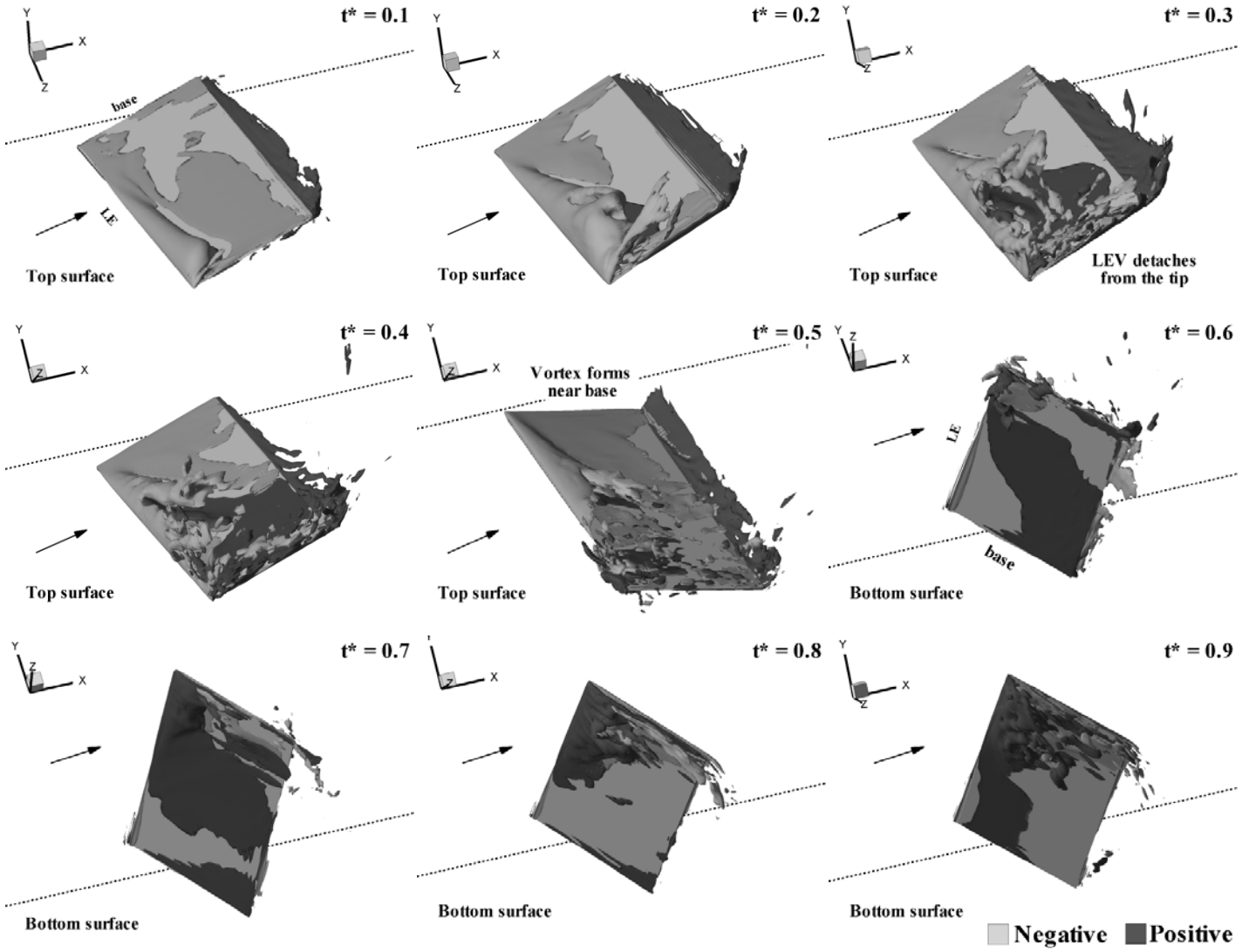

Fig.2.18 Isosurface of vorticity ω_ξ at different times (arrows represent approximate freestream direction)

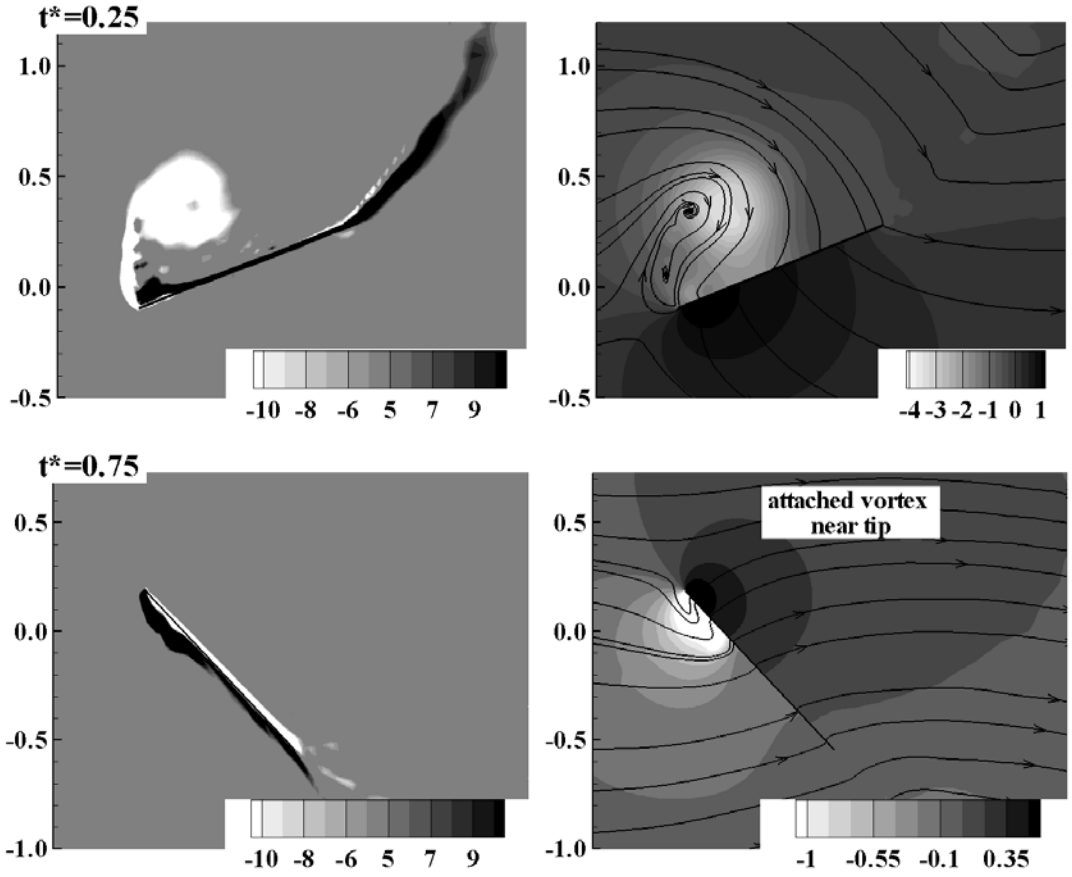

Fig.2.19 Vorticity and pressure contours along the chordwise plane at ζ =3.

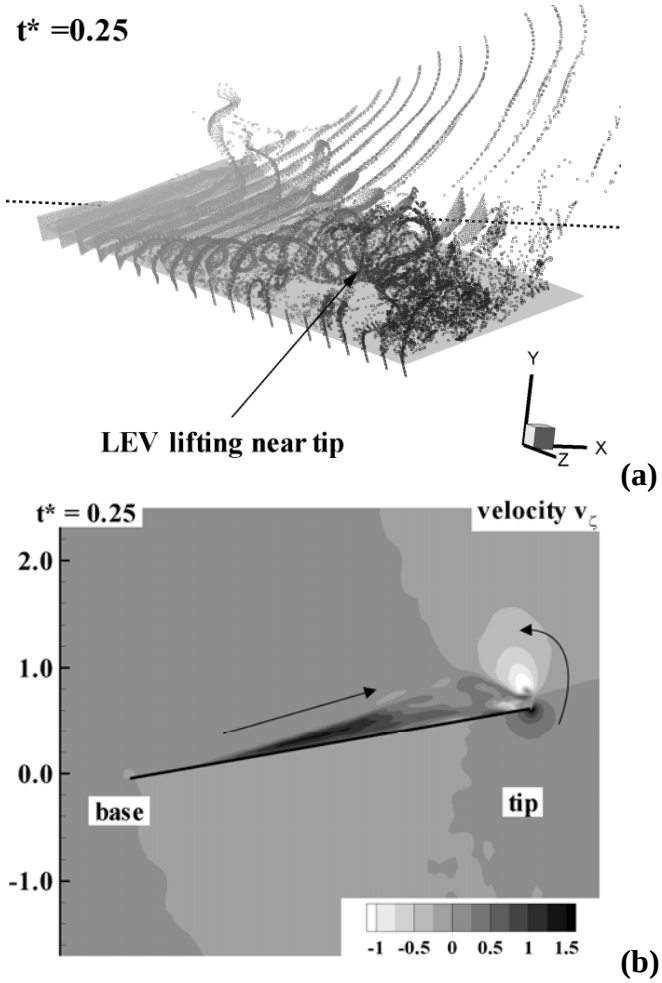

Fig.2.20 a) Particle traces obtained by releasing particles along the leading edge, which are colored based on the location of release. b) Spanwise flow along the center of LEV and the arrows indicate the direction of flow.

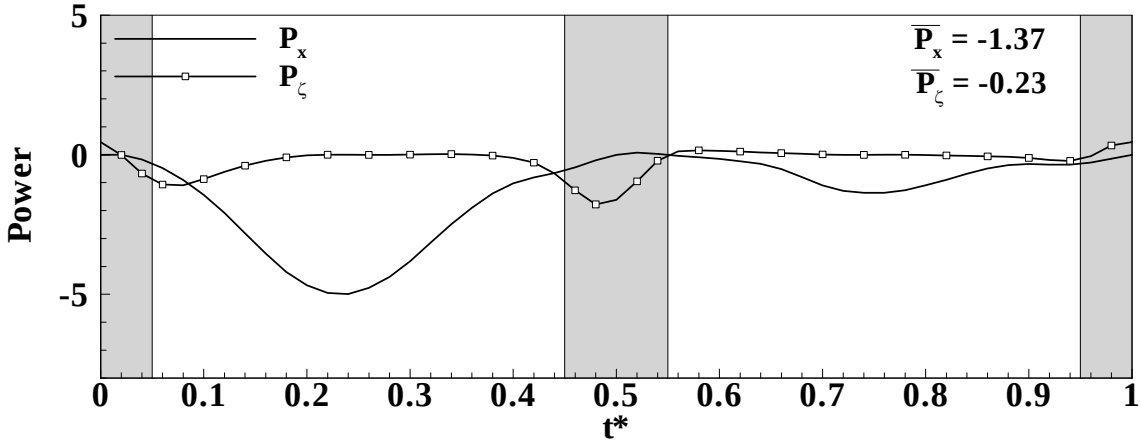

Fig.2.21 Power required for rotation and flapping

2.5 References

[1] Hirt, C. W., Amsden, A. A., and Cook, J. L. An Arbitrary Lagrangian-Eulerian Computing Method for All Flow Speeds. Journal of Computational Physics 1972;14:227-253.

[2] Donea, J., Giuliani, S., and Halleux, J. P. An Arbitrary Lagrangian-Eulerian Finite Element Method for Transient Dynamic Fluid-Structure Interactions. Computer Methods in Applied Mechanics and Engineering 1982;33:689-723.

[3] Ramaswamy, B. and Kawahara, M. Arbitrary Lagrangian-Eulerian Finite Element Method for Unsteady, Convective, Incompressible Viscous Free Surface Fluid Flow. International Journal For numerical Methods in Fluids 1987;7:1053-1075.

[4] Ushijima, S. Three-Dimensional Arbitrary Lagrangian–Eulerian Numerical Prediction Method for Non-Linear Free Surface Oscillation. International Journal for Numerical Methods in Fluids 1998;26:605–623.

[5] Li, J., Hesse, M., Ziegler, J., and Woods, A. W. An Arbitrary Lagrangian Eulerian Method for Moving-Boundary Problems and Its Application to Jumping over Water. Journal of Computational Physics 2005;208 289–314.

[6] Nithiarasu, P. An Arbitrary Lagrangian Eulerian (ALE) Formulation for Free Surface Flows Using the Characteristic-Based Split (CBS) Scheme. International Journal for Numerical Methods in Fluids 2005;48:1415–1428.

[7] Thomas, P. D. and Lombard, C. K. Geometric Conservation Law and Its Application to Flow Computation on Moving Grid. 11th Fluid and Plasma Dynamics Conference, 1978;17:1030-1036.

[8] Demirdzic, I. and Peric, M. Space Conservation Law in Finite Volume Calculation of Fluid Flow. International Journal For numerical Methods in Fluids 1988;8:1037-1050.

[9] Demirdzic, I. and Peric, M. Finite Volume Method for Prediction of Fluid Flow in Arbitrarily Shaped Domains with Moving Boundaries. International Journal For numerical Methods in Fluids 1990;10:771-790.

[10] Tezduyar, T., Aliabadi, S., Behr, M., Johnson, A., and Mittal, S. Parallel Finite Element Computation of 3D Flows. Computer 1993;26:27-36.

[11] Johnson, A. A. and Tezduyar, T. E. Mesh Update Strategies in Parallel Finite Element Computations of Flow Problems with Moving Boundaries and Interfaces. Computer Methods in Applied Mechanics and Engineering 1994;119:73-94.

[12] Batina, J. T. Unsteady Euler Airfoil Solutions Using Unstructured Dynamic Meshes. 27th Aerospace Sciences Meeting, Reno 1989.

[13] Stein, K., Tezduyar, T., and Benney, R. Mesh Moving Techniques for Fluid-Structure Interactions with Large Displacements. Journal of Applied Mechanics 2003;70:58-63.

[14] Stein, K., Tezduyar, T., and Benney, R. Automatic Mesh Update with the Solid-Extension Mesh Moving Technique. Computer Methods in Applied Mechanics and Engineering 2004;193:2019-2032.

[15] Dubuc, L., Cantariti, F., Woodgate, M., Gribben, B., Badcock, K. J., and Richards, B. E. A Grid Deformation Technique for Unsteady Flow Computations. International Journal for Numerical Methods in Fluids 2000;32:285-311.

[16] Tsai, H. M. and Wong, A. S. F. Unsteady Flow Calculations with a Parallel Multiblock Moving Mesh Algorithm. American Institute of Aeronautics and Astronautics journal 2001;39:1021-1029.

[17] Potsdam, M. A. and Guruswamy, G. P. A Parallel Multiblock Mesh Movement Scheme for Complex Aeroelastic Applications. 39th AIAA Aerospace Sciences Meeting & Exhibit, 2001;AIAA-2001-716

[18] Sadeghi, M. and Liu, F. Coupled Fluid-Structure Simulation for Turbomachinery Blade Rows. AIAA Aerospace Sciences Meeting and Exhibit, Reno, Nevada 2005; AIAA-2005-18

[19] Li, J., Liu, Z., and Huang, S. Deforming Grid Technique Applied to Unsteady Viscous Flow Simulation by a Fully Implicit Solver. Journal of Aircraft 2005;42:1371-1374.

[20] Pan, H., Pan, L. S., Xu, D., Ng, T. Y., and Liu, G. R. A Projection Method for Solving Incompressible Viscous Flows on Domains with Moving Boundaries. International Journal for Numerical Methods in Fluids 2004;45:53-78.

[21] Kim, J. and Moin, P. Applications of a Fractional Step Method to Incompressible Navier-Stokes Equations. Journal of Computer Physics 1985;59:308-323.

[22] Tafti, D. K. GenIDLEST - a Scalable Parallel Computational Tool for Simulating Complex Turbulent Flows. Proc. ASME Fluids Engineering Division, ASME-IMECE, New York 2001;256.

[23] Germano, M., Piomelli, U., Moin, P., and Cabot, W. H. A Dynamic Subgrid-Scale Eddy Viscosity Model. Physics of Fluids A 1991;3:1760-1765.

[24] Obayashi, S., "Free-Stream Capturing in Fluid Conservation Law for Moving Coordinates in Three Dimensions," NASA Contractor Report 177572 (1991).

[25] Blackburn, H. M. and Henderson, R. D. A Study of Two-Dimensional Flow Past an Oscillating Cylinder. J. Fluid Mech. 1999;85:255-286.

[26] Stewart, B., Leontini, J., Hourigan, K., and Thompson, M. C. Vortex Wake and Energy Transitions of an Oscillating Cylinder at Low Reynolds Number. Australian and New Zealand Industrial and Applied Mathematics Journal 2005;46 (E):C181-C195.

[27] Blackburn, H. and Henderson, R. Lock-in Behavior in Simulated Vortex-Induced Vibration. Experimental Thermal and Fluid Science 1996;12:184-189.

[28] Williamson, C. H. K. and Roshko, A. Vortex Formation in the Wake of an Oscillating Cylinder. Journal of Fluids and Structures 1988;2:355-381.

[29] Lai, J. C. S. and Platzer, M. F. Jet Characteristics of a Plunging Airfoil. AIAA Journal 1999;37:1529-1537.

[30] Tuncer, I. H. and Platzer, M. F. Computational Study of Flapping Airfoil Aerodynamics. Journal of Aircraft 2000;37:514-520.

[31] Young, J. and Lai, J. C. S. Oscillation Frequency and Amplitude Effects on the Wake of a Plunging Airfoil. AIAA Journal 2004;42;2042-2052.

[32] Theodorsen, T., "General Theory of Aerodynamic Instability and the Mechanism of Flutter," NACA Report No. 496 (1935).

[33] Garrick, I. E., "Propulsion of a Flapping and Oscillating Airfoil," Report No. 567 (1936).

[34] Platzer, M. F. and Jones, K. D. Flapping wing Aerodynamics – Progress and Challenges. 44th AIAA Aerospace Sciences Meeting and Exhibit, Reno, Nevada 2006; AIAA-2006-500.

[35] Heathcote, S., Wang, Z., and Gursul, I. Effect of Spanwise Flexibility on Flapping Wing Propulsion. 36th AIAA Fluid Dynamics Conference and Exhibit, San Francisco, California 2006; AIAA 2006-2870.

[36] Sane, S. P. and Dickinson, M. H. The Control of Flight Force by a Flapping Wing: Lift and Drag Production. The Journal of Experimental Biology 2001;204:2607-2626.

[37] Sun, M. and Tang, J. Unsteady Aerodynamic Force Generation by a Model Fruit Fly Wing in Flapping Motion. The Journal of Experimental Biology 2002;205:55-70.

[38] Sun, M. and Lan, S. L. A Computational Study of the Aerodynamic Forces and Power Requirements of Dragonfly (Aeschna Juncea) Hovering. The Journal of Experimental Biology 2004;207:1887-1901.

[39] Ramamurti, R. and Sandberg, W. A Three-Dimensional Computational Study of the Aerodynamic Mechanisms of Insect Flight. The Journal of Experimental Biology May 2002;205:1507-1518.

[40] Ellington, C. P. The Novel Aerodynamics of Insect Flight: Applications to Micro-Air Vehicles. The Journal of Experimental Biology 1999;202:3439–3448.

Chapter 3: Effect of Rotation Kinematics and Angle of Attack on Force Production of Flapping Flight[‡]

Abstract

Unsteady aerodynamics of a rigid flapping wing at Reynolds number of 10,000 for forward flight with advance ratio of 0.5, pertaining to the development of micro air vehicles, is analyzed. The effect of timing and duration of rotation and angle of attack are analyzed using simple flapping kinematics. The flow structures obtained and time variation of lift and thrust are used to evaluate their effects. The power required for flapping and rotation is computed to evaluate the propulsive efficiency. In all the cases simulated, a strong spiral Leading Edge Vortex (LEV) is formed during the downstroke resulting in a peak lift and thrust. A strong spanwise flow from base to tip is observed in the middle of the vortex. However due to the presence of a tip vortex, a strong negative spanwise flow forms near the tip, which prevents the removal of vorticity from the LEV. Hence the LEV becomes unstable during the middle of the downstroke and separates from the wing resulting in a drop in lift. Analysis of different rotation timings show that supination results in the LEV formation near the base and the strength of the LEV depends on the flapping velocity. A stronger vortex is formed for advanced rotation and it generates high lift. Delayed rotation affects thrust production during translation and results in low propulsive efficiency. Analysis of rotation duration shows that shorter rotation results in high instantaneous lift values, while continuous long duration rotation produces thrust during the entire flapping cycle and is preferable for high thrust applications. Analysis of different angles of attack show that a moderate angle of attack, which results in high thrust to lift ratio and complete shedding of the LEV at the end of translation, is required for high propulsive efficiency.

Nomenclature

$\vec{a}^{i}$ = Contravariant basis vectors

C = Airfoil chord length

[‡] This chapter is submitted to AIAA Journal on Feb 2008, and is currently under review.

C_L = Coefficient of lift

C_T = Coefficient of thrust

f = Frequency of flapping

f_0 = fD/U_∞, Non-dimensional frequency of cylinder

$F_{x/y}$ = Force acting on the wing; suffix x, y- direction

g^{ij} = Contravariant metric tensor

$\sqrt{g}$ = Jacobian of the transformation

$\sqrt{g}U^j$ = Contravariant flux vector

$\sqrt{g}U^j_g$ = Contravariant flux due to grid movement

J = Advance ratio; U_∞/U_f; Ratio of the flight velocity to the flapping velocity

p = Pressure

$P_{x/\zeta}$ = Power required; suffix x- flapping and ζ - rotation

R = Semi-wingspan; distance from flapping axis to wing tip

Re = Reynolds number; $U_f C/\nu$

$\mathrm{Re_t}$ = Inverse of the turbulent viscosity

u_i = Cartesian velocity vector

u_i^g = Cartesian Grid velocity vector

U_∞ = Free stream velocity; Forward flight velocity

U_f = Flapping velocity; $2\Phi fR$

$\vec{x}$ = Physical space coordinate

$\vec{\xi}$ = Computational space coordinate

$\alpha_{u/d/eff}$ = Angle of attack; suffix u-upstroke, d-downstroke, and eff-effective

β = Stroke plane angle

η_{prop} = Propulsive efficiency

ϕ = Flapping amplitude

Φ = Total flapping amplitude (max to min)

ν = Kinematic viscosity

ρ = Torsional angle

τ = Shear stress on the surface of the wing

ω_ζ = vorticity; suffix – ζ component

Ω_ζ = Angular velocity of the wing; suffix – ζ component

3.1 Introduction

Micro Air Vehicles (MAVs) typically have dimensions less than 15-20 cm with gross takeoff weights of around 100 to 200g and flight speeds of around 10-15 m/s, which corresponds to a Reynolds number range between 10,000-100,000. At these low Reynolds numbers, the aerodynamic efficiency (lift to drag ratio) of conventional fixed airfoils rapidly deteriorates[1].The chief reason for the deterioration in performance is that at low Reynolds numbers, the boundary layer remains laminar downstream of the location of minimum pressure on the airfoil making it very susceptible to flow separation as the angle of attack increases resulting in an early onset of stall (Carmichael[2]). In addition, because of the low aspect ratio wings used in MAVs, the tip vortex covers a major part of the wing and the aerodynamic performance is affected greatly by the shedding of the tip vortices (Pelletier et al.[3]). On the other hand, birds and insects whose flight regime coincides with that of MAVs use flapping wings to provide both lift and thrust efficiently. They do this by taking advantage of unsteady flow mechanisms using wing kinematics evolved over millions of years. The kinematics involved in normal flapping flight are divided into two translation motions corresponding to up and down strokes and two rotational motions (pronation and supination) corresponding to stroke reversals. Pronation is achieved before the downstroke and supination is achieved before the upstroke. Figure 3.1 shows the critical kinematic parameters of flapping flight with their definitions given in Table 3.1.

A number of unsteady aerodynamic mechanisms such as clap and fling[4], delayed stall[5,6], wake capturing[7], and, rotational circulation[7] have been proposed to explain the generation of lift in birds and insects. Among these, the delayed stall mechanism involves the formation of a steady Leading Edge Vortex (LEV) and is the primary mechanism used by most birds and insects for production of lift and thrust during the translational period. During the downstroke, air swirls around the leading edge and forms

a LEV. This LEV increases the bound vortex circulation and hence the lift. In a fixed airfoil, the formation of LEV leads to dynamic stall within 3-4 chord lengths of travel. However in insects, the LEV is stable for the entire downstroke and during this period, the insect covers a distance of more than 8 chord lengths.

Table.3.1 Kinematic parameters and non-dimensional numbers for flapping flight

Parameters	***Description***
Stroke plane	The plane defined by three points: wing base (B), and the wingtip at maximum (T_T) and minimum angular position (T_B). During hovering, the stroke plane will be near horizontal and during forward flight, it will be vertical.
Stroke plane angle, β	Angle between the stroke plane and the horizontal plane. It ranges from 0^o for hovering to 90^o for forward flight.
Angle of attack, α	Angle between the wing direction (from trailing edge to leading edge) and the direction of motion.
Torsional angle, ρ	Angle between the wing direction and the direction perpendicular to stroke plane.
Flapping amplitude, ϕ	Angle between the leading edge of the wing and the plane perpendicular to the stroke plane.

The stability of the LEV plays an important role in the superior performance of birds and insects. Many experimental studies have evaluated the duration and the stability criteria of the LEV. Dickinson and Gotz[5] analyzed the effect of angle of attack during the translation period on lift and drag production using a two dimensional wing model (Re =192). They found that the LEV was generated at an angle of attack above 13.5^o due to impulsive movement and stayed attached for 2 chord lengths of travel. The presence of the LEV resulted in an 80% increase in lift similar to that of detached vortex lift for a delta-wing aircraft. The shedding of the LEV led to the formation of a secondary vortex of opposite sign near the trailing edge, correlating with a decrease in lift. Further, the study found that up to an angle of attack of 54^o, the lift characteristics remain unaltered by the change in camber. Wang et al.[8] compared results obtained from two-dimensional numerical simulation of a hovering fruit fly with three-dimensional results from a

dynamically scaled mechanical model (Re =75 to 115). They found that the numerical results matched well with three-dimensional results for cases with a short downstroke length. In the case of hovering insects, the stroke length is only 3 to 5 chords, during which the LEV remains attached to the wing even for two-dimensional cases. When the downstroke is longer than a typical stroke length, the two-dimensional cases showed a phase difference with three-dimensional results and resulted in lower lift coefficients.

Ellington[9] conducted flow visualization studies using a large mechanical model of a hawkmoth, *flapper* (Re~4000). An intense LEV on the downstroke at all flight speeds (0.4 to 5.7 m/s) was observed. The LEV spiraled out towards the wingtip with high spanwise velocities comparable to the flapping velocity, which stabilized the vortex. The flow structure obtained was similar to the conical leading edge vortex found in delta-wings. They suggested that the strong spanwise flow was created either by the pressure gradient, formed due to the velocity gradient along the flapping wing, or by centrifugal acceleration in the boundary layer, or by the induced velocity field of the spiral vortex lines. Liu et al.[10] analyzed flapping flight of a hovering hawkmoth at Re =3000 to 4000 using the finite volume method. The study showed the formation of a LEV during both upstroke and downstroke, which stayed attached to the wing during the entire translational and following rotational motions. The combined translation and rotation deformed the vortex, which led to shedding of the LEV at the start of the next translation motion. The spanwise flow, created due to spanwise pressure gradient stabilized the LEV till 70% of the span. During the second half of the downstroke, a secondary LEV formed at 75% span, which was unstable and affected strongly by the presence of the tip vortex. The LEV formed during the upstroke was weak and attached closely to the leading edge. The study showed that the lift force was produced mainly during the entire downstroke and the later part of the upstroke.

Dickinson et al.[7] conducted flow visualization studies using a dynamically scaled version of a hovering fruit fly, *robotic fly*, at Re =136. They compared the force coefficients obtained by the robotic fly with a two-dimensional model wing and found that the 3D model produced high average lift and thrust coefficients. The experimental investigation of Birch and Dickinson[11] provided contrasting proof for the stability of

LEV at low Reynolds number (100-250) relevant to small insect flights. They conducted experiments with fences and baffles on the top surface of the wing and showed that the LEV remains attached to the wing despite the absence of spanwise flow. They proposed that the downward velocity created by the tip vortices limited the growth and subsequent detachment of the LEV. Birch et al.[12] investigated flow structures and forces generated at low and high Reynolds number (Re =120 and 1400). In both cases, a stable LEV was present throughout the downstroke. At Re =1400, they observed strong spanwise flow within the core of the LEV, with velocities 150% that of the flapping velocity. The spanwise flow removed the vorticity into the wake and resulted in a spiral LEV similar to that observed by Ellington[9]. However at Re = 120, the spanwise flow was absent, which resulted in lower forces. Miller and Peskin[13] studied the effect of Reynolds number (8 to 128) on the formation of the LEV using the immersed boundary technique. At Re < 32, the LEV (negative pressure region) and trailing edge vortices (positive pressure region) remain attached, which resulted in lower lift. At Re > 64, they observed shedding of the trailing vortex during translation, which resulted in vortical asymmetry, leading to high lift production.

Tarascio et al.[14] conducted a flow-visualization experiment on a hovering flapping flight model at Reynolds number of the order of 8000. The flow field consisted of folded wakes formed by the strong starting vortex shed at the end of each half stroke during wing rotation. Due to the induced flow, the wakes were pushed downwards parallel to the flapping plane. The key finding of this study was that during translation, the top surface was covered by multiple vortices and the LEV was continually generated and shed into the wake. This result is in contrast to previous studies[7,9], where a stable single LEV is present during translation. Further, they observed that the strength of the LEV increased along the span and identified separated flow at the outboard region of the wing.

The unsteady mechanisms involved during the stroke reversal contributed significantly to lift production especially for *hovering flight*. In the experimental study by Dickinson et al.[7], two peaks in force coefficients were obtained during the rotation and early part of translation. They attributed the peak in lift during the rotation to the rotational circulation and the second peak to wake capturing. Dickinson[15] studied the

effect of rotation by varying speed, duration, angle of attack and axis of rotation using a dynamically scaled model (Re=236) of small insects *Drosophila* during hovering. The study showed that the aerodynamic performance increased significantly as the wing captured the vorticity generated during rotation. A lift coefficient value of 4 was obtained when the wing translated backwards in the Von Karman street generated by the previous stroke with 76.5^{o} angle of attack. Effects of stroke amplitude, rotation timing and duration, and shape and magnitude of stroke deviation on the aerodynamic performance was studied by Sane and Dickinson[16] using *robotic fly*. The values of drag showed large deviations from translational quasi-steady values at low stroke amplitudes due to the major influence of rotational mechanisms. Analysis on timing and duration of rotation showed that the short rotation, which precedes the translation (occurring at the end of the stroke) resulted in high lift. Further, they found that the quasi-steady analysis underestimated the average thrust coefficient in all cases showing the importance of unsteady aerodynamics.

A numerical investigation of a hovering fruit fly by Sun and Tang[17] with different rotation timing similar to that of Sane and Dickinson[16] showed a comparable trend in lift and thrust. However their results showed that wake capturing and rotational circulation effects are not significant and they proposed three other mechanisms, fast acceleration at the start of downstroke; delayed stall during translation; and fast pitching up rotation at the end of the stroke for force production. When the rotation or stroke reversal carried out at the end of the stroke, the effect of the first and third mechanisms were enhanced, which resulted in high lift. When the rotation was symmetric (half rotation during the end of the stroke and half during the start of the following stroke), the fast acceleration mechanism at the start of the stroke was affected, resulting in lower lift. The performance deteriorated when rotation occurred at the start of the stroke, which completely eliminated the pitching up rotation mechanism. Ramamurti and Sandberg[18] also showed that the thrust force was high when rotation was advanced with respect to stroke reversal.

Despite many available studies, application of flapping flights to MAVs still pose a number of challenges. Most of the previous studies have been performed at very low

Reynolds number, less than 4000, whereas MAVs could have an operational range of 10,000 to 100,000. Further, the experiments by Tarascio et al.[14] at Re=8000 shows the presence of multiple unstable vortices on the top surface of the wing, which is in contrast to the stable LEV formation during the delayed stall. This necessitates more detailed studies to evaluate the effectiveness of delayed stall in high Reynolds number range relevant to MAVs. Flow visualization[19] studies show that the insects employ different kinematics at different flight conditions to achieve the required thrust. However, most of the previous studies have concentrated on hovering flight, which require no thrust. Hence it is critical to understand how changes in kinematics affect thrust production for a forward flight. The focus of the present study is to analyze the effect of kinematics on a forward flight with an advance ratio J=0.5 at Re =10,000. The simulations are carried out for different kinematics by varying rotation timing, rotation duration, and angle of attack. The effects of kinematics are evaluated by analyzing the resulting flow structure, force production, and propulsive efficiency.

3.2 Methodology

In the present study, a structured multiblock solver with a boundary fitted dynamic grid is employed. In this framework the grid deforms with the wing motion. The method of Large-Eddy Simulations (LES) is employed with a subgrid stress model to resolve the turbulence in the flow field. The governing equations for unsteady incompressible viscous flow on moving coordinate system consist of space, mass, and momentum conservation laws. The equations are mapped from physical $(\vec{x})$ to logical/computational space $(\vec{\xi})$ by a boundary conforming transformation $\vec{x} = \vec{x}(\vec{\xi})$, where $\vec{x} = (x, y, z)$ and $\vec{\xi} = (\xi, \eta, \zeta)$. The equations are non-dimensionalized by chord length C and flapping velocity U_f and written in conservative non-dimensional form as:

Space:

$$\frac{\partial}{\partial t}\left(\sqrt{g}\right) - \frac{\partial}{\partial \xi_j}\left(\sqrt{g} U \frac{j}{g}\right) = 0 \tag{3.1}$$

Mass:

$$\frac{\partial}{\partial \xi_j}\left(\sqrt{g}U^j\right) = 0 \tag{3.2}$$

Momentum

$$\frac{\partial}{\partial t}\left(\sqrt{g}u_i\right) + \frac{\partial}{\partial \xi_j}\left(\left[\sqrt{g}U^j - \sqrt{g}U_g^j\right]u_i\right) = -\frac{\partial}{\partial \xi_j}\left(\sqrt{g}(\vec{a}^j)_i\, p\right)$$

$$+\frac{\partial}{\partial \xi_j}\left(\left(\frac{1}{\mathrm{Re}} + \frac{1}{\mathrm{Re}_t}\right)\sqrt{g}\, g^{jk}\frac{\partial u_i}{\partial \xi_k}\right) \tag{3.3}$$

where $\vec{a}^i$ are the contravariant basis vectors, $\sqrt{g}$ is the Jacobian of the transformation, g^{ij} is the contravariant metric tensor, $\sqrt{g}U^j = \sqrt{g}\left(\vec{a}^j\right)_k u_k$ is the contravariant flux vector, $\sqrt{g}U_g^j = \sqrt{g}\left(\vec{a}^j\right)_k u_k^g$ is the contravariant flux vector due to grid velocity u^g, u_i is the Cartesian velocity vector, and p is the pressure. In the above formulation, the grid velocity u^g is not used explicitly. Instead, the grid contravariant flux vector is employed which is directly computed based on the SCL. The non-dimensional time used is t^*U_f/L^* and the Reynolds number is given by $U_f C/\nu$. Re_t is the inverse of the subgrid eddy-viscosity which is modeled as

$$\frac{1}{\mathrm{Re}_t} = C_s^{\,2}(\sqrt{g})^{2/3}\left|\bar{S}\right| \tag{3.4}$$

where $\left|\bar{S}\right|$ is the magnitude of the strain rate tensor given by $\left|\bar{S}\right| = \sqrt{2\overline{S_{ik}}\,\overline{S_{ik}}}$ and the Smagorinsky constant $C_s^{\,2}$ is obtained via the dynamic subgrid stress model (Germano et al.[20]).

The equations are formulated in a finite-volume framework using a fractional-step algorithm for time advancement. Second-order central differences are used for the convective and viscous terms and a combination of an explicit Adams-Bashforth and implicit Crank-Nicolson discretizations are used for time advancement**.** During the start of each time step, the wing is moved based on the prescribed kinematics, keeping the

external boundaries of the computational domain fixed. The resulting grid movement is carried out at each time step by a combination of a spring analogy and Trans-Finite Interpolation (TFI) on displacements[21,22]. The Space Conservation Law (SCL) (Eq.3.1) is used to calculate the grid contravariant fluxes [21,22] which are used in the momentum equations to account for grid movement.

3.3 Results

The unsteady aerodynamics of flapping flight depends on many kinematic and flow parameters such as angle of attack, rotation and flapping kinematics, stroke amplitude, stroke plane angle, Reynolds number, and advance ratio. The purpose of the present study is to evaluate the effect of timing and duration of rotation and angle of attack on the force production for forward flights. All the simulations in the current study are carried out at Re=10,000 at an advance ratio J=0.5. A stroke amplitude of 60^o ($\pm 30^o$) and a vertical stroke plane $\beta=90^o$ is used. Three different rotational kinematics, delayed, symmetrical, and, advanced are analyzed to evaluate the effect of timing of rotation. The effect of duration of rotation is analyzed for symmetrical rotation with three different durations. Finally, the angle of attack during downstroke and upstroke are changed to analyze their effect on force production and the stability of LEV.

3.3.1 Validation

The dynamic mesh capability of the solver has been validated previously in a number of flow problems such as the forced oscillation of a cylinder, a pitching airfoil and a hovering fruitfly[23,24]. In the current context, analysis of the hovering flight of a fruitfly with kinematics similar to that employed by Sane and Dickinson[16] is presented. The planform of the robofly wing as shown in Fig.3.2 (obtained from Dickinson) is used to develop the grid. The coordinate (x,y,z) is used for the fixed frame, where the y-z plane represents the stroke plane (Fig.3.1). The coordinates (ξ,η,ζ) are used for the moving frame fixed to the wing, where ξ is along the chordwise direction, η is perpendicular to the wing, and ζ is along the spanwise direction (Fig.3.2). The computational domain is made of 60 blocks with about 3 million cells. The domain boundaries are placed at 10 times the chord length from the edges of the wing on all sides except the symmetry surface, which is located at 0.6 times the chord length from the wing base (Fig.3.2). The

symmetric boundary condition is applied along the axis of flapping, while a zero velocity boundary condition is applied at all other faces.

The simulation is carried out for four flapping cycles using 60 processors on System-X at Virginia Tech. Comparison of lift and thrust forces between the third and fourth flapping cycles confirmed that the flow had attained repeatability and hence the results from the fourth flapping cycle are used for the analysis A triangular wave form for the flapping angle and a square wave form for the rotation angle as shown in Fig.3.3 are employed. The normalized value of $t^*=t/t_{cycle}$ from 0 to 0.5 represents the downstroke whereas 0.5 to 1.0 represents the upstroke. The mid-stroke angle of attack is 50^o for both strokes and the rotation is carried out symmetrically with a total duration t* of 0.16. The stroke plane angle is $\beta=0^o$ and the total flapping amplitude is $\Phi=60^o$. A fluid viscosity of 120 cSt with density of 880 kg/m^3 and flapping frequency of 168 mHz along with the actual length of robofly wing[16] (25cm) are used to compute the Reynolds number for the current simulation. The Reynolds number based on the chord length C=10cm (maximum chord length) and tip velocity is 73.

The comparison of time variation of lift and thrust forces obtained during the fourth flapping cycle with experimental results[16] is shown in Fig.3.4. Since the stroke plane is horizontal ($\beta=0^o$), the lift force is given by $-F_x$ and the thrust force by $-F_y$. The lift force compares reasonably well; in particular, good agreement is observed during the upstroke, while the values differ during the downstroke. Since the kinematics are symmetrical and the freestream velocity is zero, the values of lift should be identical for the upstroke and downstroke. However, the experimental results show a deviation of around 50% between the upstroke and downstroke, most likely due to uncertainties in the force measurements. The comparison of thrust force also shows reasonable agreement in the trend but the values differ in magnitude. In particular the peak values of lift and thrust obtained at the start of the downstroke and upstroke show larger deviation from the experimental values. This deviation could be due to the kinematics used in the computations, which is curve fitted from the experimental data, and results in some smoothing during stroke reversal. A previous study[17] has shown that the acceleration and deceleration during stroke reversal is responsible for the peaks in lift and thrust. Hence a small deviation from the

experimental kinematics could result in a larger deviation in the forces. Similar quantitative deviations have been reported by previous numerical studies[17,18,25].

The pressure contours and streamlines in a chordwise plane at ξ=2 at different times are shown in Fig.3.5. Since the downstroke and upstroke are symmetric, only the results during the downstroke are used to analyze the flow structures. During the start of the downstroke, a high pressure region forms on the bottom surface of the wing due to sudden deceleration of the wing at the end of the upstroke, which when combined with the rotation results in the formation of a LEV and a peak in lift and thrust at time t*=0.05. The LEV grows and reaches a maximum size at time t*~0.4 to 0.45, and sheds during the rotation which reduces the lift and thrust production. At time t* of 0.5 (not shown) the pressure contours are similar to that of t*=0 with the positive pressure now on the top surface of the wing.

3.3.2 Analysis of forward flight

For simplicity, an infinitesimally thin rectangular rigid wing with aspect ratio of 4 as shown in Fig.3.6 is used for the analysis. A single wing configuration with a symmetry boundary condition along the flapping axis is employed in the current study assuming that there is no interference between wings, and between fuselage and wing. The rotation axis is placed at 1/4 chord length from the leading edge. The downstream boundary is placed at 15 chord lengths from the trailing edge, while 10 chord lengths are used for other boundaries. Constant velocity boundary condition is applied at all inlet faces and an outflow boundary condition is specified downstream. A symmetry condition is applied at the base of the wing. The gird consists of 60 blocks with approximately 6.5 million cells. The wing is resolved using 80x40 grid points and 80 grid points are used perpendicular to the wing as shown in Fig.3.7. The boundary layer is resolved by placing 10 grid points inside the thickness of 0.055, the typical boundary layer thickness for flow over a flat plate at Re=10,000. A grid refinement study is carried out by increasing the number of grid points perpendicular to the wing from 80 to 120. The comparison of instantaneous lift and thrust forces shows less than 2% deviation and the mean values of lift and thrust differ by less than 5%.

Table.3.2 Kinematic parameters used for different cases

Case	Rotation Timing	Rotation Duration	α_d	α_u
A	Advanced	0.1	70^o	45^o
B	Symmetric	0.1	70^o	45^o
C	Delayed	0.1	70^o	45^o
D	Symmetric	0.05	70^o	45^o
E	Sine wave	0.5	70^o	45^o
F	Sine wave	0.5	60^o	35^o
G	Sine wave	0.5	80^o	55^o

The kinematics involve a simple cosine wave form (Fig.3.8) for flapping. The stroke plane angle is kept at $\beta=90^o$ (vertical direction) and the total flapping amplitude is $\Phi=60^o$. The variations of kinematic parameters for the cases simulated in this study are given in Table.3.2. Different rotation kinematics (Fig.3.8) namely advanced, symmetric, and delayed rotation (cases A, B and C) for duration t*=0.1 are used to study the effect of timing of rotation. In order to evaluate the effect of duration of rotation, simulations with small time duration t*=0.05 (case D) and a larger duration (sinusoidal rotation; case E) are carried out. Additional simulations (cases F and G) with different angles of attack for both upstroke and downstroke are analyzed to evaluate the effect of angle of attack. For most cases, the angles of attack of 70^o and 45^o are used for the downstroke and upstroke, respectively. A lower value of angle of attack during the upstroke is used to reduce the down force. The effective angle of attack, α_{eff} is affected by both flapping velocity and free stream velocity as shown in Fig.3.9. In addition, due to the variation of flapping velocity (U_f), the effective angle of attack varies along the span with a maximum value at the tip. For the advance ratio of 0.5 and α_d of 70, the α_{eff} varies from -30^o to 33^o from base to tip. During the upstroke, for α_u of 45, the value of α_{eff} varies from 45^o to -18^o.

3.3.3 Flow structure and lift and thrust variation

The critical flow structures obtained for forward flight for case B is discussed in this section. The simulations are carried out for four flapping cycles. The comparison of

thrust and lift values between the third and fourth flapping cycles show no deviation, hence the results from the fourth flapping cycle are used for the analysis.

3.3.3.1 During downstroke

The sinusoidal variation of flapping angle results in acceleration during the first half of the downstroke and deceleration during the second half of the downstroke. The maximum flapping velocity occurs at t*=0.25, which results in a high effective angle of attack (Fig.3.9). The isosurface of ζ component of vorticity, at different times given in Fig.3.10, show the formation of the LEV (negative vorticity) and its subsequent separation during the downstroke. At t* = 0.1, the LEV forms near the tip and it is attached on the top surface of the wing. The LEV does not extend up to the base as the effective angle of attack near the base is negative. At t*=0.2, a strong spiral LEV with a maximum size near the tip is formed which results in a peak in lift (Fig.3.11). The vorticity contours and the pressure contours at different spanwise locations at time t* =0.25 are shown in Fig.3.12. The size of the LEV increases from base to tip. Strong positive vorticity is present between the LEV and the wing due to the induced velocity field and the strength of the positive vorticity also increases along the spanwise direction. In addition, the separation of the LEV results in the formation of a second LEV. The second LEV also lifts away from the surface of the wing. The pressure contours show the detachment of the LEV (low pressure region) and subsequent increase in the pressure on the surface of the wing by the entrainment of fluid from the free stream.

To analyze the structure of the LEV, particle traces are obtained by releasing particles along the leading edge. The particle traces at t*=0.25, Fig.3.13a, shows a spiral LEV attached near the base and lifted from the wing near the tip. The contours of ζ component of velocity, along the center of the LEV, Fig.3.13b, show a strong spanwise velocity of the order of flapping velocity from the base to the tip. Similar results were obtained by the flow visualization studies conducted by Ellington[9] using a large mechanical model of a hawkmoth at (Re~4000). They showed a spiral LEV with spanwise velocities comparable to the flapping velocity during the downstroke and also suggested that the spanwise flow removed the vorticity from the LEV and stabilized it. However, the present results show that the spanwise flow does not stabilize the LEV for forward flight.

The chief reason is the presence of strong negative spanwise velocity near the tip shown by the curved arrow (Fig.3.13b), which prevents the removal of vorticity from the LEV. Hence the vorticity starts building up near the tip both due to the high angle of attack and convection of vorticity from the base. This increase in vorticity leads to an instability in the LEV and consequent separation from the wing. The isosurface of vorticity at time t* =0.4 shows the complete separation of the LEV near the tip (Fig.3.10), which results in a low lift coefficient. The isosurface also shows the presence of small negative vorticity due to secondary vortex formation along the leading edge.

3.3.3.2 During Supination

The supination starts at the end of the downstroke at around 0.45 and is carried out till t* =0.55, the start of the upstroke. The isosurface contours at time t* of 0.4 (Fig.3.10) show that the LEV is still attached at around ζ=1 with no LEV formation near the base. The increase in angle of attack during supination results in the formation of a vortex near the base, which extends the LEV from the middle to the base as shown by the isosurface of vorticity at t* of 0.5 (Fig.3.10). This results in a second peak in lift. However due to the rotation, the contribution of LEV to thrust drops continuously (Fig.3.11) and results in drag during the later part of supination.

3.3.3.3 During upstroke

The behavior of flow during the upstroke is similar to that during the downstroke. During the upstroke, the angle of attack is low and it is negative only for a small portion of the wing near the tip. Hence there is no clear formation of the LEV and the vorticity contours at time t*=0.7 (Fig.3.10) show a small positive vortex attached near the tip. The vorticity and pressure contours at t*=0.75, Fig.3.14, show no apparent vortex formation at locations ζ=1.5 and 2.0. A small vortex forms near the tip, which results in a low pressure region on the bottom surface of the wing at locations ζ=2.5 and 3.0. This low pressure region results in a peak in negative lift and also generates thrust. The vortex formed is attached to the wing and there is no secondary vortex formation as observed during the downstroke. The vortex becomes unstable at around t* of 0.8 as seen in Fig.3.10 with a drop in negative lift.

3.3.3.4 During pronation

During pronation the angle of attack near the base becomes negative. This change in angle of attack does not result in the formation of a LEV near the base as observed during supination. This is probably due to the absence of a strong LEV during the upstroke. However, a strong pressure difference across the surface is established at time t*=1.0 near the base as seen in Fig.3.15 at locations ζ=1.5 and 2.0. Since the axis of rotation is at 1/4 chord from the leading edge, the trailing edge undergoes significant rotation which results in strong positive pressure on the top near the trailing edge. However, the pressure difference at locations ζ=2.5 and 3.0 is not significant due to the presence of separated vortex (Fig.3.10, t* =0.9). A second peak in the downforce occurs which results in thrust during early periods of pronation.

3.3.3.5 Lift and Thrust production

Instantaneous variations of lift and thrust coefficients (normalized based on the flapping velocity and planform area) are shown in Fig.3.11. During the first half of the downstroke, the lift increases due to the formation of the LEV and reaches a maximum value of 2.5 at time 0.2. This value is around three times higher than the maximum coefficient of lift, 0.75, of a two-dimensional thin plate under steady state condition. The thrust production is positive during most of the downstroke except during the rotation at the end of the downstroke. The contribution from the pressure forces is dominant and the torsional angle determines the ratio of thrust to lift force produced by the LEV. During the upstroke, a low pressure region forms on the bottom surface leading to a negative lift force, but the magnitude is less than that during the downstroke due to the lower angle of attack. The thrust production is positive during most of the upstroke with two peaks obtained at t* =0.75 and at t*=0.95. The average coefficients of lift and thrust are 0.59 and 0.33, respectively. For a typical semi-wingspan R=7.5cm, the lift produced can support 394 grams and the thrust force generated is 1.08 N.

3.3.3.6 Power requirement and propulsive efficiency

The power required for flapping (P_x) and rotation (P_ζ) are computed based on the torque generated by the fluid forces and angular velocity of the wing:

$$\begin{aligned} \mathrm{T} &= \int r \times (p + \tau)\, ds; \\ P &= T.\Omega \end{aligned} \tag{3.5}$$

where r is the radius from the axis, p is the pressure, τ is the shear stress and Ω is the angular velocity of the wing. The power required for acceleration of the wing is neglected as the typical mass of membrane flapping wings is small. The instantaneous variation of power requirement (normalized based on fluid density, tip velocity and chord length, $\rho U_t^3 C^2$) shown in Fig.3.16, follows a similar trend as that of lift and thrust. A peak in power requirement for flapping of around 5 occurs at t* =0.2 during the downstroke, which corresponds to the formation of the LEV. The power required during the upstroke is much lower than that during the downstroke due to lower force production. The power requirement for rotation reaches a maximum value of 2 during the middle of rotation. The average power required for flapping and rotation are 1.37 and 0.23, respectively, and the propulsive efficiency (Eq. 6) is 19.59%. The present simulation shows that flapping flight is capable of supporting the weight of MAVs and produces a propulsive thrust force.

$$\eta_{prop} = \frac{\mathrm{F_T U_\infty}}{\mathrm{P}} \tag{3.6}$$

3.3.4 Effect of rotation timing

The rotation at the end of translation changes the angle of attack and introduces vorticity ω_ζ of magnitude twice that of its angular velocity Ω_ζ. The lift and thrust variation for three different rotation kinematics (Cases A, B and C) are shown in Fig.3.17. Figure 3.18 shows the isosurface of vorticity ω_ζ for all rotation timings during the middle of supination. During supination (rotation at the end of downstroke), the change in angle of attack and the introduction of negative vorticity extends the LEV from the middle of the wing to the base, which results in a second peak in lift. The strength of the vortex formed and the magnitude of lift depend on the timing of rotation, in other words on the flapping velocity, which affects the effective angle of attack. A stronger vortex near the base for advanced rotation and a smaller vortex for symmetric rotation are observed as shown in Fig.3.18. For delayed rotation, the vortex formation is insignificant. In the case of advanced rotation, the flapping velocity (ref Fig.3.9) is in the positive

direction which enhances the change in angle of attack and hence results in a stronger vortex and high lift. On the other hand, in delayed rotation the flapping velocity is in the opposite (down) direction which counteracts the change in angle of attack resulting in no vortex formation and a small peak in lift. A similar variation in lift occurs during pronation at the end of the upstroke.

Table.3.3 Average value of lift and thrust, and propulsive efficiency

Cases	**C_L**	**C_T**	**Power Flapping**	**Power Rotation**	**Propulsive Efficiency**
A	0.58	0.36	1.65	0.32	17.36
B	0.59	0.33	1.37	0.23	19.59
C	0.54	0.23	1.18	0.17	16.19
D	0.59	0.33	1.37	0.25	19.35
E	0.52	0.37	1.59	0.21	19.53
F	0.57	0.28	1.17	0.36	17.39
G	0.45	0.30	1.98	0.08	13.83

The thrust production during upstroke and downstroke is high for advanced rotation as it facilitates the formation of the LEV earlier, which results in high average values of thrust (Table.3.3). The delayed rotation results in lower thrust (C_{Tavg} = 0.23) as it affects thrust production during translation and also results in significant drag during both supination and pronation. The symmetric rotation produces slightly lower thrust and higher lift than advanced rotation. However, symmetric rotation has better propulsive efficiency due to the lower power requirement for flapping and rotation. Delayed rotation has low propulsive efficiency which is undesirable for steady flight. Despite the differences in propulsive efficiency, different combination of rotation timing could be used to achieve a required force. For example, to maximize lift production, advanced rotation for the downstroke and delayed rotation for the upstroke are preferable.

3.3.5 Effect of duration of rotation

In order to understand the effect of duration of rotation, a short rotation, t*=0.05 (Case D) and a continuous sinusoidal rotation (Case E) are analyzed. The comparison of

lift and thrust variation for cases B, D and E is shown in Fig.3.19. The peak in lift obtained for the short duration is higher than that observed for case B, which is mainly due to the higher angular velocity. On the other hand, continuous rotation does not produce any separate peaks in lift, instead delaying the location of maximum peak in lift from time t*=0.23 to t*=0.27. In continuous rotation, the rotation introduces positive vorticity (reduces angle of attack) during the first half of the downstroke and introduces negative vorticity (increases angle of attack) during the second half of the downstroke. This change in angle of attack delays the formation of the LEV during the first half and enhances the vortex formation near the base during the second half. The variation of lift reflects this effect. A gradual increase in lift occurs till t*=0.27 and a gradual drop in lift occurs during the second half of downstroke.

For case D, since the instantaneous value of lift is high only for a short duration, the average values of lift and thrust values remain unaffected. The thrust produced by continuous rotation (C_{Tave}=0.37) is higher than other cases, which is mainly due to positive thrust production throughout the flapping cycle. The propulsive efficiencies of all three cases are equal, which shows that any duration of rotation could be utilized to achieve a desired force requirement. Hence to achieve a higher thrust, a continuous rotation is preferable, while for higher lift a combination of shorter supination and longer pronation is preferable.

3.3.6 Effect of angle of attack

To analyze the effect of angle of attack on force production, additional simulations with higher and lower angles of attack than case E are carried out. The variation of lift and thrust for cases E to G are shown in Fig.3.20. The resultant force is almost perpendicular to the wing direction during the entire flapping cycle due to the strong contribution of pressure forces. The torsional angle/angle of attack determines the contribution of total force to thrust and lift. In the case of low angle of attack, the instantaneous thrust values are higher than the other two cases and of the same order as that of lift. While at a high angle of attack, the resultant force contributes mainly to lift. In addition, the location of maximum lift and the gradient of the lift profile changes for all three cases. Isosurface of vorticity for all three cases E-G during the middle of the

downstroke are shown in Fig.3.21. In the case of high angle of attack, the LEV extends up to the base at t*=0.25 and it separates completely from the wing during the second half of the downstroke. This results in sharp changes in lift and the maximum lift occurs early. In the case of low angle of attack, the LEV formation does not extend up to the base (Fig.3.21) during the early stages of the downstroke. During first half of the downstroke, the LEV formed near the tip contributes to lift, while the formation of LEV near the base contributes to lift during the second half of downstroke. Hence, the variation of lift is gradual and the location of maximum lift shifts to t* = 0.35.

The average value of thrust is high for the moderate angle of attack case, while high lift is produced by the low angle of attack case. The low angle of attack produces high instantaneous values of thrust during the downstroke. However, due to the incomplete separation of the LEV at the end of the downstroke, it results in considerable drag during the initial stages of the upstroke. Figure 3.22 shows the pressure contours at location ζ=2.0 at time t* = 0.55 for all three angles of attack. A strong vortex and low pressure region is present for the low angle of attack, while the strength of the vortex and the pressure difference across the surface is small for the other cases. The pressure difference in case of the low angle of attack results in high lift and drag till t*=0.6, which reduces the propulsive efficiency. The propulsive efficiency of case E is high, and the high angle of attack, case G results in low propulsive efficiency. Hence, in order to achieve high thrust production an optimum value of angle of attack which results in complete shedding of the LEV at the end of the downstroke is required. Further, if high lift force is required a combination of high angle of attack during the downstroke and a low angle of attack during the upstroke could be utilized.

3.4 Conclusion

The effect of rotation kinematics and angle of attack on forward flapping flight with an advance ratio of 0.5 is analyzed at a Reynolds number of 10,000. The flow structures obtained for all cases show the presence of a spiral Leading Edge Vortex (LEV) on the top surface during the downstroke. The LEV becomes unstable and separates during the middle of the downstroke despite the presence of spanwise flow along the core of the LEV. The negative spanwise flow created by the tip blocks the removal of vorticity from

the LEV, which leads to the subsequent separation of the LEV near the tip, leading to a drop in force production. The separation of the LEV results in the formation of a secondary vortex. However, the secondary vortex is not attached to the wing and hence no increase in lift is observed during the second half of the downstroke. The average lift force generated is enough to support the typical weight requirement of 100 to 200grams, of Micro Air Vehicles (MAVs) and generates thrust with a propulsive efficiency of 20%.

Analysis of various kinematics shows that the formation and separation of the LEV and the instantaneous variation of forces depend strongly on kinematics. Analysis of different rotation kinematics shows that a stronger LEV forms near the base during advanced rotation and when rotation occurs over a small time duration. This formation of a stronger LEV leads to higher force production during supination and pronation and subsequently affects the average values of lift and thrust. For continuous rotation kinematics, thrust is produced throughout the flapping cycle resulting in high propulsive efficiency. Analysis of different angles of attack shows that the growth and the stability of the LEV depends strongly on the angle of attack. For a low angle of attack, the LEV stays attached longer and generates higher thrust during the downstroke. However the presence of the attached LEV affects thrust generation in the subsequent upstroke leading to a drop in the average thrust. Finally, among all the cases analyzed, continuous rotation with a moderate angle of attack performs better in terms of propulsive efficiency and thrust. At the same time, different combinations of rotation and/or angle of attack could be employed to achieve the desired force requirements for different flight conditions.

3.5 Figures

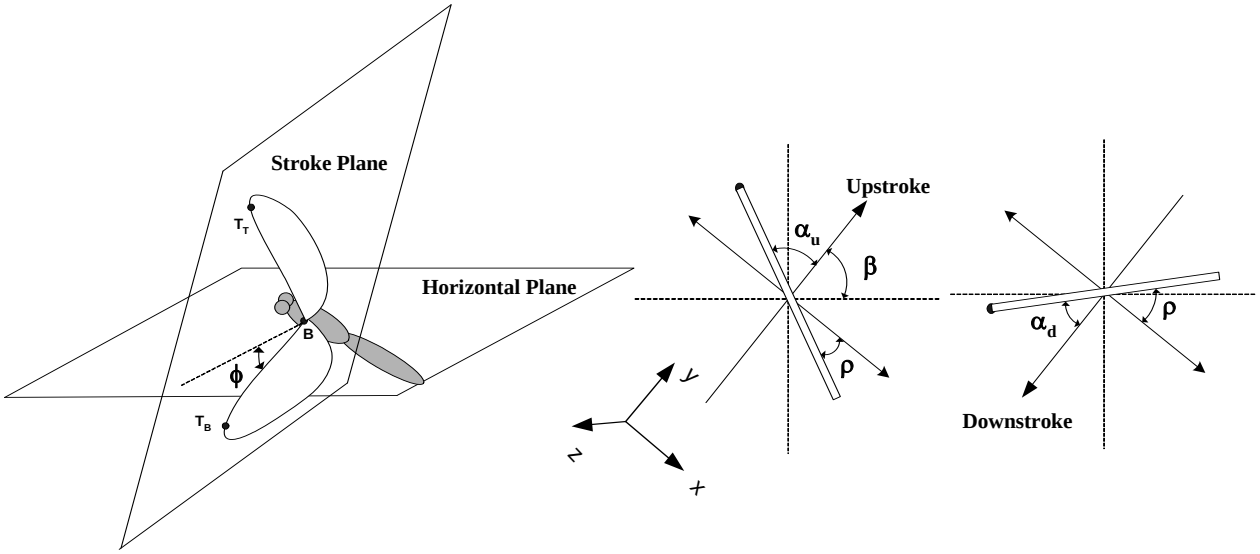

Fig.3.1 Kinematic parameters

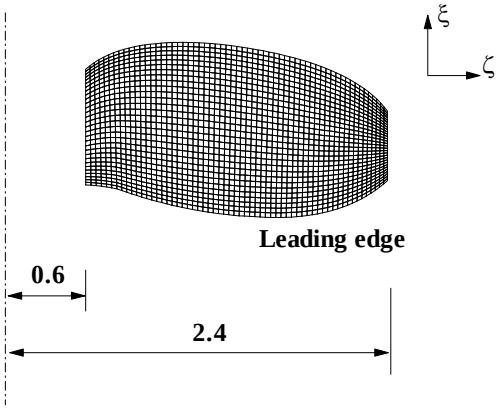

Fig.3.2 Wing planform

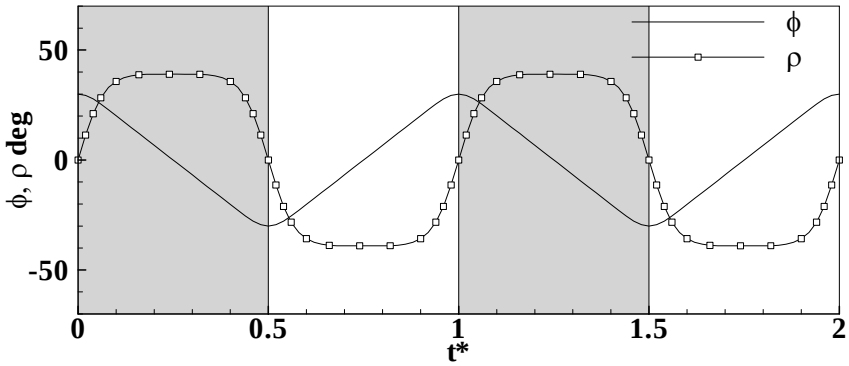

Fig.3.3 Kinematics for hovering flight (shaded region represents downstroke).

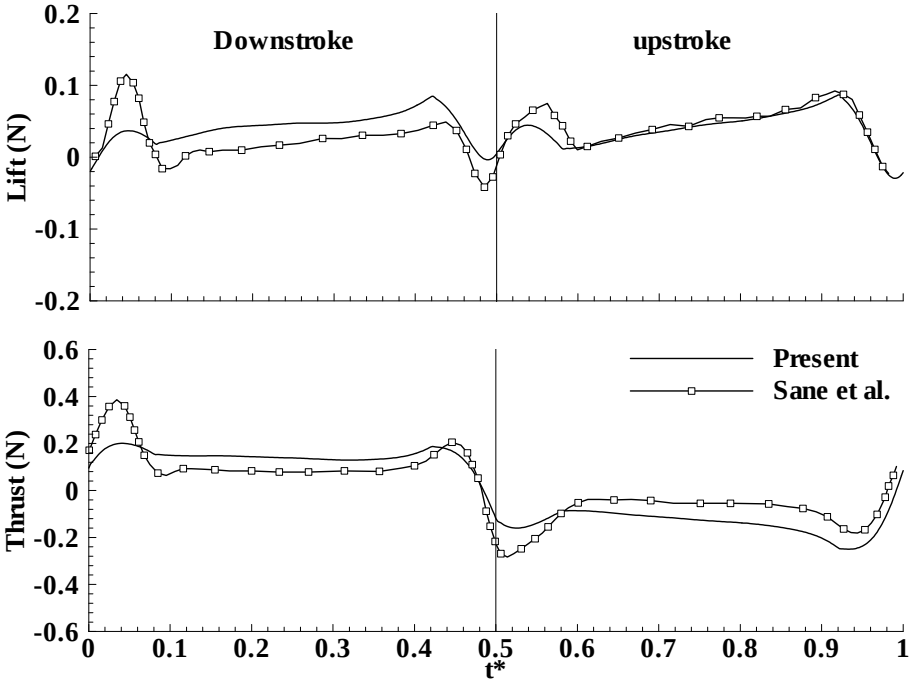

Fig.3.4 Variation of lift and thrust forces for hovering fruitfly

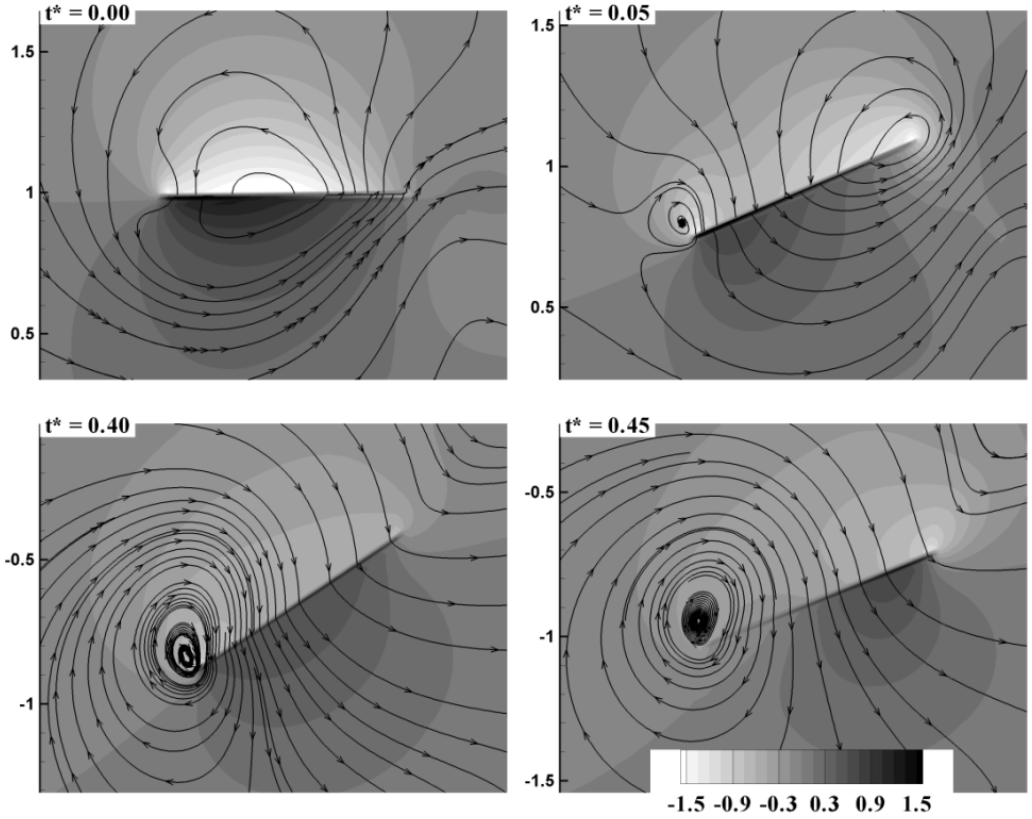

Fig.3.5 Pressure contours and streamlines along chordwise plane at ζ=2.

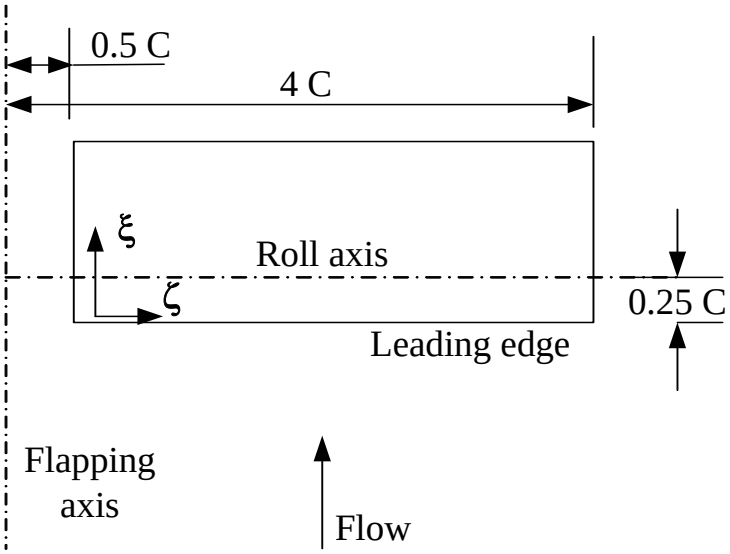

Fig.3.6 Rectangular wing configuration

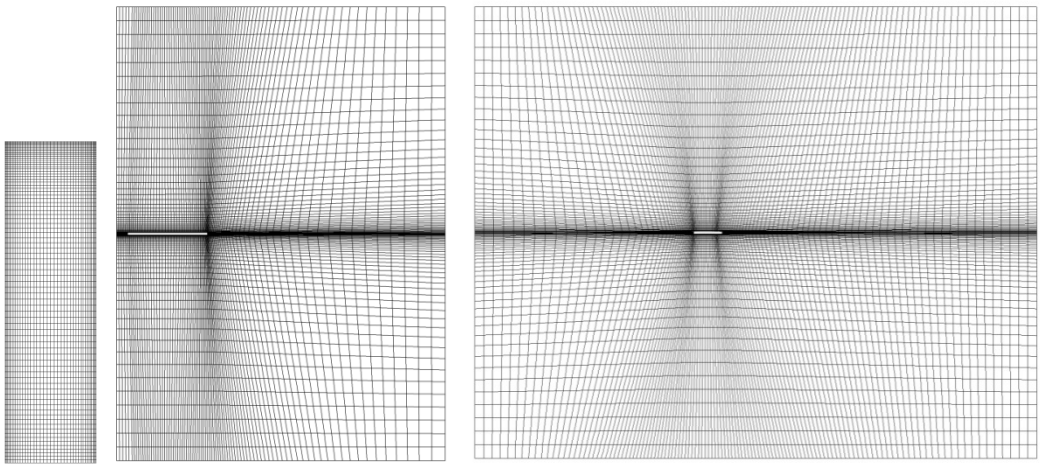

(a) **(b)** **(c)**

Fig.3.7 Grid distribution (a) wing (b) spanwise plane (c) chordwise plane (every other grid line is shown for b and c)

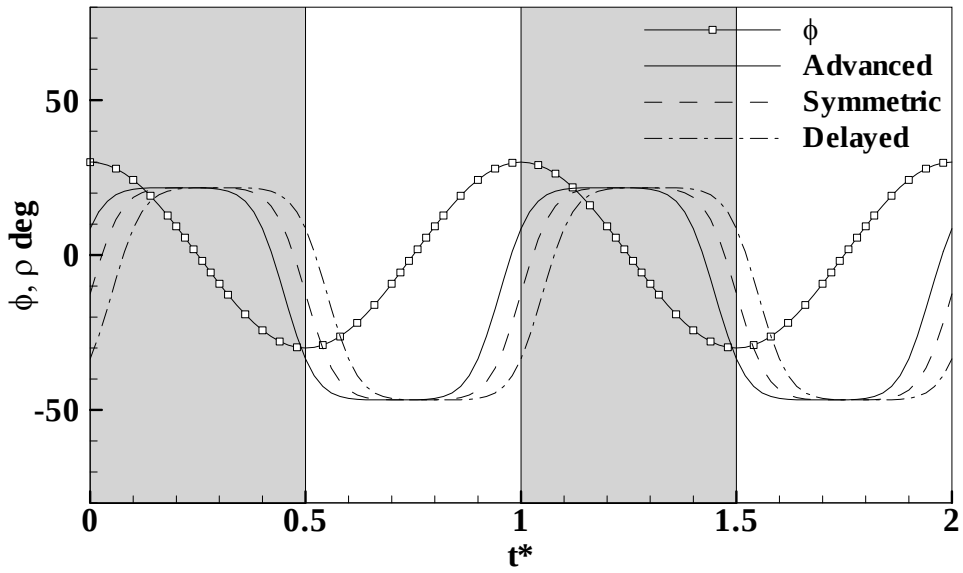

Fig.3.8 Kinematics employed for cases A, B and C (shaded region represents downstroke)

During Downstroke

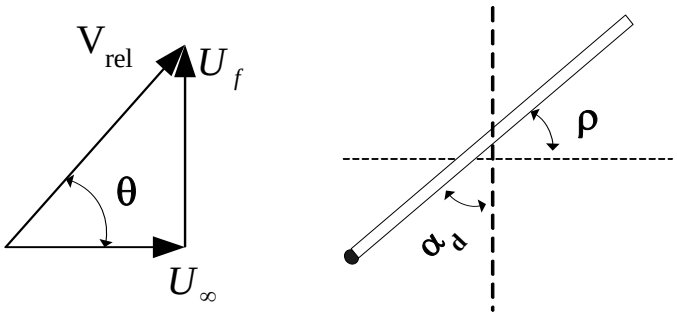

$$\theta = \tan^{-1}[U_f / U_\infty] = \tan^{-1}[1/J]$$

$$\alpha_{eff} = \theta - \rho = \theta + \alpha_d - 90^o$$

Fig.3.9 Effective angle of attack during downstroke

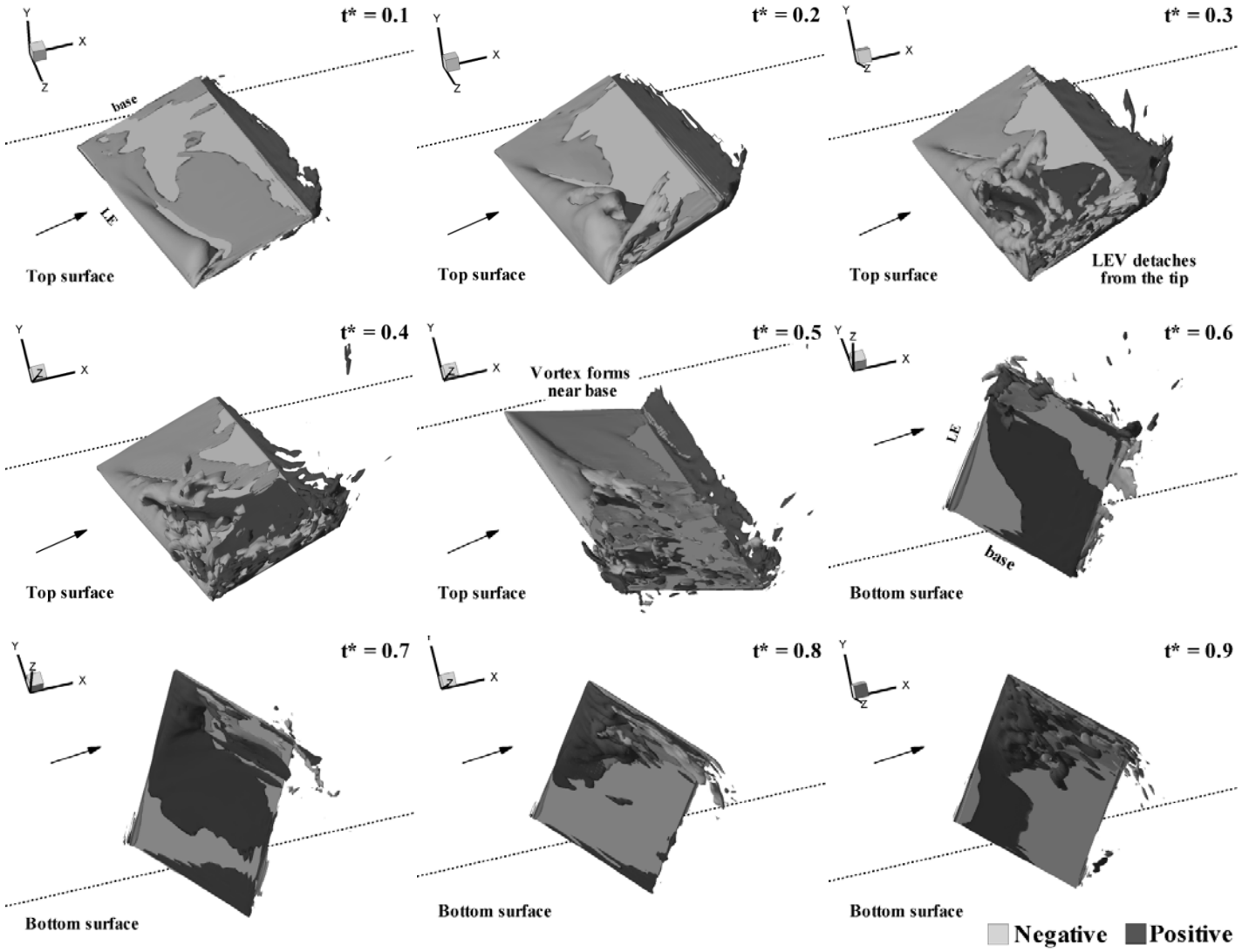

Fig.3.10 Isosurface of ζ component of vorticity at different times. Arrows represent approximate freestream direction and the dotted line represents the axis of flapping

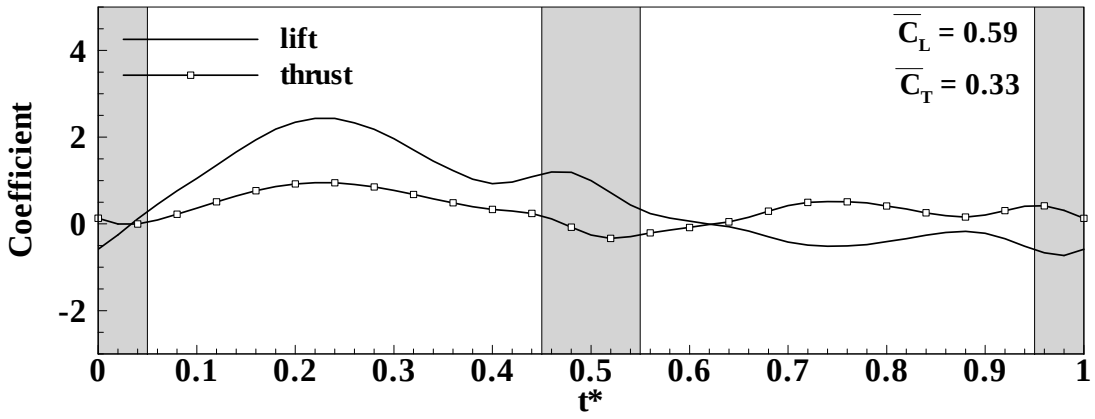

Fig.3.11 Variation of lift and thrust coefficients. Shaded region represents rotation.

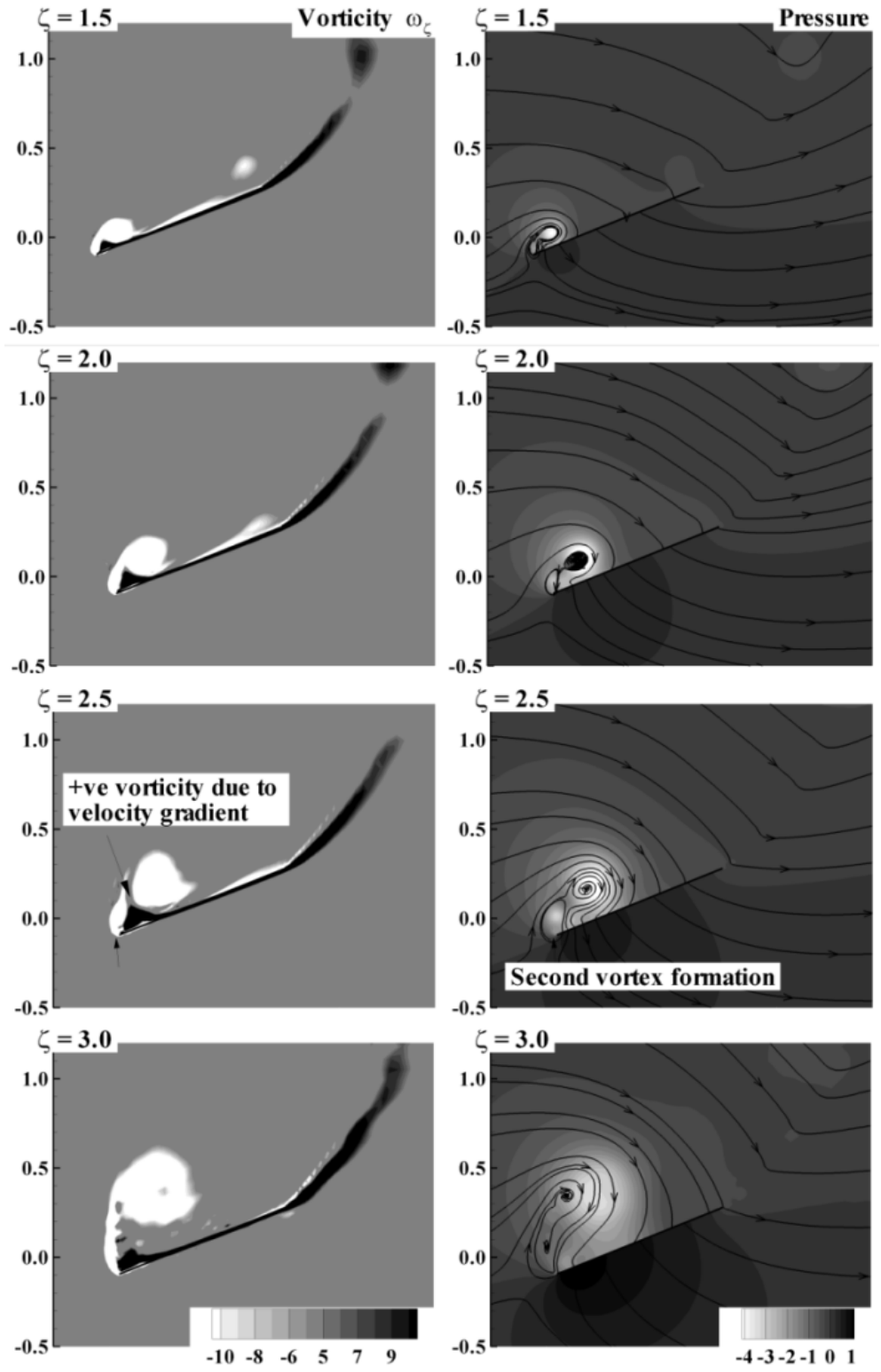

Fig.3.12 Vorticity and pressure contours at various spanwise location for time t* = 0.25

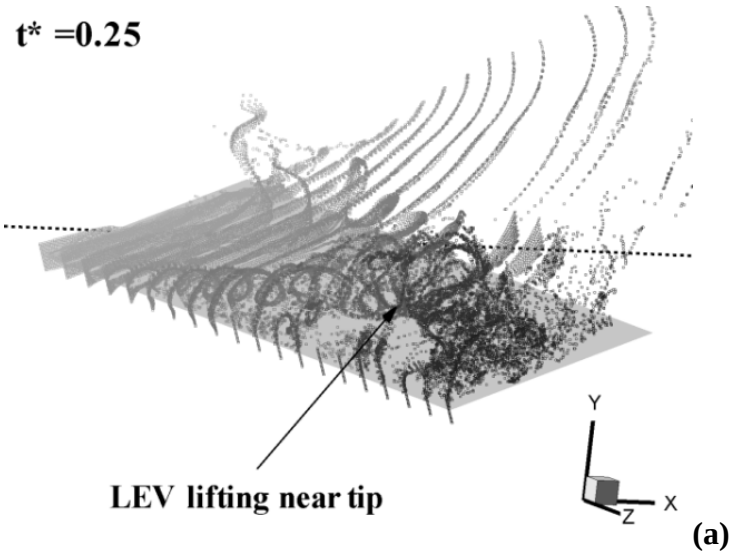

(a)

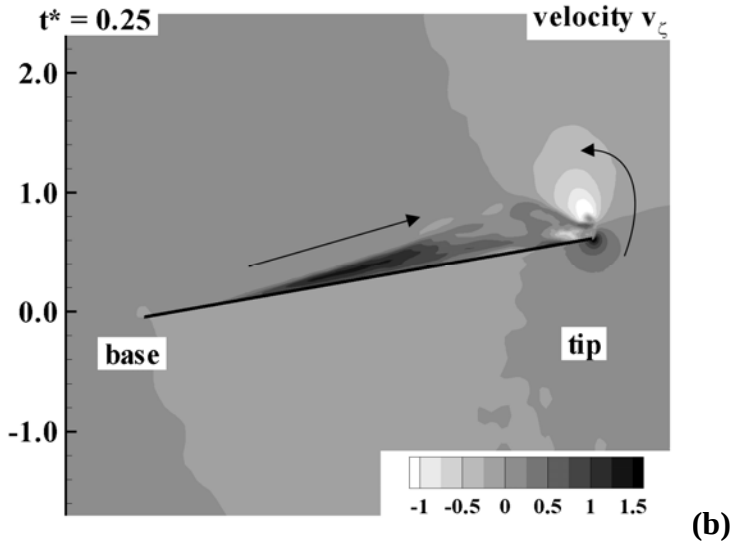

(b)

Fig.3.13 a) Particle traces obtained by releasing particles along the leading edge, which are colored based on the location of release. b) Spanwise flow along the center of LEV and the arrows indicate the direction of flow.

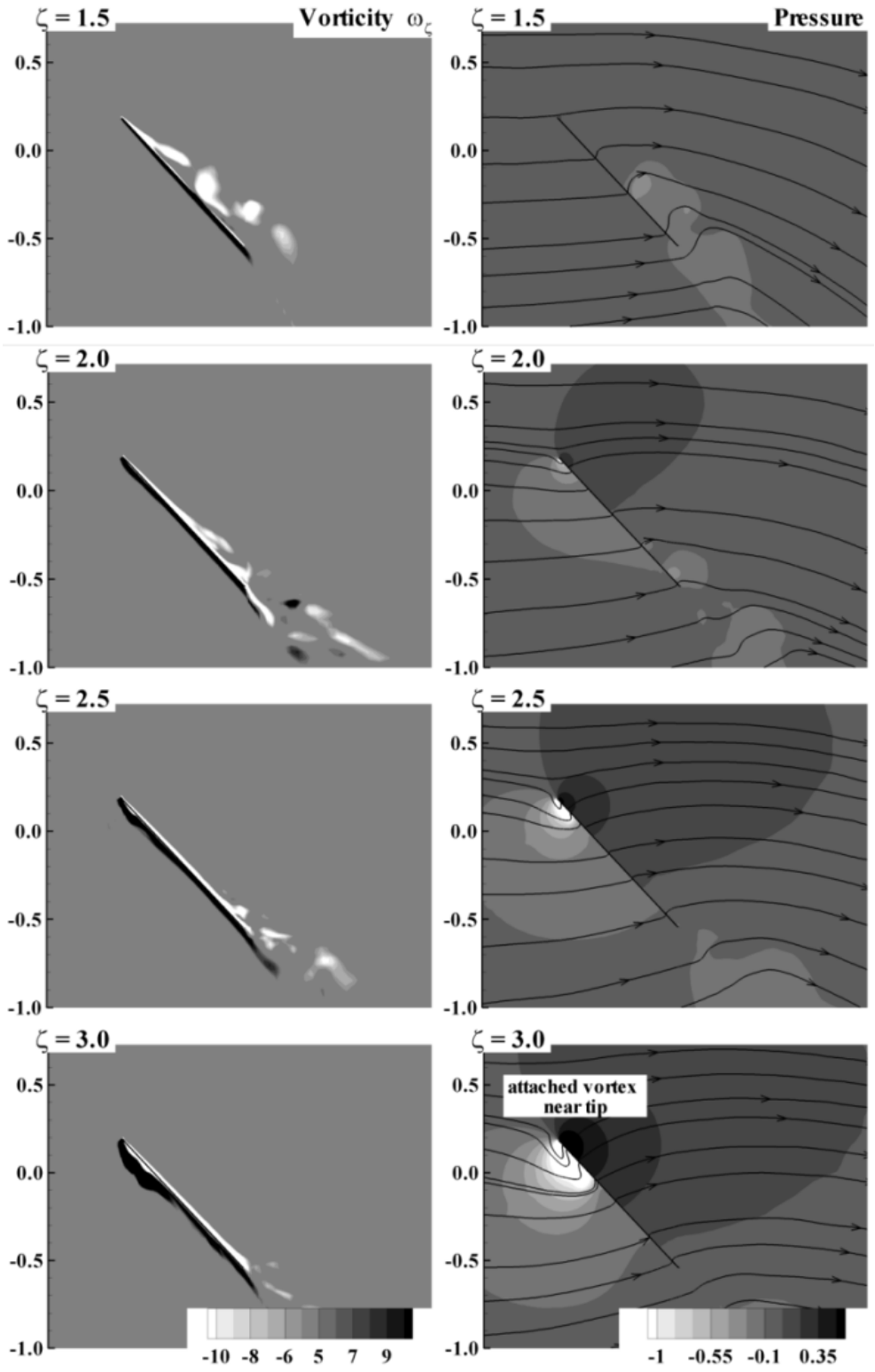

Fig.3.14 Vorticity and pressure contours at various spanwise location for time t* = 0.75

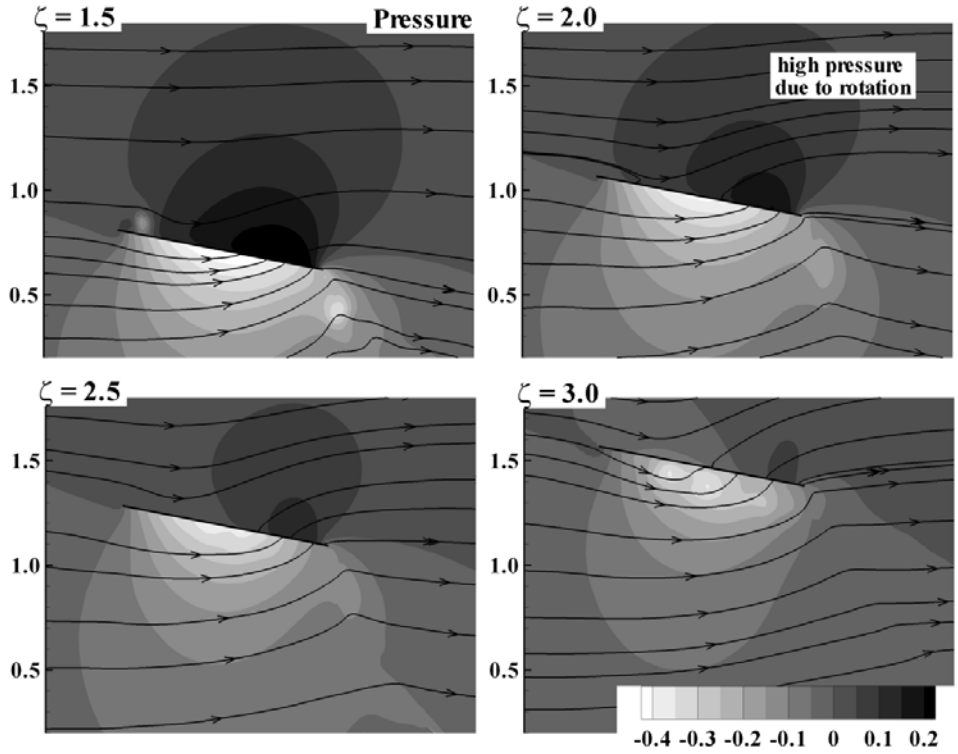

Fig.3.15 Pressure at various spanwise location for time t* = 1.0

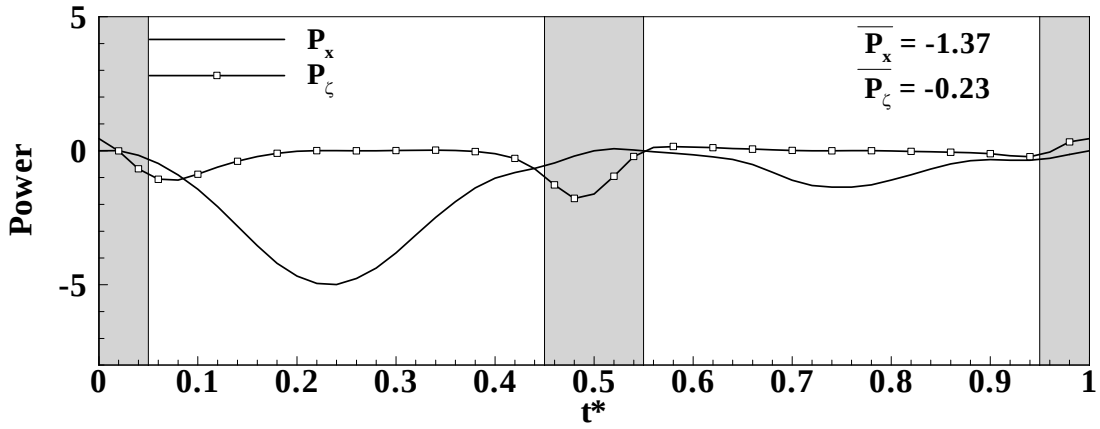

Fig.3.16 Power required for rotation and flapping

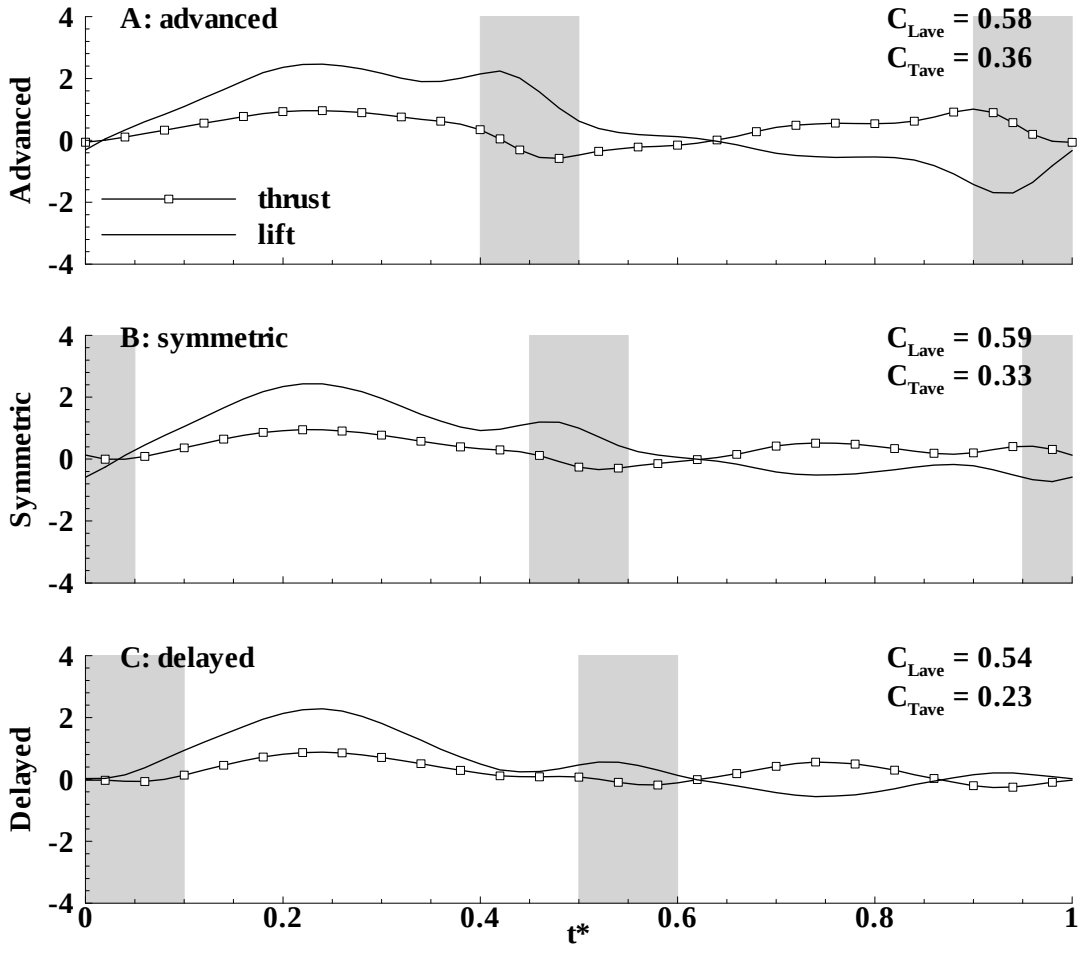

Fig.3.17 Variation of lift and thrust for three different rotation timings (shaded region represents rotation).

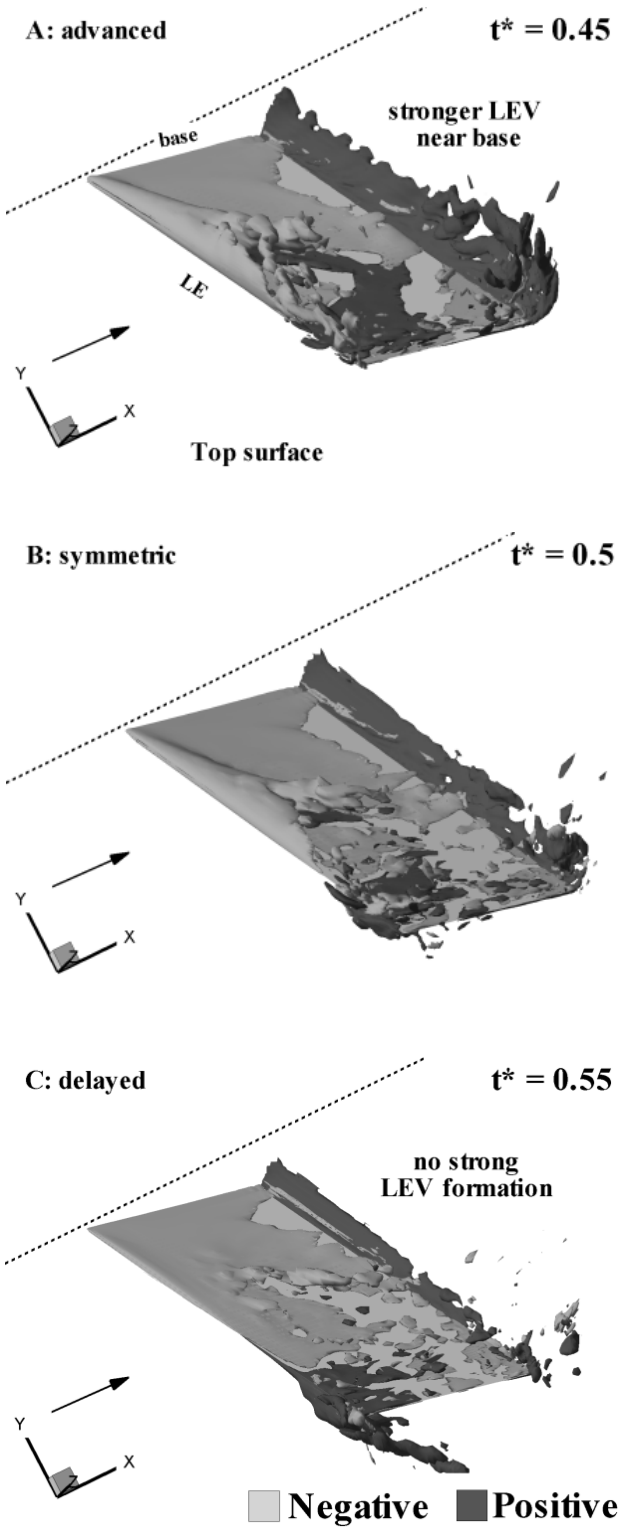

Fig.3.18 Isosurface of ζ component of vorticity during the middle of supination for different rotation timings

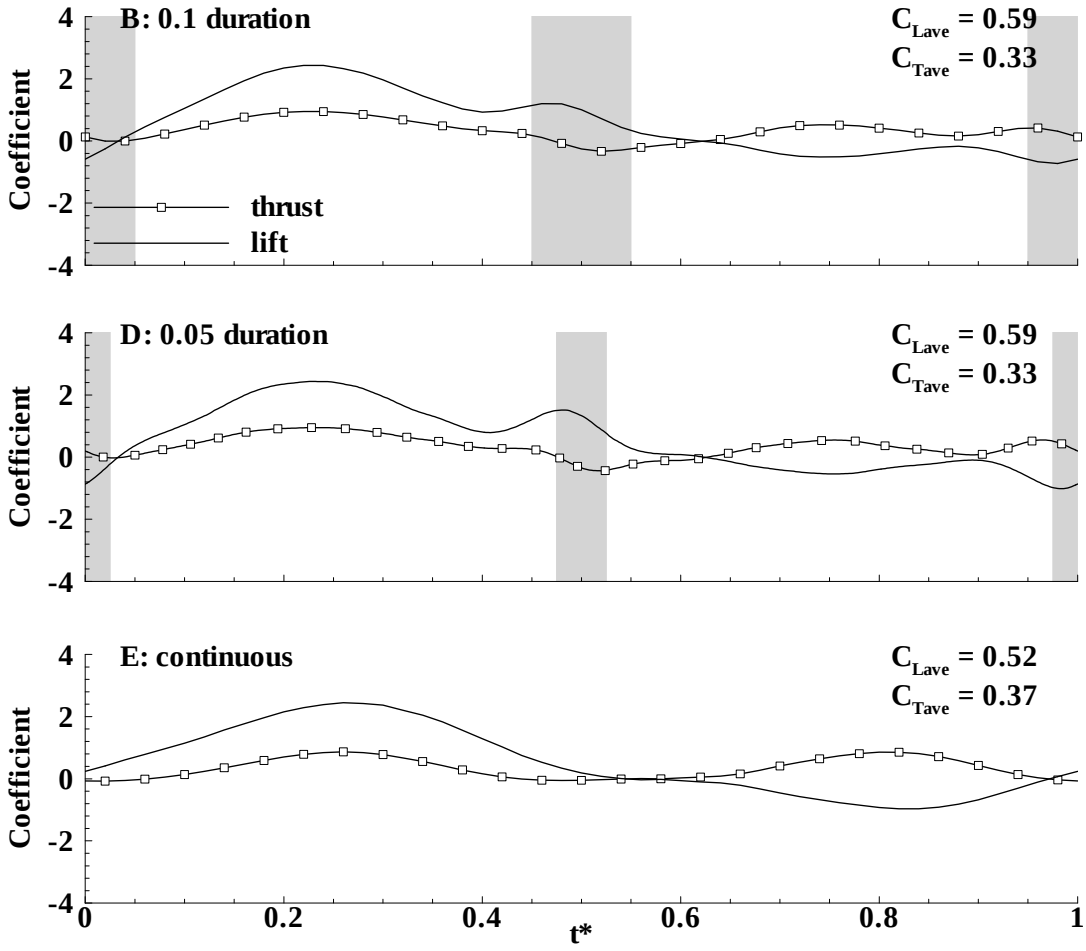

Fig.3.19 Variation of lift and thrust for different rotation duration (Cases B, D and E)

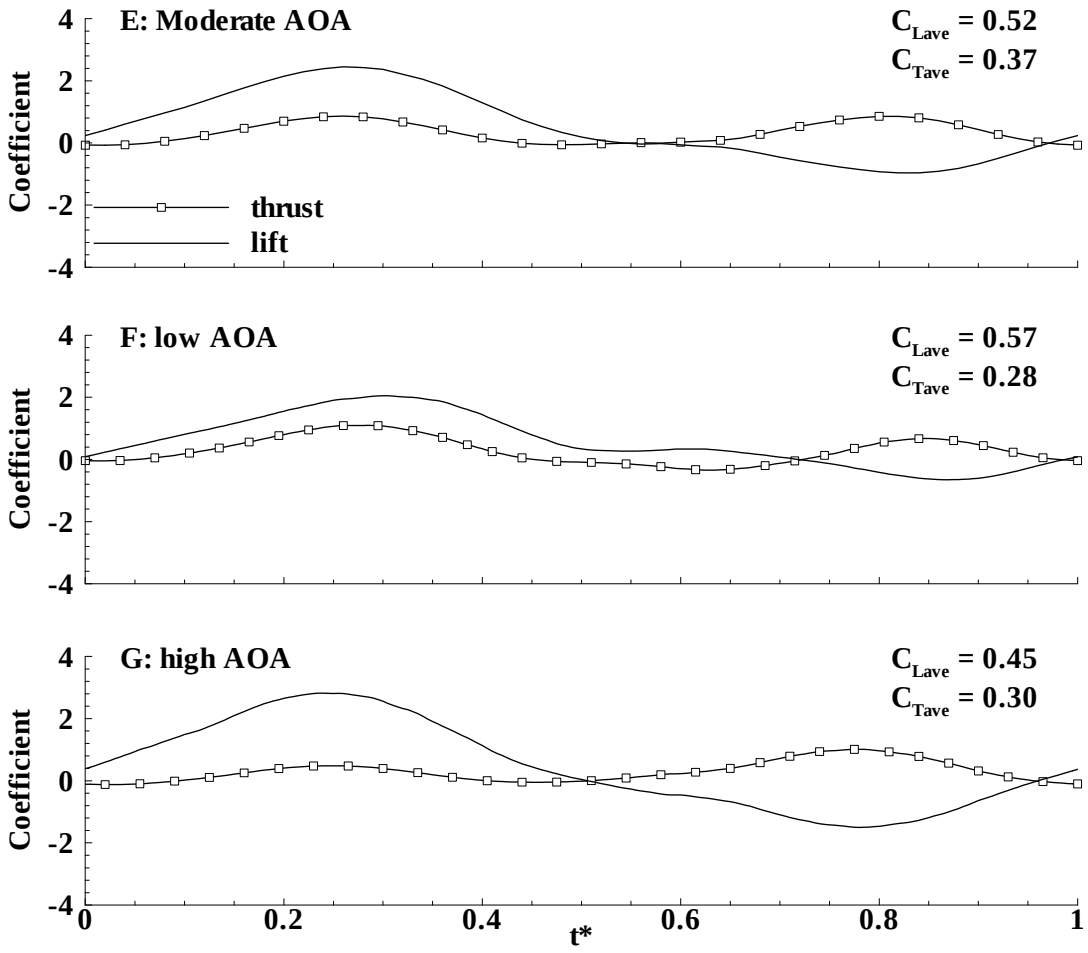

Fig.3.20 Variation of lift and thrust for different angle of attacks

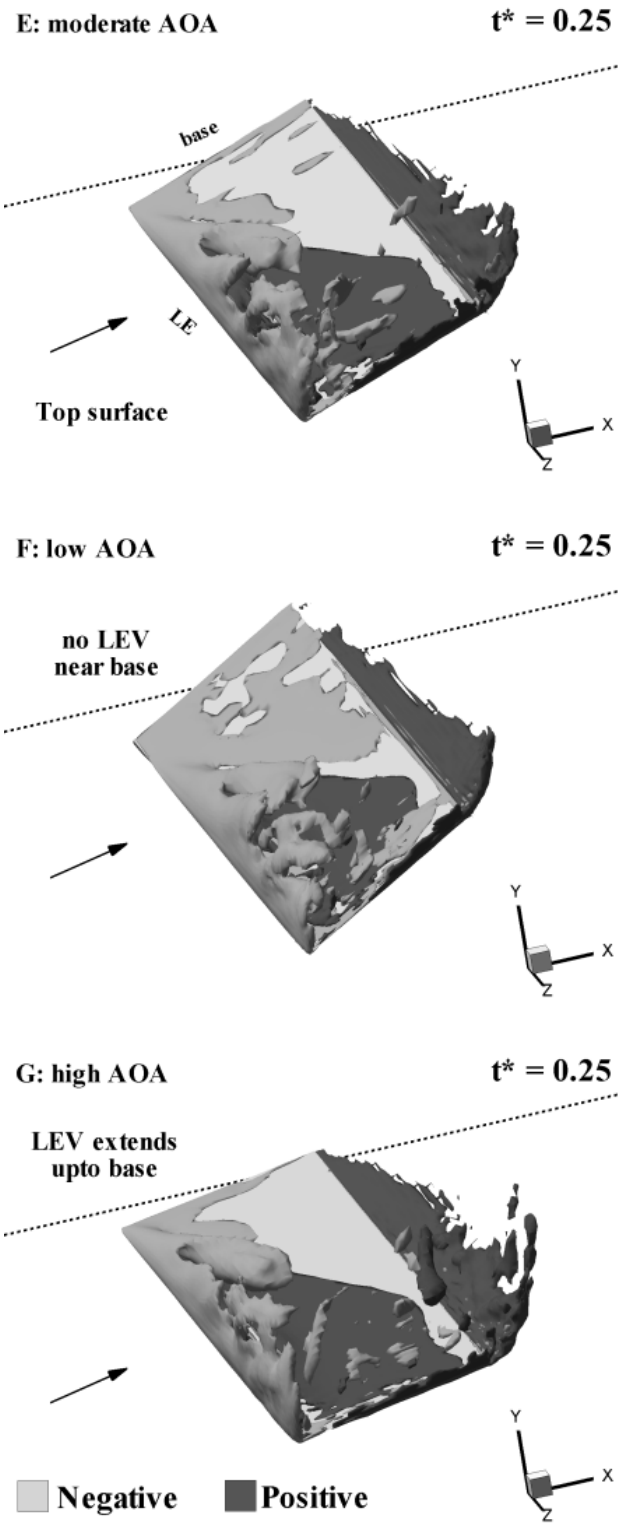

Fig.3.21 Isosurface of vorticity during the middle of downstroke for different angle of attacks a)case E –moderate b) case F-low and c) Case G -high

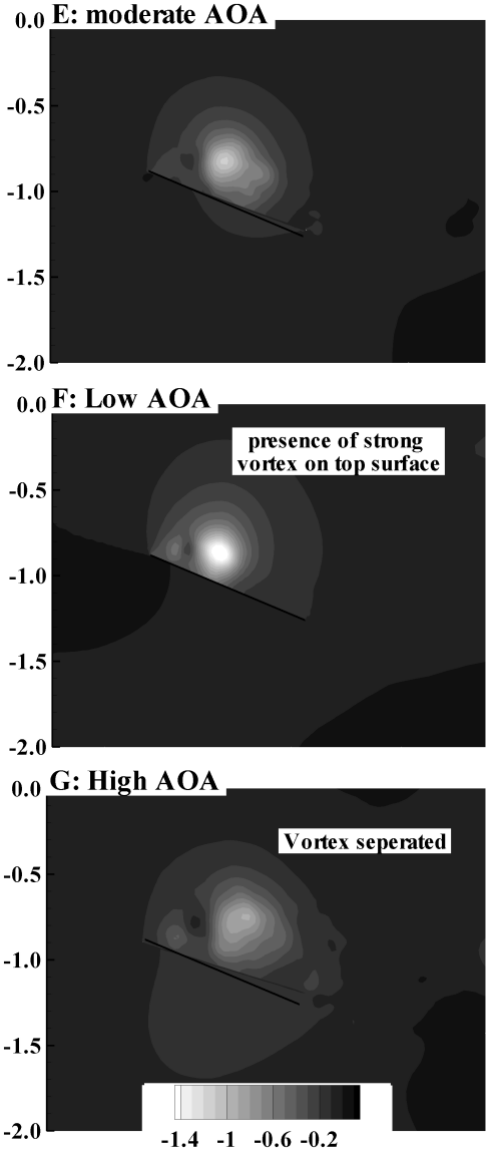

Fig.3.22 pressure contour at location ζ=2.0 at time t* = 0.55 for cases E, F and G

3.6 References

[1] McMasters, J. H. and Henderson, M. L. Low Speed Single Element Airfoil Synthesis. Tec. Soaring 1980;2:1-21.

[2] Carmichael, B. H., “Low Reynolds Number Airfoil Survey,” NASA Contractor Report (Nov 1981).

[3] Pelletier, A. and Mueller, T. J. Low Reynolds Number Aerodynamics of Low-Aspect-Ratio, Thin/Flat/Cambered-Plate Wings. Journal of Aircraft 2005;37:825-832.

[4] Weis-Fogh, T. Quick Estimate of Flight Fitness in Hovering Animals, Including Novel Mechanisms for Lift Production. The Journal of Experimental Biology 1973;59:169-230.

[5] Dickinson, M. H. and Götz, K. G. Unsteady Aerodynamic Performance of Model Wings at Low Reynolds Numbers. The Journal of Experimental Biology 1993;174:45-64.

[6] Ellington, C. P., Berg, C. V. D., Willmott, A. P., and Thomas, A. L. R. Leading-Edge Vortices in Insect Flight. Nature 1996;384:626-630.

[7] Dickinson, M. H., Lehmann, F.-O., and Sane, S. P. Wing Rotation and the Aerodynamic Basis of Insect Flight. Science 1999;284:1954-1960.

[8] Wang, Z. J., Birch, J. M., and Dickinson, M. H. Unsteady Forces and Flows in Low Reynolds Number Hovering Flight: Two-Dimensional Computations Vs Robotic Wing Experiments. The Journal of Experimental Biology 2004;207:449-460.

[9] Ellington, C. P. The Novel Aerodynamics of Insect Flight: Applications to Micro-Air Vehicles. The Journal of Experimental Biology 1999;202:3439–3448.

[10] Liu, H., Ellington, C. P., Kawachi, K., Berg, C. V. D., and Willmott1, A. P. A Computational Fluid Dynamic Study of Hawkmoth Hovering. The Journal of Experimental Biology 1998;201:461–477.

[11] Birch, J. M. and Dickinson, M. H. Spanwise Flow and the Attachment of the Leading-Edge Vortex on Insect Wings. Nature Aug 2001;412:729-733.

[12] Birch, J. M., Dickson, W. B., and Dickinson, M. H. Force Production and Flow Structure of the Leading Edge Vortex on Flapping Wings at High and Low Reynolds Numbers. The Journal of Experimental Biology 2004;207:1063-1072.

[13] Miller, L. A. and Peskin, C. S. When Vortices Stick: An Aerodynamic Transition in Tiny Insect Flight. The Journal of Experimental Biology 2004;207:3073-3088.

[14] Tarascio, M. J., Ramasamy, M., Chopra, I., and Leishman, J. G. Flow Visualization of Micro Air Vehicle Scaled Insect-Based Flapping Wings. Journal of Aircraft Apr 2005;42:385-390.

[15] Dickinson, M. H. The Effects of Wing Rotation on Unsteady Aerodynamic Performance at Low Reynolds Numbers. The Journal of Experimental Biology 1994;192:179-206.

[16] Sane, S. P. and Dickinson, M. H. The Control of Flight Force by a Flapping Wing: Lift and Drag Production. The Journal of Experimental Biology 2001;204:2607-2626.

[17] Sun, M. and Tang, J. Unsteady Aerodynamic Force Generation by a Model Fruit Fly Wing in Flapping Motion. The Journal of Experimental Biology 2002;205:55-70.

[18] Ramamurti, R. and Sandberg, W. A Three-Dimensional Computational Study of the Aerodynamic Mechanisms of Insect Flight. The Journal of Experimental Biology May 2002;205:1507-1518.

[19] Thomas, A. L. R., Taylor, G. K., Srygley, R. B., Nudds, R. L., and Bomphrey, R. J. Dragonfly Flight: Free-Flight and Tethered Flow Visualizations Reveal a Diverse Array of Unsteady Lift-Generating Mechanisms, Controlled Primarily Via Angle of Attack. The Journal of Experimental Biology 2004;207:4299-4323.

[20] Germano, M., Piomelli, U., Moin, P., and Cabot, W. H. A Dynamic Subgrid-Scale Eddy Viscosity Model. Physics of Fluids A 1991;3:1760-1765.

[21] Demirdzic, I. and Peric, M. Space Conservation Law in Finite Volume Calculation of Fluid Flow. International Journal For numerical Methods in Fluids 1988;8:1037-1050.

[22] Demirdzic, I. and Peric, M. Finite Volume Method for Prediction of Fluid Flow in Arbitrarily Shaped Domains with Moving Boundaries. International Journal For numerical Methods in Fluids 1990;10:771-790.

[23] Gopalakrishnan, P. and Tafti, D. K. A Parallel Boundary Fitted Dynamic Mesh Solver for Applications to Flapping Flight. under review, Computers and Fluids Feb 2008;

[24] Gopalakrishnan, P. and Tafti, D. K. A Parallel Multiblock Boundary Fitted Dynamic Mesh Solver for Simulating Flows with Complex Boundary Movement. AIAA 38th Fluid Dynamic conference, Seattle, Washington June 2008.; AIAA-2008-4142

[25] Sun, M. and Lan, S. L. A Computational Study of the Aerodynamic Forces and Power Requirements of Dragonfly (Aeschna Juncea) Hovering. The Journal of Experimental Biology 2004;207:1887-1901.

Chapter 4: Effect of Reynolds number, tip shape and stroke deviation on Flapping Flight[‡]

Abstract

In the current study the effects of Reynolds number, tip shapes and stroke deviation on the performance of flapping flight are analyzed. Three Reynolds numbers, Re =100, 10,000, and 100,000 are evaluated. At Re=100, a single coherent Leading Edge Vortex (LEV) forms during the downstroke, while at the higher Reynolds numbers, a less coherent LEV forms, which sheds near the wing tip and convects downstream. At higher Reynolds numbers the location of the LEV remains close to the surface as it sheds and convects, which leads to high values of lift and thrust coefficients. At all Reynolds numbers, a strong spanwise flow of the order of the flapping velocity is observed along the core of the LEV, which contradicts previous observations of spanwise flow only at high Reynolds numbers. Analysis of three different tip shapes, straight, rounded, and tapered show that the tip vortex does not have a significant effect on the lift and thrust production. During the downstroke, a continuous LEV forms for the rounded tip, while a discontinuous vortex forms for straight and tapered tip shapes. However, the time of LEV separation and the location of the LEV at different phases of the flapping cycle are identical for all the tip shapes. Flapping flight with stroke deviation alters the force production significantly during the upstroke as it captures the LEV shed during the downstroke. It reduces the average value of lift coefficient for the case analyzed, while the thrust coefficient remains the same.

Nomenclature

$\vec{a}^{i}$ = Contravariant basis vectors

C = Airfoil chord length

C_L = Coefficient of lift

[‡] This chapter is submitted to 39th AIAA Fluid Dynamics Conference on Nov 2008, and is currently under review.

C_T = Coefficient of thrust

f = Frequency of flapping

f_0 = fD/U_∞. Non-dimensional frequency of cylinder

$F_{x/y}$ = Force acting on the wing; suffix x, y- direction

g^{ij} = Contravariant metric tensor

$\sqrt{g}$ = Jacobian of the transformation

$\sqrt{g}U^j$ = Contravariant flux vector

$\sqrt{g}U^j_g$ = Contravariant flux due to grid movement

J = Advance ratio; U_∞/U_f; Ratio of the flight velocity to the flapping velocity

p = Pressure

$P_{x/\zeta}$ = Power required; suffix x- flapping and ζ - rotation

R = Semi-wingspan; distance from flapping axis to wing tip

Re = Reynolds number; $U_f C/\nu$

$\mathrm{Re_t}$ = Inverse of the turbulent viscosity

u_i = Cartesian velocity vector

u_i^g = Cartesian Grid velocity vector

U_∞ = Free stream velocity; Forward flight velocity

U_f = Flapping velocity; $2\Phi fR$

$\vec{x}$ = Physical space coordinate

$\vec{\xi}$ = Computational space coordinate

$\alpha_{u/d/eff}$ = Angle of attack; suffix u-upstroke, d-downstroke, and eff-effective

β = Stroke plane angle

η_{prop} = Propulsive efficiency

ϕ = Flapping amplitude

Φ = Total flapping amplitude (max to min)

ν = Kinematic viscosity

ρ = Torsional angle

τ = Shear stress on the surface of the wing

ω_ζ = vorticity; suffix – ζ component

Ω_ζ = Angular velocity of the wing; suffix – ζ component

4.1 Introduction

Small birds and insects whose flight regime coincides with that of Micro Air Vehicles (MAVs) use flapping wings to provide both lift and thrust to overcome the deteriorating performance of fixed wings. They do this by taking advantage of unsteady flow mechanisms using complex wing kinematics. A number of unsteady aerodynamic mechanisms such as clap and fling[1], delayed stall[2,3], wake capturing[4], and, rotational circulation[4] have been proposed to explain the generation of lift in birds and insects. The clap and fling mechanism was proposed by Weis and Fogh[1] based on the flight of small wasps. This mechanism is used by small insects whose flight regime ranges from Reynolds number of 10-100. The main disadvantage of clap and fling mechanism is the mechanical damage caused to the wings. This and the fact that the mechanism loses its lift producing effectiveness at higher Reynolds number (Re>200) [5-7], clap and fling is only limited to very small insects and is not used by larger insects and birds.

The wing stroke of large insects and birds is divided into four kinematic portions: two translational phases (upstroke and downstroke) with high angles of attack, and two rotational phases (pronation and supination), where the wing rapidly rotates and reverses its direction. Figure.4.1 shows the critical kinematic parameters of flapping flight with their definitions given in Table 4.1. During the downstroke, air swirls around the leading edge and forms a Leading Edge Vortex (LEV). This LEV increases the bound vortex circulation and hence the lift. In a fixed airfoil, the formation of the LEV leads to dynamic stall within 3-4 chord lengths of travel. However in insects, the LEV is stable for the entire downstroke and during this period, the insect covers a distance of more than 8 chord lengths. The stability of the LEV which leads to *delayed stall* is responsible for the high lift production. While delayed stall explains the lift generated during the translational kinematics, *rotational circulation* and *wake capture* mechanisms are

proposed for the high lift produced during the rotational period. However, the validity of these models is unclear and some studies[8,9] have provided alternate reasoning for enhanced force production during the rotational period. The relative contribution of these mechanisms varies according to the kinematics of wing motion and flight conditions. However, since wing translation usually comprises a major part of the kinematics, the LEV dynamics is the most influential factor affecting overall lift and thrust generated by a flapping wing.

Table.4.1 Kinematic parameters and non-dimensional numbers for flapping flight

Parameters	**Description**
Stroke plane	The plane defined by three points: wing base (B), and the wingtip at maximum (T_T) and minimum angular position (T_B). During hovering, the stroke plane will be near horizontal and during forward flight, it will be vertical.
Stroke plane angle, β	Angle between the stroke plane and the horizontal plane. It ranges from 0^o for hovering to 90^o for forward flight.
Angle of attack, α	Angle between the wing direction (from trailing edge to leading edge) and the direction of motion.
Torsional angle, ρ	Angle between the wing direction and the direction perpendicular to stroke plane.
Flapping amplitude, ϕ	Angle between rotation axis of the wing and the plane perpendicular to the stroke plane.
Deviation angle, γ	The angle between the rotation axis of the wing and the stroke plane.

The stability of the LEV plays an important role in the superior performance of birds and insects. Many experimental studies evaluated the duration and stability criteria of the LEV. Dickinson and Gotz[2] analyzed the effect of angle of attack during the translation period on lift and drag production using a two dimensional wing model (Re =192). They found that the LEV was generated at an angle of attack above 13.5^o due to impulsive movement and stayed attached for 2 chord lengths of travel. The presence of the LEV

resulted in an 80% increase in lift similar to that of detached vortex lift for a delta-wing aircraft. The shedding of the LEV led to the formation of a secondary vortex of opposite sign near the trailing edge correlating with a decrease in lift. Further, the study found that up to an angle of attack of 54^o, the lift characteristics remain unaltered by the change of camber. Wang et al.[10] compared the results obtained from a 2D numerical simulation of a hovering fruit fly with 3D results from a dynamically scaled mechanical model (Re =75 to 115). They found that the numerical results matched well with 3D results for cases with a short downstroke length. In the case of hovering insects, the stroke length is only 3 to 5 chords, during which the LEV remains attached to the wing even for 2D cases. When the downstroke is longer than a typical stroke length, the 2D cases showed a phase difference with 3D results and resulted in lower lift coefficients.

Ellington[11] conducted flow visualization studies using a large mechanical model of hawkmoth, *flapper* (Re~4000). An intense LEV on the downstroke at all flight speeds (0.4 to 5.7 m/s) was observed. The LEV spiraled out towards the wingtip with high spanwise velocity comparable to the flapping velocity, which stabilized the vortex. The flow structure obtained was similar to the conical leading edge vortex found in delta-wings. They suggested that strong spanwise flow was created either by the pressure gradient, formed due to velocity gradient along the flapping wing, or by centrifugal acceleration in the boundary layer, or by the induced velocity field of the spiral vortex lines. Liu et al.[12] analyzed flapping flight of hovering hawkmoth at Re =3000 to 4000 using the finite volume method. The study showed the formation of the LEV during both upstroke and downstroke, which stayed attached to the wing during the entire translational and following rotational motions. The combined translation and rotation deformed the vortex, which led to shedding of the LEV at the start of the next translation motion. The spanwise flow, created due to spanwise pressure gradient stabilized the LEV till 70% of the span. During the second half of the downstroke, a secondary LEV is formed at 75% span, which is unstable and affected strongly by the presence of the tip vortex. The LEV formed during the upstroke was weak and attached closely to the leading edge. The study showed that the lift force was produced mainly during the entire downstroke and the later part of the upstroke.

Dickinson et al.[4] conducted flow visualization studies using a dynamically scaled version of a hovering fruit fly, *robotic fly* at Re =136. They compared the force coefficients obtained by the robotic fly with a 2d model wing and found that the 3D model produced high average lift and thrust coefficients. Sane and Dickinson[13] later introduced different shape and magnitude of stroke deviation into simple kinematics and analyzed their effects on the aerodynamic performance. The results showed that the kinematics with stroke deviation resulted in lower lift, which might be utilized for maneuvering. The experimental investigation of Birch and Dickinson[14] provided contrasting proof for the stability of the LEV at low Reynolds number (100-250) relevant to small insect flights. They conducted experiments with fences and baffles on the top surface of the wing and showed that the LEV remains attached to the wing despite the absence of spanwise flow. They proposed that the downward velocity created by the tip vortices limits the growth and subsequent detachment of the LEV. Birch et al.[15] investigated flow structures and forces generated at low and high Reynolds number (Re =120 and 1400). In both cases, a stable LEV was present throughout the downstroke. At Re =1400, they observed strong spanwise flow within the core of the LEV, with velocities 150% of the flapping velocity. The spanwise flow removed the vorticity into the wake and resulted in a spiral LEV similar to that observed by Ellington[11]. However at Re = 120, the spanwise flow was absent, which resulted in lower forces. Miller and Peskin[16] studied the effect of Reynolds number (8 to 128) on the formation of the LEV using the immersed boundary technique. At Re < 32, the LEV (negative pressure region) and trailing edge vortices (positive pressure region) remain attached, which resulted in lower lift. At Re > 64, they observed shedding of the trailing edge vortex during translation, which resulted in vortical asymmetry, leading to high lift production.

Tarascio et al.[17] conducted a flow-visualization experiment on a hovering flapping flight model at Reynolds number of the order of 8000. The flow field consisted of folded wakes formed by the strong starting vortex shed at the end of each half stroke during wing rotation. Due to the induced flow, the wakes were pushed downwards parallel to the flapping plane. The key finding of this study was that during translation, the top surface was covered by multiple vortices and the LEV was continually generated and shed into

the wake. This result is in contrast to previous studies[4,11], where a stable single LEV is present during translation. Further, they observed that the strength of the LEV increased along the span and identified separated flow at the outboard region of the wing.

Our previous analysis[18] of forward flapping flight at Re=10,000 and at advance ratio, J= 0.5 showed the presence of a strong spanwise flow along the core of the LEV similar to that of the flow visualization studies conducted by Ellington[11]. In addition, our results showed that the LEV becomes unstable near the tip before mid-downstroke. We surmised that the primary reason is the presence of negative spanwise flow created by the tip vortex, which blocks or slows down the removal of vorticity from the LEV. This led to vorticity buildup near the tip and the subsequent instability of the LEV. Hence, analyzing flow patterns such as the spanwise flow, which in turn depends on Reynolds number and tip vortex are critical for evaluating the stability criteria for the LEV. In the present study, analysis of forward flapping flight is carried out by varying Reynolds number and tip shape. Further, previous analysis of stroke deviation for hovering flight[13] showed that it reduces lift production and could be used for steering. Hence, the present study also evaluates the effect of stroke deviation on the aerodynamic performance in forward flight. The resulting flow structures and the lift and thrust variations from the simulations are used to evaluate the effect of each parameter on aerodynamic performance.

4.2 Methodology

In the present study, a structured multiblock solver with a boundary fitted dynamic grid is employed. In this framework the grid deforms with the wing motion. The method of Large-Eddy Simulations (LES) is employed with a subgrid stress model to resolve the turbulence in the flow field at high Reynolds numbers. The governing equations for unsteady incompressible viscous flow on moving coordinate system consist of space, mass, and momentum conservation laws. The equations are mapped from physical $(\vec{x})$ to logical/computational space $(\vec{\xi})$ by a boundary conforming transformation $\vec{x} = \vec{x}(\vec{\xi})$, where $\vec{x} = (x, y, z)$ and $\vec{\xi} = (\xi, \eta, \zeta)$. The equations are non-dimensionalized by chord length C and flapping velocity U_f and written in conservative non-dimensional form as:

Space:

$$\frac{\partial}{\partial t}\left(\sqrt{g}\right)-\frac{\partial}{\partial \xi_j}\left(\sqrt{g}U_g^j\right)=0 \tag{4.1}$$

Mass:

$$\frac{\partial}{\partial \xi_j}\left(\sqrt{g}U^j\right)=0 \tag{4.2}$$

Momentum

$$\frac{\partial}{\partial t}\left(\sqrt{g}u_i\right)+\frac{\partial}{\partial \xi_j}\left(\left[\sqrt{g}U^j-\sqrt{g}U_g^j\right]u_i\right)=-\frac{\partial}{\partial \xi_j}\left(\sqrt{g}(\vec{a}^j)_i\,p\right)$$

$$+\frac{\partial}{\partial \xi_j}\left(\left(\frac{1}{\mathrm{Re}}+\frac{1}{\mathrm{Re}_t}\right)\sqrt{g}\,g^{jk}\frac{\partial u_i}{\partial \xi_k}\right) \tag{4.3}$$

where $\vec{a}^i$ are the contravariant basis vectors, $\sqrt{g}$ is the Jacobian of the transformation, g^{ij} is the contravariant metric tensor, $\sqrt{g}U^j=\sqrt{g}\left(\vec{a}^j\right)_k u_k$ is the contravariant flux vector, $\sqrt{g}U_g^j=\sqrt{g}\left(\vec{a}^j\right)_k u_k^g$ is the contravariant flux vector due to grid velocity u^g, u_i is the Cartesian velocity vector, and p is the pressure. In the above formulation, the grid velocity u^g is not computed explicitly. Instead, the grid contravariant flux vector is employed which is directly computed based on the Space Conservation Law (SCL[19,20]). The non-dimensional time used is t^*U_f/C and the Reynolds number is given by $U_f C/\nu$. Re_t is the inverse of the subgrid eddy-viscosity which is modeled as

$$\frac{1}{\mathrm{Re}_t}=C_s{}^2(\sqrt{g})^{2/3}\left|\bar{S}\right| \tag{4.4}$$

where $\left|\bar{S}\right|$ is the magnitude of the strain rate tensor given by $\left|\bar{S}\right|=\sqrt{2\overline{S_{ik}}\,\overline{S_{ik}}}$ and the Smagorinsky constant $C_s{}^2$ is obtained via the dynamic subgrid stress model (Germano et al.[21]).

The equations are formulated in a finite-volume framework using a fractional-step algorithm for time advancement. Second-order central differences are used for the convective and viscous terms and a combination of an explicit Adams-Bashforth and implicit Crank-Nicolson discretizations are used for time advancement**.** During the start of each time step, the wing is moved based on the prescribed kinematics, keeping the external boundaries of the computational domain fixed. The resulting grid movement is carried out at each time step by a combination of a spring analogy and Trans-Finite Interpolation (TFI) on displacements[19,20]. The Space Conservation Law (SCL) (Eqn. 1) is used to calculate the grid contravariant fluxes [19,20] which are used in the momentum equations to account for grid movement.

4.3 Results

The focus of the current study is to evaluate the critical flow structures responsible for the stability of the LEV in flapping flights. For evaluating the effect of the Reynolds number, three Reynolds numbers Re =100, 10,000, and 100,000 are analyzed (Table 4.2). For evaluating the effect of tip vortex, wings with three different tip shapes straight, rounded, and tapered (Cases A,D,E) are analyzed at Re=10,000. Finally, a sinusoidal stroke deviation angle is introduced to evaluate its effects on thrust and lift production. All the simulations are carried out for forward flapping flight with advance ratio J= 0.5.

4.3.1 Wing Configuration and Kinematics

A rectangular wing with aspect ratio of 4 from base to tip as shown in Fig.4.2a is used for most of the analysis. The pitching axis is placed at one fourth of chord length from the leading edge. The coordinate (x,y,z) is used for the fixed frame, where the y-z plane represents the stroke plane (Fig.4.1). The coordinates (ξ,η,ζ) are used for the moving frame fixed with the wing, where ξ is along the chordwise direction, η is perpendicular to the wing, and ζ is along the spanwise direction (Fig.4.2a). For kinematics, a sinusoidal variation of flapping angle and torsional angle as shown in Fig.4.2b is provided. For stroke deviation, a sinusoidal stroke deviation with amplitude 10^o is provided. The selection of the kinematics is based on our previous analysis on the effect of rotation kinematics[18,22], which showed that the continuous rotation results in high thrust. The

movement of the wing tip for the prescribed kinematics is shown in Fig.4.3a. During the start of the translation, the angle of attack is close to 90^o and it drops during the first half to its lowest value and increases to the initial value during the second half of the translation. The angle of attack during the mid-downstroke is 75^o and during the mid-upstroke it is 45^o. A lower value of angle of attack during the upstroke is used to reduce the downward force. The effective angle of attack depends on the flapping velocity, the free stream velocity and the prescribed angle of attack (α_u, α_d) as shown in Fig.4.3b. Due to variation in the flapping velocity (U_f), the effective angle of attack also varies along the span with a maximum value being at the tip. The other kinematic parameters used are the stroke amplitude, 60^o ($\pm 30^o$) and the stroke plane angle, $\beta=90^o$.

4.3.2 Computational Grid

The grid is made of 60 blocks with approximately 6.5 million cells is used for Re =100 and 10,000. The flow domain is defined from 10 chord lengths upstream of the leading edge and extends 15 chord lengths downstream from the trailing edge. In the direction normal to the wing, the flow domain extends 10 chord lengths on either side and in the spanwise direction from the tip. Constant velocity boundary condition is applied at all inlet faces and an outflow boundary condition is specified at the downstream boundary. The symmetry condition is applied along the flapping axis at the base of the wing. For Re =10,000 and less, the wing is resolved using 80x40 grid points and 80 grid points are used perpendicular to the wing as shown in Fig.4.4. A grid refinement study is carried out by increasing the number of points along the perpendicular direction from 80 to 120. The comparison of instantaneous lift and thrust forces show no perceptible change and the mean values of lift and thrust differ by less than 1%. More validation studies such as forced oscillation of a cylinder and a heaving airfoil related to the dynamic mesh capability of the solver is available in our previous studies[23,24]. In the case of a heaving airfoil, the analysis was carried out at different plunging velocities to obtain different wake structures, which showed good comparison with Lai et al.[25]. In addition, the values of thrust and propulsive efficiency were in good agreement with the experiments of Heathcote et al.[26]. Further, an analysis of hovering fruitfly was also

carried out[22] and reasonable agreement with the experimental results of Sane and Dickinson[13] were obtained.

For Re=100,000, the wing is resolved with 80x40 grid points and 120 grid points are used along the perpendicular direction. The results obtained with this grid showed small oscillations in the instantaneous variation of lift and thrust coefficients. Hence, the wing surface is refined to 100x50 points, which removed the oscillations in the lift and thrust profile. The comparison of lift and thrust variation between these grids are shown in Fig.4.5. The difference in instantaneous values and mean values of thrust and lift are less than 1%. Hence, the fine grid with approximately 13.5 million cells is used for Re =100,000 simulation.

4.3.3 Flow structure

Before discussing the effect of Reynolds number, the flow structures at various phases of flapping flight for Re = 10,000 are analyzed. The isosurface of vorticity along the spanwise direction in the wing reference frame ω_ζ, at different times is given in Fig.4.6. The isosurfaces show the formation of LEV (negative vorticity) and its subsequent separation during the downstroke. At t* = 0.1, a spiral LEV with size gradually increasing from base to tip forms and it is attached on the top surface of the wing. The size of the LEV grows with time until its separation. At t*=0.2, the spiral LEV is the strongest which results in a peak in lift (Figure.4.8 shows the instantaneous lift and thrust profile for all Reynolds numbers). The pressure contour and streamlines in the chordwise plane, ζ=3 at different times in Fig.4.7 show detailed slices of LEV evolution and separation. The LEV starts to lift away from the wing as early as t* of 0.1 and its separation leads to the formation of multiple secondary LEVs. The secondary LEVs also lift away from the surface of the wing and the pressure contours show the detachment of the LEV (low pressure region) and increase in pressure on the surface of the wing by the entrainment of freestream fluid. The isosurface of the vorticity shows that the LEV near the base is attached for most of the downstroke whereas the LEV near the tip sheds and completely dissipates into the flow during the end of the downstroke (t*=0.4 to 0.5). The vorticity contours also show the growth of a Trailing Edge Vortex (TEV) during the

downstroke with its maximum size near the tip. The TEVs are also shed at the end of downstroke (t*=0.4 to 0.5) and dissipate into the flow.

The behavior of flow during the upstroke is similar to that during the downstroke. During the upstroke, the angle of attack is low and the effective angle of attack is negative only for a small portion of the wing near the tip. Hence there is no clear formation of the LEV on the bottom surface and the vorticity contours (Fig.4.6) show only a small positive vortex attached near the tip. The streamlines and pressure contours, Fig.4.7, show no apparent vortex formation at locations ζ=3.0. At around t*=0.8, a small low pressure region and presence of multiple small LEVs are observed. This low pressure region results in a peak in negative lift and also generates thrust. These LEVs become unstable and shed during the end of the upstroke.

Table 4.2 Parameters for different case and the average values of lift and thrust

Cases	**Re**	**Tip shape**	**Stoke deviation**	**C_T**	**C_L**
Case-A	10000	Rectangle	No	0.37	0.56
Case -B	100	Rectangle	No	0.19	0.46
Case -C	100,000	Rectangle	No	0.37	0.57
Case -D	10,000	Rounded	No	0.33	0.54
Case-E	10,000	Tapered	No	0.32	0.56
Case-F	10,000	Rectangle	Yes	0.37	0.44

4.3.4 Effect of Reynolds number

The stability of the LEV depends strongly on the flow structures such as the spanwise flow created along the core of the LEV and the tip vortex. Previous studies proposed different phenomena for the stability of LEV at different Reynolds numbers. In order to evaluate the effect of Reynolds number, the present study analyzes the forward flapping flight at three Reynolds numbers. The comparison of instantaneous lift and thrust coefficient for different Reynolds numbers is shown in Fig.4.8. The variation of lift and thrust coefficients, in particular locations of maximum values of lift and thrust are

identical for all three Reynolds numbers. However, the peak values obtained for Re =100 are lower than the higher Reynolds numbers. This leads to low average value of thrust and lift for Re =100 (Table .4.2). There is no difference between the average values of lift and thrust between Re=10,000 and Re=100,000. The isosurface contours of vorticity along the spanwise direction for all three cases at t*=0.25 are shown in Fig.4.9. At Re=100, a coherent LEV is observed and it is attached along the leading edge. Also a coherent attached TEV is observed. At higher Reynolds numbers, the LEV is less coherent and it is only attached near the base of the wing. The LEV separates from the leading edge near the tip and the formation of secondary LEVs are observed. The other critical difference between Re=100 and the higher Reynolds numbers is the location of the LEV from the surface of the wing. At Re=100, the core of the LEV is located far from the wing surface, whereas at higher Reynolds numbers the LEV is closer to the wing surface.

The pressure contours along the chordwise section at locations ζ=3.0 are shown in Fig.4.7, Fig.4.10 and Fig.4.11, for Re=10,000, 100 and 100,000 respectively. For Re=100, a single LEV forms during the downstroke as shown in Fig.4.10 from t*=0.15 to t*=0.35 and it is attached to the leading edge during most of the downstroke. However, the core of the LEV lifts away from the wing and the location of minimum pressure is well above the surface of the wing. For higher Reynolds numbers (Fig.4.7 and Fig.4.11), the LEV separates from the tip and secondary LEVs form during the second half of the downstroke. In addition, the separated LEV moves downstream close to the surface of the wing as shown in Fig.4.7 and Fig.4.11 at t*=0.15 and at t*=0.25. This moves the location of the minimum pressure closer to the wing surface and creates a low pressure throughout the upper surface of the wing. This generates high values of lift and thrust coefficients and results in high average values. During the upstroke, a similar variation in the LEV structure is observed between the Reynolds numbers. For Re=100, a small coherent LEV forms around mid-upstroke and its center moves away from the surface. At higher Reynolds numbers, the LEV and low pressure region slides along the surface of the wing as seen in Fig.4.7 and Fig.4.11 at t*=0.75 and at t*=0.85.

One of the significant difference reported in previous studies[14,15] is the absence of spanwise flow along the core of the LEV at low Reynolds numbers. However, our results show that a strong positive spanwise flow of the order of flapping velocity exists along the core of the LEV at all Reynolds numbers as shown in Fig.4.12. The results also show that the strength of the spanwise flow increases with Reynolds number.

The primary impact of Reynolds number is that at high Reynolds numbers the LEV separates near the tip which leads to the formation of secondary LEVs. Further, the separated LEV moves along the surface of the wing causing a low pressure region on the entire top surface. This results in high instantaneous lift and thrust coefficients at higher Reynolds numbers. No significant difference is observed between Re=10,000 and Re=100,000.

4.3.5 Effect of tip shapes

In order to evaluate the effect of tip vortex on the LEV structure, three different tip shapes as shown in Fig.4.13 are analyzed at Re=10,000 and at an advance ratio, J=0.5. The comparison of lift and thrust profiles for all three cases are shown in Fig.4.14 and the average values are listed in Table 4.2. The variation of lift and thrust is similar for all three tip shapes with only small difference during the start of the upstroke. The location of maximum values of thrust and lift coefficients are identical for all three shapes, and they do not vary significantly. In order to understand the effect of tip shapes, coherent vortex structures obtained based on the method of Chong et al.[27], during the downstroke are analyzed in Fig.4.15. At t* = 0.1, a continuous vortex along the leading edge and tip is observed for the rounded tip wing, while a discontinuous vortex is observed for straight and tapered wing. We surmised that the rounded edge will enhance the stability of the LEV by providing a way for the removal of vorticity from the LEV with the formation of a continuous vortex. However, the coherent vortex structures at t*=0.2 show that the LEV separates from the wing and the location of the separated LEV is identical for all tip shapes as shown in Fig.4.15. A small coherent vortex structure, which corresponds to the formation of secondary LEVs, is observed along the leading edge for all three cases. At t*=0.3, the separated LEV moves further away from the

surface and the location is identical for all three cases. The results from this analysis show that the tip shape has very little impact on the stability of the LEV for the cases simulated.

4.3.6 Effect of stroke deviation

In order to analyze the effect of stroke deviation, a sinusoidal variation of stroke deviation angle with the same frequency as that of the flapping angle (Fig.4.2b) is applied to the kinematics. The wing tip covers a circular motion for this case as shown in Fig.4.16. Comparison of lift and thrust coefficients between the case A using kinematics without stroke deviation and case F using kinematics with stroke deviation is shown in Fig.4.17. During the downstroke, the lift and thrust coefficients variation is identical between the two cases including the peak values and the timing of peak values. However, there are significant differences observed during the upstroke. In the case of stroke deviation, two peaks in thrust and lift coefficients are observed. The first peak in thrust and lift (down force) occurs during the early stage of the upstroke at around $t^* = 0.6$ and the second peak occurs at around $t^* = 0.85$. The magnitude of the second peak is lower than that obtained for no stroke deviation at $t^* = 0.85$. The average value of lift coefficient obtained with stroke deviation is lower than that with no stroke deviation due to the additional peak in downforce obtained during the upstroke. The average value of thrust is the same for both cases.

The instantaneous pressure contours along the chordwise section at $\zeta = 3$ at different times is shown in Fig.4.7 and Fig.4.18 for the case A and case F, respectively. During the downstroke, the formation and separation of the LEV is similar for both cases. At $t^* = 0.2$ the LEV starts to move downstream and lifts away from the surface. The pressure contour shows strong negative pressure at the center of the LEV for case F. During the upstroke, the kinematics with stroke deviation encounters the LEV shed during the downstroke. This creates a low pressure region on the entire bottom surface of the wing as seen at $t^* = 0.65$ and $t^* = 0.75$ of Fig.4.18. In contrast, in the case of no stroke deviation, the low pressure region forms only near the leading edge. This explains the peak of negative lift and thrust produced at $t^* = 0.65$ for case F. During the second half of the

upstroke, the pressure contours show the formation of a weak low pressure region for case F, which leads to the small second peak in negative lift and thrust coefficients at t*=0.85. The results show that introduction of stroke deviation alters the flow structure, in particular during the upstroke by capturing the vortex shed during the downstroke.

4.4 Conclusions

The effects of Reynolds number, tip shape and stroke deviation on flapping flight performance are analyzed. For the effect of Reynolds number, three different cases, Re= 100, 10,000, and 100,000 are analyzed. At Re =100, a coherent Leading Edge Vortex (LEV) forms and stays attached to the leading edge during most of the downstroke. At higher Reynolds numbers, the LEV sheds near the tip during the mid-downstroke and convects downstream causing a low pressure region on the entire upper surface of the wing, which generates high values of thrust and lift. In addition, secondary LEVs form during the second half of the downstroke. Comparison of lift and thrust coefficients show that the trends are similar for all Reynolds numbers in the location of peak values and the variation of force coefficients. However, instantaneous values obtained for Re=100 are lower and result in lower average coefficients of lift and thrust. There is no difference in average values between Re=10,000 and Re=100,000. Another critical finding of the study is that a strong spanwise flow of the order of flapping velocity along the core of the LEV is observed at Re=100. This is in contrast to previous studies, which observed spanwise flow only at high Reynolds numbers.

Analysis of different tip shapes, straight, rounded, and tapered show that the lift and thrust production are not very sensitive to the tip shape. The timing of separation of the LEV and the location of separated LEV is identical for all three tip shapes signifying little or no impact of the tip vortex on flapping flight performance. The introduction of stroke deviation to the kinematics makes a significant difference in instantaneous lift and thrust production during the upstroke. The stroke deviation generates high negative lift and thrust during the start of the upstroke, as the LEV shed during the downstroke interacts with the wing. This lowers the average value of lift, while the average thrust value remains the same.

4.5 Figures

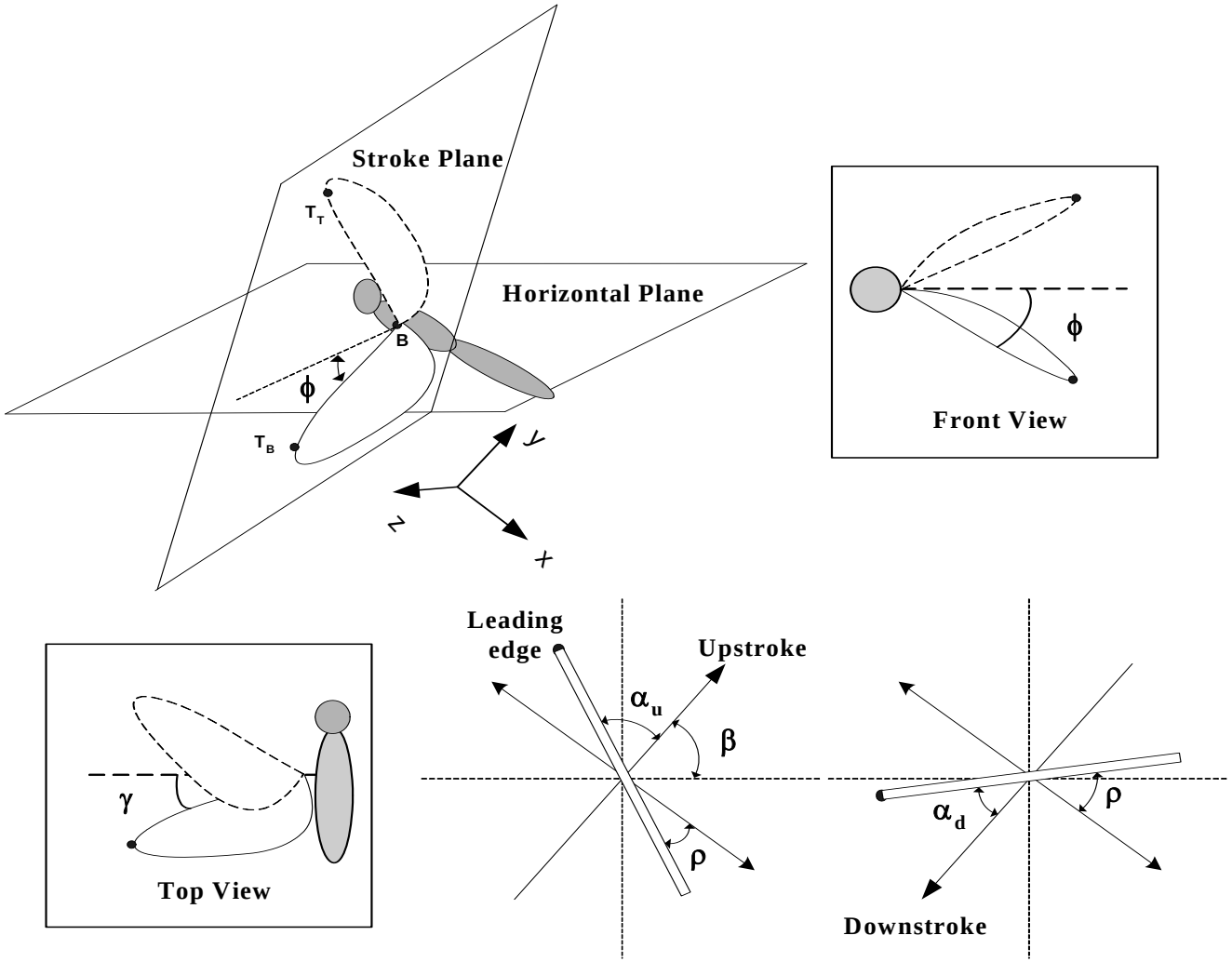

Fig.4.1 Kinematic parameters

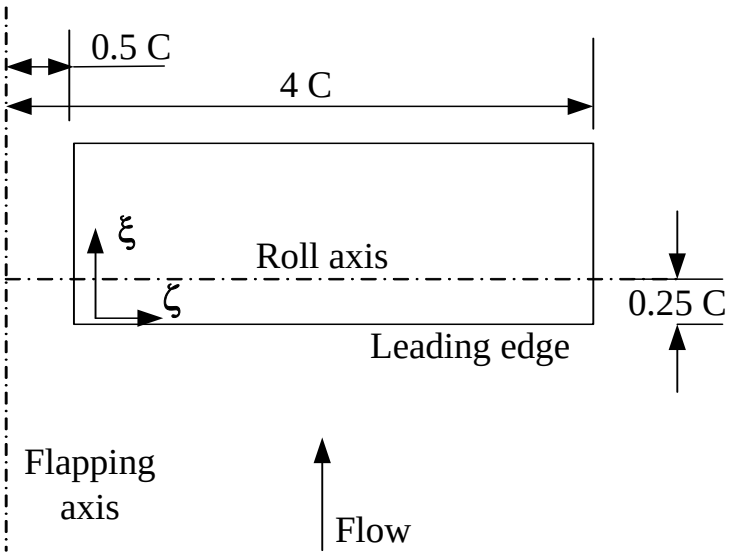

(a)

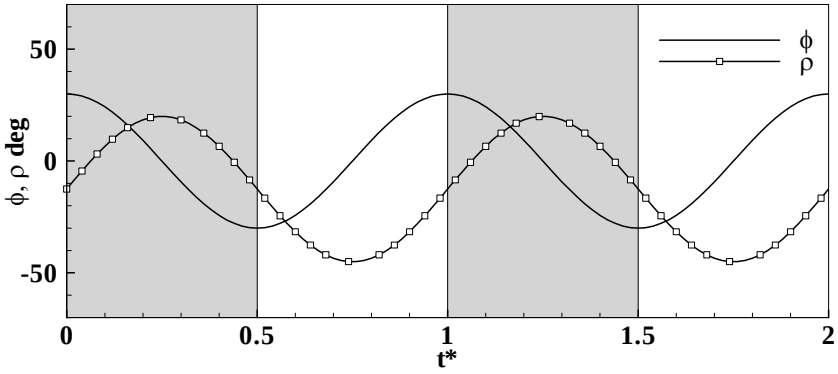

(b)

Fig.4.2 (a) Rectangular wing configuration. (b) Variation of flapping and torsional angle; shaded region represents downstroke.

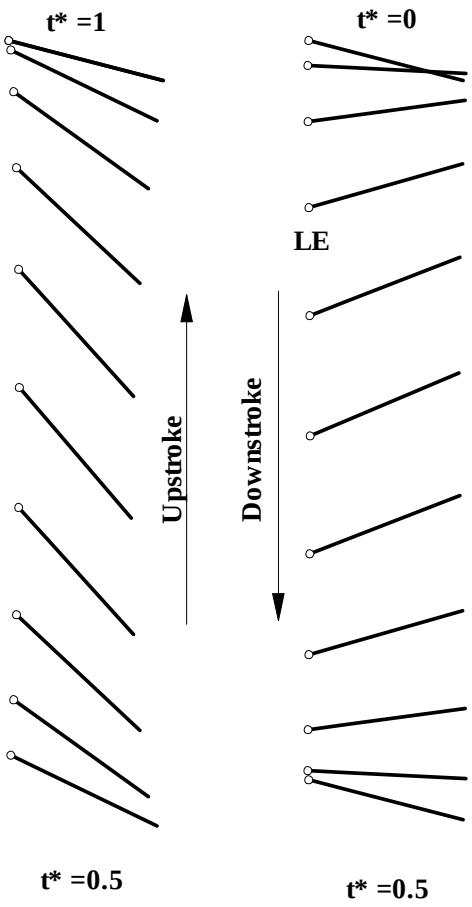

(a)

During Downstroke

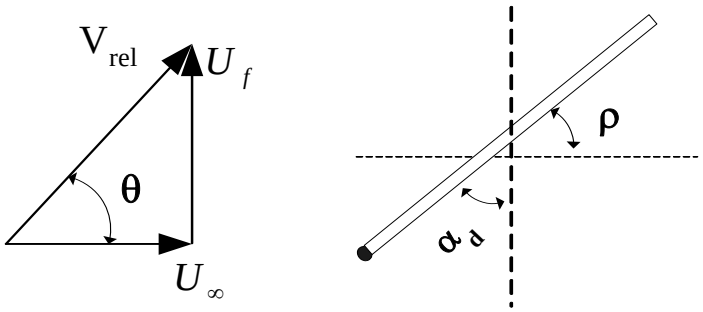

$\theta = \tan^{-1}[U_f / U_\infty]$ $\quad \alpha_{eff} = \theta - \rho$

$= \tan^{-1}[1/J]$ $\quad = \theta + \alpha_d - 90^o$

(b)

Fig.4.3 (a) wing positions at different times, (b) Effective angle of attack during downstroke

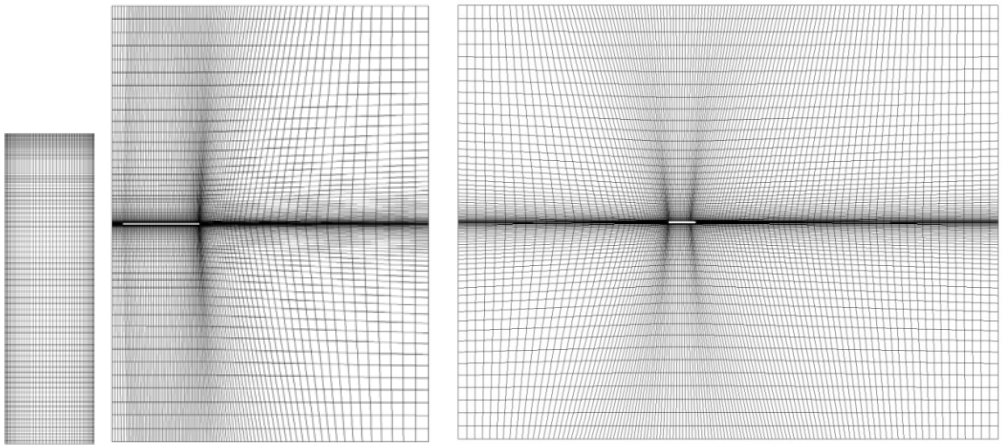

Fig.4.4 Grid distribution (a) wing (b) spanwise plane (c) chordwise plane (every other grid line is shown for b and c)

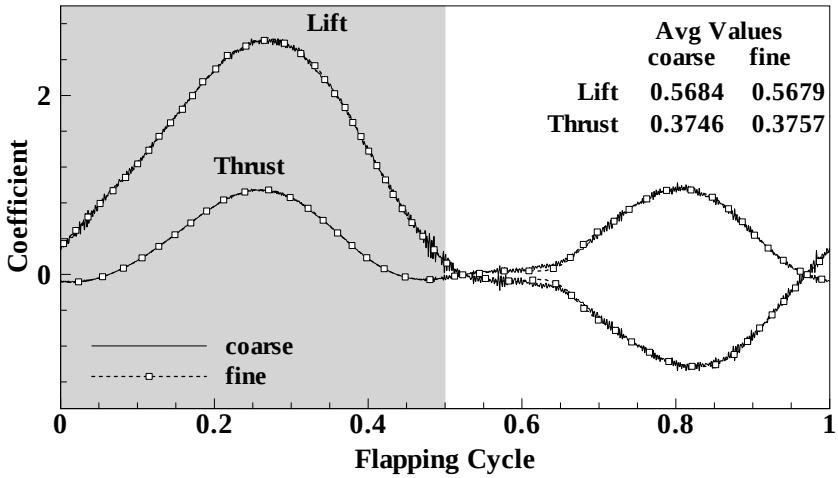

Fig.4.5 Comparison of lift and drag coefficients for different grid size

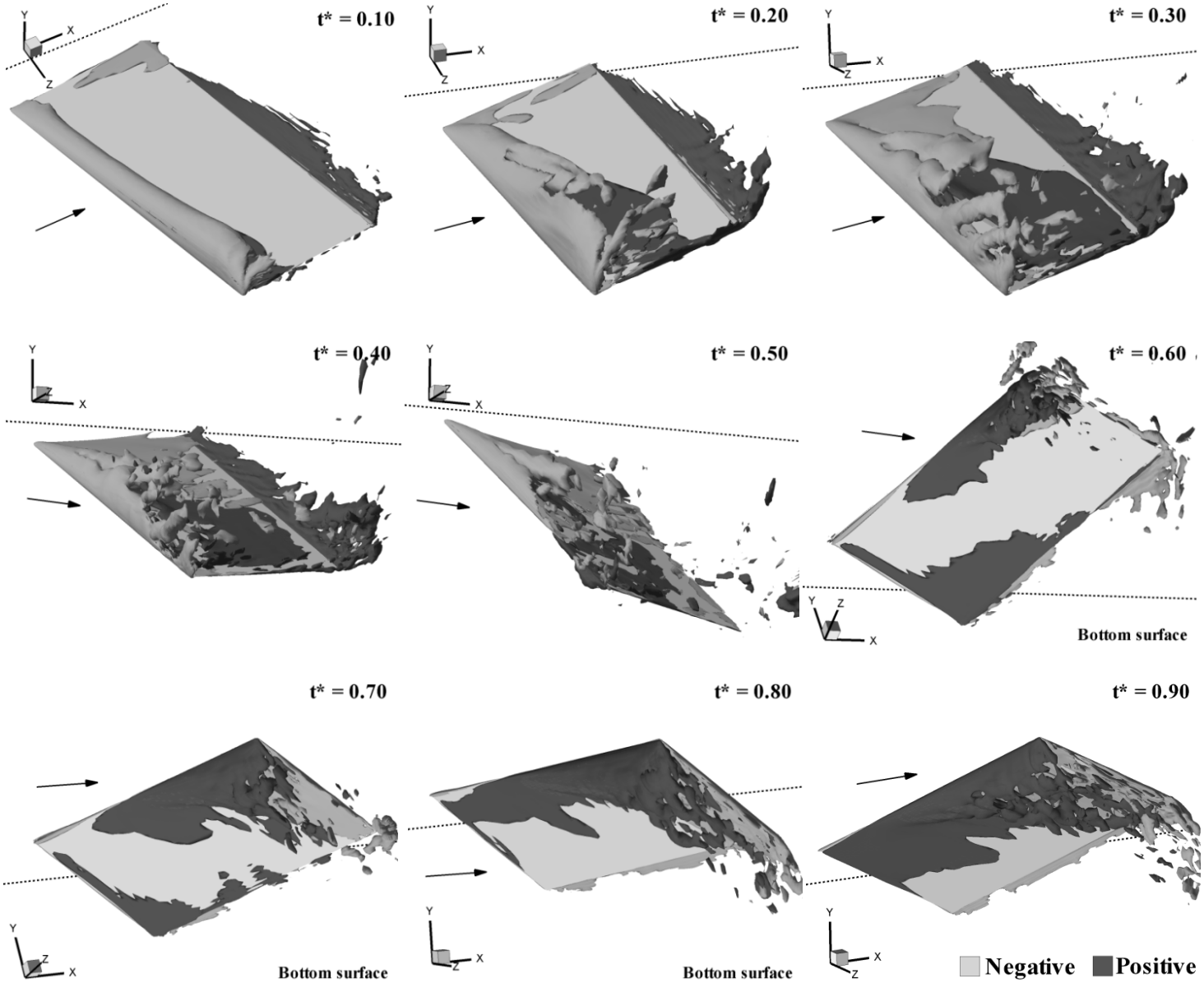
t* = 0.10
t* = 0.20
t* = 0.30
t* = 0.40
t* = 0.50
t* = 0.60
Bottom surface
t* = 0.70
t* = 0.80
t* = 0.90
Bottom surface
Bottom surface
Negative
Positive

Fig.4.6 Isosurface contours of vorticity along the spanwise direction at various times for Re=10,000 (case A)

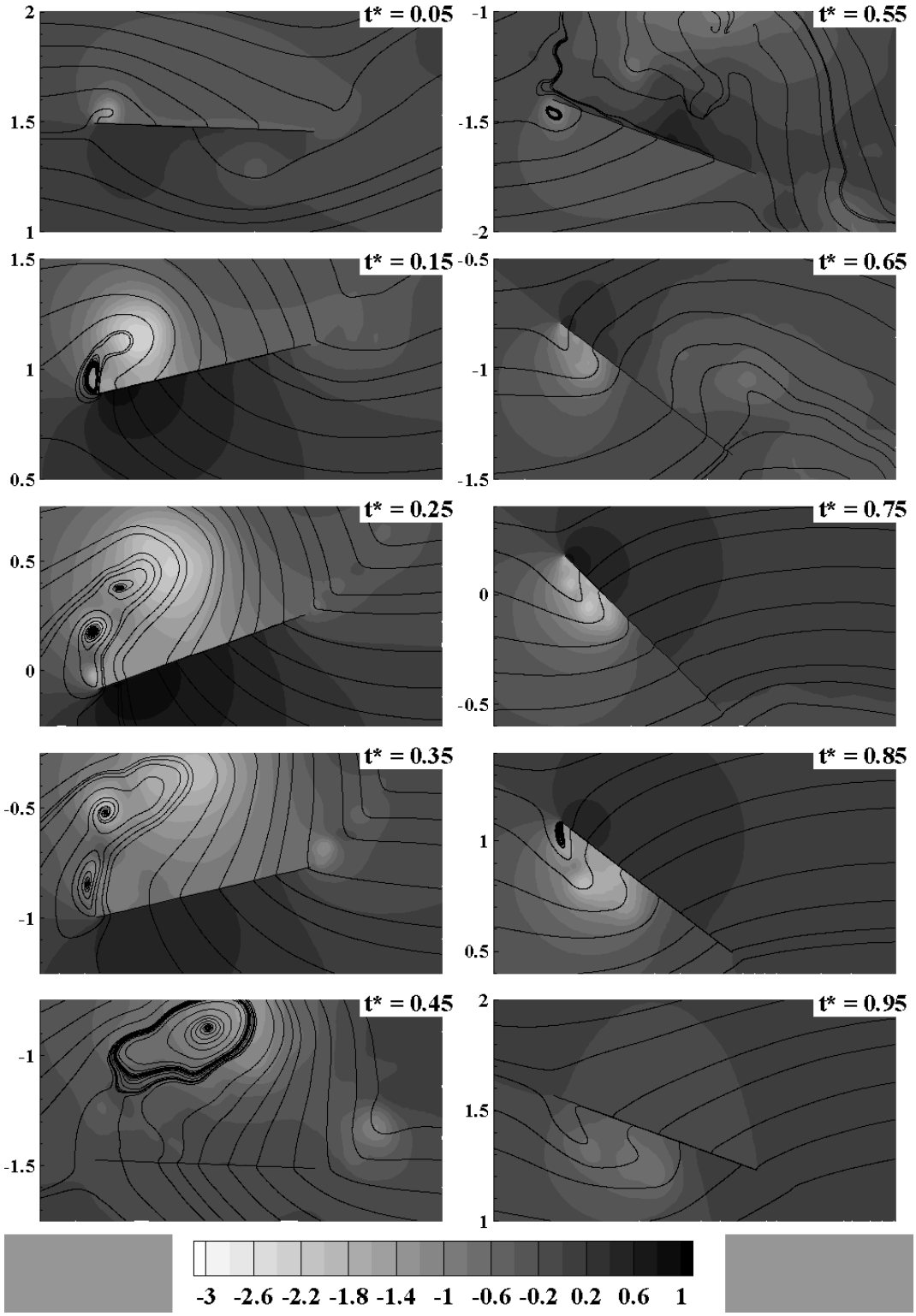

Fig.4.7 Instantaneous pressure contours and streamlines in a chordwise plane at ζ = 3 for Re =10,000 (Case A)

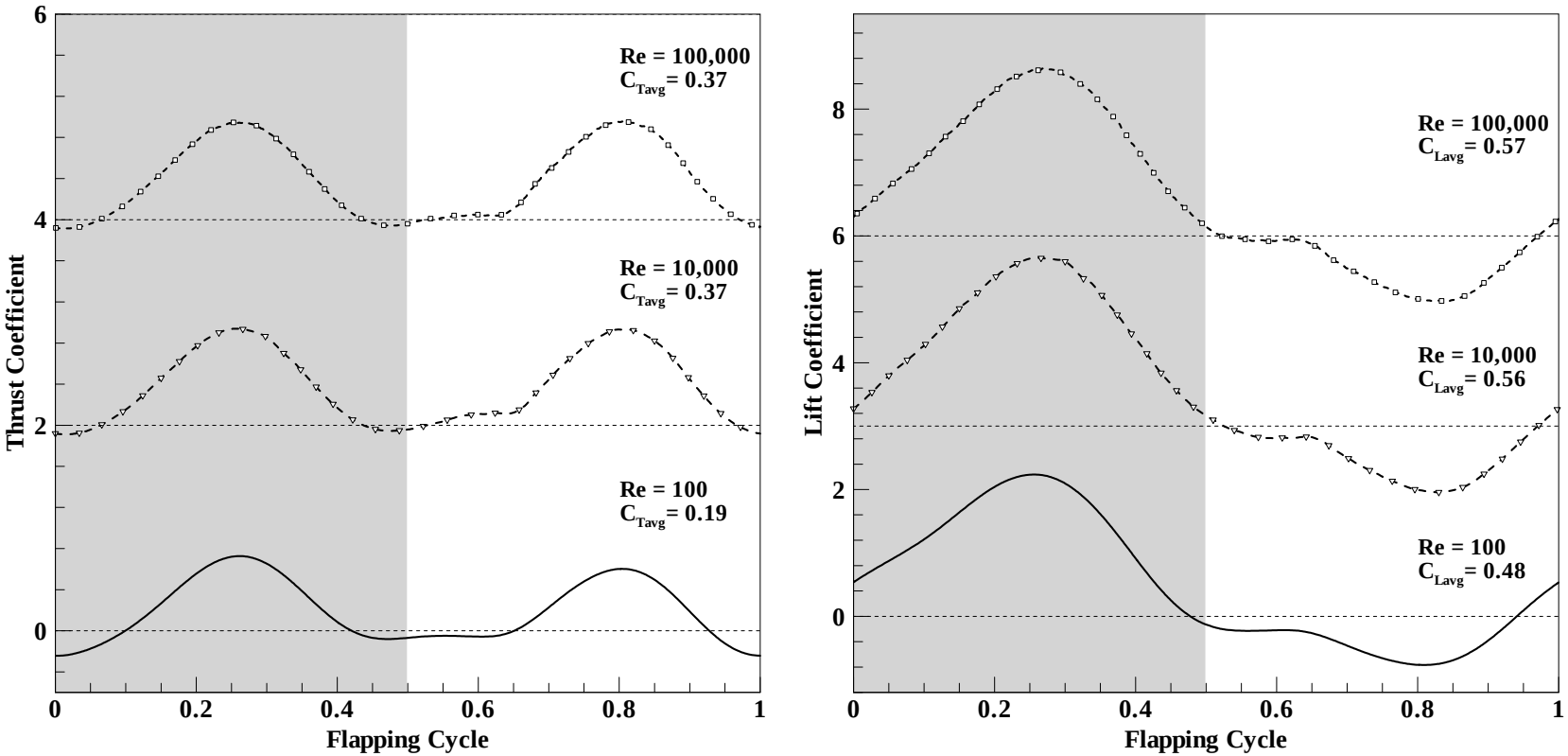

Fig.4.8 Comparison of thrust and lift coefficient for three different Reynolds numbers

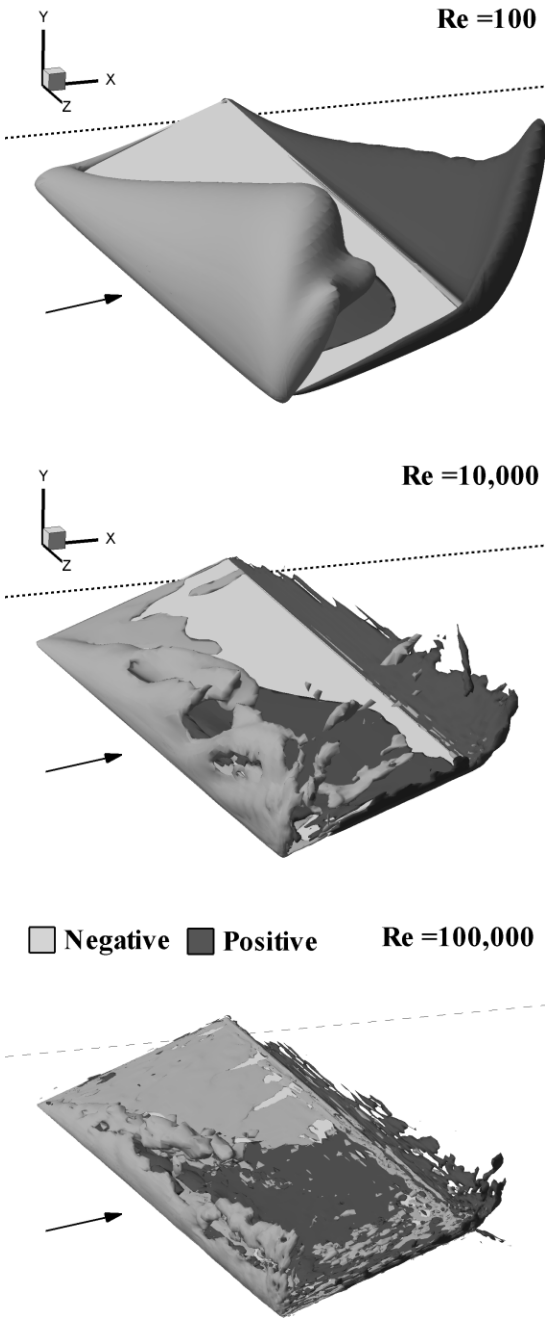

Fig.4.9 Isosurface vorticity contours at t* =0.25 for three different Reynolds numbers (isosurface levels +5,-5 for Re =100, +20, -20 for Re =10,000 and +35, -35 for Re =100,000)

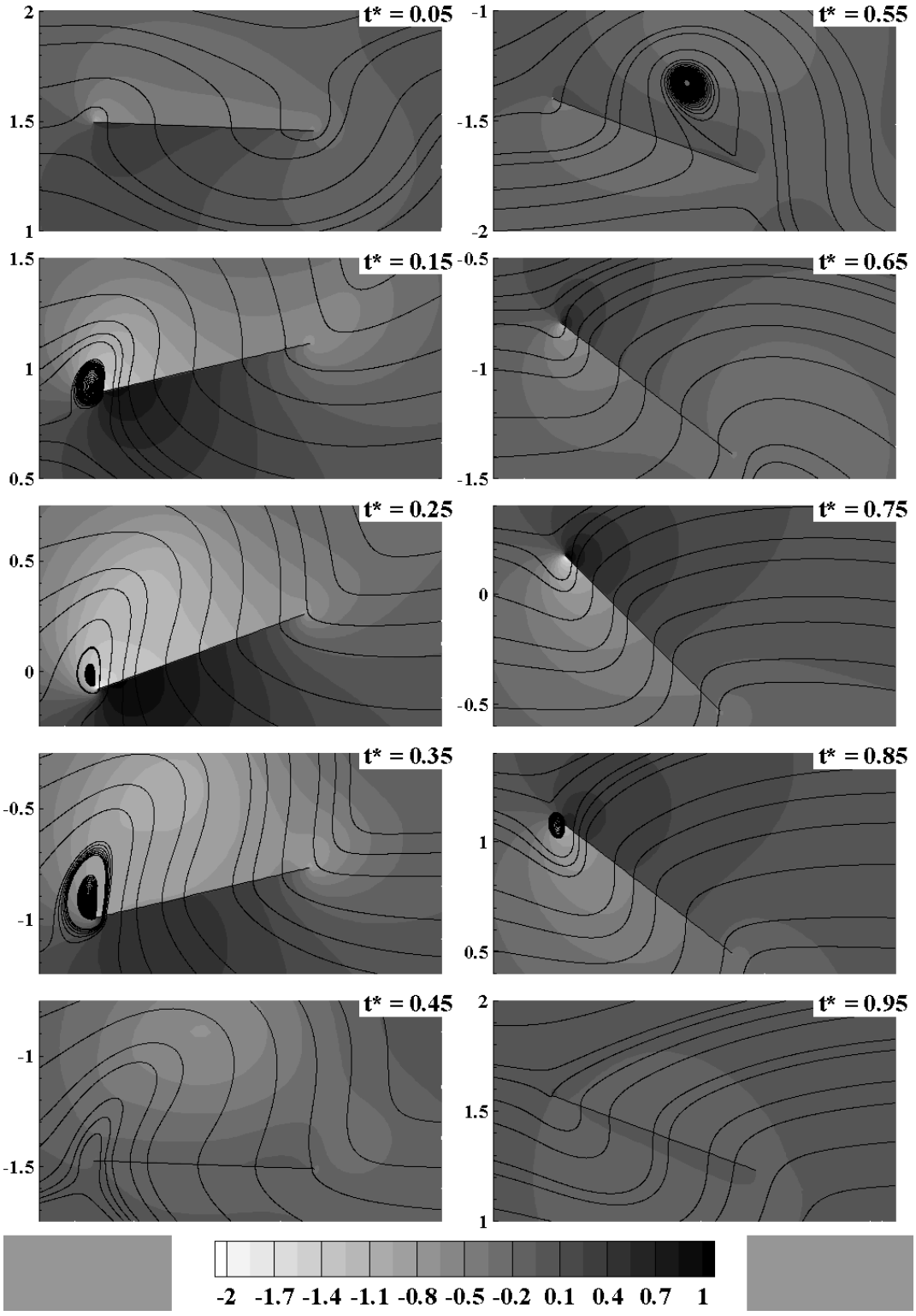

Fig.4.10 Instantaneous pressure contours and streamlines in a chordwise plane at $\zeta = 3$ for Re =100

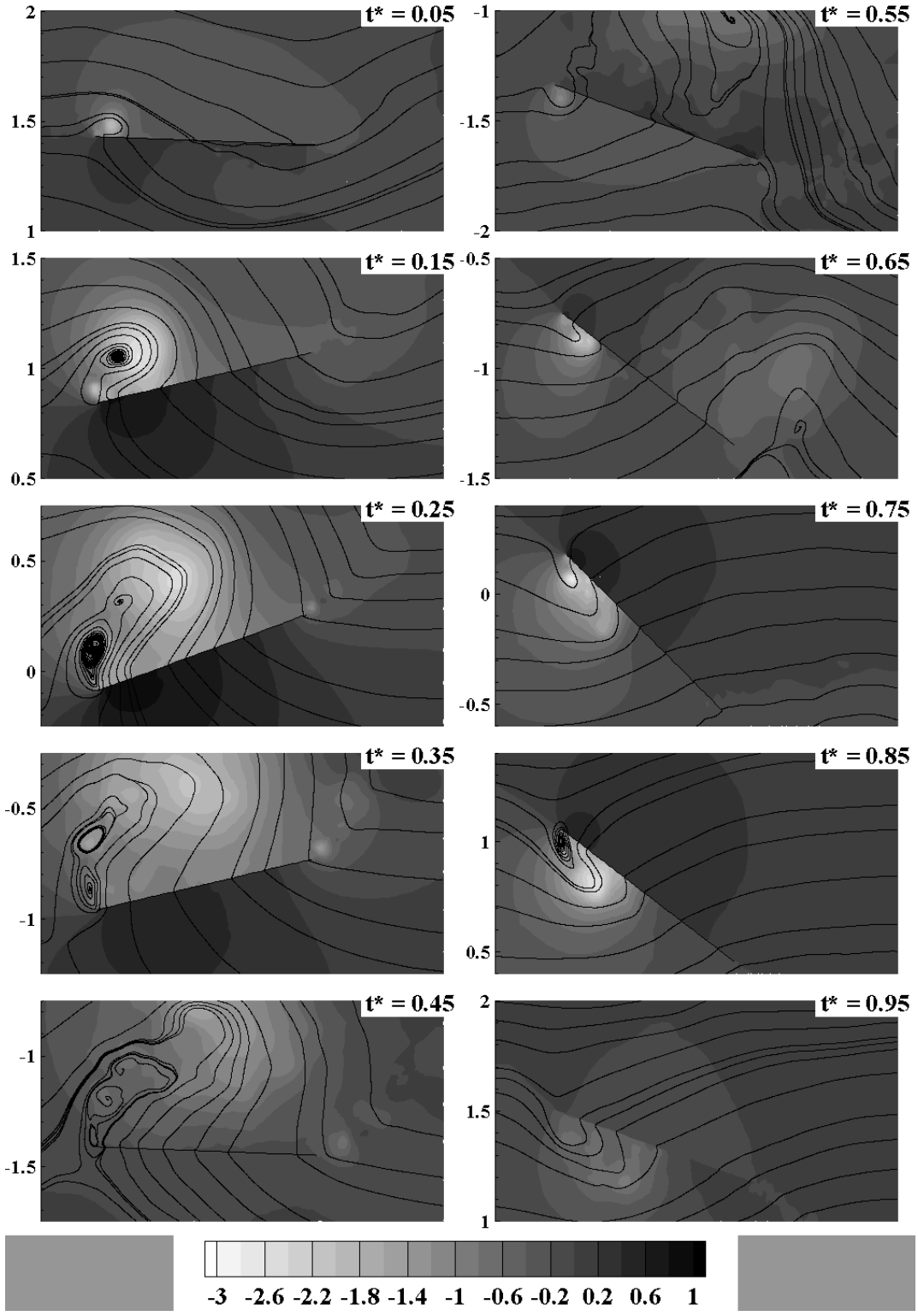

Fig.4.11 Instantaneous pressure contours and streamlines in a chordwise plane at ζ = 3 for Re =100,000

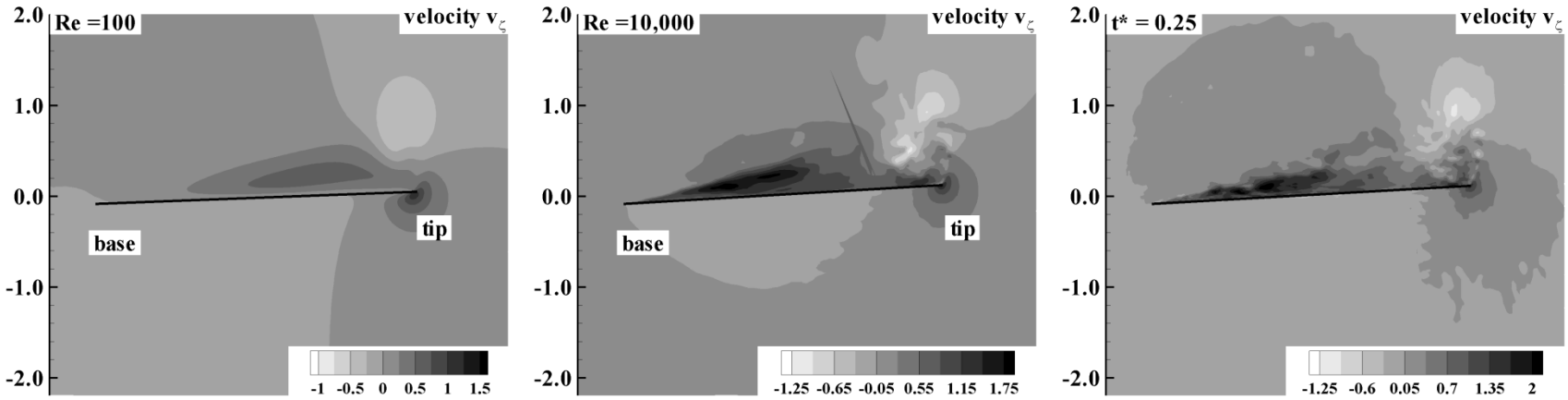

Fig.4.12 Spanwise flow along the LEV core for all Reynolds number cases

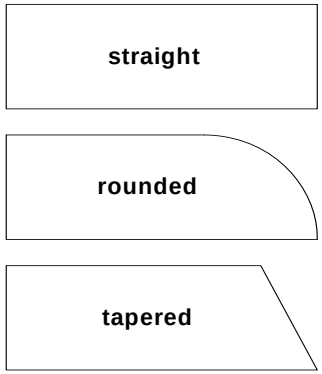

Fig.4.13 Wing tip shapes used to study the effect of tip vortex

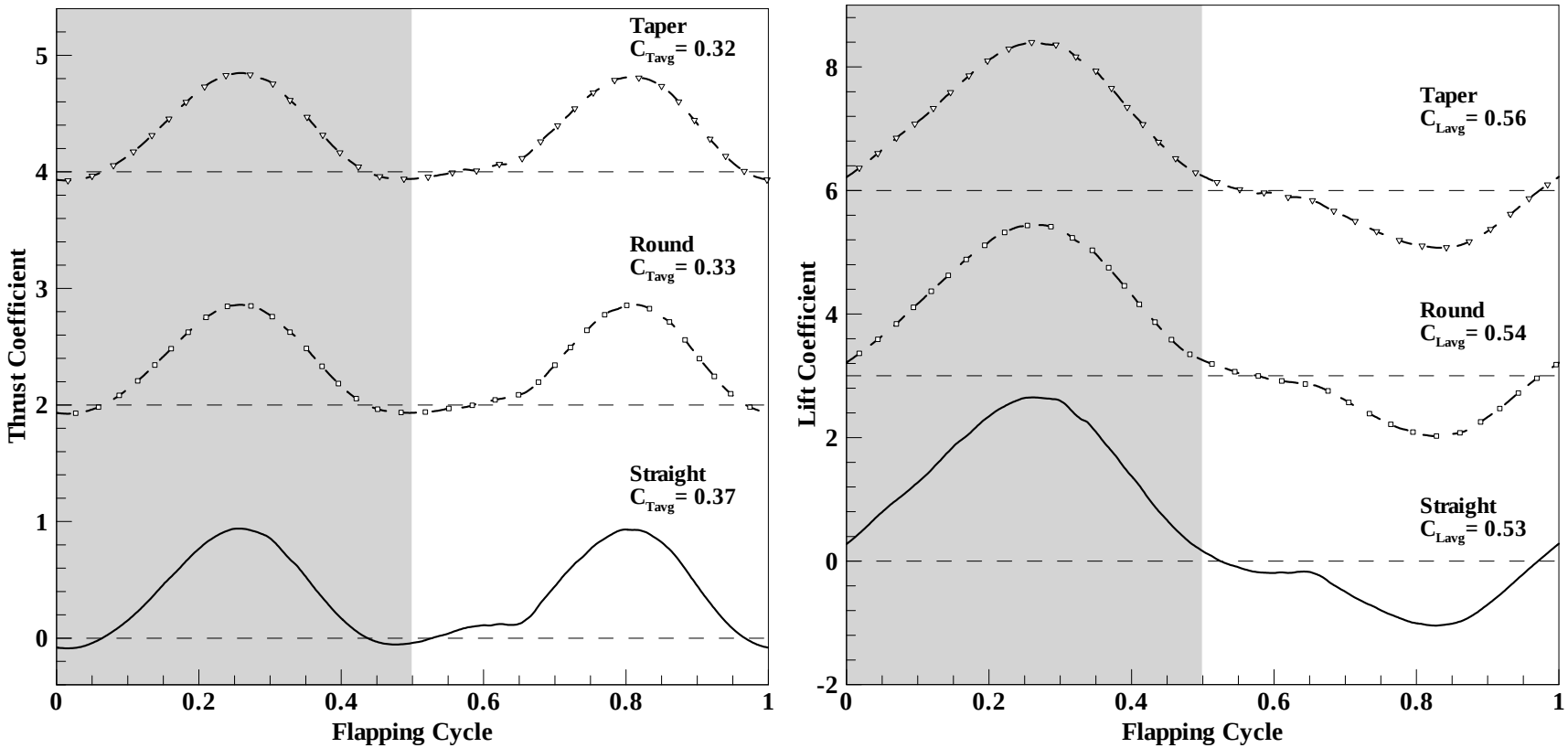

Fig.4.14 Comparison of thrust and lift coefficients for different wing shapes

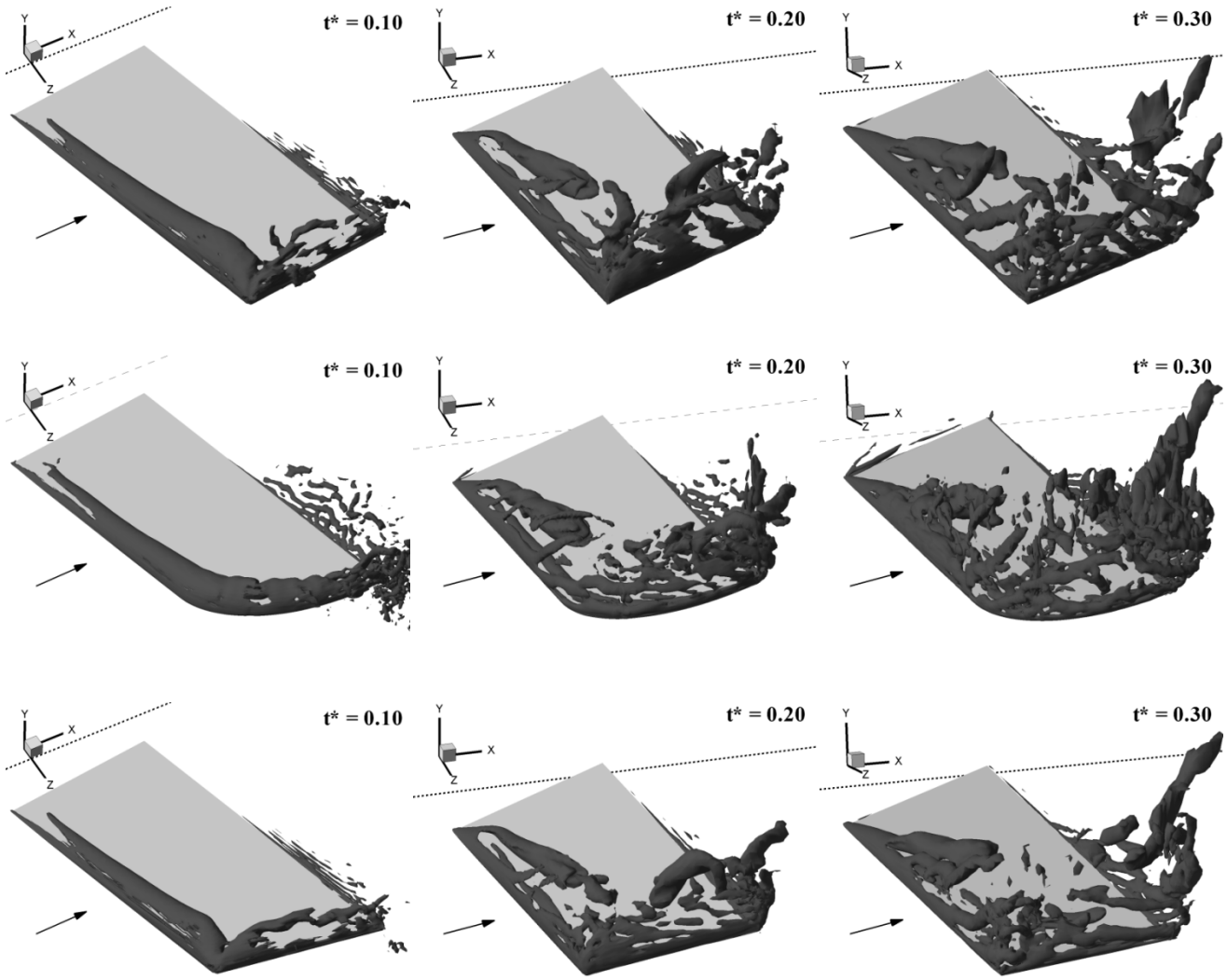

Fig.4.15 Coherent structures at different times during the downstroke for wing shapes a) Straight b) Rounded edge c) Tapered Edge

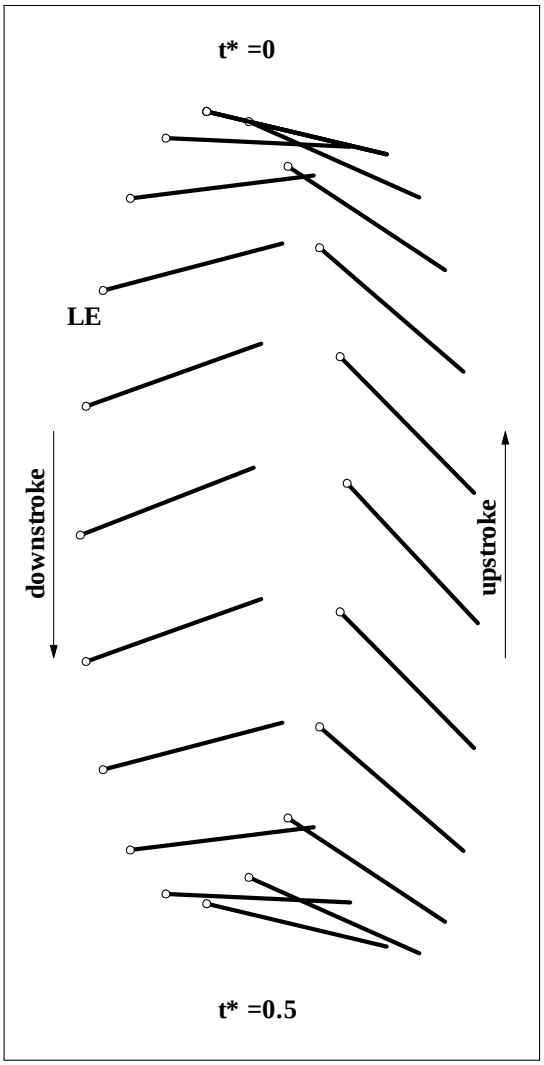

Fig.4.16 Movement of wing tip for stoke deviation case F

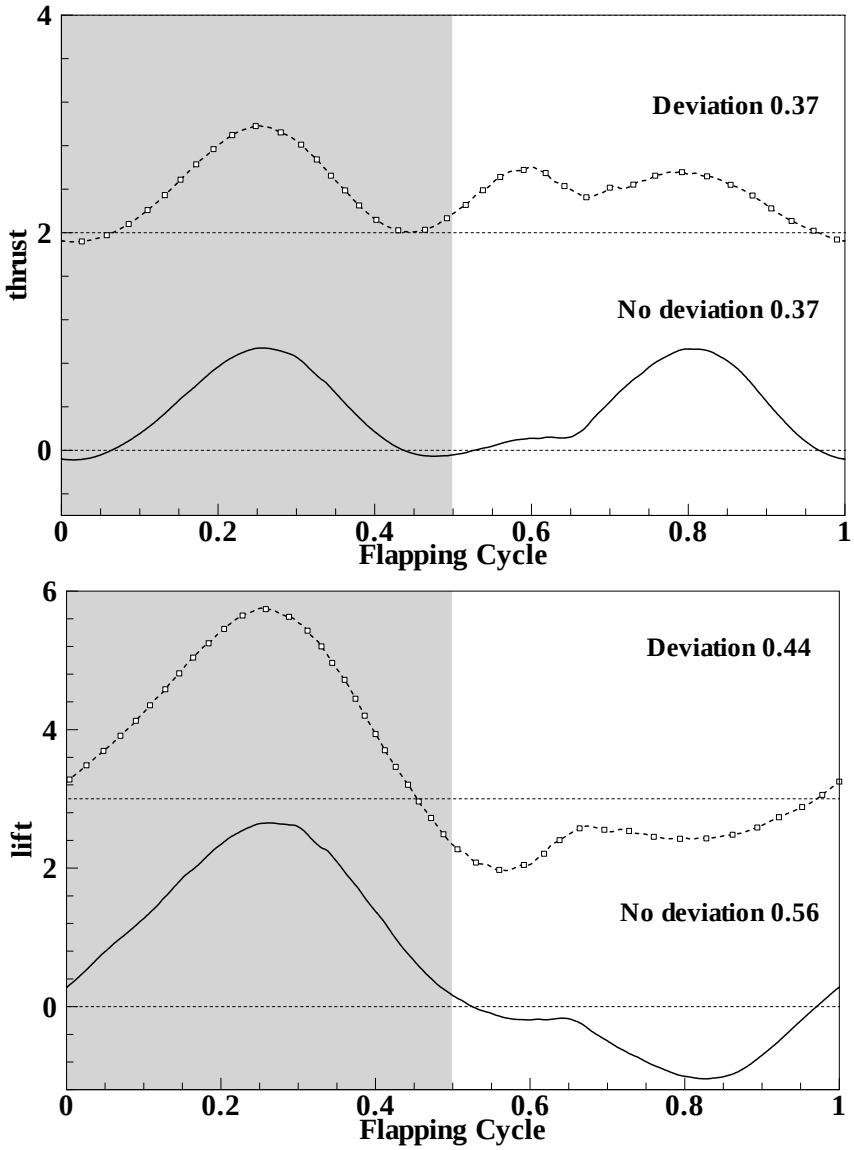

Fig.4.17 Comparison of thrust and lift between no stroke deviation (case A) and stroke deviation (case F)

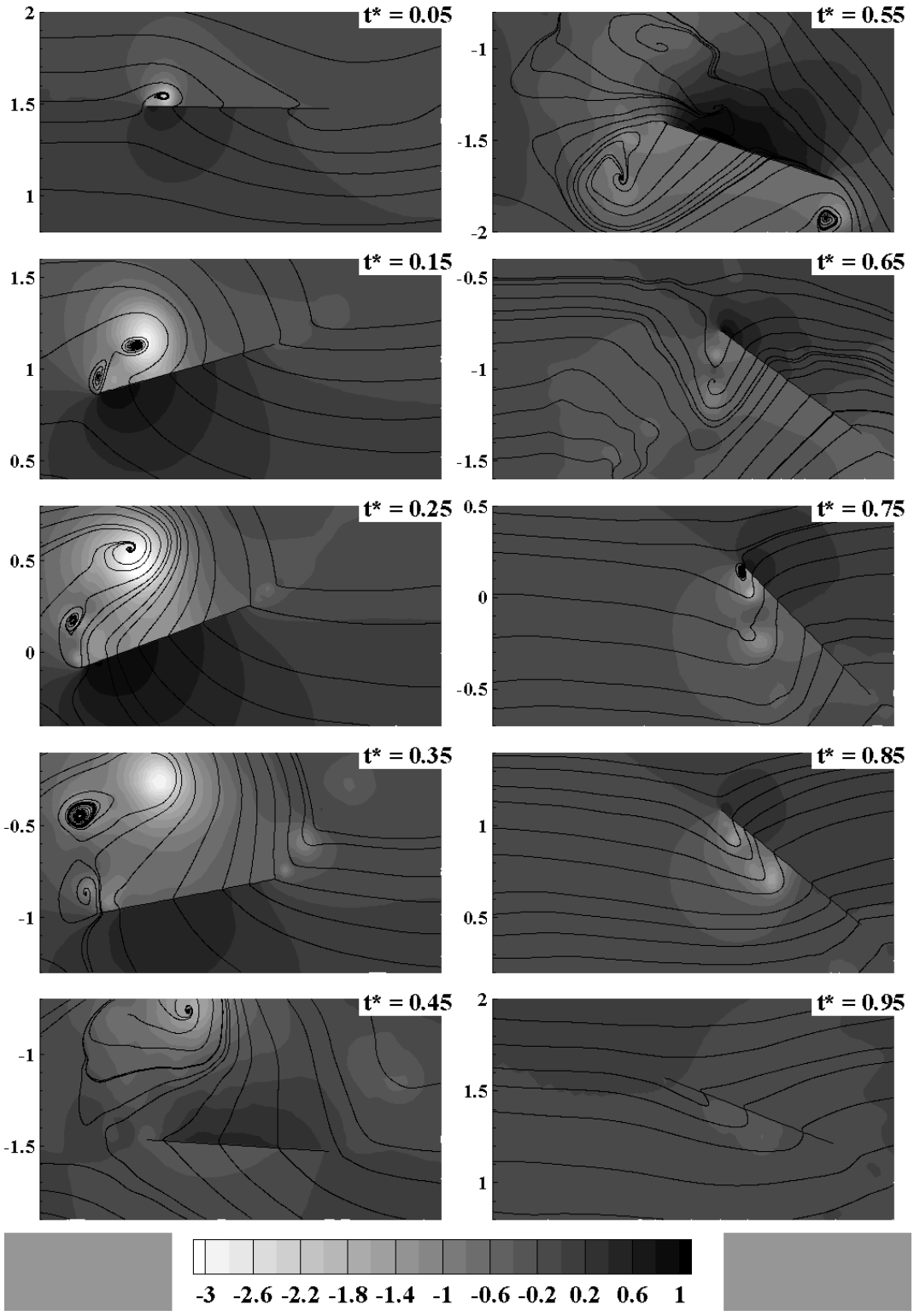

Fig.4.18 Instantaneous pressure contours and streamlines in a chordwise plane at $\zeta = 3$ for stoke deviation case

4.6 References

[1] Weis-Fogh, T. Quick Estimate of Flight Fitness in Hovering Animals, Including Novel Mechanisms for Lift Production. The Journal of Experimental Biology 1973;59:169-230.

[2] Dickinson, M. H. and Götz, K. G. Unsteady Aerodynamic Performance of Model Wings at Low Reynolds Numbers. The Journal of Experimental Biology 1993;174:45-64.

[3] Ellington, C. P., Berg, C. V. D., Willmott, A. P., and Thomas, A. L. R. Leading-Edge Vortices in Insect Flight. Nature 1996;384:626-630.

[4] Dickinson, M. H., Lehmann, F.-O., and Sane, S. P. Wing Rotation and the Aerodynamic Basis of Insect Flight. Science 1999;284:1954-1960.

[5] Lehmann, F.-O., Sane, S. P., and Dickinson, M. The Aerodynamic Effects of Wing–Wing Interaction in Flapping Insect Wings. The Journal of Experimental Biology 2005;208:3075-3092.

[6] Miller, L. A. and Peskin, C. S. A Computational Fluid Dynamics of 'Clap and Fling' in the Smallest Insects. The Journal of Experimental Biology 2005;208:195-212.

[7] Sun, M. and Yu, X. Aerodynamic Force Generation in Hovering Flight in a Tiny Insect. AIAA Journal July 2006;44:1532-1540.

[8] Walker, J. A. Rotational Lift: Something Different or More of the Same? The Journal of Experimental Biology 2002;205:3783-3792.

[9] Sun, M. and Tang, J. Unsteady Aerodynamic Force Generation by a Model Fruit Fly Wing in Flapping Motion. The Journal of Experimental Biology 2002;205:55-70.

[10] Wang, Z. J., Birch, J. M., and Dickinson, M. H. Unsteady Forces and Flows in Low Reynolds Number Hovering Flight: Two-Dimensional Computations Vs Robotic Wing Experiments. The Journal of Experimental Biology 2004;207:449-460.

[11] Ellington, C. P. The Novel Aerodynamics of Insect Flight: Applications to Micro-Air Vehicles. The Journal of Experimental Biology 1999;202:3439–3448.

[12] Liu, H., Ellington, C. P., Kawachi, K., Berg, C. V. D., and Willmott1, A. P. A Computational Fluid Dynamic Study of Hawkmoth Hovering. The Journal of Experimental Biology 1998;201:461–477.

[13] Sane, S. P. and Dickinson, M. H. The Control of Flight Force by a Flapping Wing: Lift and Drag Production. The Journal of Experimental Biology 2001;204:2607-2626.

[14] Birch, J. M. and Dickinson, M. H. Spanwise Flow and the Attachment of the Leading-Edge Vortex on Insect Wings. Nature Aug 2001;412:729-733.

[15] Birch, J. M., Dickson, W. B., and Dickinson, M. H. Force Production and Flow Structure of the Leading Edge Vortex on Flapping Wings at High and Low Reynolds Numbers. The Journal of Experimental Biology 2004;207:1063-1072.

[16] Miller, L. A. and Peskin, C. S. When Vortices Stick: An Aerodynamic Transition in Tiny Insect Flight. The Journal of Experimental Biology 2004;207:3073-3088.

[17] Tarascio, M. J., Ramasamy, M., Chopra, I., and Leishman, J. G. Flow Visualization of Micro Air Vehicle Scaled Insect-Based Flapping Wings. Journal of Aircraft Apr 2005;42:385-390.

[18] Gopalakrishnan, P. and Tafti, D. K. Effect of Rotation and Angle of Attack on Force Production of Flapping Flights. under review, AIAA Journal 2008.

[19] Demirdzic, I. and Peric, M. Space Conservation Law in Finite Volume Calculation of Fluid Flow. International Journal For numerical Methods in Fluids 1988;8:1037-1050.

[20] Demirdzic, I. and Peric, M. Finite Volume Method for Prediction of Fluid Flow in Arbitrarily Shaped Domains with Moving Boundaries. International Journal For numerical Methods in Fluids 1990;10:771-790.

[21] Germano, M., Piomelli, U., Moin, P., and Cabot, W. H. A Dynamic Subgrid-Scale Eddy Viscosity Model. Physics of Fluids A 1991;3:1760-1765.

[22] Gopalakrishnan, P. and Tafti, D. K. Effect of Phasing of Rotation on Delayed Stall in Flapping Flights Related to Mavs at Re=10000. AIAA 38th Fluid Dynamic conference, Seattle, Washington June 2008; AIAA-2008-4301.

[23] Gopalakrishnan, P. and Tafti, D. K. A Parallel Boundary Fitted Dynamic Mesh Solver for Applications to Flapping Flight. under review, Computers and Fluids 2008.

[24] Gopalakrishnan, P. and Tafti, D. K. A Parallel Multiblock Boundary Fitted Dynamic Mesh Solver for Simulating Flows with Complex Boundary Movement. AIAA 38th Fluid Dynamic conference, Seattle, Washington June 2008; AIAA-2008-4142.

[25] Lai, J. C. S. and Platzer, M. F. Jet Characteristics of a Plunging Airfoil. AIAA JOURNAL 1999;37:1529-1537.

[26] Heathcote, S., Wang, Z., and Gursul, I. Effect of Spanwise Flexibility on Flapping Wing Propulsion. 36th AIAA Fluid Dynamics Conference and Exhibit, San Francisco, California 2006.

[27] Chong, M. S., Perry, A. E., and Cantwell, B. J. A General Classification of Three-Dimensional Flow Fields. Phys. Fluids A 1990;2:766-777.

Chapter 5: Effect of Wing Flexibility on Lift and Thrust Production in Flapping Flight[‡]

Abstract

In bird and insect flight, wing morphing plays a critical role in improving their aerodynamic performance. The wing deformation is produced by neuromuscular control and/or by aeroelasticity effects. The focus of the current study is evaluating the effects of wing deformation by using a linear elastic membrane model. Different membrane pre-stresses are investigated to give a desired camber in response to the aerodynamic pressure. All simulations are carried out at Re=10,000 for a forward flight with advance ratio of 0.5. The results show that the camber introduced by a flexible wing increases the thrust and lift production considerably. Analysis of flow structure reveal that for flexible wings, the leading edge vortex stays attached on the top surface of the wing and glides along the camber and covers a major part of the wing, which results in high force production. On the other hand, for rigid wings the leading edge vortex lifts off from the surface resulting in low force production. Further, introduction of camber increases the force component contributing to thrust leading to high thrust to lift ratio. A 40% increases in thrust is observed for the low-pre-stress case which results in a camber of thickness 0.25 chord. However, for the low pre-stress case, the wing deformation is highly non uniform. Hence to improve the uniformity of cambering, analyses with different pre-stresses along the chordwise and spanwise directions are carried out. The results show that the wing with a high spanwise pre-stress and low chordwise pre-stress offers better aerodynamic performance, both in terms of force production and uniform cambering.

Nomenclature

$\vec{a}^{i}$ = Contravariant basis vectors

C = Airfoil chord length

C_L = Coefficient of lift

[‡] This chapter is submitted to AIAA Journal on Jun 2008, and is currently under review.

C_T = Coefficient of thrust

f = Frequency of flapping

f_0 = fD/U_∞. Non-dimensional frequency of cylinder

$F_{x/y}$ = Force acting on the wing; suffix x, y- direction

g^{ij} = Contravariant metric tensor

$\sqrt{g}$ = Jacobian of the transformation

$\sqrt{g}U^j$ = Contravariant flux vector

$\sqrt{g}U^j_g$ = Contravariant flux due to grid movement

h = wing thickness

J = Advance ratio; U_∞/U_f; Ratio of the flight velocity to the flapping velocity

N_ξ = pre-stress along the chord

N_ζ = pre-stress along the span

$N_{\xi\zeta}$ = pre-stress in shear

p = Pressure

$P_{x/\zeta}$ = Power required; suffix x- flapping and ζ - rotation

R = Semi-wingspan; distance from flapping axis to wing tip

Re = Reynolds number; $U_f C/\nu$

Re_t = Inverse of the turbulent viscosity

u_i = Cartesian velocity vector

u_i^g = Cartesian Grid velocity vector

U_∞ = Free stream velocity; Forward flight velocity

U_f = Flapping velocity; $2\Phi fR$

w = Out of plane deformation

$\vec{x}$ = Physical space coordinate

$\vec{\xi}$ = Computational space coordinate

$\alpha_{u/d/eff}$ = Angle of attack; suffix u-upstroke, d-downstroke, and eff-effective

β = Stroke plane angle

η_{prop} = Propulsive efficiency

ϕ = Flapping amplitude

Φ = Total flapping amplitude (max to min)

ν = Kinematic viscosity

ρ = Torsional angle

ρ_a = density of air

ρ_w = density of wing

τ = Shear stress on the surface of the wing

ω_ζ = vorticity; suffix – ζ component

Ω_ζ = Angular velocity of the wing; suffix – ζ component

5.1 Introduction

Flapping flight utilizes unsteady aerodynamic mechanisms to generate thrust and lift effectively at low Reynolds number regime, where the performance of conventional fixed wing airfoils is limited. This merit of the flapping flight is highly suitable for Micro Air Vehicles (MAVs), which by requirement are compact with dimensions less than 15-20 cm and flight speeds of around 10-15 m/s with gross takeoff weights of 200g or less and operates in the low Reynolds number (10^4-10^5) regime. At these low Reynolds numbers, the aerodynamic efficiency (lift to drag ratio) of conventional fixed airfoils deteriorates rapidly[1]. The chief reason for the deterioration in performance is that at low Reynolds numbers, the boundary layer remains laminar downstream of the location of minimum pressure on the airfoil making it very susceptible to flow separation as the angle of attack increases resulting in an early onset of stall (Carmichael[2]). In addition, for low aspect ratio wings, the tip vortex covers a major part of the wing and the aerodynamic performance is affected greatly by the shedding of the tip vortices (Pelletier et al.[3]). On the other hand, birds and insects whose flight regime coincides with that of MAVs use flapping flexible wings to overcome the disadvantages of steady aerodynamics. They do this by taking advantage of complex wing kinematics evolved over millions of years. The kinematics involved in normal flapping flight is divided into two translation motions corresponding to up and down strokes and two rotational motions (pronation and supination) corresponding to stroke reversals. Pronation is done before the downstroke

and supination is done before the upstroke. Figure 5.1 shows the critical kinematic parameters of flapping flight with their definitions given in Table 5.1.

Table.5.1 Kinematic parameters and non-dimensional numbers for flapping flight

Parameters	***Description***
Stroke plane	The plane defined by three points: wing base (B), and the wingtip at maximum (T_T) and minimum angular position (T_B). During hovering, the stroke plane will be near horizontal and during forward flight, it will be vertical.
Stroke plane angle, β	Angle between the stroke plane and the horizontal plane. It ranges from 0^o for hovering to 90^o for forward flight.
Angle of attack, α	Angle between the wing direction (from trailing edge to leading edge) and the direction of motion.
Torsional angle, ρ	Angle between the wing direction and the direction perpendicular to stroke plane.
Flapping amplitude, ϕ	Angle between the leading edge of the wing and the horizontal plane.

In addition to simple kinematics, birds and insects employ large-scale morphing of their wing geometries to improve the aerodynamic efficiency. The geometric variation comes through neuromuscular control and/or due to aeroelasticity of flexible wings. Wang et.al.[4] measured the kinematics of dragonfly flight for forward and maneuvering flight conditions. Their results showed that the camber varies significantly from -0.1 to 0.12 due to wing flexibility during a flapping cycle. They also conducted flow analysis of a 2D dragonfly model with and without camber variation and showed that camber significantly affects the lift production. The study on hovering of a hummingbird by Warrick et.al.[5] showed the importance of camber on lift generation. Despite the kinematic symmetry of upstroke and downstroke, the humming bird generates 75% of lift during the downstroke due to a positive camber and generates only 25% of lift during the upstroke as it does not reverse the camber (into negative). Liu et al.[4] measured the wing geometry and kinematics of seagull, merganster, teal and owl and they observed

that the wing sections are highly cambered (0.085C) and are similar to low Reynolds number airfoils S1223.

5.1.1 Unsteady Aerodynamics of Flapping Flight

A number of unsteady aerodynamic mechanisms such as clap and fling[6], delayed stall[7,8], wake capturing[9], and, rotational circulation[9] have been proposed to explain the generation of lift in birds and insects. Among these, the delayed stall mechanism involves the formation of a steady Leading Edge Vortex (LEV) and is the primary mechanism used by most birds and insects for production of lift and thrust during the translational period. During the downstroke, air swirls around the leading edge and forms a LEV. This LEV increases the bound vortex circulation and hence the lift. In a fixed airfoil, the formation of LEV leads to dynamic stall within 3-4 chord lengths of travel. However in insects, the LEV is stable for the entire downstroke and during this period, the insect covers a distance of more than 8 chord lengths.

The stability of the LEV plays an important role in the superior performance of birds and insects. Many experimental studies have evaluated the duration and stability criteria of the LEV. Dickinson and Gotz[7] analyzed the effect of angle of attack during the translation period on lift and drag production using a two dimensional wing model (Re =192). They found that the LEV was generated at an angle of attack above 13.5^{o} due to impulsive movement and stayed attached for 2 chord lengths of travel. The presence of the LEV resulted in an 80% increase in lift similar to that of a detached vortex lift for a delta-wing aircraft. The shedding of the LEV led to the formation of a secondary vortex of opposite sign near the trailing edge correlating with a decrease in lift. Further, the study found that up to an angle of attack of 54^{o}, the lift characteristics remain unaltered by the change of camber. Wang et al.[10] compared the results obtained from 2D numerical simulations of a hovering fruit fly with 3D results from a dynamically scaled mechanical model (Re =75 to 115). They found that the numerical results matched well with 3D results for cases with a short downstroke length. In the case of hovering insects, the stroke length is only 3 to 5 chords, during which the LEV remains attached to the wing even for 2D cases. When the downstroke is longer than a typical stroke length, the

2D cases showed a phase difference with 3D results and resulted in lower lift coefficients.

Ellington[11] conducted flow visualization studies using a large mechanical model of hawkmoth, *flapper* (Re~4000). An intense LEV on the downstroke at all flight speeds (0.4 to 5.7 m/s) was observed. The LEV spiraled out towards the wingtip with high spanwise velocity comparable to the flapping velocity, which stabilized the vortex. The flow structure obtained was similar to the conical leading edge vortex found in delta-wings. They suggested that the strong spanwise flow was created either by the pressure gradient, formed due to velocity gradient along the flapping wing, or by centrifugal acceleration in the boundary layer, or by the induced velocity field of the spiral vortex lines. Liu et al.[12] analyzed flapping flight of hovering hawkmoth at Re =3000 to 4000 using finite volume method. The study showed the formation of the LEV during both the upstroke and downstroke, which stayed attached to the wing during the entire translational and following rotational motions. The combined translation and rotation deformed the vortex, which led to shedding of the LEV at the start of the next translation motion. The spanwise flow, created due to a spanwise pressure gradient stabilized the LEV till 70% of the span. During the second half of the downstroke, a secondary LEV is formed at 75% span, which is unstable and affected strongly by the presence of the tip vortex. The LEV formed during the upstroke was weak and attached closely to the leading edge. The study showed that the lift force was produced mainly during the entire downstroke and the later part of the upstroke.

Dickinson et al[9] conducted flow visualization studies using a dynamically scaled version of a hovering fruit fly, *robotic fly* at Re =136. They compared the force coefficients obtained by the *robotic fly* with a 2d model wing and found that the 3D model produced high average lift and thrust coefficients. The experimental investigation of Birch and Dickinson[13] provided contrasting proof for the stability of the LEV at low Reynolds number (100-250) relevant to small insect flights. They conducted experiments with fences and baffles on the top surface of the wing and showed that the LEV remains attached to the wing despite the absence of spanwise flow. They proposed that the downward velocity created by the tip vortices limits the growth and subsequent

detachment of the LEV. Birch et al.[14] investigated flow structures and forces generated at low and high Reynolds number (Re =120 and 1400). In both cases, a stable LEV was present throughout the downstroke. At Re =1400, they observed strong spanwise flow within the core of the LEV, with velocities 150% that of the flapping velocity. The spanwise flow removed the vorticity into the wake and resulted in a spiral LEV similar to that observed by Ellington[11]. However at Re = 120, the spanwise flow was absent, which resulted in lower forces. Miller and Peskin[15] studied the effect of Reynolds number (8 to 128) on the formation of the LEV using the immersed boundary technique. At Re < 32, the LEV (negative pressure region) and trailing edge vortices (positive pressure region) remain attached, which resulted in lower lift. At Re > 64, they observed shedding of the trailing vortex during translation, which resulted in vortical asymmetry, leading to high lift production.

Tarascio et al.[16] conducted a flow-visualization experiment on a hovering flapping flight model at Reynolds number of the order of 8000. The flow field consisted of folded wakes formed by the strong starting vortex shed at the end of each half stroke during the wing rotation. Due to the induced flow, the wakes were pushed downwards parallel to the flapping plane. The key finding of this study was that during translation, the top surface was covered by multiple vortices and the LEV was continually generated and shed into the wake. This result is in contrast to previous studies[9,11], where a stable single LEV is present during translation. Further, they observed that the strength of the LEV increased along the span and identified separated flow at the outboard region of the wing.

5.1.2 Flexible wings and Aeroelasticity analysis

Wing morphing of birds and insects significantly affect the unsteady mechanisms and the force production. For numerical analysis of their effects, a solver capable of solving both fluid and structural equations is necessary. In this section, a brief review of previous studies focused on aeroelastic analysis related to MAVs, both fixed and flapping wings are provided. Shyy et al.[17] and Ho et al.[18] provided a detailed review of performance of flexible *fixed* wings for MAVs. Shyy et al.[19] analyzed stationary airfoil performance at Reynolds number of 7.5×10^4 in a sinusoidal freestream with three different types of flexibility; rigid, flexible and hybrid. The initial camber of all airfoils was fixed at 6^0. In

the case of the flexible airfoil, the camber was allowed to change above and below the initial camber, while in the case of the hybrid airfoil, a decrease in camber was prevented by a wire construction beneath the flexible membrane. The results showed that the flexible airfoil had a higher sensitivity to freestream fluctuation and produced higher lift-to-drag ratio than the fixed airfoils at high velocities. However, the camber of the flexible membrane collapsed at low velocity due to freestream fluctuations, which resulted in massive separation over the whole surface. On the other hand the hybrid airfoil with low camber value fixed was less sensitive to freestream fluctuation and produced superior performance at all flow velocities. Shyy et al.[20] analyzed the effect of a flexible membrane placed on top of the Clary-Y airfoil on the aerodynamic performance. The flexible membrane adjusted the profile based on the fluctuation of the freestream, which resulted in better performance.

Smith[21] included the aeroelastic effects while analyzing tethered moth flapping flight using an unsteady panel method. He modeled the veins in the wing as three-dimensional tubular beam elements and the wing surface as a quadrilateral orthotropic plane stress membrane. The unsteady panel method employed did not account for the separation at the leading edge, which resulted in a deviation of the computed force from experimental results. Ho et al.[18] compared the aerodynamic performance of a cicada wing, which is rigid along the spanwise direction with a flexible titanium alloy wing without leading edge support. The results showed that the stiffness along leading edge is critical for the stability of the LEV, as the cicada wings produced higher lift than the flexible wing. They also showed that the stiffness distribution is a key parameter in defining vortex interaction and thrust production. Their results showed that high stiffness is required at the outboard region of the wing to enhance lift and flexibility required in the inward region for producing thrust.

Stanford et. al[22,23] analyzed the flexible membrane effect on a fixed airfoil by both experiments and numerical modeling. They modeled the membrane as inextensible using linear stress-stiffening model. The linear stress-strain assumption holds good, since the strain accumulated due to aerodynamic load was small in comparison with the pre-strain of the membrane. Their results showed that the efficiency of the rigid wing increased

with Reynolds number, where as it dropped for the flexible membrane as it provided a non-optimal airfoil shape at high Reynolds number. Stanford et. al[24] analyzed flow over a flexible fixed wing using a static aeroelastic model by coupling a laminar flow solver and structural membrane solver. They compared the numerical results with experiments and showed that the numerical model failed to predict the exact location of separation and reattachment. They identified that the unsteady nature of the flow, turbulence effects, and membrane wrinkling are the primary reason for poor performance of the static aeroelastic model.

Previous research on flapping flights has focused mainly on the aerodynamics of rigid wings. However, kinematic studies show that birds and insects undergo significant wing morphing to improve the aerodynamic efficiency. In addition, studies related to the effect of flexibility show that flexible wings offer better performance than rigid wings. Hence, it is crucial to examine the effect of wing flexibility for flapping flights. The present study addresses this issue by analyzing flapping flight for a flexible wing at Re=10,000. The study employs a linear elastic membrane solver coupled with unsteady Large Eddy simulation (LES) flow solver to analyze the flapping flight. The wing is considered as an elastic membrane with in-plane pre-stresses. The pre-stresses of the wing are tailored to get the required camber and their effect is analyzed based on changes in flow structure and variation of thrust and lift.

5.2 Methodology

5.2.1 Flow solver

The governing equations for unsteady incompressible viscous flow in a moving grid coordinate system consist of space, mass, and momentum conservation laws. The equations are mapped from physical $(\vec{x})$ to logical/computational space $(\vec{\xi})$ by a boundary conforming transformation $\vec{x} = \vec{x}(\vec{\xi})$, where $\vec{x} = (x, y, z)$ and $\vec{\xi} = (\xi, \eta, \zeta)$. The equations are non-dimensionalized by chord length (C) and flapping velocity (U_f) and written in conservative nondimensional form as:

Space:

$$\frac{\partial}{\partial t}\left(\sqrt{g}\right)-\frac{\partial}{\partial \xi_j}\left(\sqrt{g}U_g^j\right)=0 \tag{5.1}$$

Mass:

$$\frac{\partial}{\partial \xi_j}\left(\sqrt{g}U^j\right)=0 \tag{5.2}$$

Momentum

$$\frac{\partial}{\partial t}\left(\sqrt{g}u_i\right)+\frac{\partial}{\partial \xi_j}\left(\left[\sqrt{g}U^j-\sqrt{g}U_g^j\right]u_i\right)$$

$$=-\frac{\partial}{\partial \xi_j}\left(\sqrt{g}(\vec{a}^j)_i p\right)+\frac{\partial}{\partial \xi_j}\left(\left(\frac{1}{\mathrm{Re}}+\frac{1}{\mathrm{Re}_t}\right)\sqrt{g}g^{jk}\frac{\partial u_i}{\partial \xi_k}\right) \tag{5.3}$$

where $\vec{a}^i$ are the contravariant basis vectors, $\sqrt{g}$ is the Jacobian of the transformation, g^{ij} is the contravariant metric tensor, $\sqrt{g}U^j=\sqrt{g}\left(\vec{a}^j\right)_k u_k$ is the contravariant flux vector, $\sqrt{g}U_g^j=\sqrt{g}\left(\vec{a}^j\right)_k u_k^g$ is the contravariant flux vector due to grid velocity u^g, u_i is the Cartesian velocity vector, and *p* is the pressure. In the above formulation, the grid velocity u^g is not used explicitly. Instead, the grid contravariant flux vector is employed which is directly computed based on the SCL. The non-dimensional time used is $t^* U_f/C$ and the Reynolds number is given by $U_f C/\nu$. Re_t is the inverse of the subgrid eddy-viscosity which is modeled as

$$\frac{1}{\mathrm{Re}_t}=C_s^{\,2}(\sqrt{g})^{2/3}\left|\bar{S}\right| \tag{5.4}$$

where $\left|\bar{S}\right|$ is the magnitude of the strain rate tensor given by $\left|\bar{S}\right|=\sqrt{2\overline{S_{ik}}\,\overline{S_{ik}}}$ and the Smagorinsky constant C_s^2 is obtained via the dynamic subgrid stress model (Germano et

al.[25]). To this end, a second test filter, denoted by $\hat{G}$, is applied to the filtered governing equations with the characteristic length scale of $\hat{G}$ being larger than that of the grid filter, $\overline{G}$. The test filtered quantity is obtained from the grid filtered quantity by a second-order trapezoidal filter which is given by $\hat{\phi} = \frac{1}{4}(\overline{\phi}_{i-1} + 2\overline{\phi}_i + \overline{\phi}_{i+1})$ in one dimension of computational coordinates. The resolved turbulent stresses, representing the energy scales between the test and grid filters, $L_{ij} = \widehat{\overline{u_i}\overline{u_j}} - \widehat{\overline{u}_i}\widehat{\overline{u}_j}$, are then related to the subtest, $T_{ij} = \widehat{\overline{u_i}\overline{u_j}} - \widehat{\overline{u}_i}\widehat{\overline{u}_j}$, and subgrid-scales stresses $\tau_{ij} = \overline{u_i u_j} - \overline{u}_i\overline{u}_j$ though the identity, $L_{ij}^a = T_{ij}^a - \hat{\tau}_{ij}^a$ The anisotropic subgrid and subtest-scale stresses are then formulated in terms of the Smagorinsky eddy viscosity model as:

$$\widehat{\tau_{ij}^a} = -2C_s^2(\sqrt{g})^{\frac{2}{3}}\widehat{|\overline{S}|\overline{S}_{ij}} \tag{5.5}$$

$$T_{ij}^a = -2C_s^2\alpha(\sqrt{g})^{\frac{2}{3}}\widehat{|\overline{S}|}\,\widehat{\overline{S}_{ij}} \tag{5.6}$$

Using the identity

$$\widehat{L_{ij}^a} = \widehat{L_{ij}} - \frac{1}{3}\delta_{ij}L_{kk} - 2C_s^2\left(\sqrt{g}\right)^{\frac{2}{3}}\left[\alpha\,\widehat{|\overline{S}|}\,\widehat{\overline{S}_{ij}} - \widehat{|\overline{S}|\overline{S}_{ij}}\right] = -2C_s^2\left(\sqrt{g}\right)^{\frac{2}{3}}M_{ij} \tag{5.7}$$

Here α is the square of the ratio of the characteristic length scale associated with the test filter to that of grid filter and is taken to be $\left[\hat{\Delta}_i / \overline{\Delta}_i = \sqrt{6}\right]$ for a representative one-dimensional test filtering operation. Using a least-squares minimization procedure of Lilly, a final expression for $C_s^{\,2}$ is obtained as:

$$C_s^{\,2} = -\frac{1}{2}\frac{1}{(\sqrt{g})^{2/3}}\frac{L_{ij}^a \bullet M_{ij}}{M_{ij} \bullet M_{ij}} \tag{5.8}$$

The value of $C_s^{\,2}$ is constrained to be positive by setting it to zero when $C_s^{\,2} < 0$.

5.2.2 Elastic Membrane Model

The wing is modeled as a linear elastic membrane structure which is pre-stressed by stretching at its boundaries. The out of plane deformation is computed using the non-dimensional dynamic membrane equation[26] in the wing reference coordinate (Fig.5.2a)

$$N_{\xi}\frac{\partial^2 w}{\partial \xi^2}+2N_{\xi\zeta}\frac{\partial^2 w}{\partial \xi \partial \zeta}+N_{\zeta}\frac{\partial^2 w}{\partial \zeta^2}+p=\rho_w h_w\frac{\partial^2 w}{\partial t^2} \tag{5.9}$$

where, w is out of plane displacement, p is the applied aerodynamic differential pressure across the wing, ρ_w is density of the wing, h_w is thickness of the wing, and N_{ξ}, N_{ζ} and $N_{\xi\zeta}$ are in-plane pre-stresses along the chordwise, spanwise, and in shear, respectively. The equation is non-dimensionalized with the same characteristic parameters, chord length and flapping velocity used for the flow solver. The pre-stresses are normalized by $\rho u_f^2 C$ and $\rho_w h_w$ is normalized by $\rho_a C$. In practice, the linearity assumption employed in Eq.5.9 is strictly valid only if the strain accumulated by the deformation is small in comparison to the pre-strain in the membrane. However, for simplification the present study employs a linear assumption for all the prestress values studied. Further, the inertial forces due to flapping are not considered in the current study.

5.2.3 Coupling

An explicit time advancement method using the latest available information is employed for coupling between the flow solver and the membrane solver. For each fluid time step the membrane deformation is of O (1×10^{-4}) and has no significant effect on the flow and pressure distribution. The steps involved in coupling are

1. The flow is advanced to time level n+1 with known deformation values at n.
2. The pressure values are transferred from the fluid solver to the membrane solver. Since the same grid distribution is used for both solvers, no interpolations are necessary.
3. The membrane solver is advanced using the pressure values at n+1 level and known deformation at level n and n-1. A second order central difference at time level n is employed for both spatial and temporal derivatives.

4. The deformation values are then transferred to the flow solver.
5. The steps 1 to 4 are repeated for the next time advancement.

5.3 Results

The main focus of the study is to evaluate the effects of aeroelastic cambering on flow structures and aerodynamic performance. To estimate their effect, simulations with different pre-stresses (cases A-C) as given in Table 5.2 are carried out and the resulting performance is compared against that of a rigid wing. The pre-stress values (N_ξ and N_ζ) are tailored to obtain the camber in the order of 0.05 to 0.25 chord and the pre-stress in shear $N_{\xi\zeta}$ is kept at zero for all the simulations. In addition, the different pre-stresses are used in the spanwise and chordwise directions to analyze their effects on the performance. All the simulations are carried out at Re=10,000 and at advance ratio J=0.5, which corresponds to a flapping velocity U_f of 8 m/s and a forward (freestream) velocity U_∞ of 4m/s for a wing with semi-wing span of 8 cm. For aeroelastic analysis, the material properties of light weight ornithopter[27] wings are used. The ornithopter wings are made of titanium alloy ρ_w = 4500 kg/m^3 with thickness, h_w of 15 μm. A zero displacement boundary condition is specified at all edges of the wing.

Table.5.2 Membrane prestress used for the analysis

Simulation	**N_ξ N/m**	**N_ζ N/m**
Fixed	N/A	N/A
Case -A	8	8
Case -B	4	4
Case -C	2	2
Case -D	2	8
Case -E	8	2

5.3.1 Wing Configuration and Kinematics

A rectangular wing with chord length of 2cm and aspect ratio of 4 from base to tip as shown in Fig.5.2a is used for the analysis of flapping flight. The pitching axis is placed at one fourth of the chord length from the leading edge. The coordinate (x,y,z) is used for

the fixed frame, where the y-z plane represents the stroke plane (Fig.5.1). The coordinates (ξ,η,ζ) are used for the moving frame fixed with the wing, where ξ is along the chordwise direction, η is perpendicular to the wing, and ζ is along the spanwise direction (Fig.5.2a). For the kinematics, a sinusoidal variation of flapping angle and torsional angle as shown in Fig.5.2b is provided. The selection of kinematics is based on results from our previous analysis on the effect of rotation kinematics[28,29], which showed that a continuous rotation results in high thrust. The movement of the wing tip for the prescribed kinematics is shown in Fig.5.3a. During the start of the translation, the angles of attack is close to 90^o and it drops during the first half to its lowest value and increases to the initial value during the second half of the translation. The angle of attack during the middle of downstroke is 75^o and during upstroke it is 45^o. A lower value of angle of attack during upstroke is used to reduce the downward force. The effective angle of attack depends on flapping velocity, free stream velocity and prescribed angle of attack (α_u, α_d) as shown in Fig.5.3b. Due to the variation in flapping velocity (U_f), the effective angle of attack also varies along the span with a maximum value being at the tip. The other kinematics parameters used are stroke amplitude, 60^o ($\pm 30^o$) and stroke plane angle, $\beta=90^o$.

5.3.2 Computational grid and Validation

The grid is made of 60 blocks with approximately 6.5 million cells. The flow domain is defined from 10 chord lengths upstream of the leading edge and extends 15 chord lengths downstream from the trailing edge. In the direction normal to the wing, the flow domain extends 10 chord lengths on either side and in the spanwise direction from the tip. A constant velocity boundary condition is applied at all inlet faces and an outflow boundary condition is specified at the downstream boundary. The symmetry condition is applied along the flapping axis at the base of the wing. The wing is resolved using 80x40 grid points and 80 grid points are used perpendicular to the wing as shown in Fig.5.4. A grid refinement study is carried out by increasing the number of points along the perpendicular direction from 80 to 120. The comparison of instantaneous lift and thrust forces in Fig.5.5 do not show any perceptible difference and the mean values of lift and thrust differ by less than 1%. More validation related to the dynamic mesh capability of

the solver is available in our previous studies[30,31]. Further, an analysis of a hovering fruitfly was also carried out[29] and the resultant forces show good comparison with experimental results.

5.3.3 Rigid Wing Performance

Before analyzing the effect of the flexible membrane on performance, critical flow structures obtained for a rigid wing are presented in this section. The results obtained during the fourth flapping cycle are used for the analysis.

5.3.3.1 During downstroke

The isosurface of vorticity along the spanwise direction in wing reference frame ω_ζ, at different times is given in Fig.5.6. The isosurfaces show the formation of the LEV (negative vorticity) and its subsequent separation during the downstroke. At t* = 0.05, a spiral LEV with its size gradually increasing from base to tip forms and it is attached on the top surface of the wing. The size of the LEV grows with time until its separation. At t*=0.2, the spiral LEV is the strongest which results in a peak in lift (Fig.5.5). The pressure contours and streamlines in the chordwise plane, ζ=3 at different times in Fig.5.7 show detailed slices of the LEV evolution and separation. The LEV starts to lift away from the wing as early as t* of 0.1 and its separation leads to the formation of multiple secondary LEVs. The secondary LEVs also lift away from the surface of the wing and the pressure contours show the detachment of the LEV (low pressure region) and increase in pressure on the surface of the wing by the entrainment of freestream fluid. The isosurfaces of vorticity show that the LEV near the base is attached for most of the downstroke whereas the LEV near the tip sheds and completely dissipates into the flow during the end of downstroke (t*=0.4 to 0.5). The vorticity contours also show the growth a Trailing Edge Vortex (TEV) during the downstroke with its maximum size near the tip. The TEVs are also shed at the end of downstroke (t*=0.4 to 0.5) and dissipate into the flow.

To analyze the structure of the LEV, particle traces are obtained by releasing particles along the leading edge. The particle traces at t*=0.25, Fig.5.8a, show a spiral LEV attached near the base and lifted from the wing near the tip. The spanwise velocity v_ζ

contours along the center of the LEV, Fig.5.8b, show a strong positive velocity of the order of the flapping velocity from the base to the tip. Similar results were obtained by the flow visualization studies conducted by Ellington[11] using a large mechanical model of hawkmoth, *flapper* at (Re~4000). They showed a spiral LEV with a spanwise velocity comparable to the flapping velocity during the downstroke and also suggested that the spanwise flow removed the vorticity from the LEV and stabilized it. However, the present results show that despite the presence of the spanwise flow, the LEV separates from the wing as early as t* of 0.1. We surmise that the presence of strong negative spanwise velocity due to the tip vortex shown by the curved arrow (Fig.5.8b) is the primary reason for the separation of the LEV, as it prevents the removal of vorticity from the LEV. Vorticity starts building up near the tip, both due to the high angle of attack and convection of vorticity from the base. This increase in vorticity leads to an instability in the LEV and its separation from the wing.

5.3.3.2 During upstroke

The behavior of flow during the upstroke is similar to that during the downstroke. During the upstroke, the angle of attack is low and the effective angle of attack is negative only for a small portion of the wing near the tip. Hence there is no clear formation of the LEV on the bottom surface and the vorticity contours (Fig.5.6) show only a small positive vortex attached near the tip. The streamlines and pressure contours, Fig.5.7, show no apparent vortex formation at locations ζ=3.0. A small low pressure region at around t* =0.8 and the presence of multiple small LEVs are observed. This low pressure region results in a peak in negative lift and also generates thrust (Fig.5.5). These LEVs become unstable and shed during the end of upstroke.

5.3.4 Effect of Flexible Wing

To analyze the effects of aeroelastic deformation on the flow structure, three simulations (cases A-C) with different pre-stresses are carried out. The deflection for the cases ranges from 0.05 to 0.25 chord. For maximum thrust production, positive deflection during the downstroke and negative deflection during the upstroke are preferred. Figure 5.9 shows the deformation contour at different times for all three cases. During the downstroke, the deformation is positive which introduces a positive camber and the

maximum value near the tip corresponds to the location where the size of the LEV and the pressure difference across the surface are maximum. In case of pre-stresses 8 and 4 N/m the camber reaches a maximum during the middle of the downstroke (at t* =0.25) and the deformation introduces a uniform camber structure. In case of low pre-stress condition 2 N/m, the deformation at the start of downstroke is non-uniform, having negative displacement near the base and positive displacement near the tip. The negative displacement forms due to the presence of a low pressure region on the bottom surface formed during the previous upstroke. In addition, the deformation during the middle of the downstroke introduces an uneven camber due to the separation of the LEV.

During the upstroke, a negative camber forms for all the simulations and its maximum value is lower than that during the downstroke due to a low angle of attack. The time of formation of negative camber differs significantly between the three cases. In case of high pre-stress the maximum camber occurs at around t* of 0.75 while it is t* =0.85 and t* =0.95 for cases B and C, respectively, as the pre-stress decreases. For the low pre-stress membrane, at the start of the upstroke, the deformation is positive near the base due to the presence of the unshed LEV near the base during the previous downstroke.

5.3.4.1 Effect on flow structure

The effect of camber on flow structure is shown by the vorticity contours at different times for all three cases in Fig.5.10 and the streamlines and pressure contour in a chordwise plane at ζ = 3 in Figs 5.11 to 5.13. At the start of the downstroke, the introduction of camber reduces the effective angle of attack and hence delays the formation of the LEV. This effect is prominent in the case of low pre-stress 2 N/m, where the formation of the LEV is not continuous at time t*=0.1 and the streamlines in the chordwise plane ζ= 3 show no formation of the LEV. During the first part of the downstroke, the LEV grows and starts to lift away from the surface for high pre-stress values. However for the low pre-stress case, due to the introduction of the camber the LEV does not separate from the wing, instead it glides over the camber as shown in Fig.5.13 at t* of 0.15. At t* of 0.25, the flexible wings introduce positive cambers of the order of 0.05, 0.12 and 0.25 chord for pre-stresses 8, 4 and 2 N/m, respectively. The

location of the maximum camber is near the center of the LEV. In the case of the rigid wing, the LEV separates near the tip as early as t* =0.1 and lifts off completely from the wing during the middle of the downstroke and dissipates into the flow. In the case of flexible wings, the streamlines in the chordwise plane ζ = 3 show the presence of multiple LEVs for cases A and B, while a single attached LEV is observed for case C and it covers almost half of the wing from the leading edge. The isosurface vorticity contours shown in Fig.5.10 also reflects this phenomena where the negative vorticity covers most of the wing surface. This gliding of the LEV due to the adaptive camber increases the pressure difference across the wing and results in high force production. In addition, due to the introduction of a camber the resultant force direction shifts towards the forward direction resulting in high thrust to lift ratio. At t* of 0.35, the LEV starts separating from the wing for all cases and the camber decreases with the location of maximum camber moving towards the trailing edge. During t* = 0.4 to 0.5 the LEVs dissipate into the flow and only a small portion of the LEV is attached near the base.

During the upstroke, the flexible wings introduce negative camber and the value of camber is high for low pre-stress. During the first half, a small LEV forms near the tip for all three cases and glides along the camber as shown in Figs.5.11 to 5.13 during the second half. At the end of the upstroke the vortex on the bottom surface sheds and dissipates into the flow. The flow structure obtained for the low pre-stress case differs from case A and B due to the introduction of a non-uniform camber. At the start of the upstroke, the low pre-stress has positive deformation near the base due to the unshed LEV formed during the previous downstroke. In addition, the deflection is positive near the trailing edge at t*=0.75(Fig.5.13) due to the shedding of a TEV. This results in high pressure near the trailing edge for a low pre-stress which reduces the force production.

5.3.4.2 Lift and thrust comparison

The variation of instantaneous lift and thrust coefficient, normalized based on flapping velocity and planform area is shown in Fig.5.14 for the flexible wings and the rigid wing. During the first half of the downstroke, the lift increases due to the formation of the LEV and the maximum value is obtained at around t*= 0.25 for all cases. The maximum value of the lift coefficient increases with adaptive camber and a value of

around 3 is obtained for low pre-stress. During the second half of the downstroke the lift drops due to the shedding of the LEV. During the upstroke the lift is negative and the maximum value of around 1 is obtained at t* =0.825. The peak negative value of lift for cases A and B is higher than the rigid wing. While for case C the peak value reduces due to the shedding of the TEV and formation of positive pressure near trailing edge.

The thrust produced by flapping flight is positive throughout the flapping cycle and two peaks are produced at around t* =0.25 and 0.82. The peak value increases with decreasing pre-stress and a maximum value of 1.6 is obtained for case C. The average values of thrust and lift for all simulations are listed in Table 5.2. The aeroelastic deformation increases both average values of lift and thrust and maximum values of C_T= 0.53 and C_L=0.66 are obtained for case C, which can support 248 grams and produces ~1N thrust force. The thrust and lift increases with camber and a 43% rise in thrust and 18% rise in lift are obtained for a pre-stress of 2N/m.

5.3.5 Effect of Different Pre-Stress

The analysis of flexible membrane flapping flight reveals that introduction of adaptive camber increases thrust and lift production significantly. In particular, for the low pre-stress case, an increase in thrust of the order of 40% is obtained. However, the low pre-stress case results in deformation even for small differential pressures leading to a non-uniform camber during the start of translation and during the upstroke. One way to reduce uneven camber is to introduce different pre-stresses in the spanwise and chordwise directions. Combes and Daniels[32,33] measured flexural stiffness of wings in both the spanwise and chordwise directions for 16 insect species. These measurements show that the spanwise flexural stiffness scales strongly with the cube of wing span, whereas the chordwise flexural stiffness scales with the square of chord length. Hence, to understand how different pre-stresses affects the flow, two simulations, Case D-chordwise stiff, and case E-spanwise stiff (Table 5.2) are analyzed. The pre-stress combination of 2 N/m and 8 N/m are used for both simulations. The deformation contours for case D and E are shown in Fig.5.15. In the case of chordwise stiff wing, the deformation curvature is in the spanwise direction and the maximum deformation is only 0.06 C, which is much lower than that of the low pre-stress case. The maximum

deformation is located very near the tip and the deformation is non uniform throughout the flapping cycle. In the case of spanwise stiff wing, the membrane deformation introduces a uniform camber structure and the deformation is 0.18 C which is slightly less than case C. In addition, there is no non uniformity in deformation during the start of translation as observed in case C.

The effect on the flow structure is shown by the pressure contours and streamlines in the chordwise plane at ζ=3, Fig.5.16. For chordwise stiff wings, the LEV starts to form early and separates from the wing at around t*=0.15. The streamlines during the middle of the downstroke show the lifting of the LEV and the presence of multiple LEVs. The camber produced is low and the maximum camber location is at the center of the wing. At the end of the downstroke the LEV sheds and dissipates into the flow. The camber introduced during the upstroke is very small -0.04 and the presence of a small vortex is observed during the second half of the upstroke.

In the case of spanwise stiff wing, the flow structure resembles that of the low pre-strain case. Introduction of camber reduces the angle of attack and hence delays the formation of the LEV during the start of downstroke. At t* of 0.25, a single LEV is observed in the chordwise plane and it slides over the camber and covers most of the wing surface. At this time, the maximum camber location is very close to the leading edge and it moves towards the trailing edge during the second half of the downstroke. The LEV starts to separate from the wing at around t*=0.35 and sheds into the flow. During the start of the upstroke the deformation is not large like that of the low pre-strain case. At t*=0.75, the deformation near the trailing edge is slightly positive and pressure contours do not show positive pressure on the bottom surface as observed in case C. The negative camber is smooth during the second half of the upstroke and a similar vortex gliding effect is observed.

The instantaneous variation of lift and thrust coefficients for cases D and E are compared with the low pre-strain case C. The chordwise stiff wing results in low average values of lift and thrust and have similar patterns as that of case A. The peak thrust value obtained during the middle of the downstroke is around unity for chordwise stiff while it is 1.6 for the spanwise stiff wing. The average lift value of the spanwise stiff wing

matches with that of the case C and the average thrust value is 0.5, which is slightly lower than case C. The results prove that low stiffness along the chordwise direction and high stiffness along the spanwise direction is preferable to obtain better thrust and lift characteristics and a uniform cambering effect.

Table.5.3 Average values of lift and drag, power required and propulsive efficiency

Cases	C_L	C_T	Power Flapping	Power Rotation	Propulsive Efficiency
Rigid	0.56	0.37	1.60	0.20	17.98
Case-A	0.59	0.40	1.65	0.23	18.62
Case -B	0.62	0.44	1.71	0.24	19.74
Case -C	0.66	0.53	1.88	0.21	22.19
Case -D	0.59	0.41	1.66	0.26	18.68
Case-E	0.66	0.50	1.82	0.26	21.03

5.3.6 Propulsive Efficiency

The membrane wing shows better aerodynamic performance in terms of lift and thrust. For a more comprehensive comparison, propulsive efficiencies are computed based on power required for flapping (P_x) and rotation (P_ζ) for all simulations. The power requirement is computed based on the torque generated by the fluid forces and angular velocity of the wing:

$$\begin{aligned} \mathrm{T} &= \int r \times (p + \tau)\ ds; \\ P &= T.\Omega \end{aligned} \tag{5.10}$$

where r is the radius from the axis, p is the pressure, τ is the shear stress and Ω is the angular velocity of the wing. The power required for the acceleration (inertial power requirement) of the wing is neglected as they are conservative. The instantaneous variation of power requirement (normalized based on fluid density, tip velocity and chord length, $\rho U_f^3 C^2$) for chordwise stiff case E is shown in Fig.5.19. It follows a similar trend as that of lift and thrust. The propulsive efficiency of flapping flight is computed as

$$\eta_{prop} = \frac{F_T U_\infty}{P} \tag{5.11}$$

The average values of power requirement and propulsive efficiency for all simulations are given in Table 5.3. The performance of all flexible wing configurations is better than that of the rigid wing. The low pre-stress case offers the best propulsive efficiency of 22% followed by the spanwise stiff wing with 21%.

5.4 Conclusion

The effects of aeroelastic cambering on flapping flight performance are analyzed using a linear elastic membrane model. All the simulations are carried out at Re=10,000 for forward flight with advance ratio of 0.5. The flapping flight analysis with a rigid wing shows the formation of a spiral LEV during the downstroke, which results in high thrust and lift values. However the LEV lifts off from the surface during the middle of downstroke and sheds leading to a drop in lift and thrust. There is no significant vortex formation during the upstroke due to a low angle of attack. Aeroelastic analysis of the flexible wing membrane is carried out with different pre-stresses and the deformation is computed using a linear elastic membrane model. The flexible membrane introduces a positive camber during the downstroke and a negative camber during the upstroke. The introduction of camber increases lift and thrust production and has high propulsive efficiency. The main reason for the increase in force production is attributed to the gliding of the LEV along the camber, which covers most of the wing leading to high pressure difference across the wing surface. Introduction of the camber increases the force component in the direction of flight resulting in a high thrust to lift ratio. A 40% increase in thrust and 20% increase in lift are observed for the pre-stress of 2 N/m. However, the deformation for this case is highly non uniform leading to both negative and positive deformation during the start of translation. In order to avoid a non uniform camber formation, a combination of high and low pre-stress is used for the chordwise and spanwise directions, respectively. The results from these simulations show that having low pre-stress along the chord and high pre-stress along the span offers the best aerodynamics and aeroelastic performance. The deformation contours for the spanwise

stiff wing show uniform camber formation resulting in high lift and thrust forces and high propulsive efficiency.

Acknowledgement

We would like to thank Prof. Mayuresh Patil of the Aerospace and Ocean Engineering Department at Virginia Tech for his guidance on the development of the elastic membrane model. The calculations were performed on Virginia Tech's Terascale computing facility, System-X. The allocation grant and support provided by the staff is gratefully acknowledged.

5.5 Figures

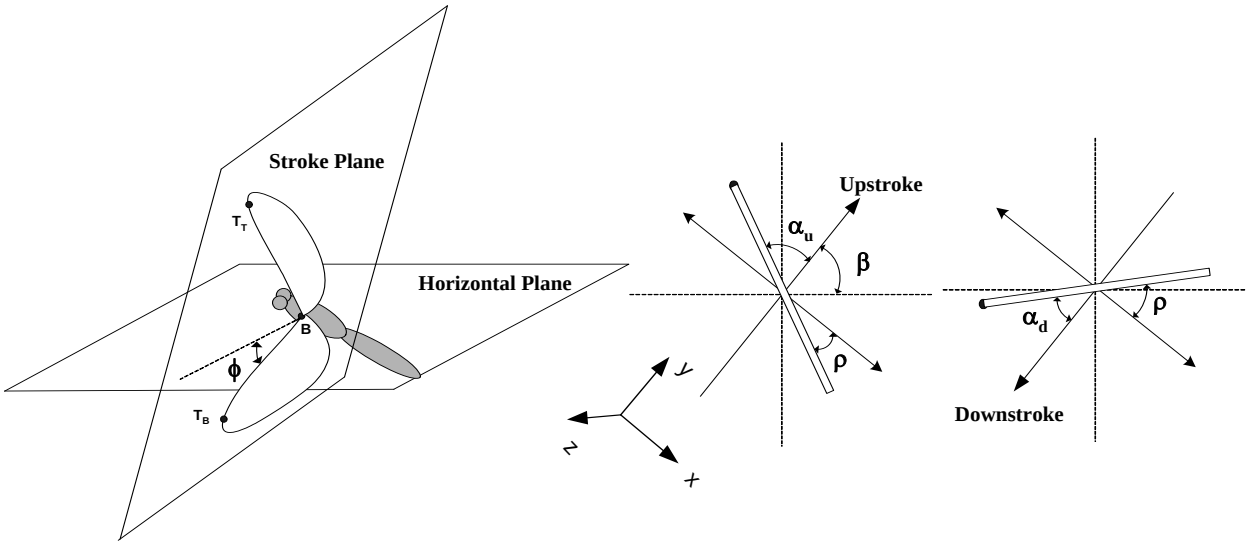

Fig.5.1 Kinematic parameters

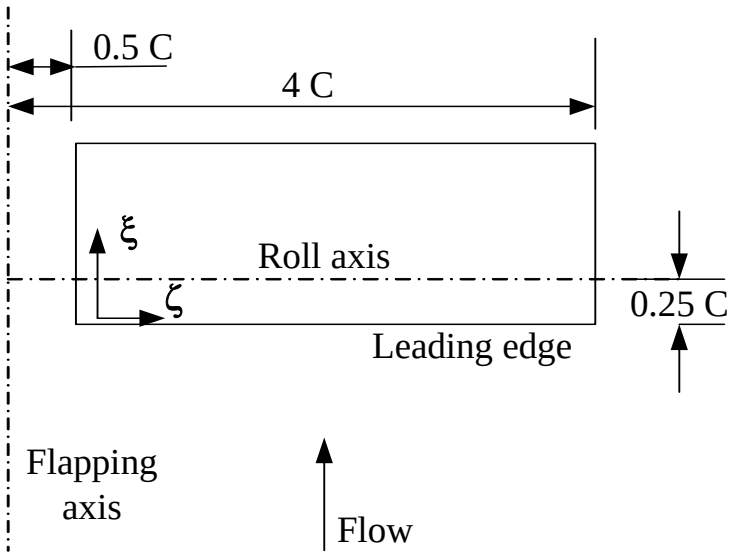

(a)

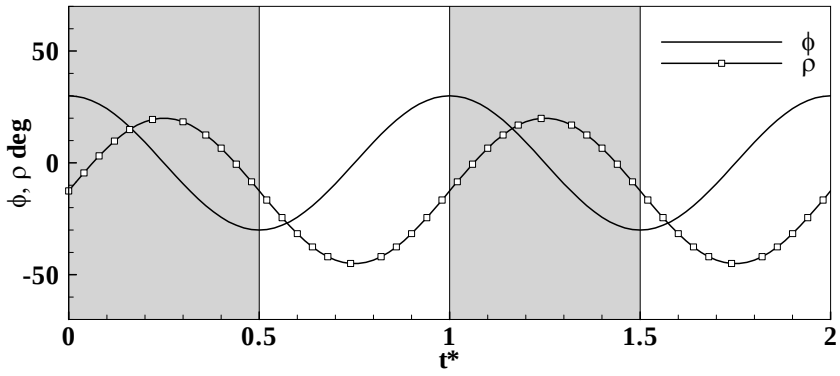

(b)

Fig.5.2 (a) Rectangular wing configuration. (b) Variation of flapping and torsional angle; shaded region represents downstroke.

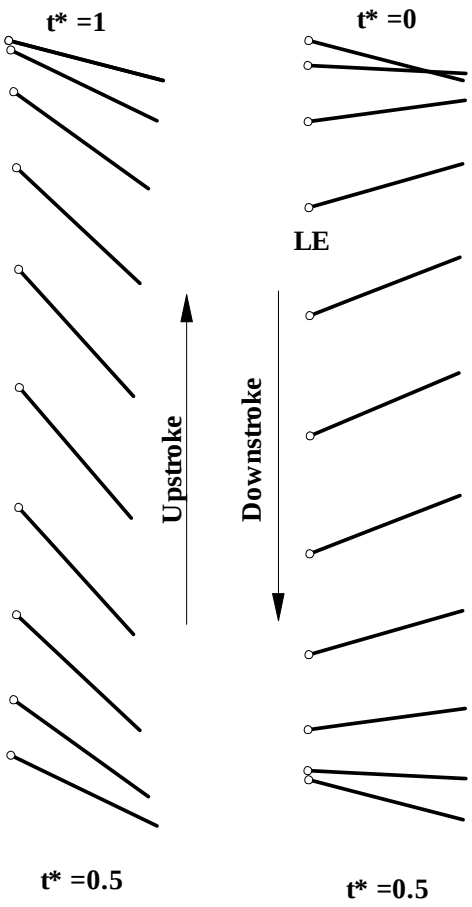

(a)

During Downstroke

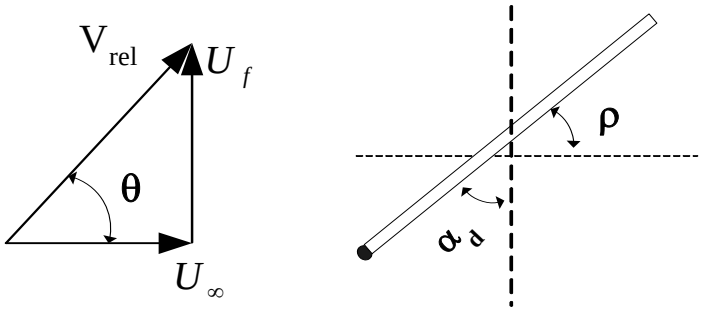

$$\theta = \tan^{-1}[U_f / U_\infty] = \tan^{-1}[1/J]$$

$$\alpha_{eff} = \theta - \rho = \theta + \alpha_d - 90^o$$

(b)

Fig.5.3 (a) wing positions at different times, (b) Effective angle of attack during downstroke

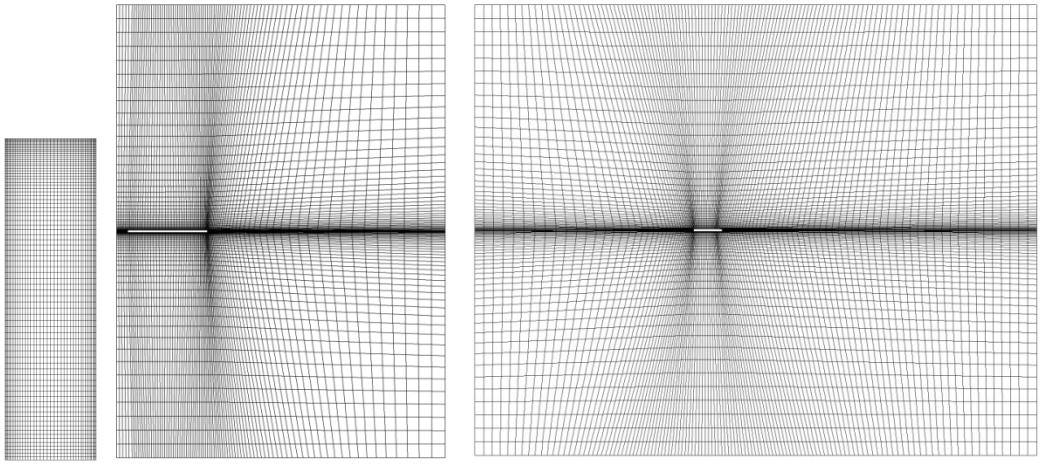

(a) **(b)** **(c)**

Fig.5.4 Grid distribution (a) wing (b) spanwise plane (c) chordwise plane (every other grid line is shown for b and c)

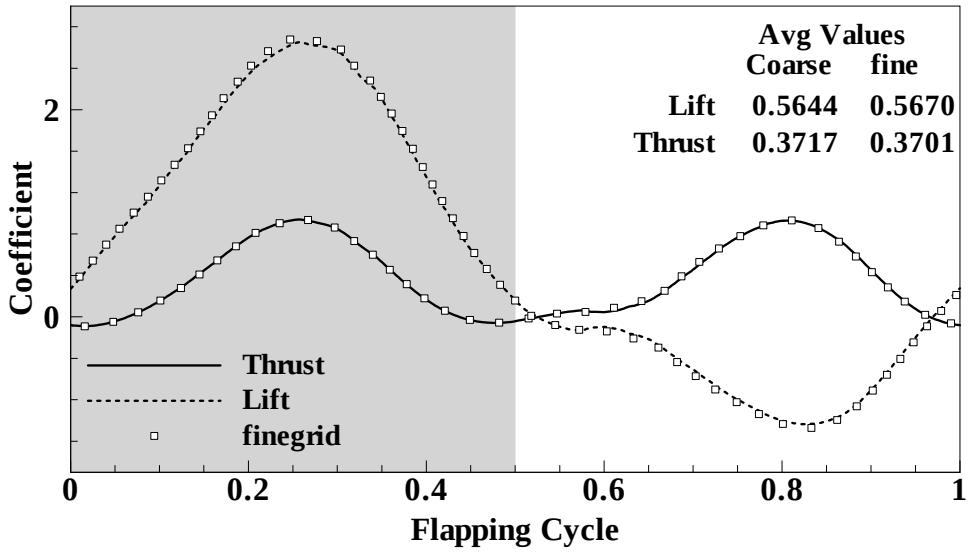

Fig.5.5 Comparison of lift and drag for different grid size

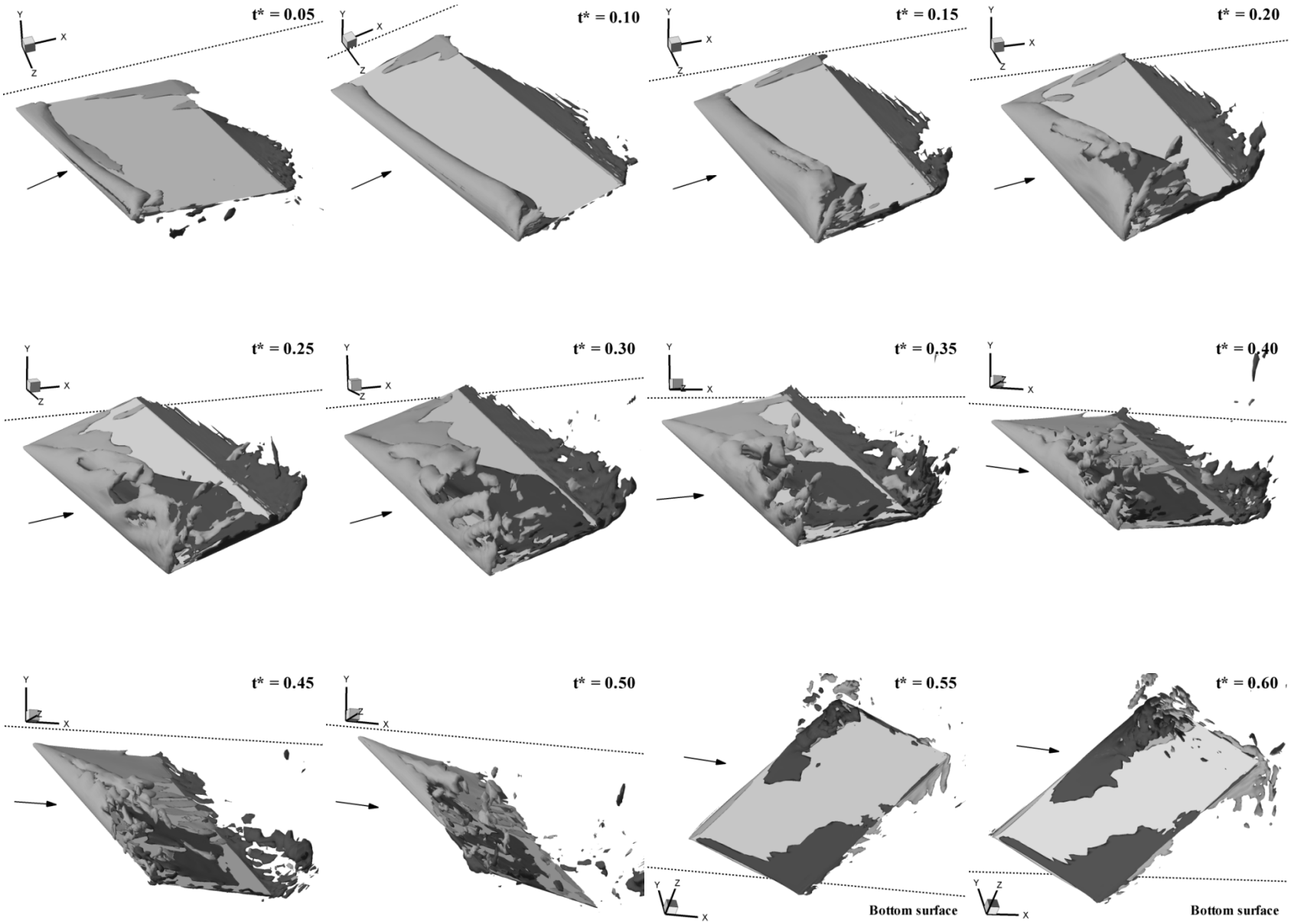

Fig.5.6 Isosurface of spanwise vorticity ω_ζ at different times for rigid wing (continued)

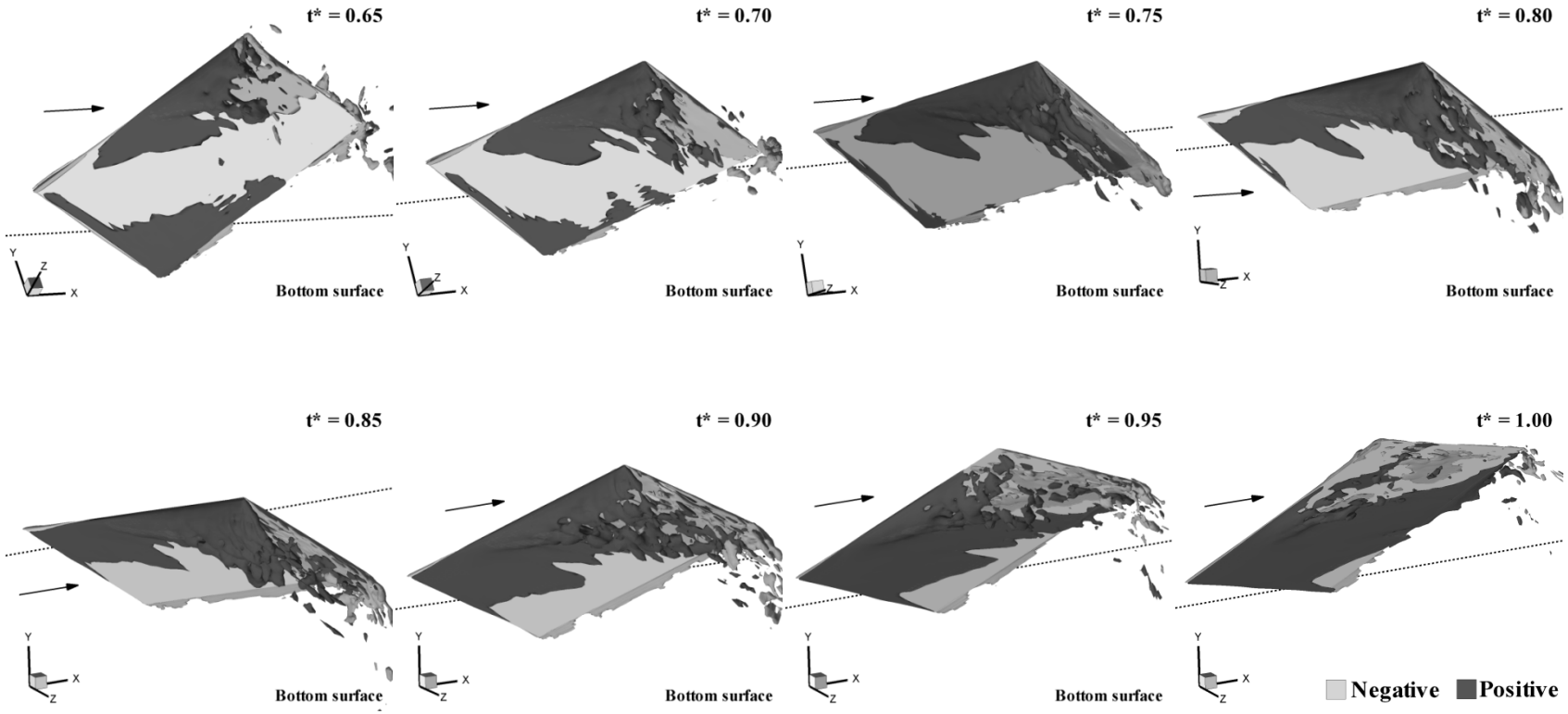

Fig.5.6 Isosurface of spanwise vorticity ω_ζ at different times for rigid wing

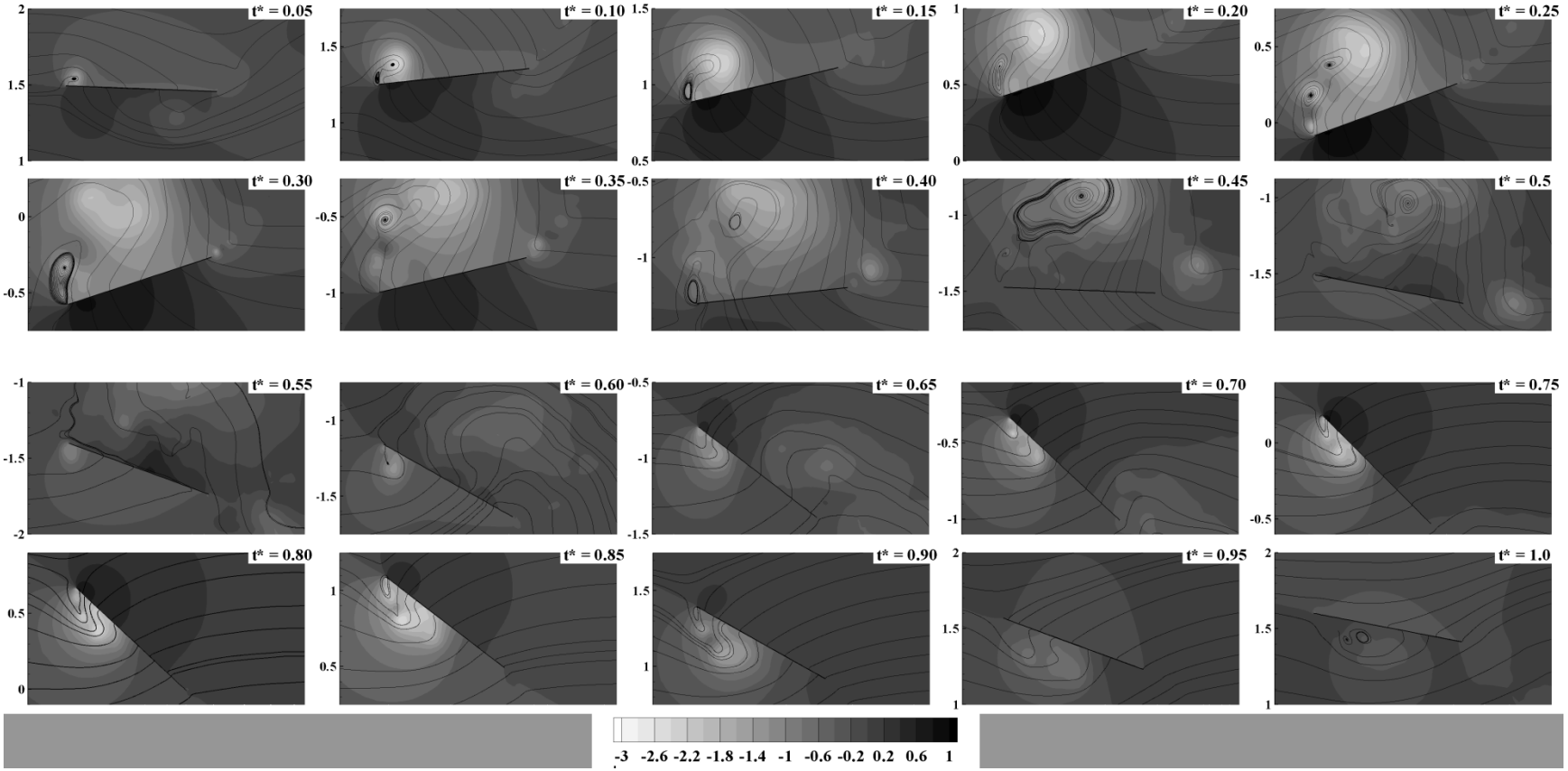

Fig.5.7 Instantaneous pressure contours and streamlines in a chordwise plane at ζ = 3 for rigid wing

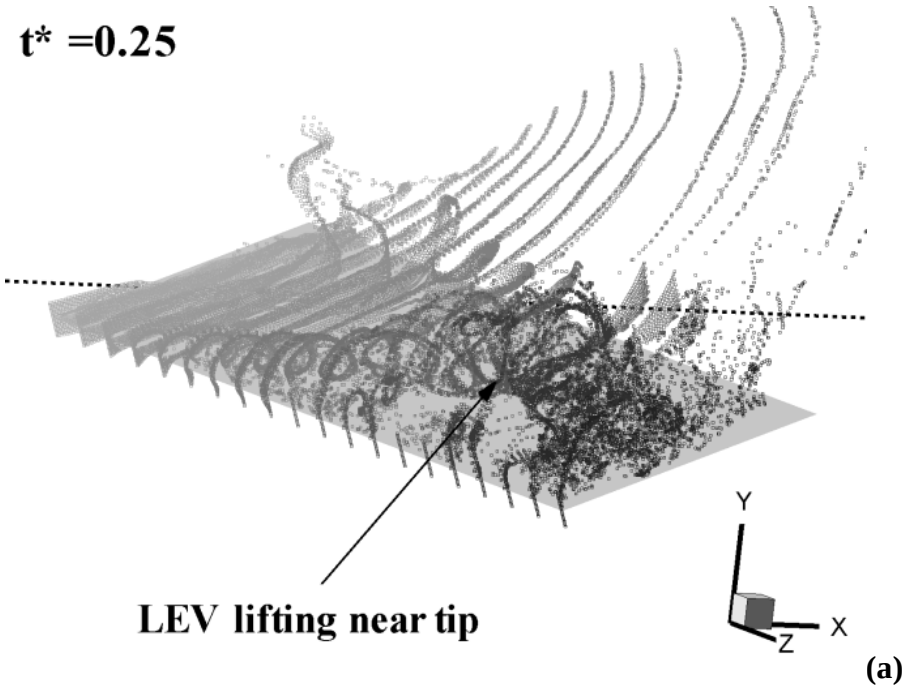

Fig.5.8 a) Particle tracing showing structure of LEV and b) spanwise velocity along the center of LEV at time t* = 0.25

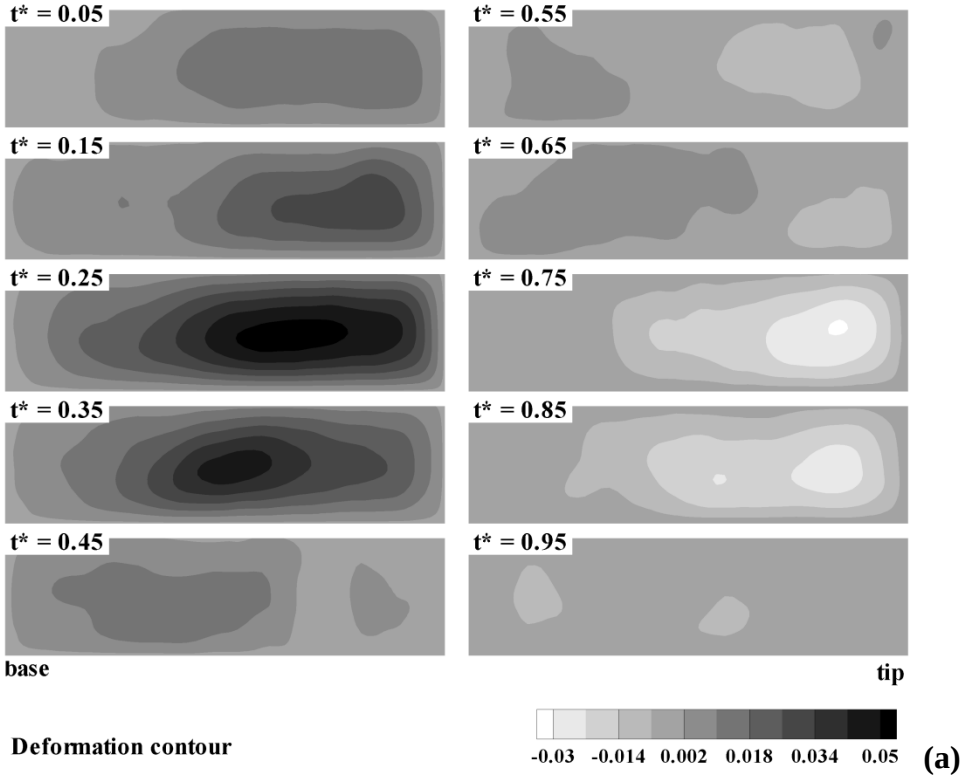

Fig.5.9 Deformation contours at during flapping cycle for prestress a) 8 N/m, b) 4 N/m

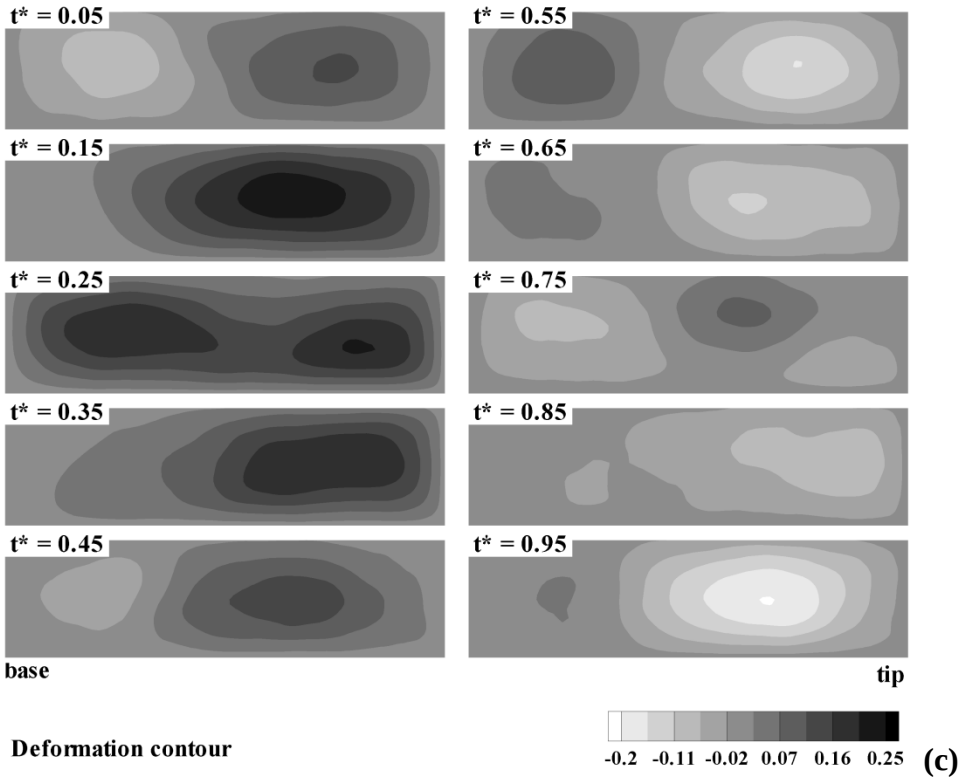

Fig.5.9 c) Deformation contours at during flapping cycle for prestress 2 N/m

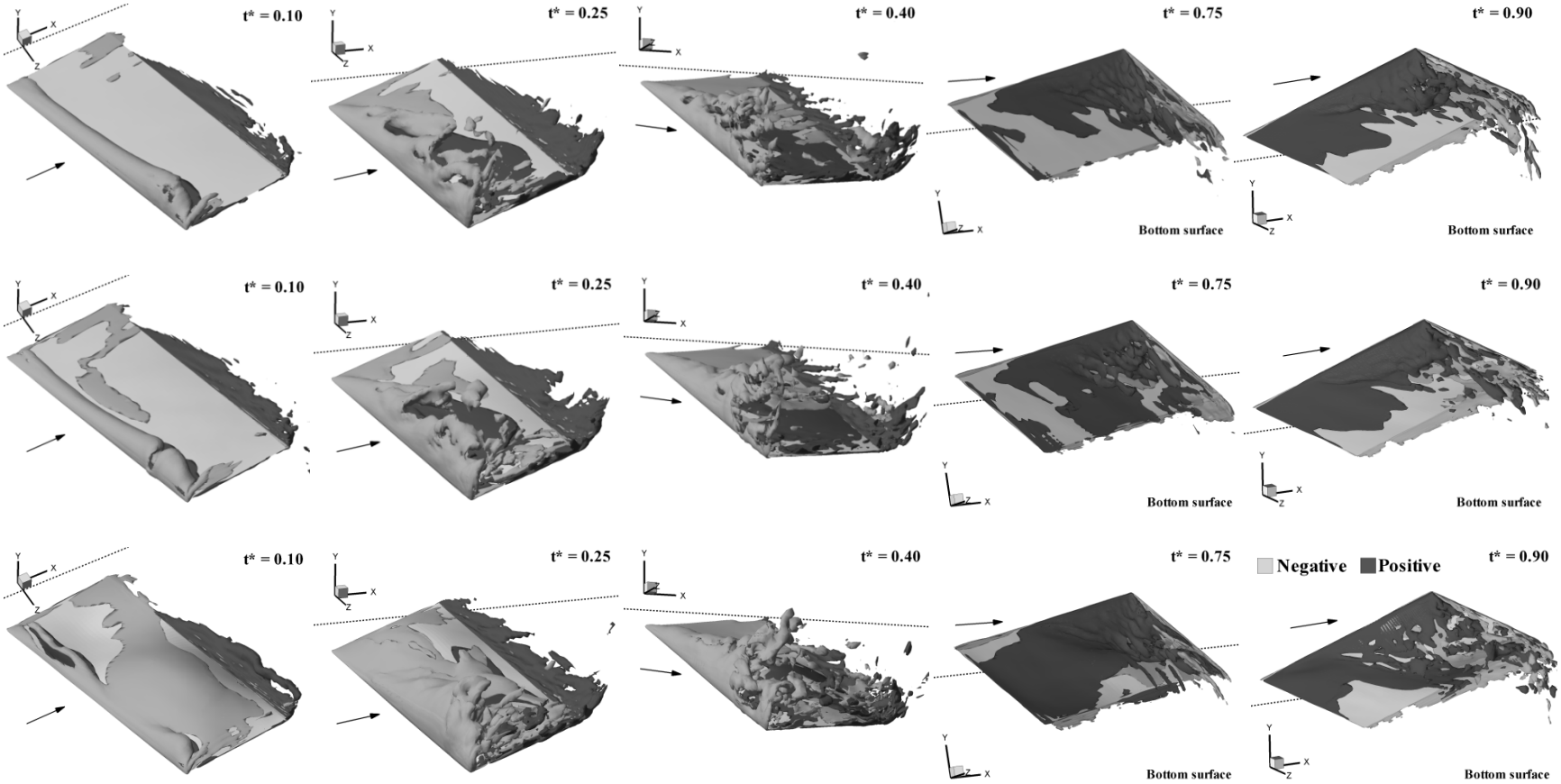

Fig.5.10 Isosurface of vorticity ω_ζ at different times for flexible wings with different pre-stress a) 8 N/m b) 4 N/m and C) 2 N/m

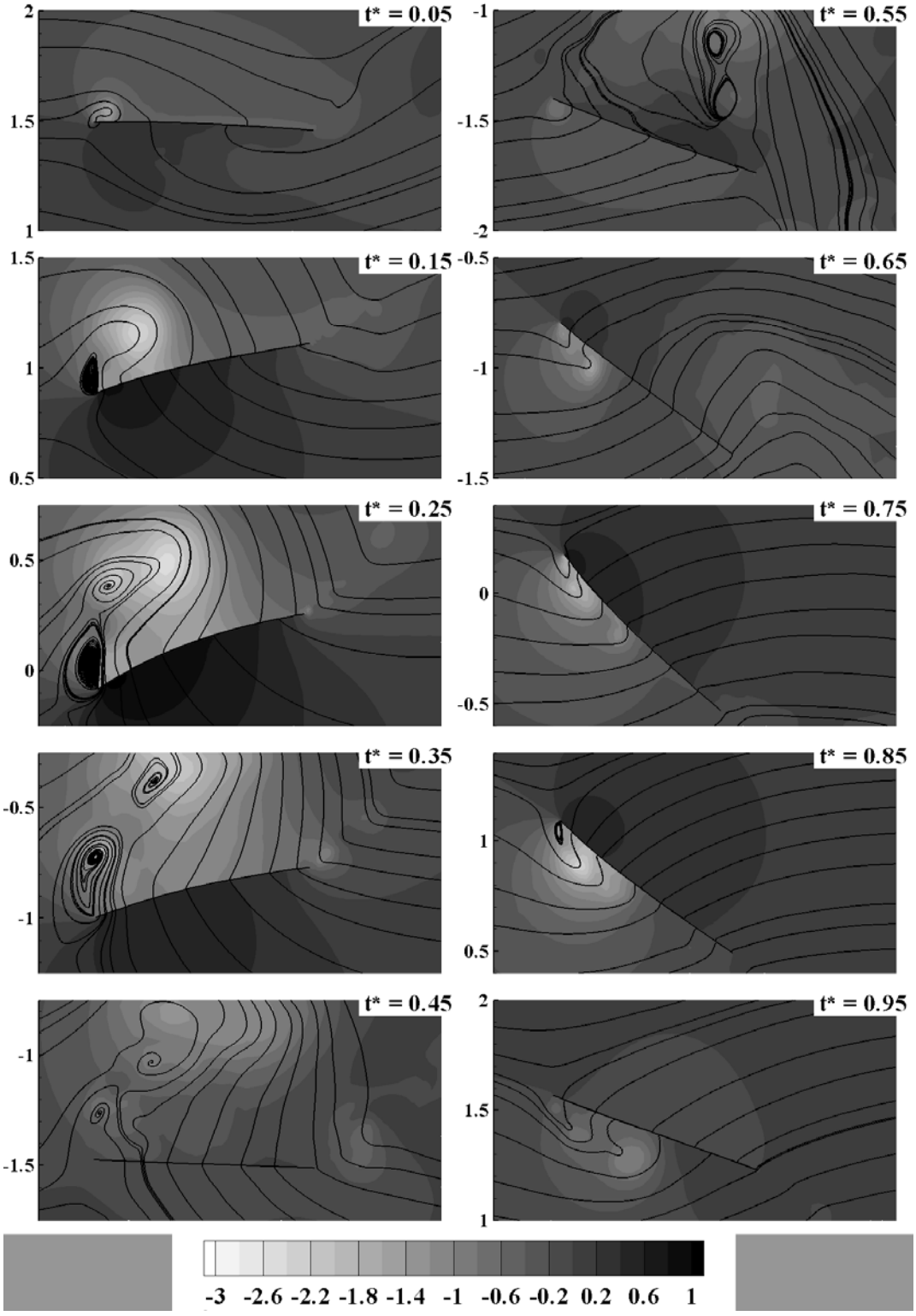

Fig.5.11 Instantaneous pressure contours and streamlines in a chordwise plane at ζ = 3 for Case A prestress = 8 N/m

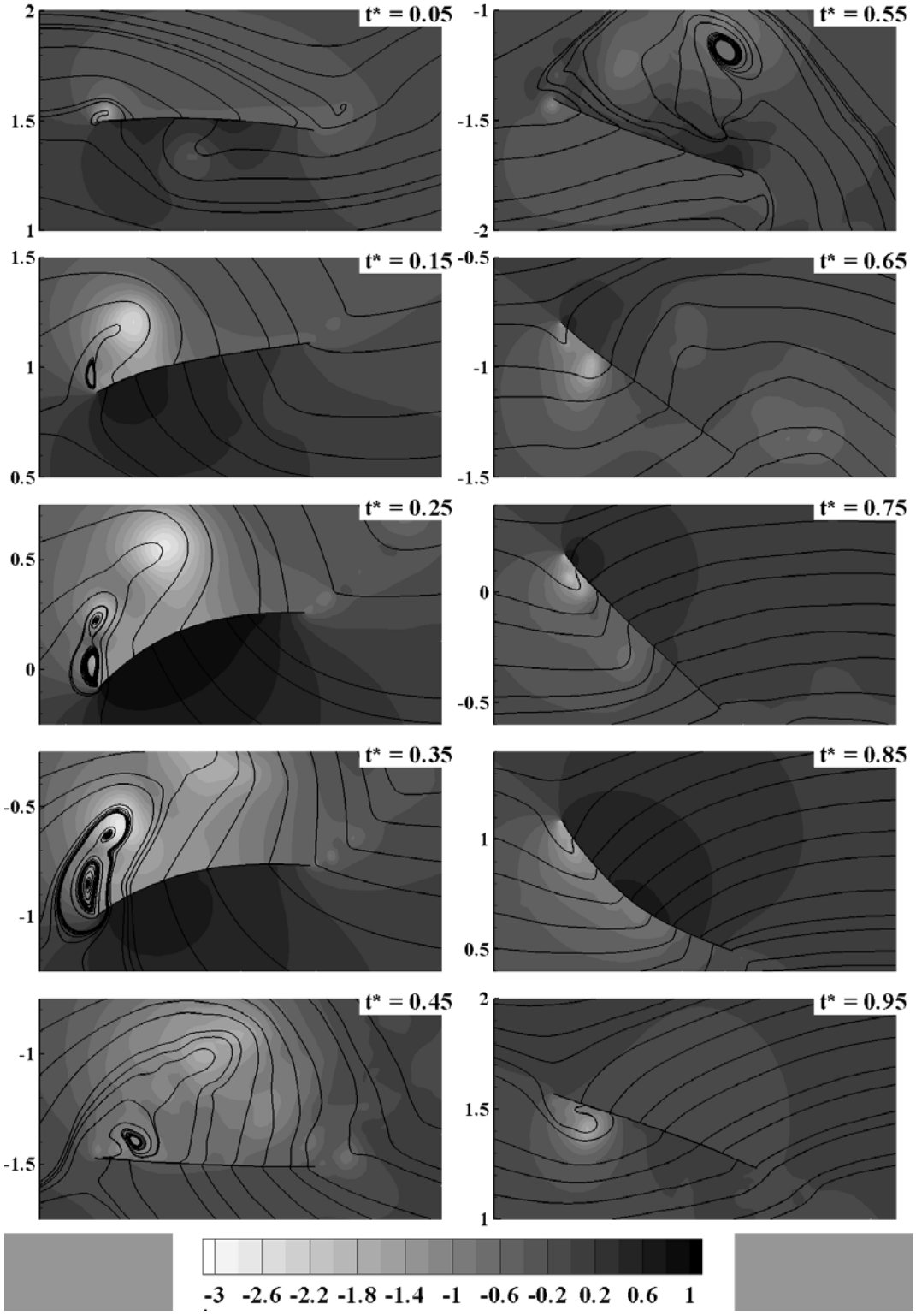

Fig.5.12 Instantaneous pressure contours and streamlines in a chordwise plane at ζ = 3 for Case B prestress = 4 N/m

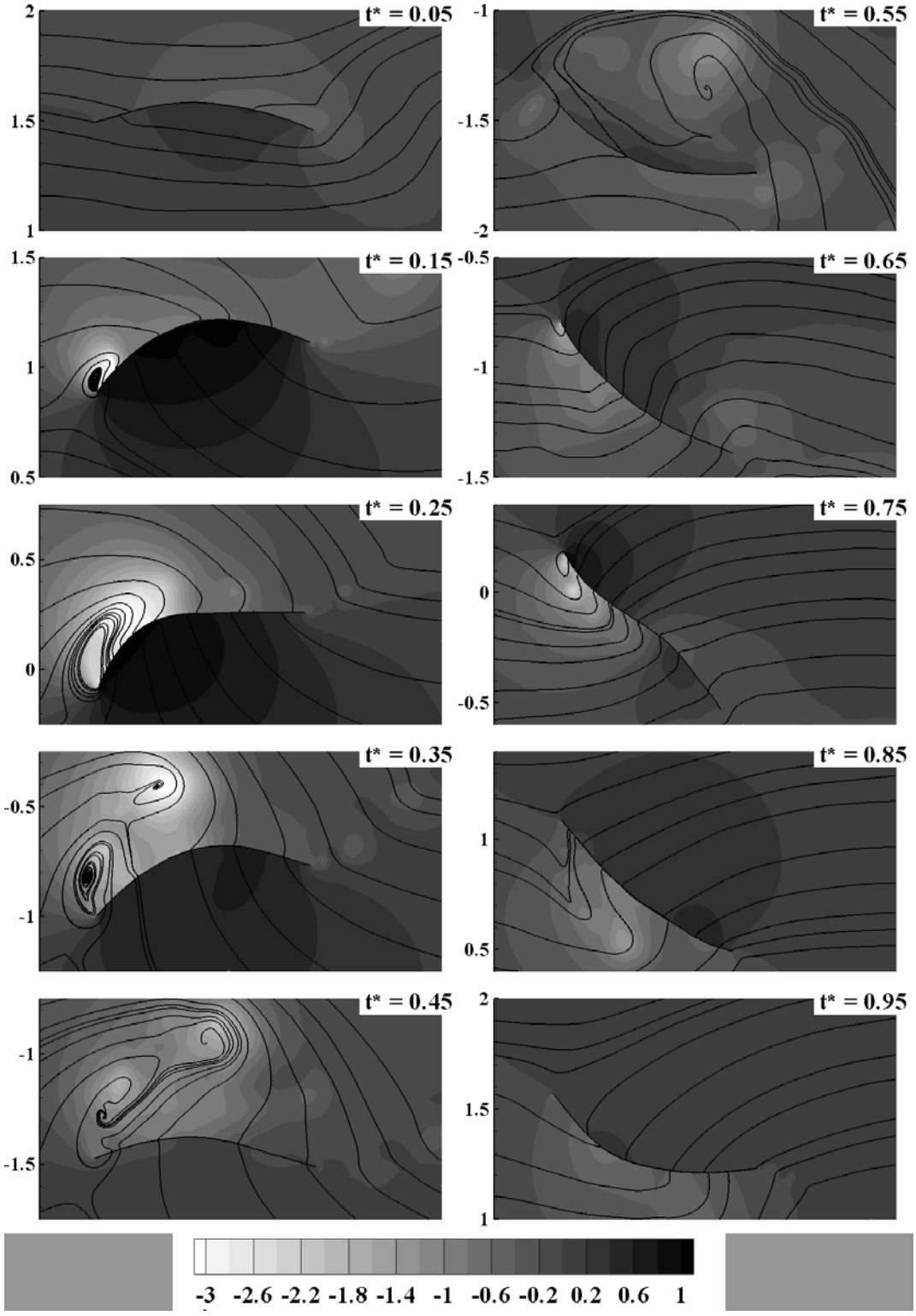

Fig.5.13 Instantaneous pressure contours and streamlines in a chordwise plane at ζ = 3 for Case C prestress = 2 N/m

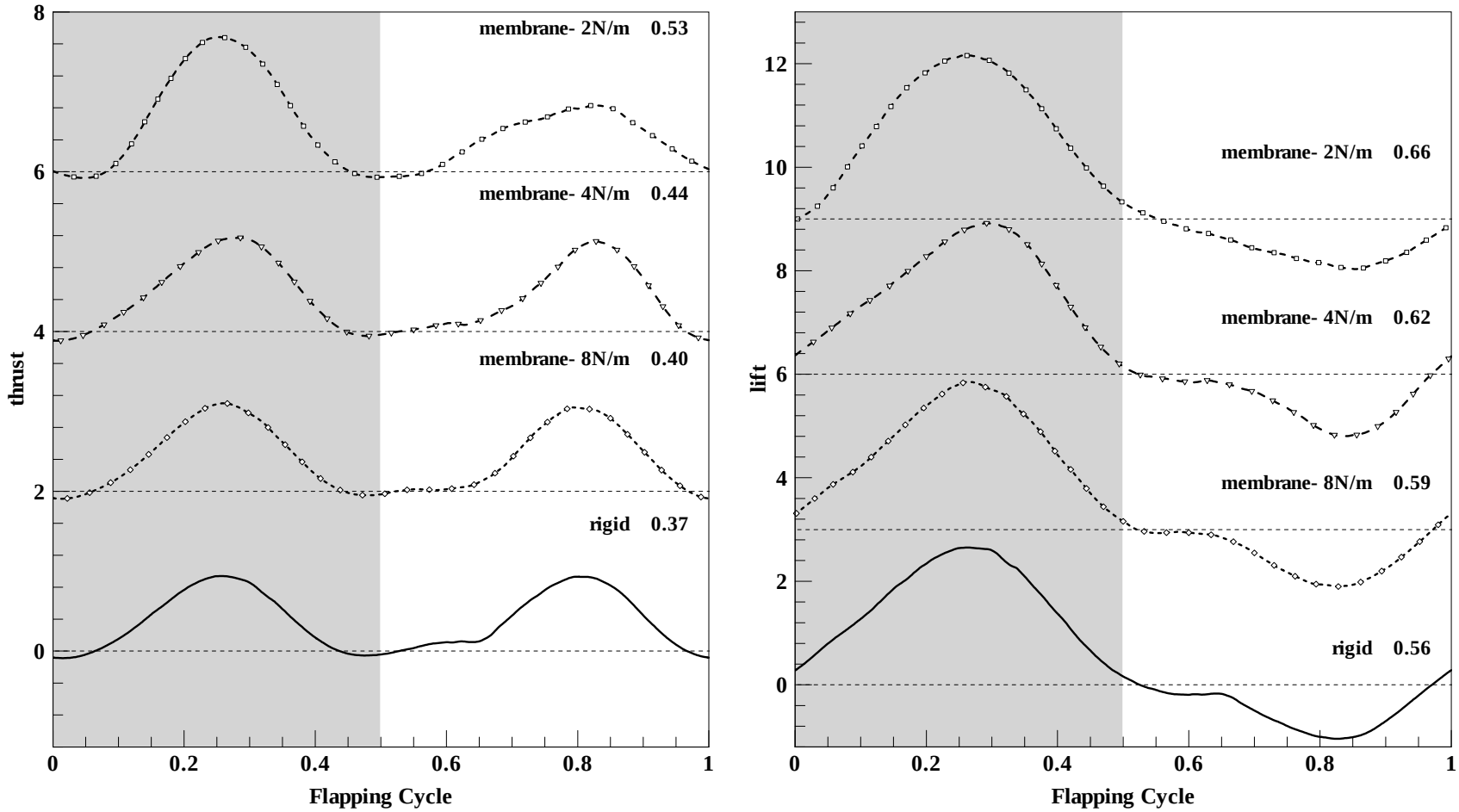

Fig.5.14 Comparison of lift and thrust variation for flexible wings to rigid wing

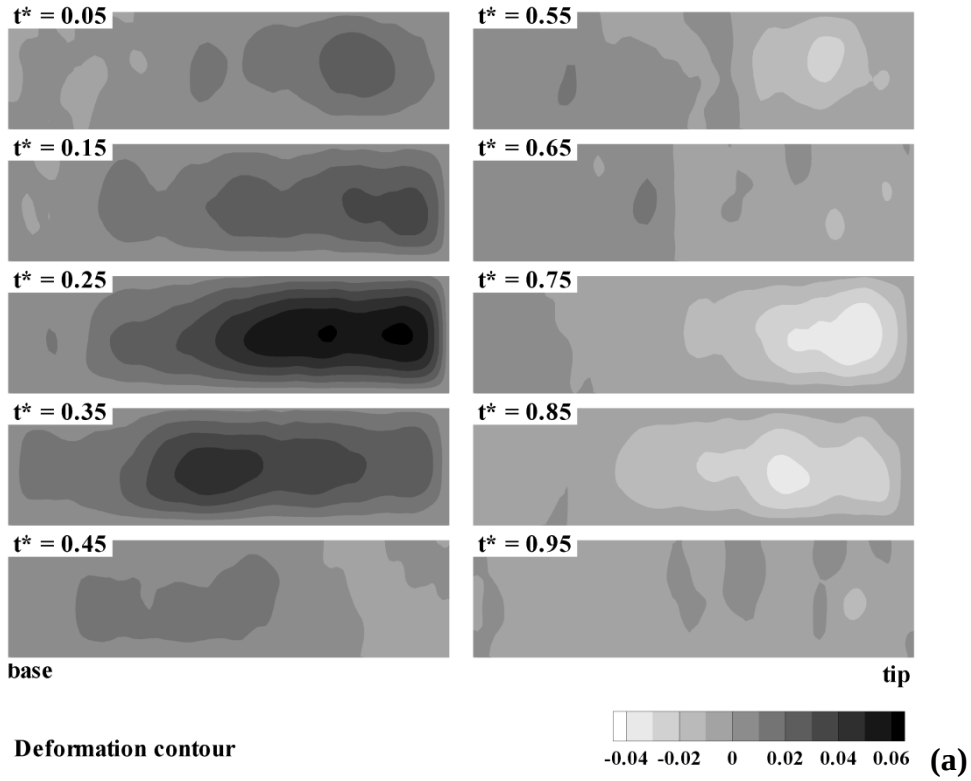

Fig.5.15 Deformation contours for a) chordwise stiff and b) spanwise stiff wing

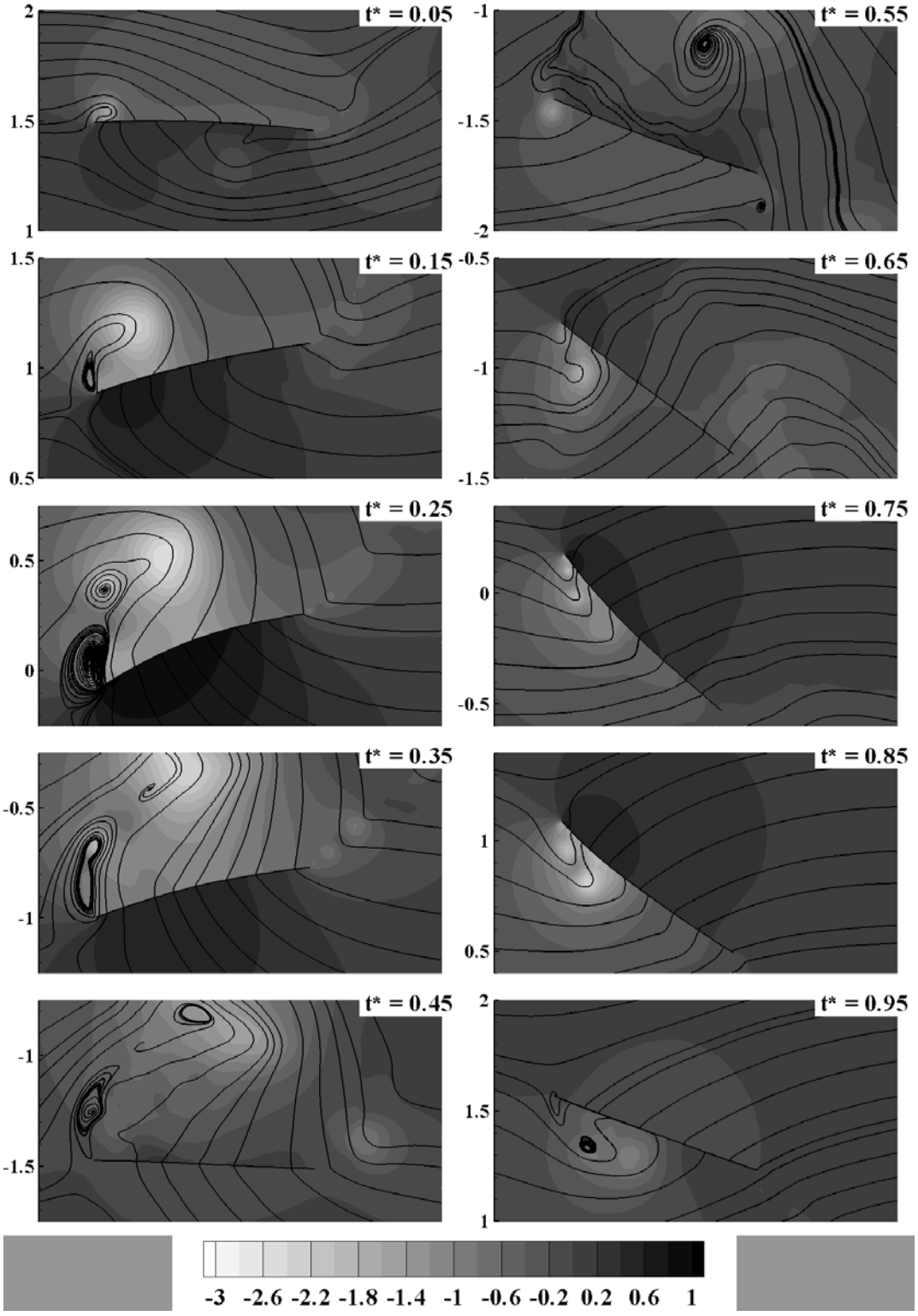

Fig.5.16 Instantaneous pressure contours and streamlines in a chordwise plane at $\zeta = 3$ for chordwise stiff wing

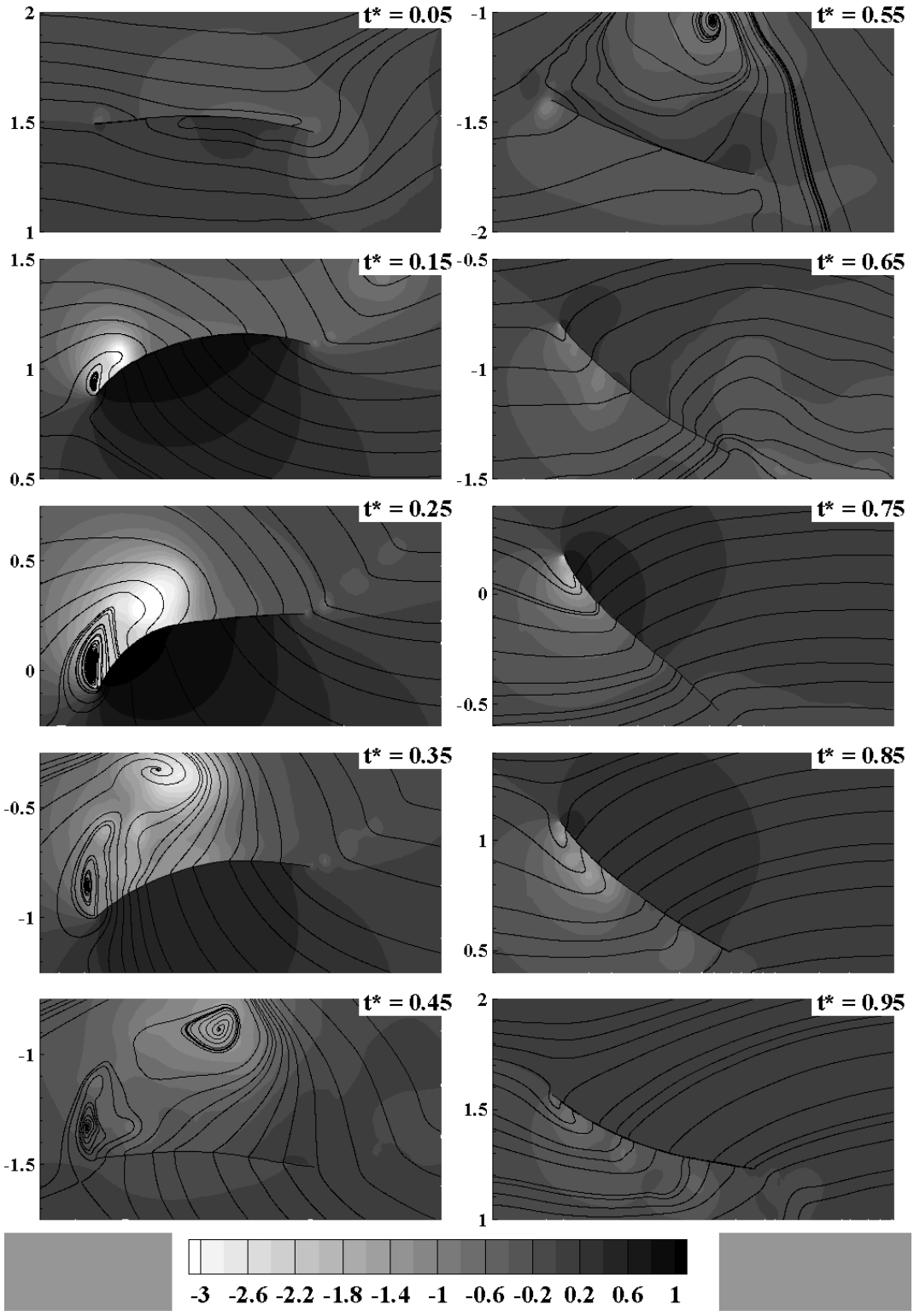

Fig.5.17 Instantaneous pressure contours and streamlines in a chordwise plane at $\zeta = 3$ for spanwise stiff wing

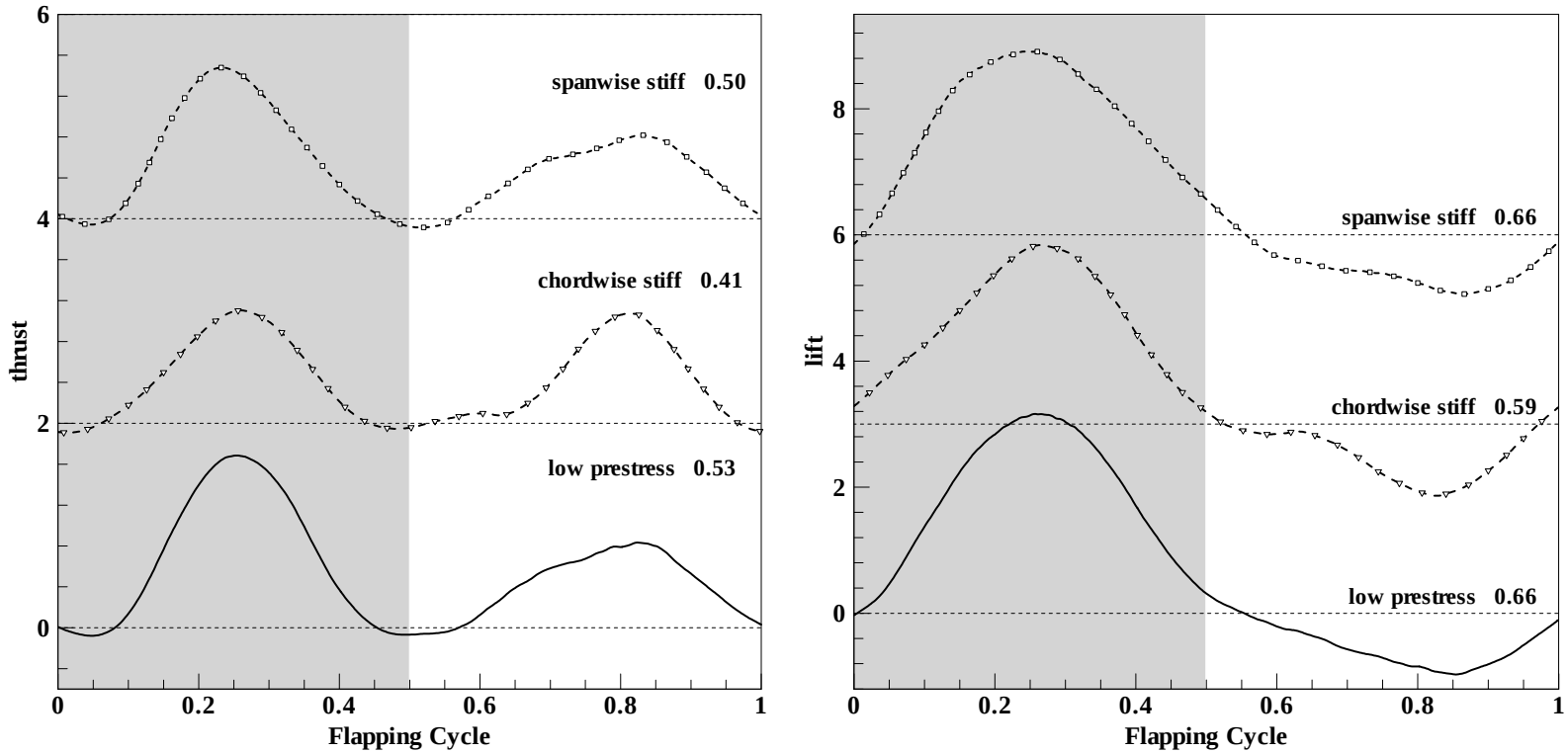

Fig.5.18 Variation of lift and thrust for different prestress cases C to E

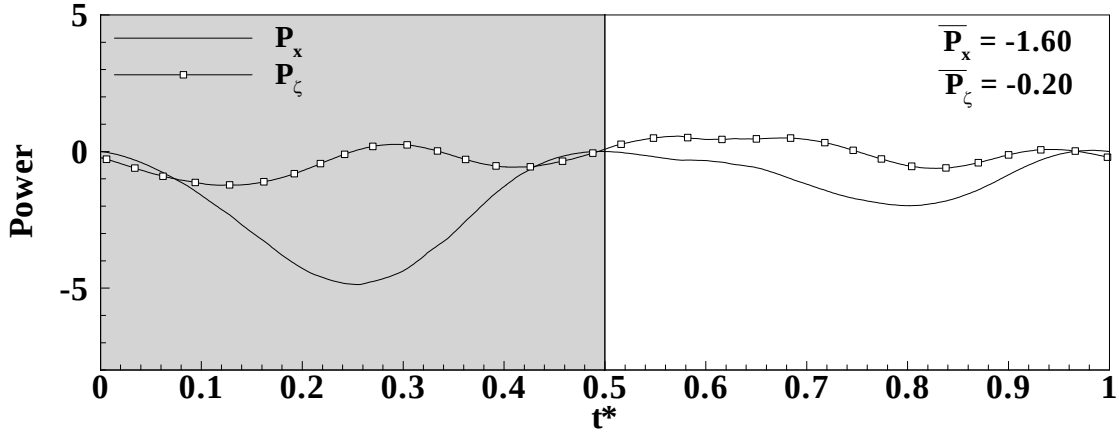

Fig.5.19 Instantaneous variation of power requirement for spanwise rigid wing (case E)

5.6 References

[1] Mcmasters, J. H. and Henderson, M. L. Low Speed Single Element Airfoil Synthesis. Tec. Soaring 1980;2:1-21.

[2] Carmichael, B. H., "Low Reynolds Number Airfoil Survey," NASA Contractor Report (Nov 1981).

[3] Pelletier, A. and Mueller, T. J. Low Reynolds Number Aerodynamics of Low-Aspect-Ratio, Thin/Flat/Cambered-Plate Wings. Journal of Aircraft Oct 2005;37:825-832.

[4] Wang, H., Zeng, L., Liu, H., and Yin, C. Measuring Wing Kinematics, Flight Trajectory and Body Attitude During Forward Flight and Turning Maneuvers in Dragonflies. The Journal of Experimental Biology 2002;206:745-757.

[5] Tobalske, B. W., Warrick, D. R., Clark, C. J., Powers, D. R., Hedrick, T. L., Hyder, G. A., and Biewener, A. A. Three-Dimensional Kinematics of Hummingbird Flight. The Journal of Experimental Biology 2007;210:2368-2382.

[6] Weis-Fogh, T. Quick Estimate of Flight Fitness in Hovering Animals, Including Novel Mechanisms for Lift Production. The Journal of Experimental Biology 1973;59:169-230.

[7] Dickinson, M. H. and Götz, K. G. Unsteady Aerodynamic Performance of Model Wings at Low Reynolds Numbers. The Journal of Experimental Biology 1993;174:45-64.

[8] Ellington, C. P., Berg, C. V. D., Willmott, A. P., and Thomas, A. L. R. Leading-Edge Vortices in Insect Flight. Nature 1996;384:626-630.

[9] Dickinson, M. H., Lehmann, F.-O., and Sane, S. P. Wing Rotation and the Aerodynamic Basis of Insect Flight. Science 1999;284:1954-1960.

[10] Wang, Z. J., Birch, J. M., and Dickinson, M. H. Unsteady Forces and Flows in Low Reynolds Number Hovering Flight: Two-Dimensional Computations Vs Robotic Wing Experiments. The Journal of Experimental Biology 2004;207:449-460.

[11] Ellington, C. P. The Novel Aerodynamics of Insect Flight: Applications to Micro-Air Vehicles. The Journal of Experimental Biology 1999;202:3439–3448.

[12] Liu, H., Ellington, C. P., Kawachi, K., Berg, C. V. D., and Willmott1, A. P. A Computational Fluid Dynamic Study of Hawkmoth Hovering. The Journal of Experimental Biology 1998;201:461–477.

[13] Birch, J. M. and Dickinson, M. H. Spanwise Flow and the Attachment of the Leading-Edge Vortex on Insect Wings. Nature Aug 2001;412:729-733.

[14] Birch, J. M., Dickson, W. B., and Dickinson, M. H. Force Production and Flow Structure of the Leading Edge Vortex on Flapping Wings at High and Low Reynolds Numbers. The Journal of Experimental Biology 2004;207:1063-1072.

[15] Miller, L. A. and Peskin, C. S. When Vortices Stick: An Aerodynamic Transition in Tiny Insect Flight. The Journal of Experimental Biology 2004;207:3073-3088.

[16] Tarascio, M. J., Ramasamy, M., Chopra, I., and Leishman, J. G. Flow Visualization of Micro Air Vehicle Scaled Insect-Based Flapping Wings. Journal of Aircraft Apr 2005;42:385-390.

[17] Shyy, W., Berg, M., and Ljungqvist, D. Flapping and Flexible Wings for Biological and Micro Air Vehicles. Progress in Aerospace Sciences 1999;35 455-505.

[18] Ho, S., Nassef, H., Pornsinsirirak, N., Tai, Y.-C., and Ho, C.-M. Unsteady Aerodynamics and Flow Control for Flapping Wing Flyers. Progress in Aerospace Sciences 2003;39 635–681.

[19] Shyy, W., Jenkins, D. A., and Smith, R. W. Study of Adaptive Shape Airfoils at Low Reynolds Number in Oscillatory Flows. AIAA Journal April 1997;35:1545-1548.

[20] Shyy, W., Klevebring, F., Nilsson, M., Sloan, J., Carroll, B., and Fuentes, C. Rigid and Flexible Low Reynolds Number Airfoils. Journal of Aircraft May 1999;36:523-529.

[21] Smith, M. J. C. Simulating Moth Wing Aerodynamics: Towards the Development of Flapping-Wing Technology. AIAA Journal 1996;34:1348-1355.

[22] Stanford, B. and Ifju, P. Membrane Micro Air Vehicles with Adaptive Aerodynamic Twist: Numerical Modeling. AIAA/ASME/ASCE/AHS/ASC Structures, Structural Dynamics, and Materials Conference, Honolulu, Hawaii April 2007.

[23] Stanford, B., Albertani, R., Viieru, D., Shyy, W., and Ifju, P. Static Aeroelastic Model Validation of Membrane Micro Air Vehicle Wings. 45th AIAA Aerospace Sciences Meeting and Exhibit, Reno, Nevada January 2007.

[24] Stanford, B., Sytsma, M., Albertani, R., Viieru, D., Shyy, W., and Ifju, P. Static Aeroelastic Model Validation of Membrane Micro Air Vehicle Wings. AIAA Journal Dec 2007; 45:2828-2837.

[25] Germano, M., Piomelli, U., Moin, P., and Cabot, W. H. A Dynamic Subgrid-Scale Eddy Viscosity Model. Physics of Fluids A 1991;3:1760-1765.

[26] Banerjee, S. P. and Patil, M. J. Aeroelastic Analysis of Membrane Wings. 49th AIAA/ASME/ASCE/AHS/ASC Structures, Structural Dynamics, and Materials, Schaumburg, IL April 2008.

[27] Pornsin-Sirirak, T. N., Lee, S. W., Nassef, H., Grasmeyer, J., Tai, Y. C., Ho, C. M., and Keennon, M. MEMS Wing Technology for a Battery-Powered Ornithopter. The Thirteenth Annual International Conference on Micro Electro Mechanical Systems, Miyazaki, Japan 2000.

[28] Gopalakrishnan, P. and Tafti, D. K. Effect of Rotation and Angle of Attack on Force Production of Flapping Flights. under review, AIAA Journal 2008.

[29] Gopalakrishnan, P. and Tafti, D. K. Effect of Phasing of Rotation on Delayed Stall in Flapping Flights Related to MAVs at Re=10000. AIAA 38th Fluid Dynamic conference, Seattle, Washington June 2008; AIAA-2008-4301.

[30] Gopalakrishnan, P. and Tafti, D. K. A Parallel Boundary Fitted Dynamic Mesh Solver for Applications to Flapping Flight. under review, Computers and Fluids 2008.

[31] Gopalakrishnan, P. and Tafti, D. K. A Parallel Multiblock Boundary Fitted Dynamic Mesh Solver for Simulating Flows with Complex Boundary Movement. AIAA 38th Fluid Dynamic conference, Seattle, Washington June 2008; AIAA-2008-4142.

[32] Combes, S. A. and Daniel, T. L. Flexural Stiffness in Insect Wings I. Scaling and the Influence of Wing Venation. The Journal of Experimental Biology Sep 2003;206:2979-2987.

[33] Combes, S. A. and Daniel, T. L. Flexural Stiffness in Insect Wings Ii. Spatial Distribution and Dynamic Wing Bending. The Journal of Experimental Biology Sep 2003;206:2989-2997.

Chapter 6: Conclusion and Recommendations Future Work

6.1 Conclusion

In this study, the unsteady aerodynamics and aeroelastic analysis of forward flapping flight in the Reynolds number range of 100 to 100,000 using Large Eddy Simulation (LES) is carried out. In order to analyze the flapping flight, a boundary fitted dynamic grid method is developed for a 3D flow solver, GenIDLEST, in a structured-multiblock framework. The capability of the solver is tested with classical flow problems such as forced oscillation of a cylinder, a heaving airfoil, a moving indentation channel, and a hovering fruitfly. The results obtained both in terms of flow structure and force measurements were in good agreement with previous experimental and numerical studies. Analysis of forward flapping flight is carried at an advance ratio of 0.5 by varying the Reynolds numbers, the kinematic parameters and the stiffness of the wing. The following major conclusions are reached from these analyses.

1. A spiral Leading Edge Vortex (LEV) forms during the downstroke for all the simulations carried out. A strong spanwise flow of the order of the flapping velocity is observed along the core of the LEV. In addition, the formation of a negative spanwise flow is observed near the tip due to the tip vortex, which slows down the removal of vorticity from the LEV. This leads to instability of the LEV and drop in lift and thrust production.

2. Analysis of different kinematics shows that a continuous rotation is preferred for high thrust production and high propulsive efficiency, while shorter rotation could be used to produce high lift. Analysis of different angles of attack shows that a moderate angle of attack which results in complete shedding of the LEV at the end of translation is preferred for high propulsive efficiency.

3. Analysis of flapping flight at different Reynolds numbers shows that the trend of force production is identical for all Reynolds numbers (100, 10,000 and 100,000). At low Reynolds number Re=100, the magnitude of instantaneous lift and thrust coefficients are lower, while high values are obtained at higher Reynolds numbers. The critical reasons are that at higher Reynolds numbers, the location of

the LEV is closer to the surface and the LEV sheds and convects near the tip resulting in a low pressure region on most of the upper surface. The values obtained for Re=10,000 and Re=100,000 are identical signifying less impact of Reynolds number in this range.

4. The analysis of different tip shapes show that tip shapes do not have a significant effect on the lift and thrust production.

5. Analysis with a sinusoidal stroke deviation with the same frequency as that of flapping shows that lift and thrust production are affected during the upstroke due to interaction with the LEV shed from the previous downstroke. This interaction reduces the average lift production.

6. Aeroelastic analysis with different wing stiffness showed that the membrane wing outperforms the rigid wing in terms of lift, thrust and propulsive efficiency. The main reason for the increase in force production is attributed to the gliding of the LEV along the camber, which results in a high pressure difference across the surface. In addition, a high stiffness along the spanwise direction and low stiffness along the chordwise direction results in a uniform camber which results in high lift and thrust production.

6.2 Future work

The results from our analysis show that flapping flight offers a viable alternate solution for Micro Air Vehicles (MAVs) in the Reynolds number range of 10,000 to 100,000. In addition, the results from the aeroelastic analysis show that significant improvement can be obtained by using deformable membrane wings. The following recommendations are made for future work.

1. Our analysis shows that the structure of the LEV is affected significantly by changes in kinematic parameters. Birds significantly alter kinematic parameters such as stroke plane angle, deviation from stroke plane, wingbeat amplitude, percentage of wingbeat in downstroke and angular velocity of the wing to achieve the required force for different flight conditions. For a comprehensive

understanding of flapping flight, a more detailed analysis of the effect of these parameters on the aerodynamic performance is necessary.

2. In addition to complex kinematics, birds and insects change their camber significantly to achieve the desired flight conditions. The results from our simulations show that the camber introduced by the membrane wing improves thrust and lift production by 40% and 20%, respectively. Hence analysis with a prescribed temporally varying camber could be carried out for a better understanding of the effect of camber.

3. In the present study for aeroelastic analysis, a linear membrane model is used to compute out of plane deformation with applied aerodynamic loads. For a more realistic analysis, a membrane model which allows both in plane and out of plane deformation and with both inertial and aerodynamic loads applied should be used to develop a favorable wing structure. In case of insect wings, the stiffness differs considerably along the surface of the wing. Most wings have high stiffness along the leading edge and a flexible membrane near the trailing edge which is deemed critical for the high performance of their flight. Hence aeroelastic tailoring of the wing could be used to obtain better aerodynamic performance.

4. One of the requirements for a viable MAV is the ability to withstand sudden perturbations in the wind speed. Atmospheric turbulence dictated by terrain and weather conditions can potentially introduce roll, pitch and yaw disturbances. The MAV is expected to fly within 100m from the ground where wakes shed by ground objects are also anticipated to play a significant role. Hence, analyzing flapping flight by changing the freestream condition using an impulse function with varying frequency and amplitude is necessary to get a comprehensive understanding of the effect of wind gusts on lift and thrust production.

Appendix

A.1. Moving indentation channel

The channel with a moving indentation has been studied experimentally[1] and numerically[2-4] in many previous studies. Fig.A.1 shows the configuration of the indentation channel. The shape of the indentation[4] is given by

$$y(x) = \begin{cases} h & for\ 0 < |x| < x_1 \\ 0.5h\left(1 - \tanh\left[a(x - x2)\right]\right) & for\ x_2 < |x| < x_3 \\ 0 & for\ |x| > x_3 \end{cases} \qquad \text{(A.1)}$$

where a = 4.14, $x_1 = 4$, $x_3 = 6.5$, $x_2 = 0.5(x_1 + x_2)$ and

$$h = 0.5h_{\max}\left[1 - \cos(2\pi t^*)\right], \quad t^* = (t - t_0)/T, \quad h_{\max} = 0.38$$

An upstream length of 9.85*(L_1)* and downstream length of 18*(L_2)* from the center of indentation is used for the computational domain. The Strouhal number based on channel width, mean velocity and oscillation period (*St= bU/T*) is 0.037 and the Reynolds number of the flow is 507. The flow is initialized with a fully developed velocity profile and the same is specified as the inlet boundary condition, while an outflow boundary is specified at the outlet. The simulation is carried out for a normalized time unit *t** of 1. For *t** <0.5 the indentation moves towards the middle of the channel and reaches a maximum height of *0.38* at *t** =0.5. For *t**> 0.5 the indentation moves away from the center and reaches the initial position at *t** = 1.

The stream lines downstream of the indentation at various time *t** is shown in Fig.A.2. At time *t**=0.2, a small separated eddy *A* forms near the indentation. As time progresses, the size of the eddy *A* increases while a second eddy *B* forms near the top wall at time *t**=0.4. At time *t**=0.7, three more additional eddies (*C, D, E* shown in Fig.A.2) form downstream. Further, at time *t** =0.7, the eddy *B* near the top wall breaks into two counterclockwise rotating eddies. The formation of eddies and the breakup of eddies matches well with the experimental study by Pedley et al.[1]. A maximum velocity of 2.654 occurs at *t**=0.384, while a value of 2.645 was reported in

Demirdzic[4]. The shear stress along the moving wall and top wall at time t^*=0.5 is compared with the results of Demirdzic [4] (Fig.A.3). The location of maximum and minimum shear stress matches well with the previous study, while the present study slightly under predicts the peak stress values. The difference might be due to the non-orthogonal grid near the indentation curves and resulting errors in calculating the shear stress.

Table.A.1 Parameters involved in flapping flight

Parameters	***Description***
Stroke Plane	The plane defined by three points: wing base (B), and the wingtip at maximum (T_T)and minimum angular position (T_B)
Stroke plane angle, β	Angle between the stroke plane and the horizontal plane
Angle of attack, α	Angle between the wing direction (from trailing edge to leading edge) and the direction of motion.
Torsional angle, ρ	Angle between the wing direction and the direction perpendicular to stroke plane.
Flapping Amplitude, ϕ	Angle between the leading edge of the wing and the horizontal plane
Reynolds number, $\frac{U_f c}{\nu}$	Defined based on mid-span chord length, c and flapping velocity, $U_f = 2\Phi f R$, where Φ - total flapping amplitude (max to min) R - spanwise length (wing length) f - frequency of flapping
Advance ratio, $J = \frac{U_\infty}{U_f}$	Ratio of the flight velocity to the flapping velocity

A.2. Unsteady aerodynamics of dragonfly flight

Unsteady aerodynamic theories such as delayed stall[5,6], wake capturing[7], rotational circulation[7] have been proposed for the superior performance of insect flight. Among these, delayed stall, employed by most birds and insects, involve the formation of a stable Leading Edge Vortices (LEV), which enhances the production of thrust and lift.

The other mechanisms, wake capturing and rotational circulation contribute to force production during the rotational phase of the wing. In the current study, the flow structures involved in dragonfly flight is analyzed to evaluate the contribution of these unsteady mechanisms to the total force. Before discussing the results, a brief description of kinematic parameters and non-dimensional numbers involved in the flapping flight is provided in is provided in Fig.A.4 and Table A.1.

A two dimensional model of forewing and hindwing based on the mid-span wing dimensions as shown in Fig.A.5 is employed. The lengths shown in Fig.A.5 are normalized by the mid-span chord length of the forewing (10mm). The center of rotation for both wings is placed at one quarter of their chord length and the wing thickness of 1% of forewing chord length is used. The direction of upstroke and downstroke and the free stream velocity is also shown in Fig.A.5. A 35 block grid with 15 blocks on forewing side and 20 blocks on the hindwing side is used for the simulation. The spring analogy is employed with two separate spring systems, one each for forewing and hindwing side of blocks, to compute the displacement of block corners. A linear interpolation is employed for computing dependent variables at the non-matching interface between the two wings. The grid is made fine enough for length of ±2 in the y direction to accommodate the flapping of the wings. The flow field is normalized based on flapping velocity at mid-span, $U_f = 2\Phi fR$. The values of R=20 mm, the total flapping amplitude Φ=60^o and the flapping frequency of 33.4 Hz are chosen from Wang et.al.[9], which results in the flapping velocity of 1.5372m/s. The Reynolds number of the simulation based on U_f and the chord length is 990 and the non-dimensional flapping frequency is 0.2173. The inlet velocity condition is computed based on the advance ratio, *J* of 1.0 and the stroke plane angle of 75^o. The kinematics measured by Wang et.al.[9] (Fig.A.6) during the forward flight of dragonfly, *Polycanthagyna melanictera*, is used for the simulation.

The variation of instantaneous force coefficients in the stroke plane for forewing and hindwing are shown in Fig.A.7 and the vorticity contours at various time is shown in Fig.A.8. The force production by forewing occurs mainly during its downstroke. An LEV forms on the top surface of forewing (Fig.A.8b) during the first half of its downstroke resulting in a peak of thrust and lift (Fig.A.7). This LEV sheds during the

middle of the downstroke due to strong rotation leading to a drop in lift. During the second half of the downstroke, a second LEV forms (Fig.A.8c), which results in the second peak of lift and thrust forces. During the entire upstroke, no strong vortices are present around forewing (Fig.A.8d) and the force production is low.

The hindwing experiences low pressure on the top surface at the start of the downstroke, produced by the wake vortices of the forewing. This phenomena, which is similar to wake capturing (Fig.A.8d) leads to a small peak in lift at non-dimensional time, t = 3.7. During the middle of downstroke, a peak value in lift and thrust forces is produced due to the presence of both LEV and trailing vortex (Fig.A.8a), which create a low pressure region on the top surface. A small LEV forms during the upstroke (Fig.A.8c) resulting in the second peak of lift and a peak in drag force.

The variation of coefficient of thrust and lift produced by both wings is shown in Fig.A.9. There are two peaks in the lift force; each one is produced during the downstroke of the hindwing and forewing. The peak in thrust is produced during the middle of the hindwing downstroke and at the end of the hindwing upstroke. The average values of coefficient of lift, $C_{L,}$ and thrust, C_T are 1.75 and 0.037. The lift force produced by all wings is 4.9824 mN, which is sufficient enough to support the weight of dragonflies, *Polycanthagyna melanicter*, 2.845 mN (0.29g)[9]. Under steady state conditions, the thrust produced by the wing balances the body drag. From the experimental study of Wakeling and Ellington[10], the body drag force for dragonfly, *Calopteryx splendens*, at Re=5790 and body alignment angle of 15^o is 0.0662 mN, which is lower than the thrust, 0.1053 mN computed by the present simulation. The current study of dragonfly flight proves the capability of the solver in simulating complex boundary movements.

A.3. Aeroelastic modeling

The wing is modeled as a linear elastic membrane structure which is pre-stressed by stretching at its boundaries. The out of plane deformation is computed using the non-dimensional dynamic membrane equation in wing reference coordinate

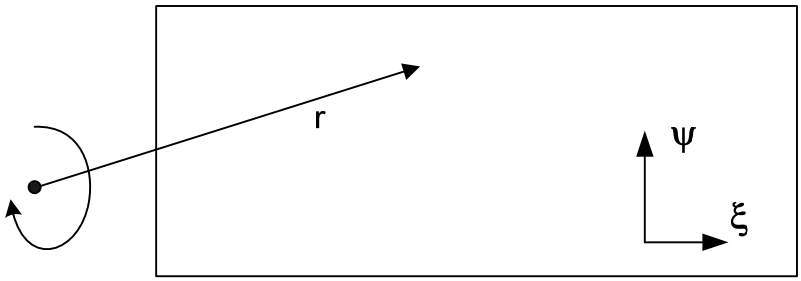

Membrane wing

$$N_x \frac{\partial^2 w}{\partial x^2} + 2N_{xy} \frac{\partial^2 w}{\partial x \partial y} + N_y \frac{\partial^2 w}{\partial y^2} + p + S_{iner} = \rho_w h_w \frac{\partial^2 w}{\partial t^2} \qquad \text{(A.1)}$$

where, w is out of plane displacement, p is the applied differential aerodynamic pressure across the wing, and N_x, N_y and N_{xy} are prestresses along chordwise, spanwise and in shear, respectively. The inertial source term is given by

$$S_{iner} = -\rho_w h_w (\dot{V} + \dot{\Omega} \times r + 2\Omega \times V + \Omega \times \Omega \times r) \qquad \text{(A.2)}$$

where, V and Ω are the prescribed wing linear and angular velocity at the reference point, r is the distance from the reference point, ρ_w is density of the wing, h_w is thickness of the wing, The equation is non-dimensionalized with the same characteristic parameters, chord length and flapping velocity used for the flow solver. The pre-stresses are normalized by $\rho u_f^2 C$ and $\rho_w h_w$ is normalized by $\rho_a C$. The linearity assumption employed is strictly valid only if the strain accumulated by the deformation is small in comparison to the pre-strain in the membrane.

Coupling

An explicit time advancement method using the latest available information is employed for coupling between the flow solver and the membrane solver. For each fluid time step the membrane deformation is of O (1×10^{-4}) and has no significant effect on the flow and pressure distribution. The steps involved in coupling are

1. The flow is advanced to time level n+1 with known deformation values at n.

2. The pressure values are transferred from fluid solver to membrane solver. Since same grid distribution is used for both solvers, no interpolations are necessary.
3. The inertial loads are computed based on the prescribed motion.
4. The membrane solver is advanced using the aerodynamic and the inertial loads at n+1 level and known deformation at level n and n-1. A second order central difference at time level n is employed for both spatial and temporal derivatives.
5. The deformation values are then transferred to the flow solver.
6. The steps 1 to 5 are repeated for the next time advancement.

Validation of the membrane solver

Validation of the membrane solver is carried out based on method of manufactured solution. A known temporally varying deformation

$$w = \sin x \sin y \sin t \tag{A.3}$$

is substituted in Eq.A.1 along with prescribed values of pre-tension and the mass of the wing to get a source term. This source term is then applied to the membrane solver and the value of out of plane deformation from the solver is compared against Eq. A.3.

A.4. Figures

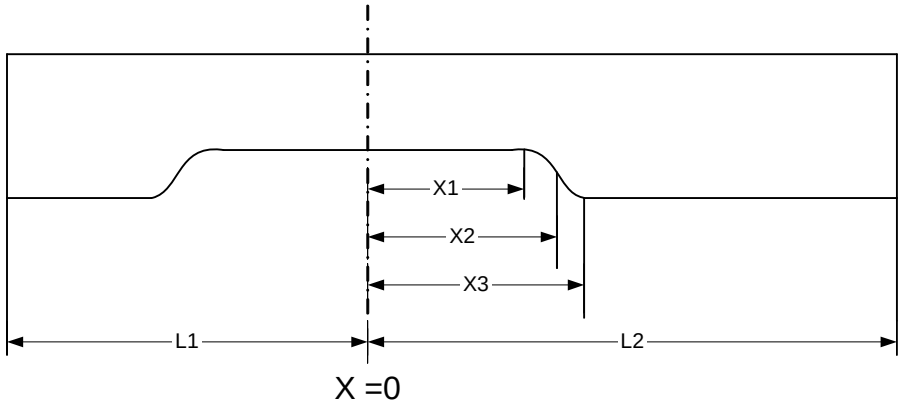

Fig.A.1 Channel with moving indentation

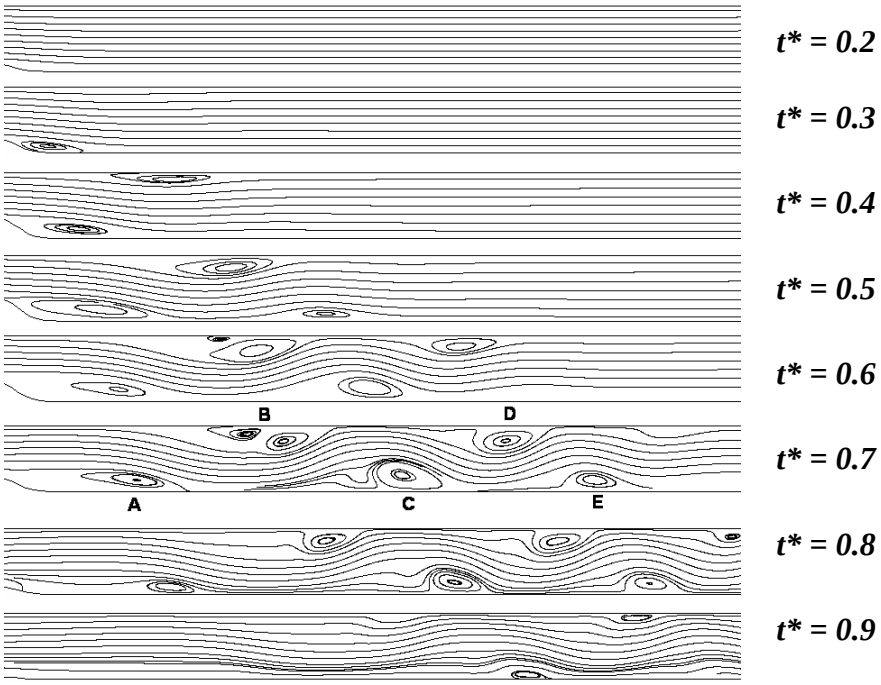

Fig.A.2 Stream lines downstream of the moving indentation channel for *t =0.2 to 0.9.**

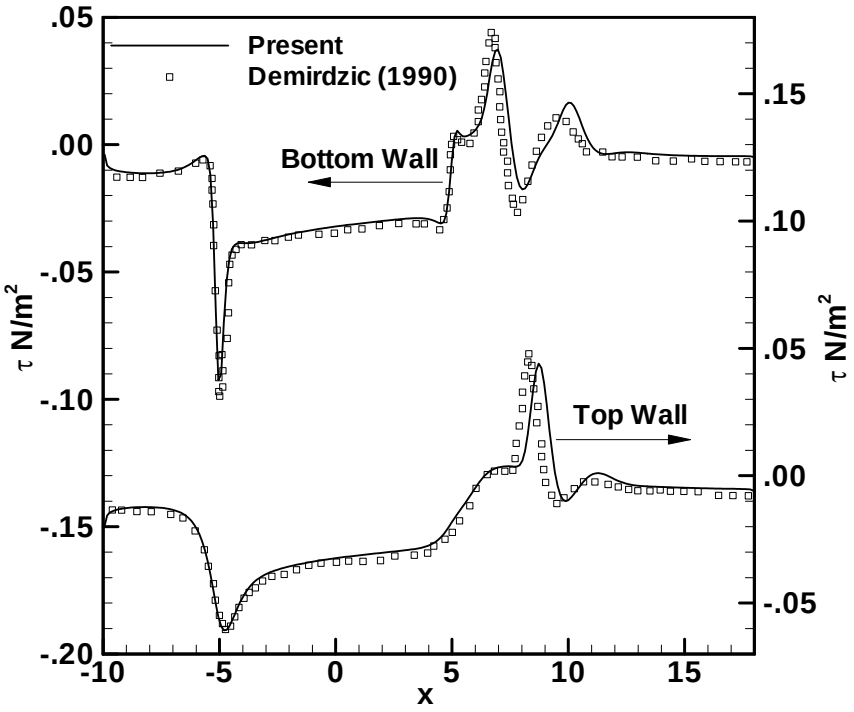

Fig.A.3 Comparison of shear stress along top and bottom wall with previous study Demirdizic.

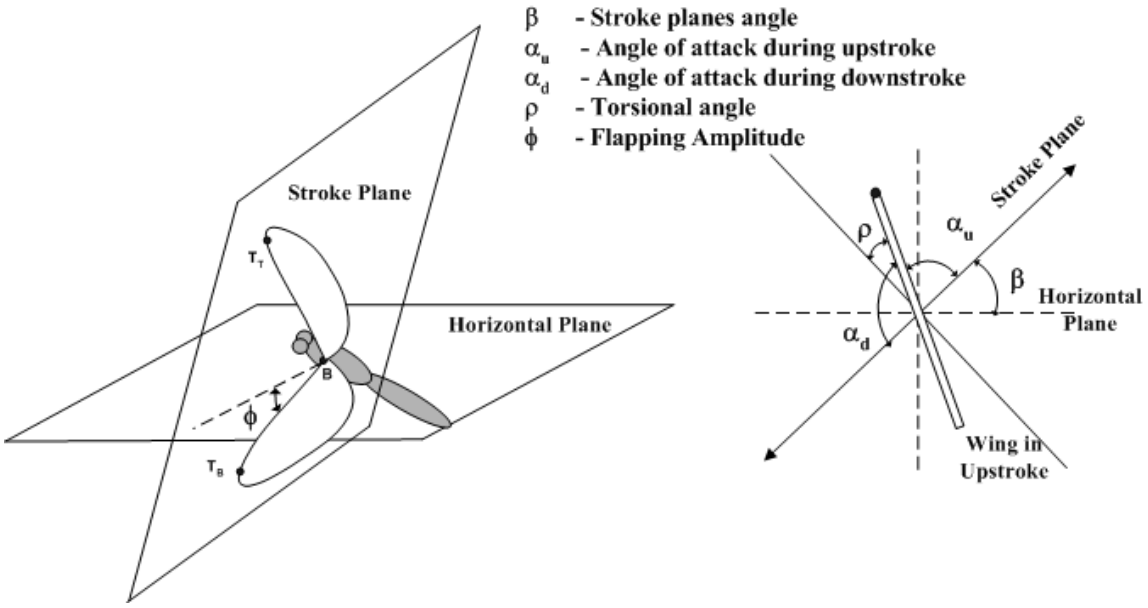

Fig.A.4 Kinematic parameters

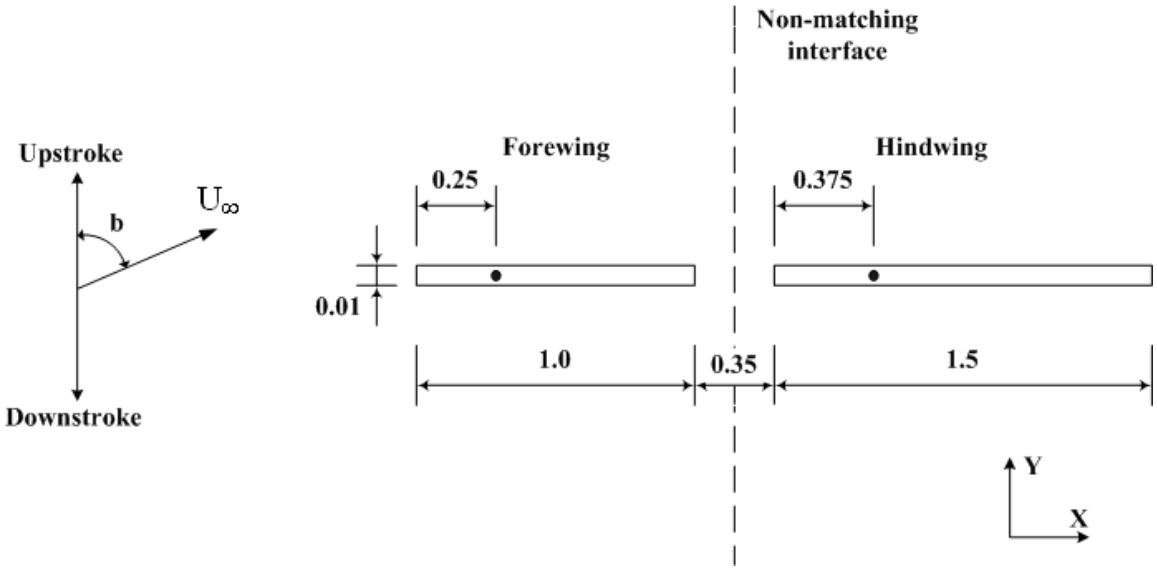

Fig.A.5 Two dimensional wing arrangement used for dragonfly simulation

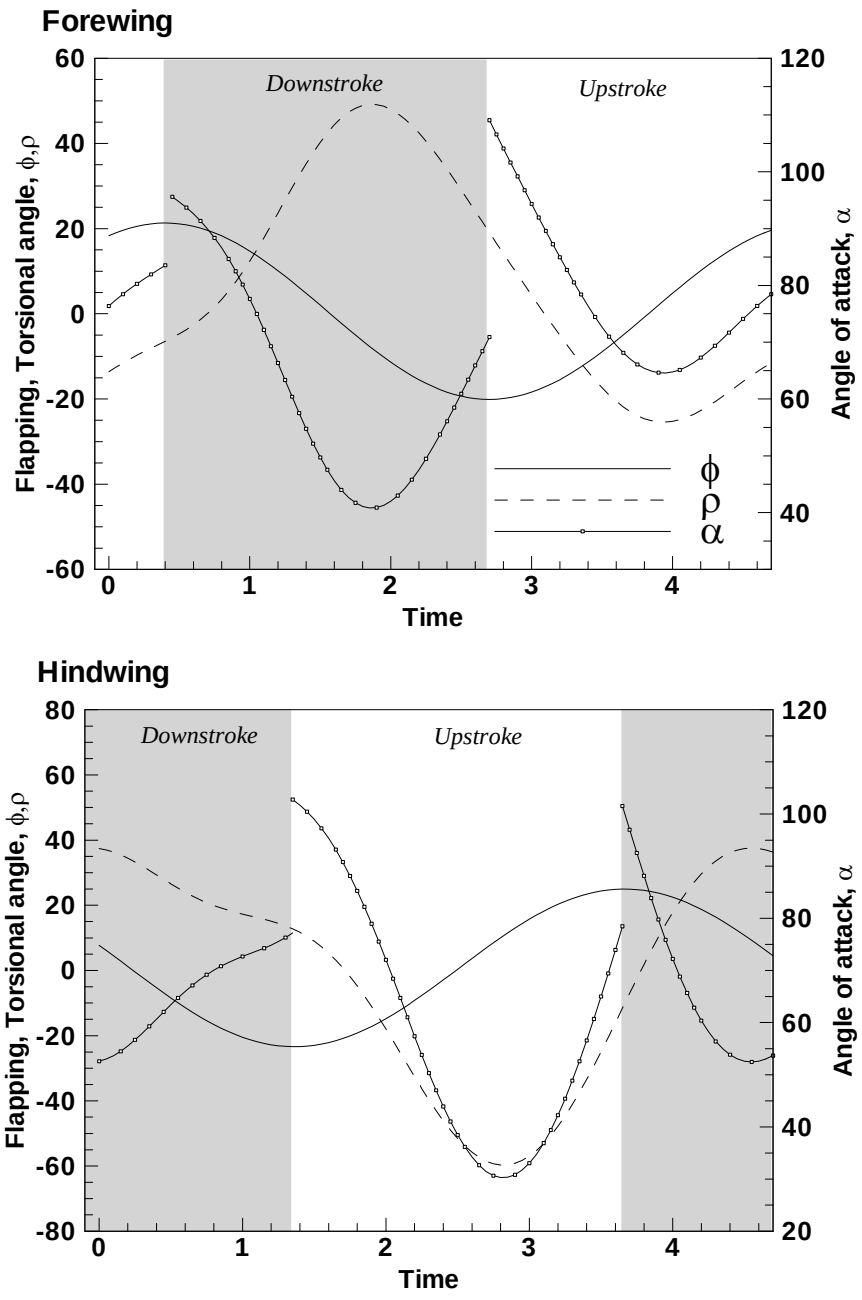

Fig.A.6 Variation of flapping and torsional angle of forewing and hindwing

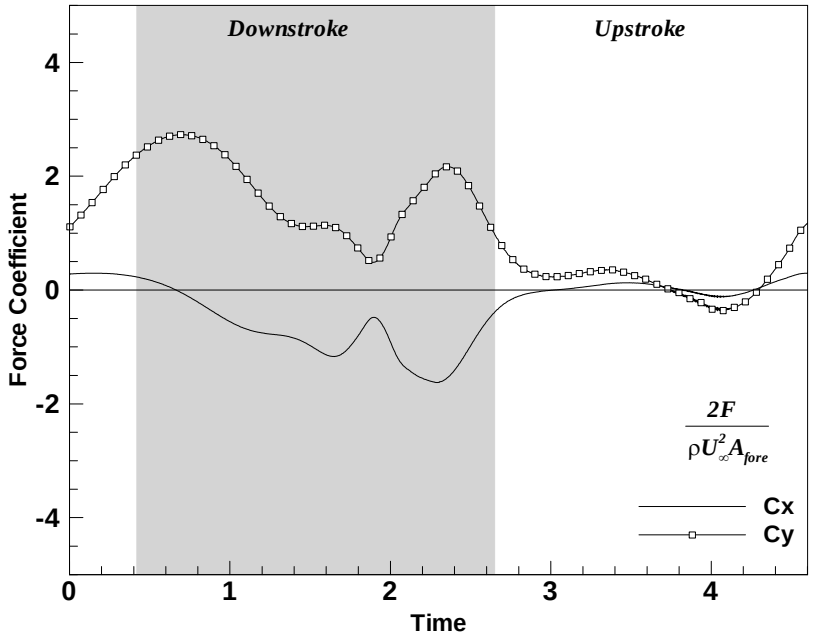

(a)

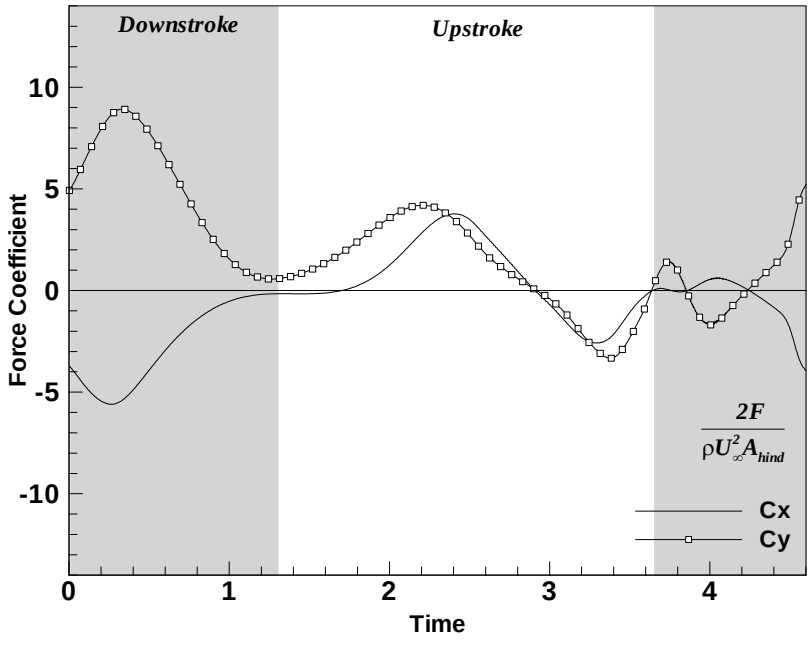

(b)

Fig.A.7 Forces generated in stroke plane by a) forewing and b) hindwing

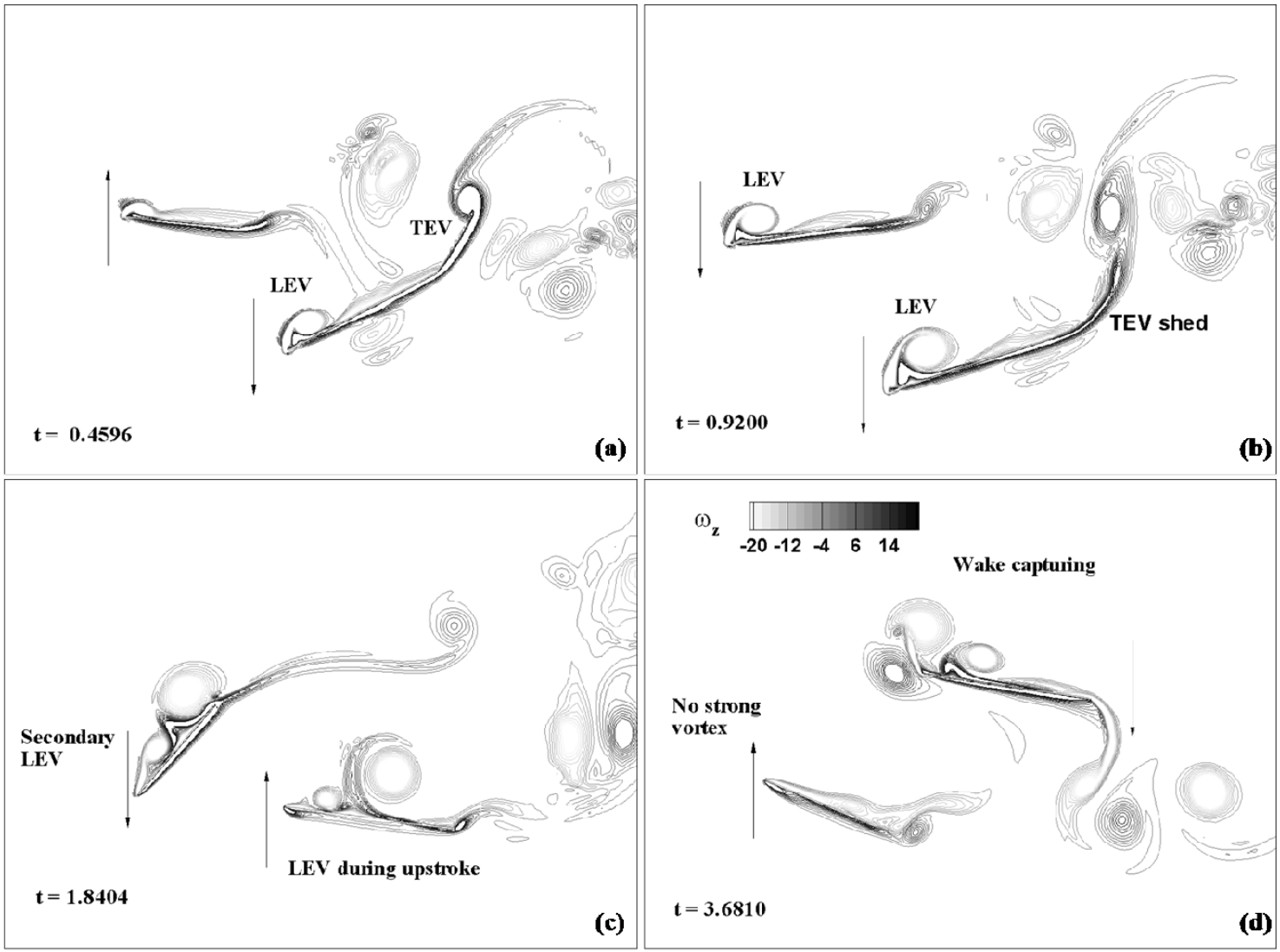

Fig.A.8 Vorticity contours at different time of flapping cycle. The arrows indicate the movement of forewing and hindwing

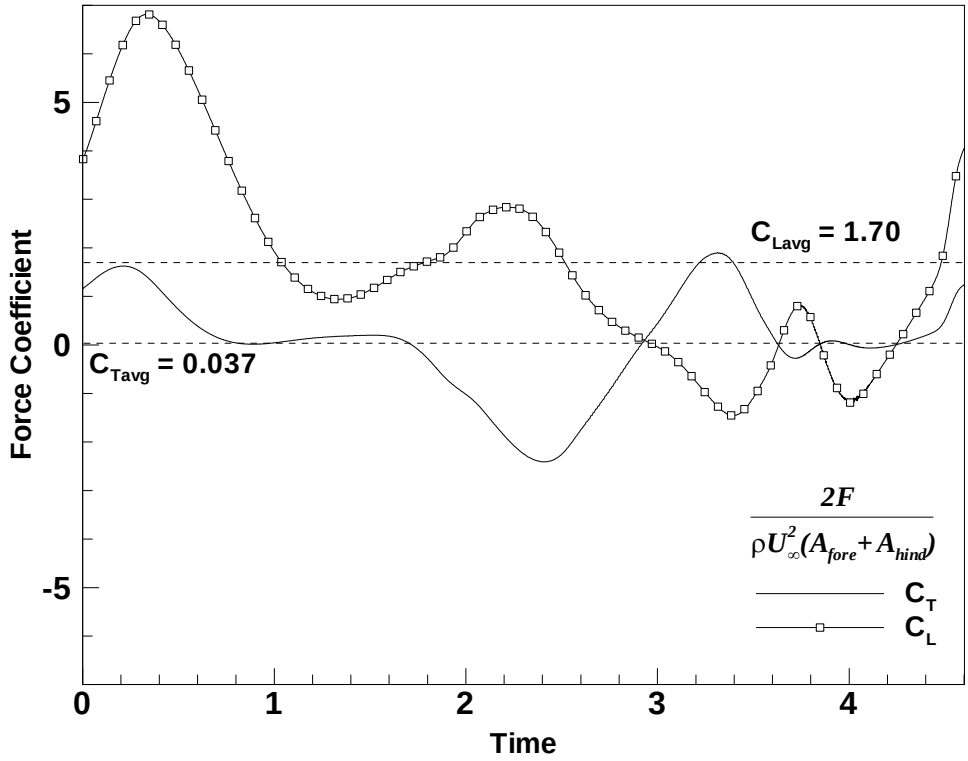

Fig.A.9 Total lift and thrust variation in a cycle

A.5. References

[1] Pedley, T. J. and Stephanoff, K. D. Flow Along a Channel with a Time-Dependent Indentation in One Wall: The Generation of Vorticity Waves. Journal of Fluid Mechanics 1985;160:337–367.

[2] Sadeghi, M. and Liu, F. Coupled Fluid-Structure Simulation for Turbomachinery Blade Rows. AIAA Aerospace Sciences Meeting and Exhibit, Reno, Nevada 2005;

[3] Pan, H., Pan, L. S., Xu, D., Ng, T. Y., and Liu, G. R. A Projection Method for Solving Incompressible Viscous Flows on Domains with Moving Boundaries. International Journal for Numerical Methods In Fluids 2004;45:53-78.

[4] Demirdzic, I. and Peric, M. Finite Volume Method for Prediction of Fluid Flow in Arbitrarily Shaped Domains with Moving Boundaries. International Journal For numerical Methods in Fluids 1990;10:771-790.

[5] Dickinson, M. H. and Götz, K. G. Unsteady Aerodynamic Performance of Model Wings at Low Reynolds Numbers. The Journal of Experimental Biology 1993;174:45-64.

[6] Ellington, C. P., Berg, C. V. D., Willmott, A. P., and Thomas, A. L. R. Leading-Edge Vortices in Insect Flight. Nature 1996;384:626-630.

[7] Dickinson, M. H., Lehmann, F.-O., and Sane, S. P. Wing Rotation and the Aerodynamic Basis of Insect Flight. Science 1999;284:1954-1960.